NUMERICAL ASSESSMENT OF PLASMA FORMATION AND POTENTIAL MITIGATION APPROACHES FOR HYPERSONIC BLACKOUT

by

PAWEL SAWICKI

M.S., New York University, 2017

M.S., University of Michigan, 2019

M.S., University of Colorado, 2022

A thesis submitted to the

Faculty of the Graduate School of the

University of Colorado in partial fulfillment

of the requirements for the degree of

Doctor of Philosophy

Department of Aerospace Engineering Sciences

2022

Committee Members:

Iain D. Boyd, Chair

Brian M. Argrow

John R. Cary

John A. Evans

Timothy K. Minton

Sawicki, Pawel (Ph.D., Aerospace Engineering Sciences)

Numerical Assessment of Plasma Formation and Potential Mitigation Approaches for Hypersonic Blackout

Thesis directed by Professor Iain D. Boyd

At high hypersonic flight velocities, the accompanying intense kinetic energies increase the temperature of the flow which in turn promotes chemical reactions that break up the air into its atomic and subatomic constituents. The presence of free electrons in particular has been known to impede the propagation of radio wave frequency electromagnetic waves. The corresponding disruption of the communication link to the hypersonic vehicle is commonly referred to as a communications blackout. While historically this disruption has been tolerated, with the onset of hypersonic glide vehicles maintaining continuous communication becomes paramount in ensuring mission success.

The development of any mitigation technique for blackout relies heavily on accurate computational simulations, specifically when predicting the electron number density. Thus, this work assesses the accuracy of plasma generation in the context of weakly ionized hypersonic flowfields around the RAM-C vehicle. Good agreement is observed to available flight data when the relevant flow physics are captured in the simulations. The sensitivity from the chemical kinetics models and transport mixing rules on plasma formation is investigated and found to vary considerably based on altitude, velocity, and position along the body.

The levels of ionization surrounding a slenderer glide vehicle shape along a representative equilibrium glide path are also evaluated for varying nose radii and cone half-angles. The work details a major trade-off with geometry selection. An increased nose radius and half-cone angle lead to more ionization throughout the flow but reduce the heat flux. Both quantities of interest are in good agreement with trends described in the literature. Varying flight trajectories also introduces a trade-off between downrange distance of the glide vehicle

and expected blackout periods.

From the study, a slender geometry is selected that is used as a platform for evaluating two popular categories of mitigation strategies for glide vehicles. It is universally observed that the electron density depleted at a faster rate in presence of water vapor injection, due to cooler air flow and ionization obstruction. However, it is also found that an increase of the mass flow rate is not linearly correlated to a higher reduction, due to the detrimental additions of atomic oxygen and hydrogen ions. The efficacy of water vapor additive fares well with that of liquid water injection during the RAM-C I flight. Water vapor injection provides a feasible means of blackout mitigation for glide vehicles but has key limitations to its practical use. Conversely, MHD techniques are postulated to have a negligible impact on the relatively low temperature, low degree of ionization flowfield conditions associated with glide vehicles. In such flows, the electrical conductivity levels are predicted to be low, resulting in small magnetic interaction parameters.

It is concluded that, instead of a universal answer to hypersonic blackout, it is far more likely that a solution has to be catered towards particular mission specifications.

To my parents.

ACKNOWLEDGEMENTS

The work presented in this dissertation represents more than just my own personal efforts over the last several years. Instead, this dissertation represents a culmination of decades of continuous support, encouragement, and mentorship from family, friends, professors, instructors, and colleagues. I would like to express my sincerest gratitude and deepest appreciation to all those that have made this work possible. The below is not indicative by any means of a comprehensive listing.

First and foremost, I would like to express great appreciation to my advisor, Professor Iain D. Boyd, for your knowldegeable guidance, gracious support, and invaluable patience throughout these years. I would also like to extend my gratitude to the other members of the committee, Professors Brian Argrow, John Cary, John Evans, and Timothy Minton for offering your valuable time in reviewing this dissertation.

I am extremely appreciative of the generous support provided by L3Harris Technologies for this research (under Grant AWD-20-02-0082). I am also tremendously appreciative of all the fruitful discussions and feedback provided by Drs. Joel Johnson, David Chester, and Marcus Ni. Your perspectives from a vehicle communications standpoint truly helped shape this dissertation. I additionally thank Professor Edward Thomas for joining these discussions and adding your expertise in plasma physics.

I would also like to acknowledge and thank members, both past and present, of the Nonequilibrium Gas and Plasma Dynamics Laboratory for their unhesitating assistance. Specifically, I thank Drs. Kyle Hanquist, Ross Chaudhry, Sam Chen, Nicholas Campbell,

Minkwan Kim, Michael Holloway, and Ronald Chan for an immeasurable amount of informative discussions, valuable guidance, and overall mentorship. I also thank current members Tommy Kava, Tim Aiken, Jens Rataczak, and Mitchell Wall for lending me a helping hand during different stages of this thesis.

Lastly, and most importantly, my family. To my sisters, Agata and Dorota, thank you both for continuously offering unending support and encouragement, and for paving the way for me throughout life. I am proud to be your little brother. And to my parents, bez Was obojga nie byłoby to w ogóle możliwe. Dla mojego tatusia, pokazałeś mi prawdziwego znaczenia ciężkej pracy i jaką wartość ma nauka. Widząc jak ciężko pracujesz każdego dnia, zainspirowałeś mnie abym się, tak samo jak Ty, nigdy nie poddawał i przez to, dałeś Mi siłe kontynuować w najdłuższych godzinach. Dla mojej mamy, nauczyłaś mnie aby marzyć wysoko, że żadne marzenie nie jest za duże do osiągnięcia jeśli się naprawdę chce. Zawsze popieralaś mnie w moich marzeniach i dlatego stało się to możliwe. Dziękuję Wam za wszystko.

CONTENTS

CHAPTER

APPENDIX

TABLES

Table

FIGURES

Figure

CHAPTER 1

INTRODUCTION

1.1 Radio Communications Blackout

Radio blackout describes a complete radio wave frequency communication link disruption. At sufficiently high flight velocities, a plasma layer may form around a hypersonic vehicle. The presence of free electrons in the flow field has been known to interrupt the transmission and reception of radio waves. While maintaining a communications link can be an essential part of navigation and control, the problem of blackout has nevertheless remained a widespread occurrence in a broad range of hypersonic flight profiles.

1.1.1 History and Prevalence of Blackout

When Guglielmo Marconi transmitted radio waves across the Atlantic Ocean for the first time in December of 1901, a troubled Lord Rayleigh could not account for how the radio waves followed the curvature of the Earth in any manner using simple plane wave transmission. An explanation continued to elude even the brightest minds at the time, as Nicholson, MacDonald, Love, Poincare, Van der Pol, von Rybczybski, Sommerfield, and many others launched a decades-long probe of the problem [1].

In 1912, within private correspondence, Pierce and De Forest were the first to coin the phenomenon where a ground wave was interfered with by the sky as "fade out"[1] [3].

---

[1] In 1940, Darrow speculated that "if the war had begun before its discovery, it would perhaps have been called a 'black-out.' Being discovered however some years before the war, it was and is called a 'fade-out.'" This is believed to be the first use of the term "black-out" in the literature describing this phenomenon [2].

It was not until 1924 however, when Larmor used Kennelly's and Heaviside's theories on the conducting nature of the "upper air," that the phenomenon was finally accurately attributed to a refraction of the radio waves caused by a large number of free electrons in the ionosphere [1, 3]. In the pursuing decades, as rocket development progressed, so too did the number of direct measurements describing the density and nature of the ionization in these atmospheric layers [4]. One rocket in particular, the V-2, not only played an immense role in characterizing the ionosphere and delivering the coup de grace on Rayleigh's inquisition [5], but also launched a new domain where the blackout problem still lingers today.

Figure 1.1: The two-stage Bumper rocket with a combination of a V-2 and WAC Corporal, launching into the hypersonic regime on February 24th, 1949. Image from the National Air and Space Museum [6].

Even before the WAC Corporal sounding rocket used a V-2 as its first-stage and became the first human-made object to fly well into the hypersonic regime (shown in Figure 1.1) [7], transmitting radio waves through an ionized flow was already of great concern for the telemetry team. However, these initial hypersonic blackout researchers were predominantly fixated on the ionization occurring within the rocket exhaust [8,9], even though it was already established that vehicles traveling at high enough velocities could create thermally ionized flows [10]. Nevertheless, with the advent of high-speed intercontinental ballistic missiles and human spaceflight in the ensuing decades, the communications blackout problem became a pressing concern, driving substantial efforts into understanding the deleterious effects of weakly ionized flows on the transmission of radio waves [11–16].

Table 1.1: Listing of various different hypersonic vehicles with their corresponding transmission frequency that suffered plasma-induced blackout.

Vehicle	**Manufacturer**	**Maiden Voyage**	**Leading Edge Radius**	**Blackout Frequency**	**[Ref.]**
Vostok	Energia	1961	1.22 m	VHF	[17]
Mercury	McDonnell Aircraft	1961	0.95 m	UHF/C-band	[18]
ASSET	McDonnell Aircraft	1963	0.08 m	VHF/C-band	[19]
Project FIRE	NASA	1964	0.34 m	VHF/C-band	[20]
Gemini*	McDonnell Aircraft	1964	1.15 m	VHF/C-band	[18]
AS-20x / Apollo	North American Aviation	1966	1.95 m	UHF/S-band/ C-band	[21, 22]
Soyuz	RKK Energia/Korolev	1966	1.10 m	VHF/UHF/S-band	[23, 24]
Trailblazer*	USAF/OSU	1967	0.16 m	X-band	[25, 26]
RAM-C*	NASA	1968	0.15 m	VHF/S-band/X-band	[27]
PAET	NASA	1971	0.46 m	VHF/C-band	[28]
Space Shuttle*	Boeing/Rockwell	1981	0.71 m	UHF/S-band	[29–31]
BSUV	U.S. Department of Defense	1990	0.40 m	S-band/C-band	[32]
OREX	NASDA	1994	1.35 m	L-band/GPS	[33, 34]
HYFLEX	NAL/NASDA	1996	0.40 m	VHF	[35, 36]
Pathfinder	NASA JPL	1997	1.33 m	X-band	[37]
ARD	ESA	1998	1.40 m	GPS	[38]
Genesis	Lockheed Martin	2004	0.75 m	UHF/GPS/L-band	[39, 40]
Huygens	Arospatiale	2005	1.25 m	Ka-band	[41, 42]
IRDT	ESA	2005	0.61 m	VHF	[43]
Stardust SRC	Lockheed Martin	2006	0.23 m	X-band	[44]
HAYABUSA	JAXA	2010	0.20 m	L-band	[45]
Dragon	Space-X	2010	1.80 m	GPS	[46]
Mars Science Laboratory	NASA JPL	2012	2.25 m	UHF	[47]
Orion	Lockheed Martin	2014	2.51 m	GPS	[48, 49]
ExoMars Schiaparelli	Thales Alenia Space/ ESA	2016	1.20 m	UHF	[50]
HSRC	JAXA	2018	0.42 m	GPS	[51]
Starliner	Boeing	2019	2.28 m	GPS	[52, 53]

Yet, for over seventy years of hypersonic flight the presence of a surrounding plasma layer has continued to plague communication. As Table 1.1 exhibits, plasma-induced blackout has become entwined with hypersonic flight. The vehicles in Table 1.1 represent a vast array of flight configurations, geometries, and mission objectives. The vehicles listed are mostly purposed for hypersonic re-entry, which has been indicative of hypersonic vehicle design as a whole. It is readily apparent that communications blackout has been experienced by a wide range of frequency bands (VHF to Ka-band) and within several atmospheric compositions (Earth, Mars, and Titan). Additionally, in Table 1.1, an asterisk (*) signifies that a blackout mitigation approach was used successfully for at least one mission. For Gemini GT-3, RAM-C I and III, Trailblazer II, and Space Shuttle missions after STS-41, blackout was avoided through material injection [54–57] and antenna placement [31].

1.1.2 Cause of Radio Wave Cutoff

1.1.2.1 Hypersonic Aerothermodynamics

In general, aerodynamic flight is categorized based on its flow velocity with respect to the speed of sound, neatly described by the Mach number. When the flow is faster than the speed of sound, or synonymously, at a Mach number greater than 1, a shock wave forms. Most flows in common everyday occurrences operate below the speed of sound and are described as subsonic, as Figure 1.2 portrays. As the flow velocity is increased, localized regions of acceleration may start to form, and a local shock appears at what is referred to as the critical Mach number. These velocities, where only a portion of the flow has developed a shock, are categorized as transonic. If the velocity increases further and the entire flowfield is greater than Mach 1, the flow is referred to as supersonic. The definitions all work well for these regimes as the aforementioned flows are all defined by the succinct physical phenomenon of a shock wave either occurring universally, locally, or not at all. However, as flow velocities increase well past Mach 1, the categorization becomes less delineated.

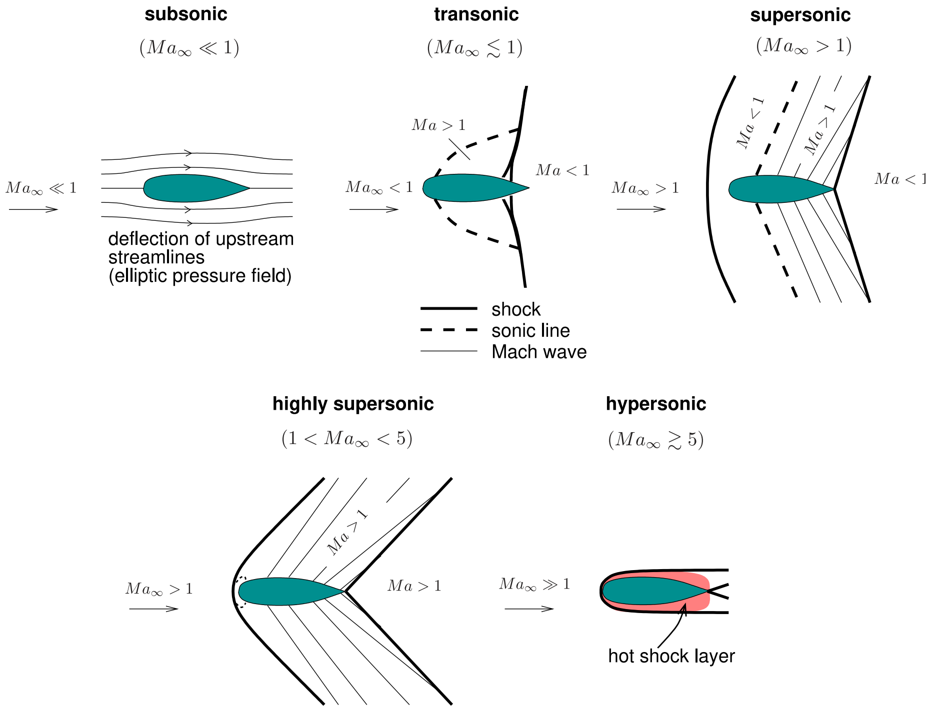

Figure 1.2: Transition across aerodynamic regimes. Image from Ref. [58].

Still, the need for a new flight regime came into the spotlight when aircraft and missiles matured well past the WAC Corporal in Figure 1.1 and brought with them entirely new aerodynamic problems. As Hayes and Probstein reasoned at the time:

> “Most of these problems arise because of extremely high flight velocities, and are characteristically different in some way from the problems which arise in supersonic flight. The term hypersonic is used to distinguish flow fields, phenomena, and problems appearing at flight speeds far greater than the speed of sound from their counterparts appearing at flight speeds which are at most moderately supersonic. The appearance of new characteristic features in hypersonic flow fields justifies the use of a new term different from the well-established term supersonic.” - Hayes and Probstein, 1959 [59].

While the general consensus is that these “hypersonic” flows occur at Mach 5, at a more fundamental level they are characterized as the velocity with which multiple of the following phenomena start to become progressively unavoidable. A hypersonic flow field generally exhibits thin shock layers, as the shock waves lie close to the vehicle surface. The flow also contains strong viscous interactions between the boundary layer and outer inviscid flow, which has a major effect on the boundary layer thickness, surface-pressure distribution (effecting lift and drag), and viscous dissipation where the boundary layer temperature, skin friction, and heat transfer are increased for the vehicle. The surrounding hypersonic flow field is also already at a significant temperature from a strong shock wave at these high velocities, as Figure 1.3 portrays with the isentropic flow equations of a calorically perfect gas. Further, if the shock-layer temperature is high enough, the fluid elements in the flow emit radiation and become nonadiabatic. The subsequent high rates of heating at the surface resulting from the shock wave, viscous dissipation, and radiation, require advanced thermal protection systems for the vehicle.

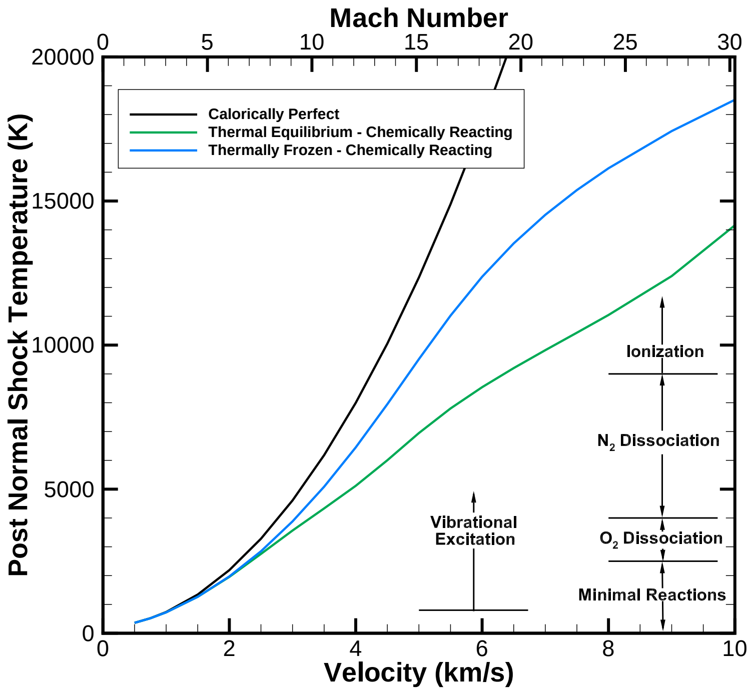

Figure 1.3: Temperature after a normal shock under atmospheric conditions (101 kPa and 272 K). Approximate temperature ranges of vibrational excitation, dissociation, and ionization at atmospheric conditions are also displayed.

These high temperature flows also correspond with a fundamental shift in the overlying gas dynamics. Whereas cooler flows can be assumed to be calorically perfect gases, high temperature gas dynamics gradually depart from this assumption as the thermochemical equilibrium restrictions break down. Shown in Figure 1.3 are the post-normal shock temperatures for a calorically perfect gas and two chemically reacting flow conditions at atmospheric conditions, calculated using NASA's Chemical Equilibrium with Applications (CEA) computer program [60]. Here, chemically reacting flows, or chemical nonequilibrium, are shown with two limits: thermal equilibrium and thermally frozen flows. As the relaxation of internal energy modes is driven by molecular collisions, thermal equilibrium assumes an infinitely large rate of collisions so that changes in flow properties lead to instant changes in internal energy. Conversely, thermally frozen flows are assumed to have no collisions and no changes occurring. Similar limits occur for chemical equilibrium and chemically frozen flows. In reality, due to the residence times of the gas molecules in the shock layer, considerations for thermochemical nonequilibrium must typically be made [61].

As it is implied in Figure 1.3, elevated temperatures within the shock layer can excite the internal energy modes of molecules and provoke chemical reactions between the different specie compositions. For example, for air held at 1 atm of pressure, at around 800 K the vibrational energy modes become excited. As the air increases to around 2500 K, the molecules of air start to dissociate, first directly with oxygen, then, through Zeldovich exchange reactions, atomic nitrogen starts to appear, and lastly, at around 4000 K, the nitrogen molecules directly dissociate. Finally, at around 9000 K the atoms of the air start to ionize, primarily first through associative ionization reactions [6].

While the excitation of internal energy modes has a direct role in the properties of the fluid and cannot be neglected, it is the chemical reactions, namely the ionization and stripping of free electrons, that inarguably influences the transmission of radio waves the most.

1.1.2.2 Ionized Flow Field

Even though there are free electrons present in a hypersonic flow field, it does not necessarily follow that the flow automatically qualifies as a plasma. Indeed, even at room temperature there are some free electrons floating around. As a gas has a wide distribution of thermal energies, an atom in room temperature air can become ionized, if, by sheer coincidence, a collision of high enough energy occurs. Using the Saha equation (Eq. 1.1), which assumes that the gas is in thermal equilibrium and fits a Maxwell-Boltzmann velocity distribution, it can be determined that a minuscule $10^{-120}\%$ of the air at room temperature is ionized [62]!

$$\alpha = \frac{n_e}{n_n + n_e} \approx \frac{2}{n_e}\left(\frac{2\pi m_e \mathrm{k_B} T}{h^2}\right)^{\frac{3}{2}} e^{\frac{-E_i}{\mathrm{k_B} T}} \tag{1.1}$$

In the Saha equation above, α is the degree of ionization, where it has been assumed in the denominator that $\mathrm{n_e}$, the electron number density, is small compared to $\mathrm{n_n}$, the number density of neutral particles. The equation also uses the Boltzmann constant, $\mathrm{k_B}$, Planck's constant, h, and the mass of an electron, $\mathrm{m_e}$. The exponential in the equation, with the ionization energy of the gas, $\mathrm{E_i}$, numerically expresses the fact that the probability of finding a high-energy atom needed for ionization collisions decay exponentially. The $\mathrm{n_e}$ in the denominator mathematically represents the dependency of recombination on the density of electrons [63, 64].

Although there are inherently numerous limitations to its use, the Saha equation can provide a rudimentary estimate to the degree of ionization in a high temperature gas. Figure 1.4 shows the Saha equation applied to nitrogen and oxygen gases at several number densities to ascertain the degree of ionization at select temperatures. It is readily apparent, through a comparison of Figures 1.3 and 1.4 that for temperatures and number densities typically seen in high-hypersonic flight (Mach 10+), the degree of ionization can become considerable.

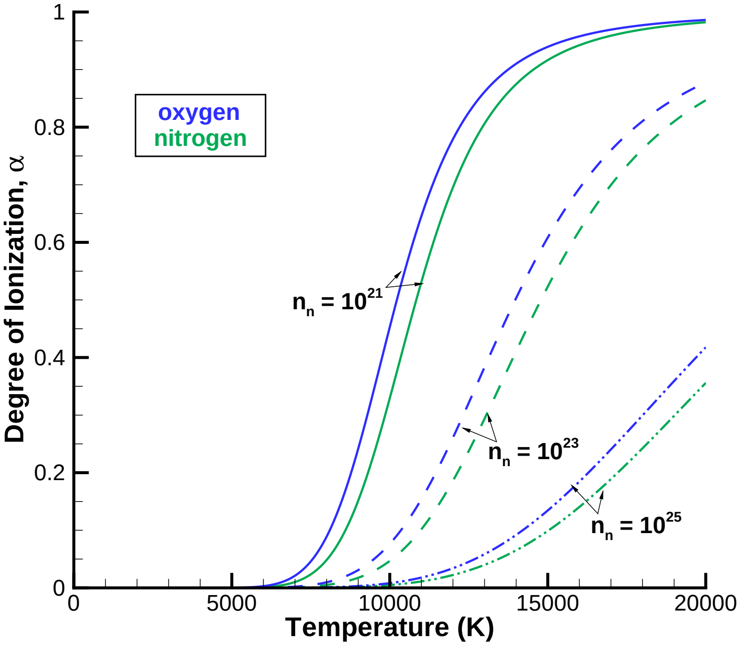

Figure 1.4: The degree of ionization calculated by the Saha equation for pure oxygen and pure nitrogen mixtures at number densities commonly encountered during hypersonic flight on Earth.

However, it has already been established that the mere presence of ionization does not necessarily qualify the gas a plasma. A useful definition is as follows: “A plasma is a quasi-neutral gas of charged and neutral particles which exhibits collective behavior. [62]” To understand this definition more clearly, two concepts must be explored further, specifically that of “quasi-neutrality” and “collective behavior.”

As nitrogen and oxygen atoms are stripped of their electrons during ionization processes, they gain an opposite charge. Since the rate of producing negatively charged particles (electrons) is matched with positively charged particles (ions) it can generally be assumed that $\mathrm{n_i} \approx \mathrm{n_e}$. However, due to the faster velocities of the electrons, a charge can accumulate on a vehicle surface which in turn produces regions of non-neutrality. These significantly nonneutral regions are referred to as plasma sheaths[2] and exhibit high electric fields. Therefore, an important criterion for an ionized gas to be a plasma is that the characteristic dimension (L_c) of the system should be much larger than the thickness of the sheath. Then, if charge accumulations are to occur, they will be shielded out in a distance shorter than the characteristic length, leaving the large majority of the plasma to be "quasi-neutral". An expression of the sheath thickness, or the Debye length, can be written as:

$$\lambda_d = \sqrt{\frac{\epsilon_0 k_B T_e}{n_e e^2}} \approx 69\sqrt{\frac{T_e}{n_e}} \tag{1.2}$$

where ϵ_0 is the permittivity of free space and e is the charge of one electron. It should be noted that as the electron number density is increased, the Debye length decreases, since each layer of plasma from the surface contains more electrons. Further, it is the electron translational temperature, T_e, that controls the Debye length, because, as was previously mentioned, electrons are more susceptible to charge accumulation at the surface. The Debye length is plotted in Figure 1.5 for electron number densities and electron temperatures commonly encountered during hypersonic flight. As quasi-neutrality requires that $L_c >> \lambda_d$, it is important to observe that the order of magnitude of the Debye length is much smaller than that of the normal characteristic lengths for hypersonic flows. The lengths given in Table 1.1 can be used as an order of magnitude reference.

The second criterion for a plasma is that it demonstrates collective behavior. In a neutral gas, the bulk nature of the flow is predicated upon the motion and collisions of the individual particles. Conversely, charged particles are capable of producing electromagnetic fields which can affect the motion of charged particles at large distances. This is what is referred to as collective behavior.

---

[2] It should be noted that the terminology "plasma sheath" has been misused in many hypersonic discussions, erroneously referring to the entire plasma layer [65].

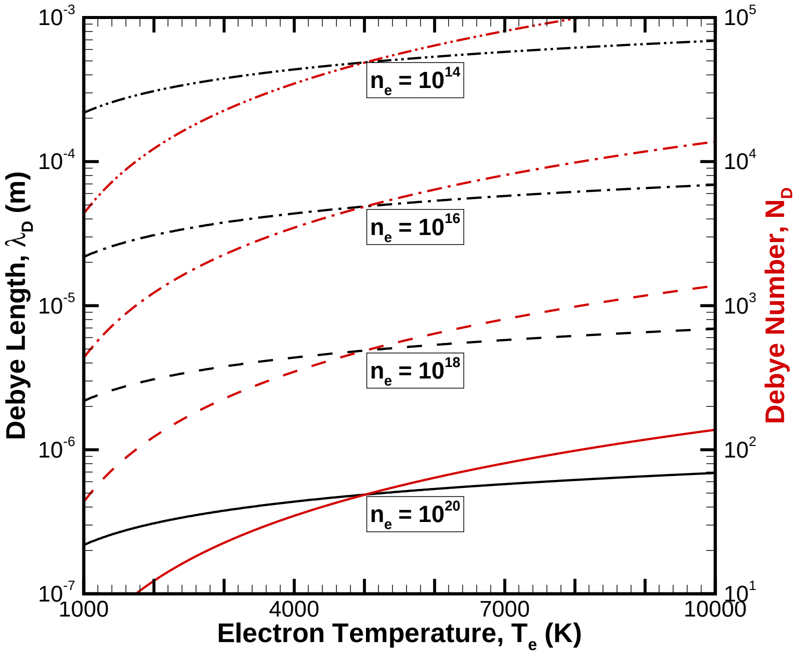

Figure 1.5: The Debye length and Debye number for electron number densities ranging between 10^{14} and 10^{18}.

To satisfy the criterion of collective behavior and ensure that the Debye length holds as a statistically valid concept, the number of charged particles contained within a sphere of one Debye length radius, or a Debye sphere, should be much greater than 1. An expression for what is referred to as the Debye number[3] is:

$$N_D = \frac{4}{3} n_e \pi \lambda_d^3 \tag{1.3}$$

The Debye number is evaluated for typical hypersonic flow electron number densities and temperatures and is shown in Figure 1.5. The $N_D >> 1$ criterion for collective behavior is satisfied for all cases shown except for high electron number densities at low electron temperatures, which are responsible for very small Debye lengths, and in turn lower the number of particles in the Debye sphere.

---

[3] Debye number is commonly referred to as the plasma parameter as they differ by only a factor of three.

A third condition that an ionized gas must satisfy to be considered a plasma requires that the charged particles do not collide with neutral particles so frequently that they are only controlled by these collisions [62]. It is therefore required that:

$$\omega_p > \tau_{en}^{-1} = \frac{\lambda_m}{\bar{v}} = n_n \bar{\sigma_T} \bar{v} = \nu_{en} \tag{1.4}$$

where ω_p is the plasma frequency, τ_en is the mean free time between electron-neutral collisions, λ_m is the mean free path, $\bar{\sigma_\mathrm{T}}$ is the total collision cross section averaged over all particles, $\bar{v}$ is the average particle speed, and ν_en is the electron-neutral collision frequency [66]. For the collisions between electrons and neutrals, the effective collision frequency can be expressed as [67]:

$$\nu_{en} = n_n \sigma_{en} \left(\frac{8 k_B T_e}{\pi m_e} \right)^{\frac{1}{2}} \tag{1.5}$$

where $\left(\frac{8\mathrm{k_B T_e}}{\pi \mathrm{m_e}} \right)^{\frac{1}{2}}$ is the average electron speed in a Maxwellian velocity distribution [66], and σ_en is the effective electron-neutral cross section given by a curve-fit of the form:

$$\sigma_{en} = a_s + b_s T_e + c_s T_e^2 \tag{1.6}$$

where the constants $\mathrm{a_s}$, $\mathrm{b_s}$, and $\mathrm{c_s}$ were obtained from curve-fits of experimental data at 5,000 K, 10,000 K, and 15,000 K and can be found for each electron-neutral pair in air in Ref. [68]. The effective cross sections are further confirmed in more recent laboratory experiments [69–71]. Equation 1.5 is plotted in Figure 1.6 for a range of individual specie number densities at an electron temperature of 10,000 K. The total number density of air expected in freestream conditions is calculated using the MSISE-00 atmospheric model [72] and is also shown in Fig. 1.6. It can be inferred that only at number densities expected of very low altitudes, does the collision frequency start to become significant. In fact, it has been regularly demonstrated that during the majority of a typical hypersonic trajectory the collision frequency is at least an order of magnitude smaller than the plasma frequency [73], and only starts to become significant at lower altitudes (approximately 35 km) [74,75]. Subsequently, the third condition is mostly satisfied during a typical hypersonic flight. Nevertheless, due to the role that the plasma frequency plays in communications blackout, it will be explored in more detail.

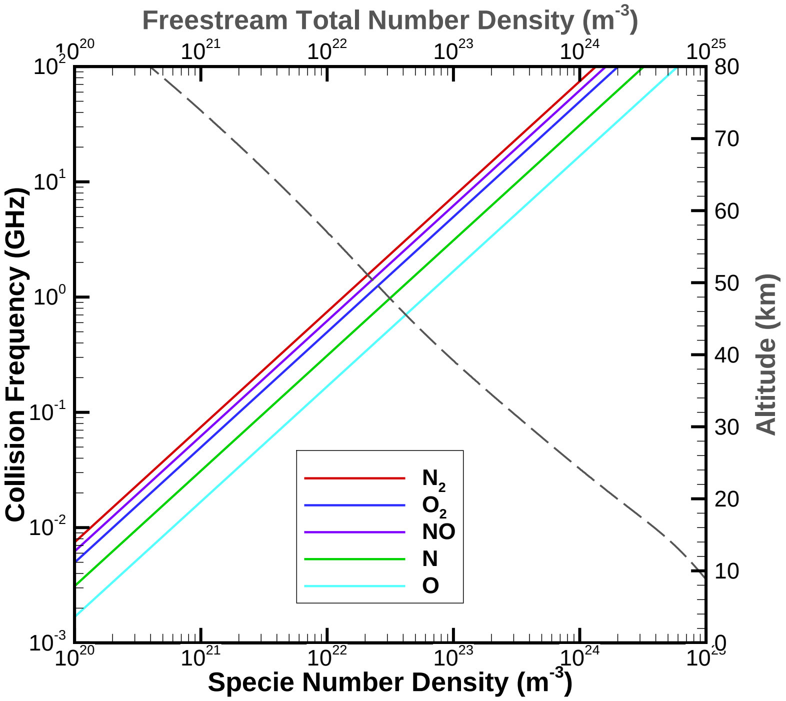

Figure 1.6: Collision frequencies of the various neutral air constituents at 10,000 K electron temperature. The total number density of the air is also plotted with a dashed line as a function of altitude.

Plasma Frequency

When electrons are displaced by an external influence, a restoring force is created in the form of an electric field, attracting the electrons and ions back to each other. Because of the relatively immense mass of the ions with respect to the system, typically 10^5 times more massive than an electron, the ions can be assumed stationary. As an electron advances towards an ion, it gains momentum, and due to the consequent inertial effects, the displaced electron will overshoot the equilibrium position. As the electron moves beyond the equilibrium position, an electric field will once again form and draw the electron back. The electron will continuously oscillate back and forth at a frequency that is a material property of the plasma. This frequency is called the plasma frequency.

To derive an expression for the plasma frequency, first consider a quasi-neutral, noncollisional, nonmagnetized plasma at rest, shown in Figure 1.7. The plasma is infinite in size. Thermal motions are assumed to be negligible, ions are fixed in a uniform distribution, and the plasma is at rest. Electron motion is restricted to one direction, which for this analysis will be the x-direction.

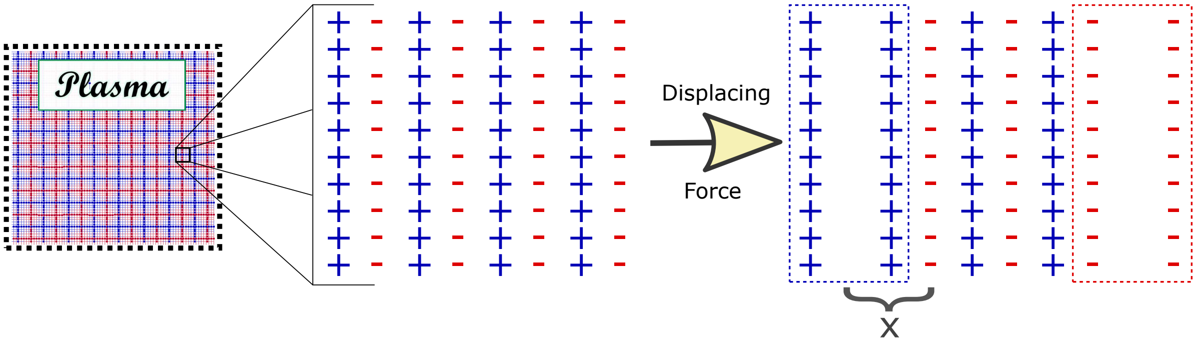

Figure 1.7: Diagram of a quasi-neutral plasma with equal densities of ions and electrons. Due to a displacing force the electrons have been displaced by a small amount x.

Now, consider a scenario where the electrons are displaced by a small amount, shown as x in Figure 1.7. A region of negative charge forms on the right side, while a region of positive charge forms on the left side. This forms what is analogous to two parallel charged capacitor plates with a total surface charge of $\pm en_e x$. Through Gauss's law, the electric field between the two charged plates can be expressed as:

$$E = \frac{en_e x}{\epsilon_0} \tag{1.7}$$

Using the linearized equation for the motion of an electron, which is valid as long as the velocity is small enough such that the quadratic terms are negligible, provides the following expression:

$$m_e \frac{\partial^2 x}{\partial t^2} = -eE = -\frac{e^2 n_e}{\epsilon_0} x \tag{1.8}$$

Rearranging Eq. 1.8 to match the equation of a simple harmonic oscillator, $\ddot{\mathrm{x}} + \omega^2\mathrm{x} = 0$, gives:

$$\frac{\partial^2 x}{\partial t^2} + \frac{e^2 n_e}{\epsilon_0 m_e} x = 0 \tag{1.9}$$

Since the ω term in the equation for a simple harmonic oscillator is the angular frequency of oscillation, the plasma frequency can be defined as [76]:

$$\omega_p = 2\pi f_p = \sqrt{\frac{e^2 n_e}{\epsilon_0 m_e}} \tag{1.10}$$

The plasma frequency is determined to only be dependent on the electron number density, an important observation in terms of hypersonic flight, where, as it has been discussed, there can be a significant amount of free electrons. The mathematical resemblance to the simple harmonic oscillator model is no coincidence. Physically, the oscillatory motion of the electron is similar to a mass on a spring system. The mass is analogous to the electron, the restoring elastic forces are analogous to the restoring electrostatic forces, and damped oscillation for a spring is analogous to collisions with other particles. The inverse of the plasma frequency can be expressed as an inertial time scale for the motion of electrons [77].

Electromagnetic Wave Interacting with a Nonmagnetized Plasma

To examine how a transverse electromagnetic wave traverses through a collisionless plasma without an applied magnetic field, the relevant Maxwell equations will be used, first with the Maxwell-Faraday equation:

$$\nabla \times \mathbf{E} = -\frac{\partial \mathbf{B}}{\partial t} \tag{1.11}$$

and the Ampere-Maxwell law:

$$c^2 \nabla \times \mathbf{B} = \frac{\mathbf{j}}{\epsilon_0} + \frac{\partial \mathbf{E}}{\partial t} \tag{1.12}$$

where **B** and **E** are the magnetic and electric field components of the electromagnetic wave, c is the speed of light (the phase velocity of the wave), and **j** is the current density. Taking the time derivative of Eq. 1.12 results in:

$$c^2 \nabla \times \frac{\partial \mathbf{B}}{\partial t} = \frac{1}{\epsilon_0} \frac{\partial \mathbf{j}}{\partial t} + \frac{\partial^2 \mathbf{E}}{\partial^2 t} \tag{1.13}$$

Inserting the curl of Eq. 1.11 into Eq. 1.13 and assuming a sinusoidal oscillation dependence, gives:

$$-\mathbf{k}\left(\mathbf{k}\cdot\mathbf{E}\right)+k^2\mathbf{E}=\frac{i\omega}{\epsilon_0 c^2}\mathbf{j}+\frac{\omega^2}{c^2}\mathbf{E} \tag{1.14}$$

where k is the angular wave number $(2\pi/\lambda)$, λ is the wavelength, and $\mathbf{k}$ is referred to as the propagation constant. If the wave travels in the x-direction, $\mathbf{k}$ will only have an x-component. For the transverse wave, $\mathbf{k}\cdot\mathbf{E}=0$, so Eq. 1.14 becomes:

$$\left(\omega^2-k^2c^2\right)\mathbf{E}=\frac{-i\omega}{\epsilon_0}\mathbf{j} \tag{1.15}$$

If the electromagnetic waves have sufficiently high frequency, where the inertial time scale of the ions becomes too large to react, they can be considered fixed. The current density $\mathbf{j}$ is solely dictated by electron motion and is described by:

$$\mathbf{j}=-n_e e\mathbf{v_e} \tag{1.16}$$

where $\mathbf{v_e}$ is the velocity of the electrons. Using a form of the linearized equation of motion of an electron, Eq. 1.8,

$$m_e\frac{\partial\mathbf{v_e}}{\partial t}=-e\mathbf{E} \tag{1.17}$$

and since it has been assumed that the oscillations are sinusoidal, the time derivatives can be replaced with $-\mathrm{i}\omega$, giving:

$$-i\omega m_e\mathbf{v_e}=-e\mathbf{E} \tag{1.18}$$

This equation can be solved for $\mathbf{v_e}$ and substituted into Eq. 1.16, which can then be used with Eq. 1.15 to yield:

$$\left(\omega^2-k^2c^2\right)\mathbf{E}=\frac{i\omega}{\epsilon_0}n_0e\frac{e\mathbf{E}}{im\omega}=\frac{n_0e^2}{\epsilon_0 m}\mathbf{E} \tag{1.19}$$

The electric field cancels out on both sides and the right hand side is recognizable from Eq. 1.10. This gives the classic dispersion relation for electromagnetic waves propagating in a plasma without an external magnetic field:

$$\omega^2 = \omega_p^2 + k^2c^2 \tag{1.20}$$

If a radio wave is transmitted at a frequency ω, the wavelength, $2\pi/\mathrm{k}$, in the plasma will be defined by a value imposed by Eq. 1.20. Consequently, as ω_p is increased, k is decreased, and ω will grow until k becomes zero and a “critical” plasma frequency is reached. As the wavelength in this case grows to infinity, the index of refraction in the plasma goes to zero, and a “cutoff” occurs[4] [62]. For larger values of ω_p, Eq. 1.20 can only be satisfied by an imaginary k value, i.e., the wave is evanescent and there is no propagation through the plasma medium.

It is important to describe a physical understanding of the how electrons interact with a radiating electromagnetic wave. It was already derived previously that electrons displaced by an external force will oscillate back and forth, at what was defined as the plasma frequency, until they are damped by collision with neutral particles. If the displacement is caused by an electromagnetic wave, the driving force will be periodic. At conditions normally seen in a hypersonic flow field, the frequency of collisions with neutrals that normally dampen the oscillatory motion are much lower than the electromagnetic frequency, or the driving force frequency [78].

When the driving frequency is much lower than the plasma frequency, the electrons will be influenced by the electromagnetic wave and will oscillate at the driving frequency. In turn the electrons produce both a forward and backward traveling electromagnetic wave, acting as a dipole radiator. As the forward traveling wave is out of phase with the original electromagnetic wave they both cancel out. The backward moving wave acts as a reflected version of the original electromagnetic wave. The thicker or denser the plasma, the more electrons present that can attenuate the original electromagnetic signal.

---

[4] Conversely, a “resonance” occurs when the wavelength goes to zero and the index of refraction becomes infinite.

When the driving force is equal to the plasma frequency, the original electromagnetic wave is completely reflected with no penetration present in the plasma. When the driving frequency is much higher than the plasma frequency, the inertial time scale for the motion of electrons is too slow for a substantial reaction.

1.1.3 Significance of Alleviating Blackout

As hypersonic vehicles can travel at substantial velocities, even a brief loss of signal (LOS) can occur over significant distances. A blackout of only a few minutes could easily correspond to a vehicle not being able to transmit or receive information for several thousands of miles. Maintaining continuous communication between these vehicles and ground control can be paramount in ensuring mission success, whether that means safe travel for crew members or an effective missile deployment.

Due to the ongoing and global nature of commercial, scientific, and defense hypersonic missions, it is expected that communication will rely on designated frequency bands based on existing regulations and infrastructure. Currently, frequency bands between 8.3 kHz and 275 GHz have been allocated for specific use based on auctions, available infrastructure, tradition, and physical constraints (antenna parameters, required capacity of the channel, use of ionosphere, rain fade, etc.). Allocations for specific frequency bands are generally allotted in accordance with the Federal Communications Commission (FCC) for civilian use and the National Telecommunications and Information Administration (NTIA), International Telecommunication Union (ITU), and the NATO Joint Civil/Military Frequency Agreement (NJFA) for military use [79].

Radio frequency bands according to the IEEE standard are shown in Figure 1.8. The VHF and UHF bands are generally used for many different types of satellites (137-138 MHz), military aircraft (225-380 MHz), standard frequency and time signal-satellite service (400 MHz), and voice communications, such as for Apollo (300 MHz) and the Space Shuttle (920 MHz). The L-band includes many Global Navigation Satellite Systems (GNSS) such as

GPS (1.23 and 1.58 GHz), the Russian GLONASS (1.25 and 1.60 GHz), and the European Galileo (1.28 and 1.58 GHz). The S-band involves many space operations and research (2.0-2.3 GHz), the unified S-band (2.29 GHz) that was used for telemetry in the Apollo missions, and is one of three frequencies (2.0-2.3 GHz, 13.7-15.0 GHz, and 22.5-27.5 GHz) available for communication with the Tracking and Data Relay Satellite System (TDRSS). The C-band and X-band are primarily used for data telemetry of research aircraft, deep space operations and military satellites. The Ku-, K-, and Ka- bands are involved in deep space operations, radar, and experimental communication. By plotting Eq. 1.10 and comparing with these frequency bands, Figure 1.8 shows just how significant a large plasma density can be in terms of deleterious effects on transmitting radio waves. A plasma density as high as 10^{19} m^{-3} can blackout all of the frequency bands that have just been discussed [79–81].

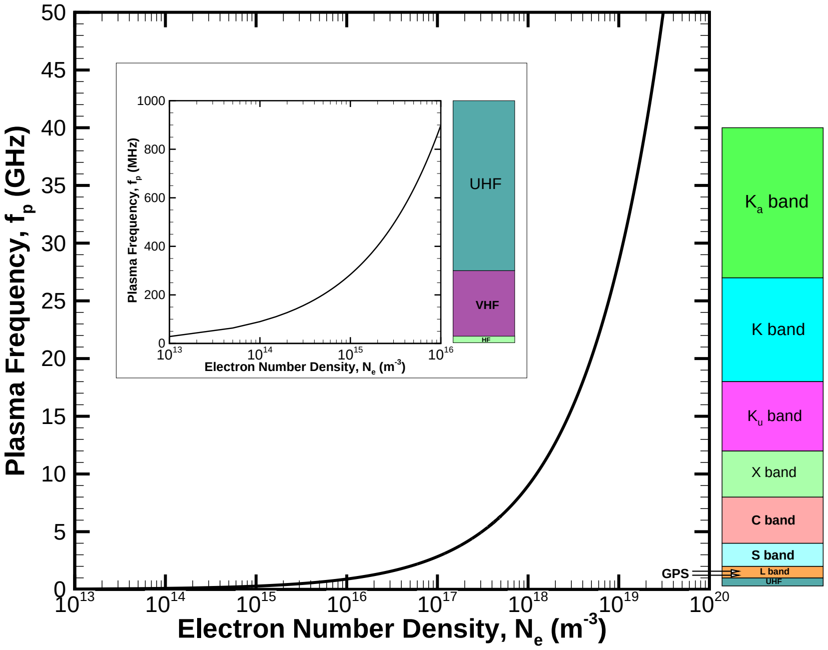

Figure 1.8: Plasma frequency as a function of electron number density. Corresponding IEEE microwave frequency bands are also shown.

A crewed spacecraft entering the atmosphere during re-entry endures the most critical periods of flight, undergoing maximum heat flux and maximum dynamic pressure, and requires an effective crew resource management. Voice communication between the crew and mission control, GPS tracking, guidance controls, and radar that is beneficial for a successful descent and landing are all heavily dependent on the successful propagation of radio waves to and from the vehicle [82]. Yet, during these critical stages, blackout can last for several minutes.

While re-entry and ballistic hypersonic vehicles follow predictable de-orbit or parabolic trajectories, a maneuvering vehicle, such as hypersonic boost glide or hypersonic cruise vehicles, could make tracking especially difficult during blackout. Further, while on-board guidance, navigation, and control (GN&C) can be performed by pre-programmed inertial control [83], this method lacks the precision and dissimilar redundancy that GPS-based positioning, navigation, and timing (PNT) provides. GPS also represents arguably the most difficult problem in terms of communicating through a plasma layer since GPS signals are at such a low power that they are normally below the noise floor and require a substantial time window to achieve the processing gain required for effective signal demodulation [84]. Further, loss of communication would severely limit the command and control of the vehicle, particularly with transmitting target and kill confirmation and thwart an adequate flight termination system (FTS) which would allow a mission abort if needed [85]. The latter is arguably one of the most important communication functions for defense applications as acceptance of a fully-autonomous, hypersonic UAV that relies solely on inertial or pre-programmed data would be highly unlikely.

Additionally, the testing and evaluation (T&E) of novel hypersonic vehicles with poor communication characteristics can be hindered prematurely at the flight test stage [86]. Standard procedures require real-time telemetry for flight safety and data collection, as a recovery of onboard recorders in case of flight failure is improbable [21]. Furthermore, a loss of signal (LOS) would make pre- or post-catastrophe analysis difficult; even a few milliseconds of telemetered data could prove invaluable in determining a source of failure. Indeed, a probe into the failed parachute deployment of the Genesis capsule was made more difficult without telemetered data during the blackout period and limited entry data measurements gathered on board the capsule [87]. Conversely, the investigation into the Columbia tragedy of 2003 was significantly aided by the telemetered data that was relayed using TDRSS. Unfortunately, voice communication with the crew and data from the 800 onboard sensors was terminated in vital moments due to switching between available TDRSS satellites [88]. Debris collected by searchers, specifically the Modular Auxiliary Data System, was crucial in filling a 30-second gap in lost data, especially that of the left-wing leading-edge spar thermocouples.

Although few serious disasters have occurred as a result of blackout, in order to ensure vehicle and passenger safety, complete data collection, and mission success, it is important that solutions are developed to overcome a loss of signal.

1.2 Review of Mitigation Approaches

Although there are currently no proven blackout amelioration techniques, a cornucopia of possible solutions have been proposed, analyzed, and tested. These techniques primarily try to avoid blackout through a vast assortment of strategies, including reducing the number of electrons around the antenna, restricting the motion of the electrons, exploiting properties of the plasma to generate detectable signals, or physically avoiding the plasma altogether.

Since these techniques are so diverse, it is fitting to categorize them. A classification scheme similar to that used in Refs. [75, 84] is employed herein. Active techniques involve manipulating or exploiting the surrounding plasma through specialized onboard equipment that requires more power, maintenance, or active monitoring than is typically required of a hypersonic communication system. Passive techniques take a more “laissez faire” approach and are generally current considerations of a typical communications link design. While mission design parameters such as vehicle and trajectory selection have been categorized as passive techniques in the past, it is highly unlikely that these will change solely based on overcoming blackout and instead should be considered drivers of what is required of a blackout mitigation scheme. Additionally, during the T&E stage of mitigation techniques, it should be assumed that little input will be given to the design parameters [84]. To emphasize this further, these techniques are categorized on their own. Some of the blackout mitigation approaches have been sorted using this classification and are cataloged in Figure 1.9. Several of the more promising techniques are highlighted with discussion below.

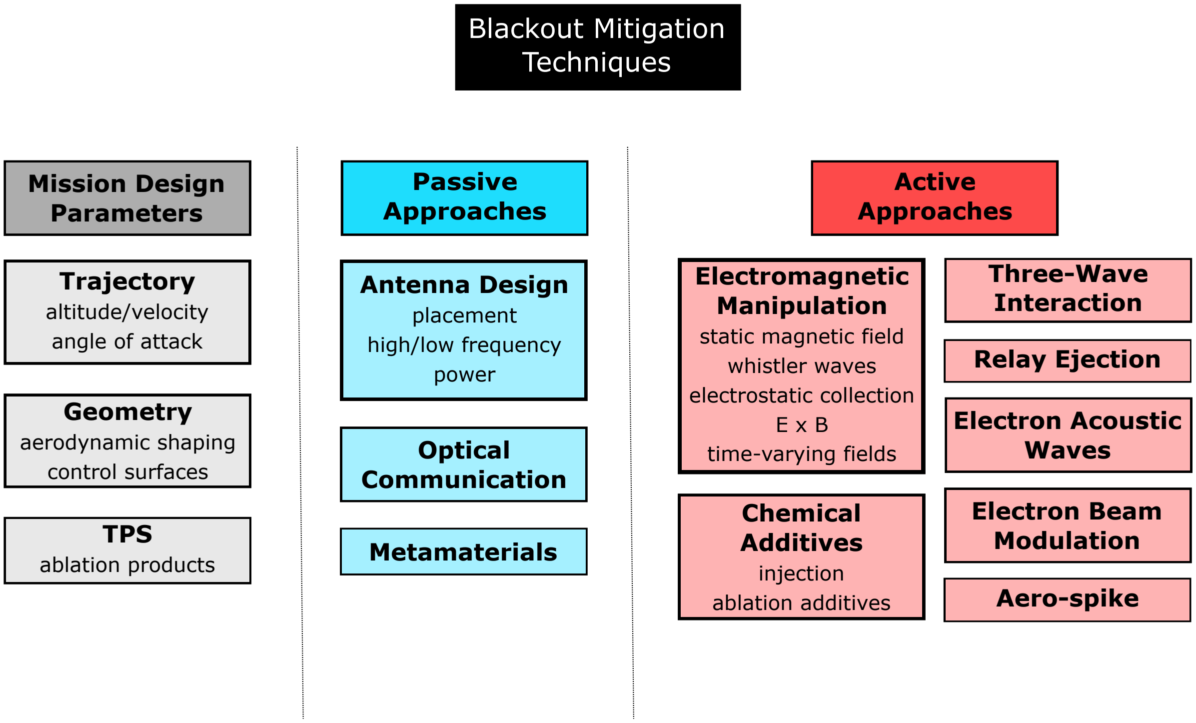

Figure 1.9: Survey of blackout mitigation techniques.

1.2.1 Mission Dependent Parameters

Flight Trajectory

The flight trajectory of a hypersonic vehicle defines the velocity, altitude, and attitude that the vehicle will experience for a certain time frame. In turn, the velocity and altitude correspond to a particular freestream Mach number, temperature, pressure, and density. The

Mach number will determine the strength of the leading shock, which along with the other freestream conditions and shape of the vehicle, will translate to a post-shock temperature (see Figure 1.3) and number density of each constituent. In turn, the selected flight trajectory has a dominant role in the ionization of the air.

The flight profile will also determine the duration of a communications blackout, as vehicles that maintain a high velocity-high density trajectory will subsequently endure a dense plasma for a longer time interval. Additionally, based on a required lift-to-drag ratio (L/D) and any heat transfer constraints in relation to a desired trajectory, the vehicle will fly at an angle of attack which will create regions of high plasma on the windward side and diminished plasma on the leeward side that can possibly be taken advantage of.

Although all of these parameters highly influence the number of electrons in the flow and in turn the presence of a blackout, other design drivers such as maximum heat flux, desired deceleration profile, and vehicle range take precedence.

Vehicle Geometry

Just like the trajectory, the shape of the vehicle will always have a substantial influence on the amount of plasma needed to be overcome with a mitigation approach. Depending on the vehicle geometry, the shock layer and corresponding flow field properties can alter considerably. If the vehicle is slender with a sharp nose the attached shock will be a weak oblique shock with a thin shock layer and less of the kinetic energy will go into the internal energy of the surrounding air and more into heating the surface of the vehicle. Blunter, capsule-shaped vehicles produce high flow deflection angles and will form a detached bow shock in front the body [89]. The curved bow shock ranges from a normal shock wave on the stagnation streamline and becomes weaker at larger streamwise distances. This strong shock wave will convert more of the kinetic energy to internal energy in the flow field and less into heating the vehicle. As stagnation point heating is consequently inversely proportional to the square root of the nose radius [6], vehicles expecting high kinetic energies are ubiquitously blunter to limit surface heat loads. In turn, the internal energy of the blunt body flow field increases which leads to more ionization. As the bow shock has a larger standoff distance, the plasma layer is also thicker than that of a sharp-nosed body.

Alas, the logical trade-off of heat load relief over a less ionized flow field is the primary reason that blackout mitigation techniques must be designed for a particular vehicle shape rather than a vehicle shape designed to mitigate blackout.

Thermal Protection System

As discussed in Section 1.1.2, the high heat loads commonly imposed on hypersonic vehicle surfaces required advanced thermal protection systems (TPS) which may come in the form of ablative materials. Ablation is a means of energy management based on physicochemical transformations of solid substances by convective or radiative heat flux [90]. Generally, as the heat is conducted into the surface, polymers in the ablative composite begin to decompose, release volatile gases, and form solid carbonaceous char, in a process called pyrolysis. The charred surface reacts with the boundary layer and causes a change in the vehicle geometry by either intumescence caused by a buildup of pyrolysis gases or recession caused by melting, vaporization, oxidation, sublimation, or spallation [91]. A change in geometry, as discussed, can affect the shape of the shock layer and subsequent generation of plasma.

This geometry change however has a minor impact on the plasma when compared to the contamination of the flow field by pyrolysis gases and removal of the surface char layer. Depending on the composition of the ablative products, the electron number density can either increase or decrease in the flowfield. The AVCOAT heat shields of space-race era capsules included trace amounts of easily ionized alkali metals [18, 92], which resulted in more plasma generation than expected. Conversely, modern heat shields produce far fewer of the ionizable metal contaminants. Instead, carbon from the ablative material oxidizes and consumes a large amount of the oxygen in the stagnation region, which in turn hinders the production of free electrons [44]. The ensuing increase in neutral particles from the ablation also results in the collision frequency of the plasma being increased [93]. Consideration of ablation products is especially important when designing communication links that propagate through the wake region which can contain circulation regions where the ablation products can accumulate.

1.2.2 Passive Techniques

Antenna Design

Antenna Frequency: As the antenna frequency is cutoff when it is lower than the plasma frequency, an intuitive amelioration approach is to simply use a higher antenna frequency. However, to be a universal solution for the possible plasma densities that can occur in hypersonic flight, this technique would require frequencies well into the K-band. While a relay link could be setup with TDRSS, this is not an approach that would allow for GPS signal reception. A new, custom-built PNT satellite ecosystem would be inherently cost prohibitive as a present-day solution. An additional concern for this approach is the high atmospheric attenuation and rain fade that is associated with high frequencies [94, 95]. Moreover, high frequencies result in higher free-space path loss driving power constraints, require a significant reduction in antenna aperture, and increase the pointing accuracy requirements [96].

A contrasting approach of using very low antenna frequencies also represents a possible solution [97]. An electromagnetic wave with a frequency lower than the plasma frequency exponentially decays over a nonzero skin depth, $\mathrm{d_s} \propto \mathrm{c/w_p}$. For a propagating frequency that is lower than both the plasma frequency and the collision frequency, the plasma behaves more like a conducting medium, and the skin depth is given by [98]:

$$d_s = \frac{c}{\omega_p}\sqrt{\frac{2\nu_{en}}{\omega}} = 7.52 \times 10^6 \sqrt{\frac{\nu_{en}}{\omega n_e}} \tag{1.21}$$

which increases as the radio frequency decreases or the collision frequency increases. Therefore, in cases where the plasma layer is thin, a large wavelength radio wave only traverses through a fraction of the required skin depth that would fully attenuate it. However, even when such a wave propagates through the plasma it still has a higher attenuation coefficient than frequencies slightly above the plasma frequency. From Eq. 1.21, in order to use such an approach, it is required that the trajectory involves a highly collisional plasma, where the collision frequency increases as rapidly as the electron density. Additionally, such a technique is not a solution for GPS reception, severely limits link bandwidth with a very low bit rate, has to also account for ionospheric attenuation, and involves large antennas that might not be suitable for hypersonic vehicles.

Antenna Power: A logical, “brute force” approach to overcoming the attenuation from the plasma is by simply increasing the applied power. However, increased power generates intense electric fields that can create an electrical breakdown of the exposed high temperature gases surrounding the antenna, causing further ionization and dissipating large amounts of the radiated energy. Additionally, if the antenna was well-matched before the breakdown occurred, the self-generated plasma would cause a significant mismatch. Thus, there is a limit on the power that can radiate through the sheath, irrespective of the power delivered to the input terminals of the antenna [99], unless complex adaptive impedance matching signal processing techniques are applied. These techniques typically require a high computational load at the expected rate of impedance change and thus translate into high size, weight and power trade considerations.

Antenna Location: Due to its unique geometry and high angle of attack, the Space Shuttle addressed its original 16-minute blackout period by utilizing antennas in areas where plasma generation is low [82]. These top, aft-body locations necessitated the formation of TDRSS because direct communication with the ground was infeasible. The data would then be relayed from TDRSS to either ground stations at White Sands Complex, NASA Goddard, or the Guam Remote Ground Terminal [100].

Another, more extreme derivative of this mitigation scheme is to use a probe containing an antenna that is long enough to physically surpass the plasma layer, either at the bow shock or the downstream region [75, 101]. However, such an antenna design would require considerable cooling to survive the tremendous heat fluxes. An extended shape into the bow shock could also produce undesirable heating on the downstream vehicle.

This type of mitigation methodology may prove to be the simplest solution to the blackout problem, i.e., taking advantage of locations in the flow field containing low plasma generation with proper antenna placement. Unfortunately, it cannot be used with most hypersonic spacecraft where the plasma envelopes the entire vehicle. Additionally, a rotation of the vehicle could also have negative consequences. Multi-path phenomena from the wake and plasma layer must also be considered with an aft side antenna placement, but their effect can be reduced using array antennas capable of forming multiple beams [75]. The further that the plasma extends beyond the vehicle the more it acts as a directional waveguide that in addition to generating multiple interfering paths, reduces the effective antenna beamwidth. As the vehicle maneuvers, LOS to a particular satellite is limited. This increases the frequency of loss of signal, propagation loss and the number and frequency of required reacquisition. Regardless of the disadvantages in its unaccompanied use, antenna placement will surely be a factor in mitigating the blackout problem.

Optical Communication

Optical, or laser, communications utilize the entirety of the electromagnetic spectrum through the use of optical wavelengths to transmit signals. Originally suggested by Poss in the 1950s, the transmission from an optical system for hypersonic communications is independent of the plasma properties, making it a viable option to traverse the plasma layer when radio communications cannot [102]. While high frequency radio communication is limited by atmospheric attenuation, in the wavelength region between 13.0 μm and 0.3 μm, referred to as the optical region, there are various windows available that can be used to combat attenuation [102]. In particular, in the near-infrared region (NIR), the minimum atmospheric radiation absorption occurs between wavelengths of 1.3 μm to 1.5 μm [103]. This region is starting to be used for satellite communications [104], and a wavelength of 1.55 μm has been demonstrated in shock tube experiments for use in reliable laser communication across a plasma layer [103, 105].

While laser communication can easily penetrate the plasma around hypersonic vehicles [106], the interactions between the carrier wave and the shock layer in terms of optical distortions, refractions, and radiation interference must be considered [107–109]. Further, while the propagation of lasers can transmit through plasma with little attenuation, the presence of ablation particulates can result in intensity fluctuations [110]. The use of optical communications has historically shown challenges with beam pointing, efficient transmitters and receivers, and high bandwidth processing. This solution is also not a GPS solution, has unique public safety concerns when it is ground based, and there is limited infrastructure currently in place. Nevertheless, this blackout mitigation technique has shown notable promise, as advantages include extremely narrow beams with small apertures, low probability of intercept, difficulty to jam, and the spectrum currently remains unregulated. Optical frequencies also allow for high channel throughput exhibited by the Lunar Laser Communications Demonstration which sent high definition video and telemetry at 622 Mbps [104].

Matching Schemes

Another way of looking at the interaction between a plasma and an electromagnetic wave is to consider the plasma as a material with a corresponding permittivity, ϵ, and permeability, μ. For a simple antenna case, an infinitesimal dipole driven by a current I_0 at a frequency f_0 and embedded in a dielectric medium is considered. The complex power for such an antenna can be expressed as [111]:

$$P = P_{rad} + iP_{reac} = \oiint \left(\frac{1}{2}E_\omega \times H_\omega^*\right) \cdot \hat{r}dS = \left(\frac{I_0 l}{\lambda}\right)^2 \frac{\eta\pi}{3}\left[1 - i\frac{1}{(kr)^3}\right] \tag{1.22}$$

where it is written as a combination of the active power, $\mathrm{P}_{\mathrm{rad}}$, which describes the radiated electromagnetic energy emitted by the antenna, and the reactive power, $\mathrm{P}_{\mathrm{reac}}$, which describes the stored energy between the electric and magnetic fields in the near field. The wave impedance, η, wavenumber, k, and wavelength, λ, are related to the permittivity and permeability as [112]:

$$\eta = \frac{\sqrt{\mu}}{\sqrt{\epsilon}} \qquad ; \qquad \lambda = \frac{1}{f_0\sqrt{\epsilon\mu}} \qquad ; \qquad k = \omega\sqrt{\epsilon\mu} \tag{1.23}$$

As the permittivity and permeability can be negative values [113, 114], there are four distinct combinations that categorize materials [115]: (i) Double-Positive (DPS) media where the permittivity and permeability are both positive, (ii) Epsilon-Negative (ENG) media where only the permittivity is negative, (iii) Mu-Negative (MNG) media where only the permeability is negative, and (iv) Double-Negative (DNG) media where both the permittivity and permeability are negative.

When the dielectric medium surrounding an antenna is a DPS material, viz., atmospheric air, the wavelength, wavenumber, and wave impedance of the antenna are all positive (Eq. 1.23), resulting in a positive $\mathrm{P_{rad}}$ and a negative $\mathrm{P_{reac}}$, via Eq. 1.22. In other words, a surrounding DPS material acts as a capacitive element of an antenna circuit. A similar result occurs with a surrounding DNG material, though DPS and DNG media are different in the direction that the phase accumulates [116]. On the other hand, when either the permittivity or permeability are negative, the wave impedance and wavelength are both negative imaginary numbers, while the wavenumber is a positive imaginary number [112]. This leads to the $\mathrm{P_{reac}}$ being the only non-zero power component, i.e., the dielectric material acts as an inductive element. The electromagnetic radiation of the antenna can no longer pass through.

Using a Drude-Lorenz model the permittivity can be related to the plasma frequency as [117]:

$$\epsilon = \epsilon_0 \left(1 + \frac{\omega_p^2}{-\omega^2 + i\omega v_{en}} \right) \tag{1.24}$$

and the permeability as:

$$\mu = \mu_0 \left(1 + \frac{\omega_{pm}^2}{-\omega^2 + i\omega \nu_m} \right) \tag{1.25}$$

where ω_{pm} and ν_{m} are the magnetic plasma frequency and magnetic collision frequency, respectively, [117]. It is immediately apparent that a non-collisional, non-magnetized plasma can become an ENG material when the plasma frequency is larger than the antenna frequency, an analogous result to Eq. 1.20.

In some very specific conditions, it has been shown that the surrounding plasma sheath can actually enhance the antenna radiation [118, 119]. This most likely occurs as a result of resonance between the inductive plasma sheath element and the capacitive surrounding air. Although these resonant conditions are rarely, if ever, met in hypersonic flight, a proposed mitigation scheme uses structural materials that can replicate these resonant conditions with their specific material properties. Such artificial materials are called plasma metamaterials [114].

These metamaterials use sandwiched layers of MNG and ENG meta-structures, combined with the plasma ENG medium, to create an equivalent DPS or DNG composite [112, 120]. When the match is exact, the composite is transparent for radio waves. One such approach that uses split-ring magnetic resonators (MNG media) and capacitively loaded strips (ENG media) to match the ENG plasma region has shown enhanced transmission properties for a unidirectional Huygens antenna in analytical studies [115].

Although this technique would theoretically allow for perfectly radiated performance characteristics of an antenna, many practical disadvantages arise. Although the far-field intensity performance is increased by this method, many other important antenna properties may degrade, such as an increase in boresight error and sidelobe levels. For lower frequency bands, the plasma may be in the antenna's near field, which requires enhanced impedance matching techniques. Further, the metamaterial properties must be continuously tuned to establish a match with the ever-changing plasma thickness and permittivity. It was also shown that at large plasma layer heights, the communication bandwidth decreases significantly where only necessary telemetry for brief periods can be transmitted. Additional significant complexities span from the aerothermodynamic effects of incorporating such a material into the skin of the craft. It is a challenge to design a metamaterial that exhibits the necessary electromagnetic and heat-resistant properties.

1.2.3 Active Techniques

Three-Wave Interaction

Another proposed mitigation method makes use of the nonlinear plasma properties themselves. By using a high frequency, intensive electromagnetic pump wave interacting with the carrier signal within the nonlinear plasma, a backscattered wave is created [121]. In other words, the interactions of three waves, namely a stimulus signal, the plasma oscillation, and the carrier signal, generate another signal that can be used for communication purposes. This three-wave interaction is similar to Raman scattering and is the reason why the scattered wave is referred to as a Stokes wave, where the frequency of this wave is $\omega_{\mathrm{s}} = \omega_{\mathrm{p}} - \omega$ [122]. An analogy can also be made that treats the pump wave as a local oscillator and the plasma as a mixer.

The advantages to this technique are clear. As the ratio of power flux of the Stokes wave is around 1%, even the reception of GPS signals is possible with a very sensitive receiver [122]. However, the stimulus signal must be well above the plasma frequency and the thickness of the plasma sheath must be enough to create the backscattered Stokes wave. Additional concerns arise from collisional damping, sensitivity to the time-varying non-uniform properties of the plasma, very short range associated with the resonance of the three-wave interactions, and power requirements for generating the pump wave.

Chemical Additives

The electron density is the only controllable parameter influencing the plasma frequency, as seen in Eq. 1.10. Accordingly, a material additive scheme generally attempts to lower this value by adding chemicals into the flow field, whether through direct injection or via releasing pyrolysis gases or intentional spallation during ablation, that can: i) attach with electrons, ii) thermally quench the hot air flow, iii) provide catalytic surface sites that promote electron-ion recombination, or iv) retard the production of plasma [123, 124]. Chemicals, such as electrophilic atoms and radicals, which possess a large electron affinity can readily absorb the free electrons. Electrophilics are generally halogen or halogen-based compounds, such as sulfur hexafluoride [SF_6], and attach electrons either through direct three-body attachments or dissociative attachments [125]. The basic principle behind thermal quenchants is to lower the temperature of the surrounding flow field which in turn lowers the electron number density required to attain equilibrium. In other words, if the flow field could at all times be in equilibrium, a reduction in temperature would directly correspond with a depletion in electrons [126]. However, the flows of interest are likely to be in nonequilibrium, where the finite rates associated with the electron-ion recombinations dictate the efficacy of an injected coolant. Nevertheless, chemicals with high heat capacities, such as hydrogen, ammonia, and water are good thermal quenchants [124]. Additionally, as dissociating reactions are generally endothermic, chemicals with high heats of atomization, such as propane, propylene, and ethane, can also serve as suitable quenchants. Both liquid and solid particulates can serve as recombination surfaces for positive ions and free electrons. Since electrons are more likely to hit these surfaces, the particulates become negatively charged, repelling additional electrons and attracting ions. These particulates can then be considered spherical Langmuir probes at floating potential, where the rate of ion collisions matches the rate of electron removal [127]. Micron-size refractory dust particles, composed of compounds like carbon black, silica, and metallic oxides, can be injected into the plasma, where in the absence of thermionic emission they can effectively absorb the electrons [73,128,129]. Chemicals with a high affinity for oxygen or nitrogen can also be injected which inhibit electron generation by competing with the dominant N+O associative ionization reaction [123]. Of the many proposed chemicals for blackout mitigation, the only three to have been previously flight tested are water [55] and two electrophilic chemicals [56, 57], Freon E-3 [$F(C_3F_6O)_3CHFCF_3$] and Freon 114B2 [$C_2Br_2F_4$].

Electromagnetic Manipulation

The exploitation of electromagnetic fields as a blackout amelioration technique dates back to the early 1960s, when Hodara proposed that static magnetic fields could be used to create a “window” through which RF transmission can pass through with limited attenuation [130]. By orienting the magnetic field lines such that the motion of the electrons is constrained through gyration, the dispersion relation in Eq. 1.20 becomes altered where a wave below the plasma frequency can propagate. The magnetic field limits the transverse motion of the electrons, and for an infinitely strong magnetic field, no interaction would take place between the transverse wave and electrons.

This technique is one of the few to have been tested in flight, as signal attenuation and antenna impedance measurements were made during the RAM A-2 flight to determine the effectiveness of a magnetic field of 750 G, though due to low signal loss the experiment was inconclusive [55]. Experiments by Russo and Hughes also confirmed the analysis of Hodara and showed that a 750 G magnetic field could provide a 20 dB reduction in signal attenuation [131], though numerical studies by Rawhouser, Starkey, and Kim have shown the possible need for stronger magnetic fields, on the order of 0.5-1.0 T [81, 82, 132]. Permanent magnets within the constraints of a hypersonic vehicle are limited to around 0.15 T and are hampered by the Curie temperature [128, 133]. With current technologies, a superconducting electromagnet would weigh over 500 kg and be difficult to implement [134]. However, projected advancements in carbon nanotube composites may lead to such magnets weighing less than 50 kg [135]. Further, advancements to high-temperature superconducting magnets can drop the expected mass even further, to around 10 kg [136, 137].

Nevertheless, many methods to reduce the magnetic field strength requirements and subsequently the system weight requirements have been proposed. Instead of immobilizing the electrons, these techniques focus on physically expelling electrons away from the area surrounding an antenna. It has been shown that using a time varying, or traveling magnetic field (TMF) can reduce the required magnetic field by creating a Hall electric field that depletes the surrounding plasma density [138, 139]. A magnet has been proposed to be removed altogether, in static or time-varying pulsed electric field which can also result in a depleted electron density [81, 96]. The hybrid use of applied fields has also shown promise.

This technique utilizes crossed electric and magnetic fields to collect both electrons and ions and accelerate the charged particles past the antenna, lowering the adjacent electron number density. This ExB drift technique has been demonstrated for use in blackout mitigation through both computer modeling and experiments employing a helicon plasma [78, 81, 140, 141].

1.3 Scope of Dissertation

1.3.1 Motivation

Historically, the communications problem has been of subsidiary concern in hypersonic design as usually the more common re-entry vehicles will only undergo blackout for a relatively short time-frame during a preset trajectory, while problems such as those dealing with heat transfer take precedence. This challenge, however, may be a more significant obstacle for hypersonic glide systems, such as that shown in Figure 1.10, as a considerable amount of the mission lies within the blackout regime, potentially compromising GPS, telemetry, and abort functionality [82]. Additionally, unlike re-entry vehicles, a continuous communication pathway with hypersonic glide vehicles is of utmost importance. Consequently, this work examines several likely geometric designs to assess the communication blackout problem for hypersonic glide vehicles.

Figure 1.10: Artistic rendering of a representative hypersonic glide body. Image from Sandia National Laboratories.

Of all the previously discussed mitigation techniques, the prevailing consensus over the past fifty years has been that vehicle/trajectory selection, electromagnetic manipulation, and chemical injection schemes are the solutions that have shown the most promise [74,75,82,84, 128]. However, it is fairly probable that there will likely be no universal elegant solution to the communications blackout problem. Instead, vehicle geometry and mission requirements will dictate a suitable mitigation strategy. The efficacy of the latter two technologies previously mentioned (electromagnetic manipulation and chemical injection) will be computationally investigated in the context of hypersonic cruise flight following the suggested communications design engineering approach for handling blackout [142], by first evaluating if communication interruptions can be avoided by antenna placement or higher frequency transmissions. If this is unachievable, then the two leading technologies will be evaluated based on primary design drivers, specifically size, weight, and power (SWaP) requirements, and use of already allocated frequency spectrum.

1.3.2 Outline

This dissertation is divided into six chapters. The first chapter introduced the cause and significance of the radio blackout problem. It also summarized a selection of past mitigation techniques and highlighted their current strengths and weaknesses. The second chapter details the modeling approach employed in this thesis to investigate weakly ionized nonequilibrium hypersonic flows. The numerical implementation of incorporating water vapor and externally applied electromagnetic fields to these flows is also described.

The main results of this work are displayed and discussed in Chapters III - VI. The third chapter investigates how particular aspects of the modeling approach, such as the decision of chemical rates and transport models, affect the formation of plasma. The fourth chapter examines the important role of trajectory and geometry selection with respect to plasma generation and the interplay with heat flux to the vehicle, a primary design driver. The fifth chapter looks at the effectiveness and practicality of a water vapor injection blackout mitigation scheme and compares results with previous flight testing. The sixth chapter explores the use of electromagnetic fields in slender hypersonic vehicles, particularly with a static magnetic field to ameliorate blackout.

The sixth chapter summarizes the key findings of this dissertation and how the results of the penultimate two chapters compare with one another. This final chapter also reviews the unique contributions included and proposes future research that would extent the current work.

CHAPTER 2

NUMERICAL MODELING

In order to accurately predict the properties of a plasma layer along a hypersonic flight path, design a well characterized mitigation strategy to combat any plasma-induced attenuation, and ensure that no resulting critical mission failures occur, extensive numerical modeling, ground experimentation, and flight-testing must first be completed. During the design stage, the use of prior flight-test data remains the most direct means of predicting future success. However, since flight mission parameters can change drastically between each hypersonic project, extrapolating from previous flight-test data can play a severely restrictive role in the development of any novel projects. Flight-testing is also exceptionally resource intensive and is therefore limiting when prototyping new geometric and trajectory configurations. Generally, flight-testing is saved for when a hypersonic vehicle design and any corresponding mitigation technique are already at a high technology readiness level (TRL).

Accordingly, ground-testing becomes utilized to ensure mission success. A wide spectrum of facilities used for such ground experiments exist, such as those shown in Figure 2.1 where shock tunnels are shown in orange, expansion tubes in blue, and other facilities in black. As Figure 2.1 implies, ground test facilities cannot ordinarily test a full-scale vehicle over a complete range of flight conditions. Comprehensive reviews of the distinct capabilities and limitations of the numerous modern test facilities found in the United States can be found in Refs. [143–145], and for those overseas in Europe in Ref. [146]. It is ubiquitously established in these reviews that no single ground testing facility can match all characteristics of hypersonic flight. It is exceptionally challenging to match just one of the Mach number, velocity, Reynolds number, total enthalpy, surface temperature, gas number density, gas chemistry, flow duration, or quality of the freestream flow [144]. It becomes nearly impossible to properly match multiple of such flow conditions using one ground test facility [147]. Instead, different facilities are suited for different objectives, and success in experimental testing is an exercise in the art of combining partial simulations that most effectively provide prescience of the true flow conditions. Even with a well-planned quilt of ground experiments that can result in large program costs, gaps from ground-to-flight extrapolation can still remain that would severely decrease performance and increase risk [143].

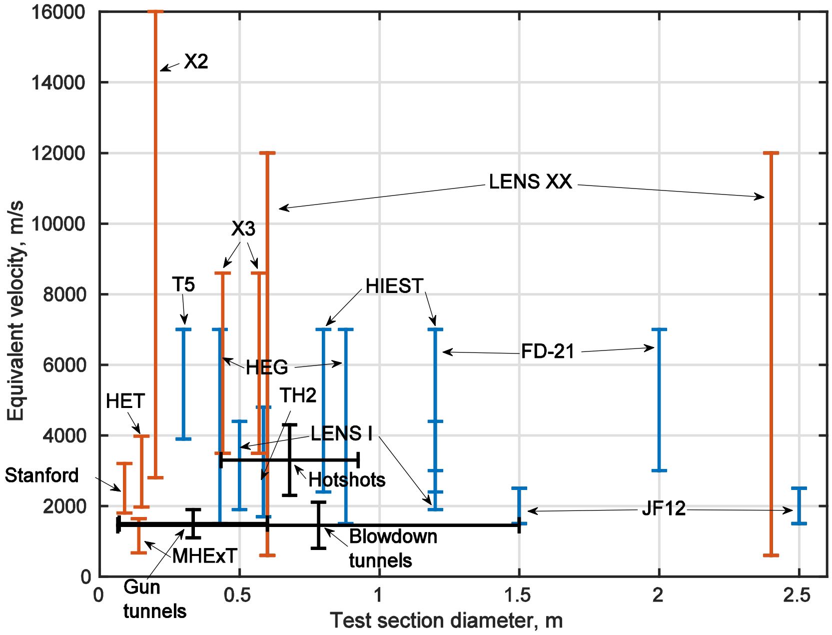

Figure 2.1: Hypersonic facilities with ranges of equivalent velocities and test section size where air is the medium used for testing. Figure from Ref. [143].

Therefore, it is paramount to fill these gaps with robust computational and analytical efforts. Further, numerical modeling is less expensive, has a quick turnaround, and can probe into a flow field in much more detail than a simulation on the ground [148, 149]. With advancements in computing power, the ability to model the aerothermodynamic environments of interest with higher fidelity models and sophisticated algorithms has improved considerably over the past several decades [150, 151]. While ground and flight tests remain vital in reducing the current insufficiencies of numerical simulations (e.g., unknown boundary conditions, parameter and model uncertainties, numerical errors), it is for the above-mentioned reasons that both the formation of hypersonic plasma and the mitigation techniques that are detailed herein are investigated numerically.

2.1 LeMANS: A Hypersonic Flow Solver

The weakly ionized hypersonic flow fields in this work are modeled through the use of the (“Le”) Michigan Aerothermodynamic Navier-Stokes Solver (LeMANS). LeMANS is specifically crafted to solve the partial differential equations that, when coupled with thermodynamic and transport relations, govern compressible flows in thermochemical nonequilibrium. This set of equations is solved within a finite-volume method framework by utilizing second-order accurate discretization in the spatial domain, while a steady-state flow field solution is carried out via an implicit first-order accurate Backward Euler time integration scheme [152].

The inviscid fluxes across cell faces are calculated using a modified form of the Steger-Warming Flux Vector Splitting (FVS) scheme due to its low numerical dissipation inside boundary layers with enough numerical dissipation within shock layers to ensure stability [153]. Near shock waves the method is switched back to the original Steger-Warming scheme with a pressure switch as this scheme has favorable dissipation to account for the shock wave discontinuity [154]. The flux of viscous components is computed using cell-centered and averaged nodal property values [155].

LeMANS is applicable to 2-dimensional, axisymmetric, and 3-dimensional unstructured and structured computational grids. The computational fluid dynamics (CFD) code is parallelized using the METIS software library that partitions the mesh and utilizes the Message Passage Interface (MPI) protocol to transfer information between processors [156]. LeMANS has undergone considerable benchmarking with US3D, DPLR, and LAURA, verification, and validation with flight data including that of Apollo, FIRE-II, and OREX, and ground test data including experiments conducted at AEDC (Tunnel B), CUBRC (LENS-I and LENS-XX), and Sandia (plasma arc tunnels) and with the HYPULSE Expansion Tube, SR3 wind tunnel, and the University of Vermont ICP torch, among others [81,149,152,157–160]. Original, more comprehensive documentation of LeMANS is provided by Scalabrin in Ref. [152].

2.1.1 Navier-Stokes Equations

The weakly ionized hypersonic flow fields in this work are governed by the compressible Navier-Stokes conservation equations:

Conservation of Mass:

$$\frac{\partial \rho_s}{\partial t} + \nabla \cdot (\rho_s \mathbf{u} + \mathbf{J_s}) = \dot{\omega}_s \tag{2.1}$$

Conservation of Momentum:

$$\frac{\partial \rho \mathbf{u}}{\partial t} + \nabla \cdot \left(\rho \mathbf{u}\mathbf{u} + p\bar{\mathbf{I}} - \tilde{\tau}\right) = 0 \tag{2.2}$$

Conservation of Energy:

$$\frac{\partial E}{\partial t} + \nabla \cdot \left[(E+p)\mathbf{u} - \tilde{\tau}\cdot\mathbf{u} + (\mathbf{q_{tr}} + \mathbf{q_{vee}}) + \sum_s (\mathbf{J_s} h_s)\right] = 0 \tag{2.3}$$

$$\frac{\partial E_{vee}}{\partial t} + \nabla \cdot \left[E_{vee}\mathbf{u} + \mathbf{q_{vee}} + \sum_s (\mathbf{J_s} e_{vee,s})\right] = \dot{\omega}_{vee} \tag{2.4}$$

where ρ_s is the mass density of a corresponding species s, $\mathbf{u}$ is the bulk velocity vector, $\mathbf{J_s}$ is the diffusion flux for species s, and $\dot{\omega}_\mathrm{s}$ is the source term that is the net of the production and consumption rates of species s due to chemical reactions. The conservation of momentum, represented by Eqs. 2.2, includes the total density, ρ, the pressure, p, the identity matrix, $\bar{\mathbf{I}}$, and the viscous stress tensor, $\tilde{\tau}$. The conservation of energy equations, Eqs. 2.3-2.4, also include the total and vibrational-electron-electronic energy per unit volume of mixture, E and $\mathrm{E_{vee}}$, respectively, the translational-rotational and vibrational-electron-electronic heat fluxes, $\mathbf{q_{tr}}$ and $\mathbf{q_{vee}}$, respectively, the species enthalpy, $\mathrm{h_s}$, the vibrational-electron-electronic energy per unit mass, $\mathrm{e_{vee,s}}$, and the vibrational-electron-electronic energy source term, $\dot{\omega}_{\mathrm{vee}}$.

It must be noted that a key assumption in the derivation and subsequent applicability of the Navier-Stokes equations is that the fluid is a continuum, where local properties can be represented as continuous, differentiable functions rather than considering the nature of the discrete particles. In fact, the Chapman-Enskog derivation approach indicates that the Navier-Stokes equations are valid for small, linear perturbations from equilibrium, generally a justified assumption for Knudsen numbers ($Kn = \lambda_m/L_c$, the ratio of the mean free path to the characteristic length) approximately less than 0.01. At higher Knudsen numbers the Navier-Stokes formulation is no longer valid and thus necessitates the use of either a higher-order set of partial differential equations, like the Burnett equations, or directly solving or simulating the interaction of particles through the Boltzmann equation. Conversely, a Knudsen number approaching zero corresponds with the use of the lower-order Euler equations. High Knudsen numbers are associated with the rarefied flows of high-altitude trajectories, inside the shock wave, or in regions associated to the wake. For the simulation cases described herein, due diligence has been taken to ensure an appropriate Knudsen number for the use of the Navier-Stokes equations.

2.1.2 Thermodynamic and Transport Properties

In a real gas, particles can be clumped together unequally, whether in terms of density, velocity, or temperature. Very broadly, the diffusion of mass, momentum, and energy all follow a generic form where the transport flux is driven by a gradient of these particle properties towards a state of equilibrium. In a continuum approach it is not possible for this to be reconciled directly and instead it must be appropriately modeled. The species mass diffusion fluxes are modeled using a modified form of Fick's law [161]:

$$\mathbf{J_s} = -\rho D_s \nabla Y_s + Y_s \sum_{k \neq e} \rho D_k \nabla Y_k \tag{2.5}$$

that enforces the sum of the diffusion mass fluxes to be zero by distributing the residual according to the species mass fraction. In Eq. 2.5, where $\mathrm{D_s}$ is the species diffusion coefficient and $\mathrm{Y_s}$ is the species mass fraction, the diffusion of species s is treated with a binary component approximation to the exact solution given by the Stefan-Maxwell equations [161]. Not present in this equation for species diffusion flux is the contribution of electrons, because the electron diffusion flux is minimal due to the relatively very small molecular weight of electrons. Imposing charge neutrality of the flow field through a single-fluid approach and assuming ambipolar diffusion, the electron diffusion flux yields,

$$\mathbf{J_e} = M_e \sum_{s \neq e} \frac{\mathbf{J_s} \mathcal{C}_s}{M_s} \tag{2.6}$$

where M is the molecular weight and $\mathcal{C}_\mathrm{s}$ is the charge of each species. Force diffusion (drift) of the charged particles is neglected.

The viscous shear stress tensor components and subsequent momentum flux are modeled assuming that the flow is a Newtonian fluid and Stokes' hypothesis is appropriate [162]:

$$\tau_{ij} = \mu \left(\frac{\partial u_j}{\partial x_i} + \frac{\partial u_i}{\partial x_j} \right) + \lambda_v \delta_{ij} \nabla \mathbf{u} \quad ; \quad \lambda_v + \frac{2}{3}\mu = 0 \tag{2.7}$$

where μ is the mixture coefficient of dynamic viscosity, λ_v is Lamé's first moduli or the second viscosity coefficient related to bulk fluid expansions, and δ_ij is the Kronecker delta.

The heat fluxes for the translational-rotational and vibrational-electron-electronic energy modes are modeled according to Fourier's law as [163]

$$q_{tr} = -\kappa_{tr} \nabla T_{tr} \qquad ; \qquad q_{vee} = -\kappa_{vee} \nabla T_{vee} \tag{2.8}$$

where κ is the mixture coefficient of thermal conductivity for each of the two energy modes.

A mixing rule for the transport properties, viz., species diffusion, viscosity, and thermal conductivity, has to be employed for multi-species flows. This can be achieved through two methods. The first employs Wilke's semi-empirical mixing rule [164], with Blottner curve fits for viscosity [165] and Eucken's relation for the thermal conductivity [166]. This simple model is generally acceptable for temperatures lower than 10,000 K [167–169]. The second approach is more general and utilizes Gupta's mixing rule [68] where the species viscosities and thermal conductivities are calculated using noncoulombic and coulombic collision cross section data [170]. Both models are utilized in this work and are discussed in more detail below.

Wilke's Mixing Rule

Using Wilke's semi-empirical mixing rule, the mixture coefficients of viscosity and thermal conductivity are given by [164]

$$\mu = \sum_s \frac{X_s \mu_s}{\phi_s} \qquad ; \qquad \kappa = \sum_s \frac{X_s \kappa_s}{\phi_s} \tag{2.9}$$

where $\mathrm{X_s}$ is the species mole fraction, μ_s and κ_s are the specie-specific coefficients of dynamic viscosity and thermal conductivity for each energy mode, respectively, and ϕ_s is a dimensionless constant for each species expressed as

$$\phi_s = \sum_k X_k \left[1 + \sqrt{\frac{\mu_s}{\mu_k}} \left(\frac{M_k}{M_s}\right)^{\frac{1}{4}}\right]^2 \left[8\left(1 + \frac{M_s}{M_k}\right)\right]^{-\frac{1}{2}} \tag{2.10}$$

For each species the coefficient of viscosity can be calculated using Blottner curve fits [165] with

$$\mu_s = 0.1 \exp\left(\left(\mathrm{A_s} \ln T + \mathrm{B_s}\right) \ln T + \mathrm{C_s}\right) \tag{2.11}$$

where the constants $\mathrm{A_s}$, $\mathrm{B_s}$, and $\mathrm{C_s}$ are found for each species. The coefficient of thermal conductivity can be found for each internal energy mode of each species through the use of Eucken's relation [166]

$$\kappa_{s,tr} = \frac{5}{2}\mu_s C_{v_{s,t}} + \mu_s C_{v_{s,r}} \qquad ; \qquad \kappa_{s,vee} = \mu_s C_{v_{s,vee}} \tag{2.12}$$

where $\mathrm{C_{v_s}}$ is the specific heat at a constant volume for an associated energy mode.

The specie-dependent mass diffusion coefficient, $\mathrm{D_s}$, in Eq. 2.5, can be determined using a simple average-value approach, where a single binary coefficient is used to ensure that the sum of diffusion fluxes is zero. The Lewis number compares mass diffusion to thermal diffusion using a ratio of the mass diffusion coefficient and thermal diffusivity. Rearranging this definition of the Lewis number therefore yields

$$D_s = \frac{\kappa_{tr}\mathrm{Le}}{\rho C_{p,tr}} \tag{2.13}$$

where Le is the mixture-averaged Lewis number that is assumed constant, and $\mathrm{C_p}$ is the mixture translational-rotational specific heat at constant pressure. This constant Lewis number approach is appropriate for velocities below 10 km/s [171] and for when an average Lewis number is known for the system. In cases where an average Lewis number is not known, the bifurcation model first considered by Bird [172], and later Bartlett et al. [173], can be employed:

$$D_s = \frac{D_{N_2}}{F_s F_{mix}} \tag{2.14}$$

where $\mathrm{D_{N_2}}$ is the diffusion coefficient of $\mathrm{N_2}$, used as a reference diffusion coefficient, and F is a diffusion factor determined by a least-squares correlation of actual diffusion coefficient data. This approach assumes unequal diffusion coefficients based on molecular weight, with a verified accuracy within 15% for species having molecular weights within an order of magnitude [173].

Gupta's Mixing Rule

Gupta's mixing rule [68] also estimates the transport properties from an approximation to the first-order Chapman-Enskog expression, but is more applicable for weakly ionized gases. The coefficient of viscosity can be calculated with this approach by

$$\mu = \sum_{s \neq e} \frac{m_s \gamma_s}{\sum_{k \neq e} \gamma_k \Delta^{(2)}_{sk} + \gamma_e \Delta^{(2)}_{se}} + \frac{m_e \gamma_e}{\sum_k \gamma_k \Delta^{(2)}_{ek}} \tag{2.15}$$

where $\mathrm{m_s}$ is the mass of each species particle, γ_s is the molar concentration of each species, and $\Delta^{(2)}_{\mathrm{sk}}$ is a collision term, or Gupta-Yos coefficient, which is evaluated at different controlling temperatures. When the mixture involves electrons, such as for $\Delta^{(2)}_{\mathrm{se}}$ and $\Delta^{(2)}_{\mathrm{ek}}$, the controlling temperature is $\mathrm{T_{vee}}$; otherwise $\mathrm{T_{tr}}$ is used. The coefficient of thermal conductivity for the translational energy mode can be calculated with

$$\kappa_t = \frac{15}{4} k_B \sum_s \left(\frac{X_s}{\sum_k \alpha_{sk} X_k \Delta_{sk}^{(2)}} \right) \tag{2.16}$$

where α_{sk} is given by

$$\alpha_{sk} = 1 + \frac{\left(1 - \frac{M_s}{M_k}\right)\left(0.45 - 2.54\frac{M_s}{M_k}\right)}{\left(1 + \frac{M_s}{M_k}\right)^2} \tag{2.17}$$

Further, the coefficient of thermal conductivity for each of the internal energy modes is expressed as

$$\kappa_{int} = \sum_s \frac{X_s C_{p_{s,int}}}{\sum_k X_k \Delta_{sk}^{(1)}} \tag{2.18}$$

The collision terms used in the above equations can be determined with

$$\Delta_{sk}^{(1)} = \frac{8}{3}\sqrt{\frac{2m^*}{\pi \mathrm{k_B} T}} \pi \sigma^2 \Omega_{sk}^{(1,1)} \tag{2.19}$$

and

$$\Delta_{sk}^{(2)} = \frac{16}{5}\sqrt{\frac{2m^*}{\pi \mathrm{k_B} T}} \pi \sigma^2 \Omega_{sk}^{(2,2)} \tag{2.20}$$

where m^* is the reduced mass, $\Omega_{\mathrm{sk}}^{(1,1)}$ corresponds to the diffusion collision integral, and $\Omega_{\mathrm{sk}}^{(2,2)}$ corresponds to the viscosity collision integral. The collision integrals are calculated based on the type of collision, e.g, neutral-neutral, electron-neutral, and ion-neutral. The collision integrals for air that are used in this study are obtained from Ref. [170].

The species diffusion coefficient used in Eq. 2.5 can be found using collision cross sections through

$$D_s = \frac{(1 - X_s)}{\sum\limits_{k \neq s,e} \left(\frac{X_k}{D_{sk}}\right)} \tag{2.21}$$

where the binary diffusion coefficient between heavy particles, $\mathrm{D_{sk}}$, is given by

$$D_{sk} = \frac{k_B T_{tr}}{p \Delta_{sk}^{(1)}} \tag{2.22}$$

2.1.3 Thermochemical Nonequilibrium

As was discussed in Section 1.1.2.1, hypersonic flows cannot be modeled with a perfect gas assumption at high velocities due to physical phenomena occurring such as the excitation of various internal energy modes and chemical reactions. When a flow field undergoes a change of thermodynamic state, e.g., an increase of temperature across a strong bow shock, the total energy is redistributed to the associated internal energy modes, while the population distribution of species shifts toward a maximum entropy state. Each change in thermodynamic state necessitates a corresponding number of collisions for a specific process to occur and allow the flow field to reach equilibrium. Thus, for any of these processes to adapt it takes a finite amount of time, defined as the characteristic time, τ_{process}. Typically, the characteristic times are observed such that

$$\tau_{translational} < \tau_{rotational} < \tau_{vibrational} < \tau_{electronic} < \tau_{dissociation} < \tau_{ionization} \tag{2.23}$$

where $\tau_{\text{translational}}$, $\tau_{\text{rotational}}$, $\tau_{\text{vibrational}}$, and $\tau_{\text{electronic}}$ refer to the relaxation time required for energy exchange to fully occur between the energy modes and $\tau_{\text{dissociation}}$ and $\tau_{\text{ionization}}$ refer to the characteristic times of chemical reactions [61, 66]. The characteristic time of the flow itself can be defined as

$$\tau_{flow} \equiv \frac{\mathcal{L}}{u} \tag{2.24}$$

where $\mathcal{L} = \left(\frac{1}{\mathrm{Q}}\frac{\partial \mathrm{Q}}{\partial \mathrm{l}}\right)^{-1}$ is a nondimensional gradient length scale related to changes of a macroscopic flow property, Q, over some distance, l, between two points in the flow field. If this characteristic flow time is markedly longer than the characteristic time of a particular process, then, relative to the flow time, a change in thermodynamic state will result in an immediate change of a particular energy mode or chemical composition. This energy mode or chemical composition is said to be in equilibrium with the flow. Conversely, if the characteristic flow time is markedly shorter than the characteristic time of a particular process, the process is said to be frozen, and a redistribution or adaptation to the new thermodynamic state never occurs.

For hypersonic flows of interest to communications blackout, considerations must be made for both the excitation of internal energy modes and chemical reactions, as the characteristic flow time is in the ballpark of the other characteristic times. For the work presented herein, LeMANS utilizes a two-temperature model with energy relaxation to account for thermal nonequilibrium and a standard finite-rate chemistry model to account for chemical nonequilibrium. Although the ensuing subsections examine these models independently, this is not indicative of the significant interdependencies between the states of the internal energy modes and chemical compositions.

2.1.3.1 Thermal Nonequilibrium

During a change of thermodynamic state, the total energy is redistributed to all available energy modes. For atoms this includes translational and electronic energy, while for molecules this additionally includes rotational and vibrational energy. The rotational, vibrational, and electronic energy modes are collectively described as the internal energy modes, with translational energy typically considered separate.

The translational energy mode of a particle describes its kinetic energy, therefore $\mathrm{e_{tr}} \propto \mathrm{mv}^2$. In turn, the translational energy of a group of particles is related to the corresponding velocity distribution function (VDF). Since the flows of interest in this work are ionized, it is also important to note that the translational energy of free electrons is generally considered separate, as electrons have significantly less mass than other particles and constitute VDFs distributed across a much wider range of thermal velocities. The rotational energy mode is associated with a molecule's angular momentum, which in turn is related to the rotational degrees of freedom. For diatomic molecules like N_2 or O_2, there are two rotational degrees of freedom, while a third is possible for polyatomic molecules like H_2O. The vibrational energy mode is fundamentally accessible due to the oscillatory nature of interactions between individual atoms along the bonds of connection within a molecular structure and is therefore governed by the potential between these individual atoms. Unlike the prior discussed energy modes, which can be assumed to be in continuum energy levels, the quantized spacing of vibrational energy modes is large and non-negligible. A diatomic molecule can have one or two degrees of vibrational freedom depending on the degree of activation, while larger molecules have additional degrees of freedom depending on their asymmetry, like H_2O with three degrees of freedom, and H_2O_2, with six. The vibrational energy mode is usually never fully activated as the molecules dissociate well before high vibrational energy levels are reached. Similar to atoms within a molecular structure, the orbital and spin angular momentum of electrons surrounding a molecule affect the internal energy. This electronic energy mode has the largest relative spacing between quantized energy levels when compared to the other internal energy modes. While the lowest possible subshell is usually the most heavily populated, a molecule can become electronically excited through collisions or through the absorption of radiation [61, 66, 159].

It requires very few collisions for the translational energy mode to adapt to a new thermodynamic state. Similarly, it takes only approximately 10 collisions for the rotational energy to be re-distributed. However, the vibrational energy mode requires on the order of 1000 collisions at 5000 K, but decreases considerably at higher temperatures [61, 66]. These collision numbers required to reach an equilibrated state directly correspond with the characteristic temperature of each energy mode. For instance, for O_2 molecules, the rotational characteristic temperature is 2.1 K, the vibrational characteristic temperature is 2,270 K, and the electronic characteristic temperature for the first excited state is 11,390 K [174].

Therefore, for flows of interest, both the translational and rotational energy modes are considered fully activated. Because the rotational energy mode equilibrates with the translational energy mode in very few collisions, it is appropriate to assume that the rotational and translational energy modes of all species are described by the same temperature,

$$T_{tr} = T_{translational} = T_{rotational} \tag{2.25}$$

Analogously, because i) the vibrational temperature of different molecules is very similar due to highly efficient vibrational-vibrational energy transfer [175, 176], ii) the energy transfer between the vibrational energy mode of molecules and the translational energy mode of electrons is very fast in air [67], and iii) the electronic energy mode is excited by the electron translational energy mode which allows the system to be represented by a single Maxwell-Boltzmann distribution [176], it can also be assumed that all of the vibrational, electronic, and electron translational energy modes are governed by a single temperature,

$$T_{vee} = T_{vibrational} = T_{electronic} = T_{electron-translational} \tag{2.26}$$

This "two-temperature" approach dates back to the 1950s with the coupled vibration-dissociation model of Hammerling et al. [177] and was further improved upon by Treanor and Marrone [178, 179] by including dissociation effects on thermal nonequilibrium. The approach was further expanded by Park [180–182], who also constructed a self-consistent chemical kinetics model based on this two-temperature approach [183]. As indicated by the two energy conservation equations, Eqs. 2.3-2.4, this two-temperature approach is employed by LeMANS in this current work.

To represent the several components that encompass the relaxation and energy transfer processes between internal energy modes, the source term in Eq. 2.4 is utilized, specifically comprising of:

$$\dot{\omega}_{vee} = \dot{\omega}_{t-v} + \dot{\omega}_{diss} + \dot{\omega}_{h-e} + \dot{\omega}_{eii} + \dot{\omega}_{epg} \tag{2.27}$$

where $\dot{\omega}_{\mathrm{t-v}}$ symbolizes the exchange of energy between the translational-rotational and vibrational-electron-electronic energy modes, $\dot{\omega}_{\mathrm{diss}}$ symbolizes the vibrational-electron-electronic internal energy removed/added by dissociation/recombination reactions treated with a non-preferential phenomenological simplification, $\dot{\omega}_{\mathrm{h-e}}$ symbolizes the energy transfer between heavy particles and electrons, $\dot{\omega}_{\mathrm{eii}}$ symbolizes the energy removed from free electrons during electron impact ionization reactions, and $\dot{\omega}_{\mathrm{epg}}$ symbolizes the approximate work done on the electrons by the electric field induced via the electron pressure gradient [67,175]. The energy transfer between the nonequilibrium energy modes can be modeled with the Landau-Teller approach [184], formulated as:

$$\dot{\omega}_{t-v} = \sum_s \rho_s \frac{e^*_{v,s} - e_{v,s}}{\tau_s} \tag{2.28}$$

where $\mathrm{e}^*_{\mathrm{v,s}}$ is the equilibrium vibrational energy of species s at the local translational temperature and $\mathrm{e}_{\mathrm{v,s}}$ is the vibrational energy of each species, provided by

$$e_{v,s}(T) = \frac{R\theta_{v,s}}{\exp\left(\frac{\theta_{v,s}}{T} - 1\right)} \tag{2.29}$$

which assumes a simple harmonic oscillator model and uses, $\theta_{\mathrm{v,s}}$, the characteristic temperature of the vibrational energy mode. The molar averaged Landau-Teller relaxation time, τ_{s}, can be found by using the following expression containing, X_{s}, the mole fraction of species s

$$\tau_s = \frac{\sum_s X_s}{\sum_s \left(\frac{X_s}{\tau_{rs}}\right)} \tag{2.30}$$

and by using the standard Millikan-White expression for the interspecies relaxation time [185]:

$$P\tau_v = \exp\left[\mathrm{A}\left(T^{-\frac{1}{3}} - \mathrm{B}\right) - \mathrm{C}\right] \quad [atm - sec] \tag{2.31}$$

where the constants, $\mathrm{A} = 1.16 \times 10^{-3} \mu_{\mathrm{m}}^{\frac{1}{2}} \theta_{\mathrm{v}}^{\frac{4}{3}}$, $\mathrm{B} = 1.5 \times 10^{-2} \mu_{\mathrm{m}}^{\frac{1}{4}}$, and $\mathrm{C} = 18.42$, are calculated with the reduced mass in atomic units, μ_{m}, and are based on empirical correlations of shock tube experiments performed within a 300 K to 8000 K temperature range.

The Landau-Teller model has inherent limitations as it assumes only small deviations from equilibrium with singular quantum jumps [61]. Although the Milikan-White formula has shown good correlation with experimental data for several molecular systems, there are some exceptions. For instance, in the $\mathrm{O_2 - O}$ system, which contains a molecule and open-shell atom, there are additional mechanisms not accounted for by the Landau-Teller approach, such as atom exchange and non-adiabatic transitions [174]. Therefore, the relaxation time,

τ_s, is further modified with the addition of high-temperature adjustments suggested by Park that limit the collision cross-section [186].

Further details about the remaining components of Eq. 2.27 and how they are implemented in LeMANS can be found in Ref. [152].

2.1.3.2 Chemical Nonequilibrium

The net rate of species mass production and destruction brought on by a chemically reacting flow is expressed by the source term, $\dot{\omega}_s$, for the conservation of mass, Eq. 2.1. All the reactions present in the flow, e.g., dissociative, exchange, and ionization reactions, can be universally represented as

$$\sum \alpha_s A \rightleftharpoons \sum \beta_s B \tag{2.32}$$

where α and β are the stoichiometric coefficients of the reactants and products A and B, and, by convention, a reaction written from the left is endergonic. The cumulative source term for each species s undergoing reactions r is provided by

$$\dot{\omega}_s = \mathcal{M}_s \sum_r \dot{\omega}_{s,r} \tag{2.33}$$

where $\mathcal{M}_s$ is the molar mass of each species and $\dot{\omega}_{s,r}$ is the net production rate of species s within a particular reaction r, which can be calculated with

$$\dot{\omega}_{s,r} = (\beta_{s,r} - \alpha_{s,r})\, 10^3 \left[k_{f,r} \prod_s \left(10^{-3} \frac{\rho_s}{\mathcal{M}_s} \right)^{\alpha_{s,r}} - k_{b,r} \prod_s \left(10^{-3} \frac{\rho_s}{\mathcal{M}_s} \right)^{\beta_{s,r}} \right] \tag{2.34}$$

Since the partial species densities ρ_s are expressed in MKS units of [kg/m^3], the 10^3 and 10^{-3} multiplicative terms are conversion factors for the forward and backward rate coefficients, k_f and k_b, which are specified in CGS units of [cm^3/mol$-$s]. The degree of chemical nonequilibrium affects the forward and backward rate coefficients. Generally the forward rate coefficients are expressed through a modified Arrhenius form, displayed in Eq. 2.35, where Θ_r relates to the activation energy and T_c is the controlling temperature for the reaction. The coefficients C and n have traditionally been found through correlation with experimental data.

$$k_f = CT^n exp\left(-\frac{\Theta_r}{T_{c,f}}\right) \tag{2.35}$$

To account for the fact that vibrationally excited molecules are more likely to dissociate, a combination of the two temperatures, provided for by Eq. 2.36, can be used to govern the reaction rates.

$$T_c = T_{tr}^a T_{vee}^b \tag{2.36}$$

The exponents a and b can vary depending on the specific reaction, but always add up to 1. In the present work, for exchange, charge exchange, and associative ionization reactions the controlling temperature in Eq. 2.35 is taken as $\mathrm{T_{tr}}$, or a = 1, while the electron impact ionization reactions use $\mathrm{T_{vee}}$, or b = 1. Generally, if $\mathrm{T_{tr}}$ or $\mathrm{T_{vee}}$ are not solely used as the controlling temperature, it is common for a = b = 0.5.

The backwards rate of each reaction is typically obtained by using Eq. 2.37. Here, Eq. 2.35 is evaluated using a backward controlling temperature, $\mathrm{T_{c,b}}$, which is not necessarily the same as that of the forward reaction. Usually, the controlling temperature for backward reactions is $\mathrm{T_{tr}}$, with the exception being reactions including electrons, such as dissociative recombination or impact ionization.

$$k_b = \frac{k_f(T_b)}{\mathrm{K_{eq}}(T_{c,b})} \tag{2.37}$$

The equilibrium constant, $\mathrm{K_{eq}}$, of Equation 2.37 is evaluated with either curve fit data or through a minimization of Gibbs free energy. These methods are discussed in more detail in Section 3.2.

2.2 Modeling Injection

The material injection process is modeled in LeMANS as a modification to the surface boundary condition. The first cell near the injecting wall is used as a control volume for the conservation equations and is illustrated in Figure 2.2. The surface mass and energy balance equations do not need to be solved for the cases detailed in this dissertation, as the wall temperature, $\mathrm{T_w}$, species mass fraction, $\mathrm{Y_{k,\omega}}$, and the mass flux, $\dot{\mathrm{m}}''_{\mathrm{w}} = \frac{\dot{m}_w}{A} = \rho_w v_w$, are all assumed to be known and are prescribed conditions. Neglecting diffusive fluxes and assuming that the flow is perpendicular to the surface, conservation of momentum for the neighboring cell can be written as:

$$p_w(\rho_w, T_w) + \rho_w v_w^2 = p_{nc} + \rho_{nc} v_{nc}^2 \equiv p_\eta \tag{2.38}$$

where the subscript "w" denotes the wall, "nc" denotes the neighboring cell, and "η" denotes the wall-normal direction. This relation is analogous to the total pressure definition, where the total pressure is akin to p_η and the static pressure is akin to $\mathrm{p_w}$. Assuming the ideal gas relation ($\mathrm{p_w} = \rho_\mathrm{w}\mathrm{RT_w}$) holds valid at the wall, the primitive variables are solved as:

$$\rho_w = \frac{p_\eta + \sqrt{p_\eta^2 - 4RT_w \dot{m}_w''^2}}{2RT_w} \tag{2.39}$$

$$v_w = \frac{2RT_w \dot{m}_w''}{p_\eta + \sqrt{p_\eta^2 - 4RT_w \dot{m}_w''^2}} \tag{2.40}$$

$$p_w = \frac{p_\eta + \sqrt{p_\eta^2 - 4RT_w \dot{m}_w''^2}}{2} \tag{2.41}$$

Once the pressure, density and velocity at the wall are found, the ghost cell (see Figure 2.2) properties are set. The ghost cells for the wall boundary condition hold properties such that the inviscid and viscous fluxes remain correct at the wall, e.g., the momentum inviscid flux for the nominal wall condition is given by the pressure only due to a zero normal velocity for the flow side of the wall. Hence, the injection condition requires that the conservative quantities in the ghost cells are set such that the flux across the wall is the prescribed mass flux. It should be noted that Eqs. 2.39-2.41 place a numerical constraint on the mass flux, $\dot{\mathrm{m}}''_{\mathrm{w}}$, such that the discriminant needs to remain positive. For any given total pressure at the wall, a higher mass flux results in a lower static pressure in the ghost cell. At the maximum flux allowable by the discriminants, the static pressure is at or near zero, invalidating the total pressure description of the momentum balance. This is compensated in the current work by spreading the mass injection over a larger area while maintaining a consistent mass flow rate with any flight conditions.

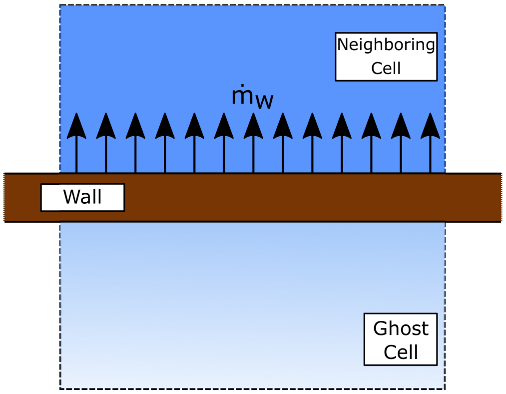

Figure 2.2: Cell volume treatment of the wall boundary condition for the mass injection sites.

Following this implementation strategy first utilized by DPLR and LAURA [187, 188], Martin et al. implemented such a blowing wall boundary condition in LeMANS to model the pyrolysis gases passing through the surface and entering the flow during material ablation [189]. This boundary condition within the LeMANS framework has been tested over a wide range of flow rates, benchmarked against similar codes, verified with analytical solutions, and validated with ground test data [190–192].

2.3 Magnetohydrodynamics

In order to adequately simulate the influence of any electromagnetic manipulation mitigation approach on the hypersonic flow field, the simulation model must properly account for magnetohydrodynamic (MHD) effects. Originally introduced by Alfvén in his Nobel Prize winning work [193], MHD examines the dynamics of magnetic fields within electrically conducting fluids by applying the Navier-Stokes equations coupled with the Maxwell's equations of electromagnetism [194]. The partial differential equations used to represent the Navier-Stokes equations, Eqs. 2.1-2.4, can be reconfigured in terms of conserved variables, $\mathbf{Q}$, inviscid flux, $\mathbf{F}$, viscous flux, $\mathbf{F_v}$, and thermochemical source terms associated with the fluid flow, $\mathbf{S_{flow}}$. The MHD effects of electric fields, current density, and magnetic fields on the fluid flow can also be conveniently described by the $\mathbf{S_{MHD}}$ source terms in:

$$\frac{\partial \mathbf{Q}}{\partial t} + \nabla \cdot (\mathbf{F} + \mathbf{F_v}) = \mathbf{S_{flow}} + \mathbf{S_{MHD}} \tag{2.42}$$

$$\mathbf{Q} = \begin{Bmatrix} \rho_1 \\ \vdots \\ \rho_{ns} \\ \rho \mathbf{u} \\ E \\ E_{vee} \end{Bmatrix} \quad ; \quad \mathbf{F} = \begin{Bmatrix} \rho_1 \mathbf{u} \\ \vdots \\ \rho_{ns} \mathbf{u} \\ \rho \mathbf{u}\mathbf{u} + p\bar{\mathbf{I}} \\ (E+p)\mathbf{u} \\ E_{vee}\mathbf{u} \end{Bmatrix} \quad ; \quad \mathbf{F_v} = \begin{Bmatrix} \mathbf{J_1} \\ \vdots \\ \mathbf{J_{ns}} \\ -\tilde{\tau} \\ -\tilde{\tau} \cdot \mathbf{u} + (\mathbf{q_{tr}} + \mathbf{q_{vee}}) + \sum_s (\mathbf{J_s} h_s) \\ \mathbf{q_{vee}} + \sum_s (\mathbf{J_s} e_{vee,s}) \end{Bmatrix}$$

$$\mathbf{S_{flow}} = \begin{Bmatrix} \dot{\omega}_1 \\ \vdots \\ \dot{\omega}_{ns} \\ 0 \\ 0 \\ \dot{\omega}_{vee} \end{Bmatrix} \quad ; \quad \mathbf{S_{MHD}} = \begin{Bmatrix} 0 \\ \vdots \\ 0 \\ \mathbf{j} \times \mathbf{B} \\ \mathbf{j} \cdot \mathbf{E} \\ \alpha\, (\mathbf{E} + \mathbf{u} \times \mathbf{B}) \cdot \mathbf{j} \end{Bmatrix}$$

where $\mathbf{j}$ is the current density vector, $\mathbf{B}$ is the magnetic field vector, $\mathbf{E}$ is the electric field vector, and α is the energy fraction of the Joule heating that goes into the vibrational-electron-electronic energy mode. The source term added to the momentum equations, $\mathbf{j} \times \mathbf{B}$, describes a reduced form of the volumetric Lorentz force[1] , $\rho_c \mathbf{E} + \mathbf{j} \times \mathbf{B}$, where the contribution of the electric force, $\rho_c \mathbf{E}$, is considered negligible when compared to the magnetic component [194]. The conservation of total energy equation is modified with the total energy deposition source term, $\mathbf{j} \cdot \mathbf{E}$, which is composed of both the reversible work, $(\mathbf{j} \times \mathbf{E}) \cdot \mathbf{u}$,

---

[1] This reduced (magnetic) Lorentz force is also referred to as the Laplace force [195].

and Joule heating[2] , $(\mathbf{E} + \mathbf{u} \times \mathbf{B}) \cdot \mathbf{j}$, which represents the transfer of energy by the electrons during dissipative collisions with other particles [77, 196]. As the electrons are accelerated due to the presence of an electric field, they are also slowed down by collisions with ions and neutral particles, and the electric current is converted into thermal energy. The term therefore represents the total Joulean work which is done by the electric field in translating the fluid through a control volume [197]. The conservation of vibrational-electron-electronic energy includes this Joule heating term, with the constant α used to partition the amount of energy converted into the different energy modes. This constant α depends on the reduced electric field and is generally determined by reference tables or via direct solutions to the Boltzmann equation [157].

The $\mathbf{S_{MHD}}$ source terms contain three additional variables, namely, $\mathbf{j}$, $\mathbf{B}$, and $\mathbf{E}$, that are typically obtained from solving Maxwell's equations, which relate the electric field, magnetic field, charge density, and current density as follows:

$$\nabla \cdot \mathbf{E} = \frac{\rho}{\epsilon_0} \tag{2.43}$$

$$\nabla \cdot \mathbf{B} = 0 \tag{2.44}$$

$$\nabla \times \mathbf{E} = -\frac{\partial \mathbf{B}}{\partial t} \tag{2.45}$$

$$\nabla \times \mathbf{B} = \mu_0 \mathbf{j} + \mu_0 \epsilon_0 \frac{\partial \mathbf{E}}{\partial t} \tag{2.46}$$

where Eq. 2.43 is Gauss's law with ρ as the charge density and ϵ_0 as the permittivity of free space, Eq. 2.44 is Gauss's law for magnetism, Eq. 2.45 is Faraday's law, and Eq. 2.46 is the Ampére-Maxwell law, with μ_0 as the permeability of free space. Solving these partial differential equations coupled to a flow solver is computationally expensive but can

---

[2] Joule heating has also been referred to as Ohmic or resistive heating.

be simplified by assuming that the flow has a small magnetic Reynolds number ($\mathrm{Re_m} << 1$) [77, 198]. The magnetic Reynolds number is a dimensionless parameter expressed as

$$\mathrm{Re_m} = \frac{uL}{\eta_m} = \frac{uL}{(\mu_0 \sigma)^{-1}} \tag{2.47}$$

where u, L, η_m, and σ, are the representative velocities, length scales, magnetic diffusivities, and electric conductivities for the flow of interest, respectively [194, 197]. The magnetic Reynolds number is analogous to the Reynolds number and Péclet number as it provides an estimate for the ratio of advection to diffusion. Thus, for a sufficiently small magnetic Reynolds number, the diffusive effects on the magnetic field lines traversing through the fluid are far more important than how they are transported by the conducting fluid through advection [77, 197]. This results in a significant computational reduction, since the induced magnetic field created by the conducting fluid motion is considered negligible [199], and **B** is instead predicated on the imposed external magnetic field [200].

It is important to assess how well such a simplification holds for the weakly ionized flows associated with hypersonic flight. The electric conductivity of the air can be related to the freestream velocity with conservative assumptions. For use as a rough assessment, the temperature after a normal shock at standard atmospheric conditions under thermally frozen conditions is found with the NASA CEA computer program [60]. As Figure 1.3 shows, the post-normal shock temperature obtained with thermally frozen conditions is much higher than that obtained with thermal equilibrium conditions. The temperature is then related to the electrical conductivity with Bush's model [201], which has been known to overpredict conductivity [157, 202]. Though post-normal shock velocities are used in this rudimentary assessment, and they are lower than the velocities present after an oblique or bow shock that is more representative of a hypersonic vehicle, this is offset by the conservative overprediction from the use of a thermally frozen flow and Bush's model. Figure 2.3 shows an estimate for a hypersonic flow field by using the abovementioned assumptions. A wide range of characteristic lengths are shown, as the length scale of interest can either be local, such as around an antenna, or the vehicle as a whole. Figure 2.3 shows that, even with conservative estimates, the hypersonic flow field satisfies a low magnetic Reynolds number criterion as long as the region of interest is not particularly large and is below orbital return velocities. Indeed, the trends of Figure 2.3 agree with those shown in previous studies [81,157,203,204], where the magnetic Reynolds number has consistently ranged on the order of 10^{-1} to 10^{-3} in the Newtonian limit of hypersonic flows [205].

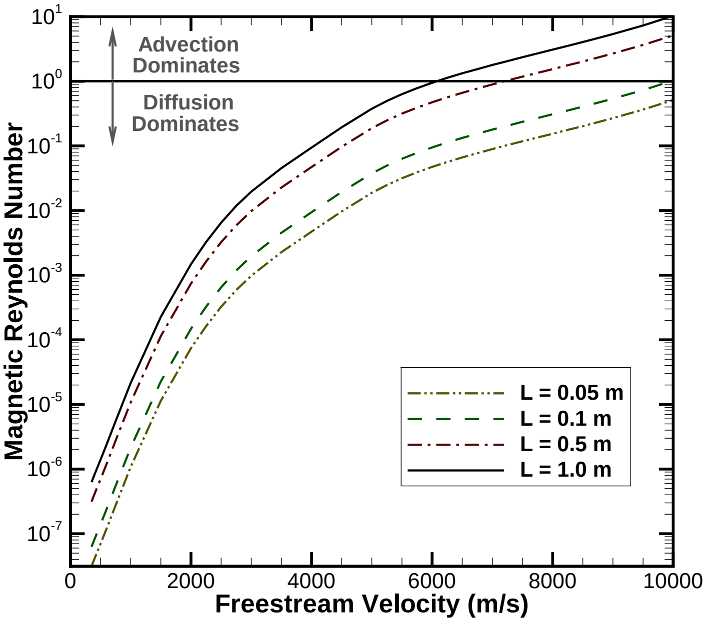

Figure 2.3: Magnetic Reynolds number calculated for post-normal shock conditions using NASA CEA thermally frozen conditions and Bush's model for electrical conductivity.

Therefore, as long as the parameters remain within adequate limits, the magnetic field is enforced as a boundary condition. Due consideration must be given to ensure that the imposed magnetic field satisfies the conservation of magnetic flux, Eq. 2.44, as magnetic monopoles lead to the presence of unphysical solutions [198]. Further, the divergence free criterion is synchronously used with the magnetic vector potential, $\mu\mathbf{B} = \nabla \times \mathbf{A}$, to assure that a vector potential, $\mathbf{A}$, must exist.

As there is a presence of a magnetic field in the flow field, a generalized Ohm's law of the tensor form

$$\mathbf{j} = \tilde{\sigma}\left(\mathbf{E} + \mathbf{u} \times \mathbf{B}\right) \tag{2.48}$$

is employed to calculate the current density, $\mathbf{j}$ [206] [3] . The electrical conductivity tensor, $\tilde{\sigma}$, concisely contains parameters for the Hall effect and ion-slip. Detailed derivations of this tensor form of the generalized Ohm's law, with simplifications made by using the electrical conductivity tensor, can be found in Refs. [81, 207].

The Ampére-Maxwell law, Eq. 2.46, can be simplified by noting that the displacement current, $\frac{\partial \mathbf{E}}{\partial t}$, is negligible compared to the conduction current in air [208]. Thus, taking the divergence of both sides of this reduced form of Eq. 2.46, and noting the vector calculus identity that the divergence of the curl is zero, leads to the equation for current density conservation,

$$\nabla \cdot \mathbf{j} = 0 \tag{2.49}$$

The electric field, $\mathbf{E}$, can be calculated by taking the divergence of the generalized form of Ohm's law, Eq. 2.48, which yields

$$\nabla \cdot \left[\tilde{\sigma}\left(\mathbf{E} + \mathbf{u} \times \mathbf{B}\right)\right] = 0 \tag{2.50}$$

The electric field vector can be further decomposed into irrotational ($-\nabla\phi$) and divergence-free ($\nabla \times \mathbf{A}$) component vector fields through the use of Helmholtz's theorem and assuming that the electric field vector is rapidly decaying and smooth. For these steady state simulations with a low magnetic Reynolds number, Eq. 2.45 leads to the electric field having only an irrotational component, which results in

$$\mathbf{E} = -\nabla\phi \tag{2.51}$$

Therefore, the generalized form of Ohm's law can be further reduced to a Poisson type equation of the form

$$\nabla \cdot \left(\tilde{\sigma}\nabla\phi\right) = \nabla \cdot \left[\tilde{\sigma}\left(\mathbf{u} \times \mathbf{B}\right)\right] \tag{2.52}$$

---

[3] It is common to rewrite the expression for Joule heating as $\frac{\mathbf{j} \cdot \mathbf{j}}{\sigma}$ using this form of Ohm's law.

Within every iteration of LeMANS, the solution to the electric potential is found using a second-order finite-volume method on Eq. 2.52 which iterates to a steady solution using an explicit Successive Over-Relaxation (SOR) iterative technique. The magnetic field in Eq. 2.52 is prescribed as an input, while the electrical conductivity tensor and velocity vector are acquired from the flow solver. Once the electrical potential is found, the electric field and current density are subsequently calculated with Eq. 2.51 and Eq. 2.49, respectively. The outputs of the MHD module, namely **B**, **E**, and **j** are then used to update the source terms in Eqs. 2.42 within each time step of the fluid solver. The original implementation of the MHD module in LeMANS was accomplished by Bisek in Refs. [157, 200, 209, 210], where more extensive documentation can be found pertaining to the implementation, boundary conditions, parallelization, and verification using analytical results.

2.4 Chapter Summary

This chapter detailed the numerical methodologies that will be utilized and explored within the ensuing chapters of this dissertation. The motivation for specifically employing a CFD approach was described and contextualized with ground experimentation and flight-testing. The governing equations, constitutive relations, and implementation practices used to computationally investigate the flows of interest, particularly weakly ionized flows in thermochemical nonequilibrium that may include magnetohydrodynamic effects, have been discussed in detail. An overview of the material injection boundary condition used in later water injection studies has also been provided.

CHAPTER 3

VALIDATION OF PLASMA FORMATION MODELING: RAM-C II

Due to the cost and complexity of creating analogous hypersonic flows in ground facilities, the development of any amelioration technique for blackout relies heavily on accurate computational simulations. As discussed in Section 1.1.2.2, blackout is predominantly caused by the free electrons' response to an electromagnetic wave, which in turn is predicated on the electron number density of the surrounding flow field. Therefore, it is of utmost importance for any simulation regarding the occurrence of blackout, and any subsequent means of mitigating it, that a prediction with a high level of confidence is attainable when modeling said electron number density.

There are numerous uncertainties associated with modeling the aerothermochemistry that influences the formation of a partially ionized hypersonic flow field. Since the net yield of free electrons is modeled in the conservation of mass equations through a source term, it is reasonable to deduce that the forward and backward rate coefficients of Eq. 2.34 have a principal influence on the generation and reduction of the hypersonic plasma. The rate coefficients recommended by Park [182] have grown into the established chemical kinetics model employed in many hypersonic CFD simulations. Since these rates were determined empirically from experiments ranging between 300 K and 7000 K, there are inherent uncertainties present when extrapolating to higher temperatures. Additionally, it has been speculated by Park that the use of his chemical kinetics model within a two-temperature framework may be inadequate for use in analysis of communications blackout [211].

Therefore, a detailed assessment of Park's chemical kinetics model for use in communications blackout simulations is necessary. Flight tests that can serve as validation platforms for these models are exceptionally scarce due to limited plasma diagnostic tools flown onboard or from a lack of publicly accessible data available. Thus, the RAM (Radio Attenuation Measurement) experiment of the 1960s [27] has been frequently used to evaluate both CFD and direct simulation Monte Carlo (DSMC) calculations at prescribed trajectory points (80.8, 76.2, 71.0, and 61.0 km) in numerous validation studies [152, 212–215]. These studies have not been directly compared with the RAM flight measurements as a function of altitude. The work in this chapter does so by evaluating Park's model against other empirically obtained reaction rates. Additionally, a newly developed chemistry set informed by ab initio calculations is assessed for use in partially ionized flows.

3.1 RAM-C II Instrumentation

In the 1960s, seven successful tests were conducted through the RAM Program to study the detrimental effects of the plasma sheath on space vehicle communications. These flight tests were performed at peak velocities ranging from 5.5 to 7.6 km/s which permitted a quantitative description of radio wave attenuation for a frequency range between 30 MHz and 10 GHz [27, 55]. Various amelioration methods were designed and tested throughout the program: use of water and electrophilic material injections, magnetic fields, and high frequency radio wave transmissions. One flight test in particular, RAM-C II, for which the vehicle payload is shown in Figure 3.1, utilized plasma diagnostic techniques to study the ionized flow field.

The flow field plasma properties of RAM-C II were measured through the use of four microwave frequency reflectometer stations and an electrostatic probe rake. These plasma diagnostic techniques are described in detail below.

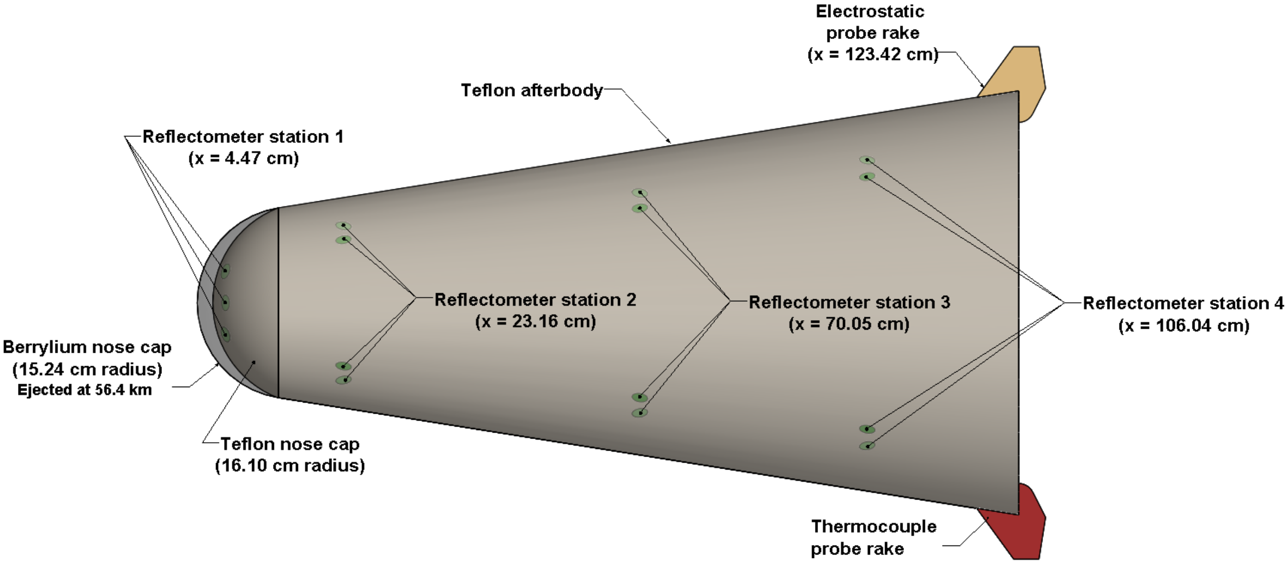

Figure 3.1: RAM-C II payload schematic depicting the reflectometer station and electrostatic probe locations and the two nose cap geometry configurations. Dimensions are obtained from Ref. [216].

3.1.1 Reflectometers

A single reflectometer antenna sends an electromagnetic wave of a particular frequency into the nonhomogeneous plasma directly adjacent to it. The wave will continue to propagate through the plasma until the transmission frequency of the wave is matched by the plasma frequency. Once these frequencies are matched, the wave will be entirely reflected and subsequently received by the reflectometer. Waves transmitted with a high enough frequency will continue to propagate through the plasma [217]. Refer to Section 1.1.2.2 for more insight into why this phenomenon occurs.

As Figure 3.1 shows, four reflectometer stations containing multiple reflectometer antennas were installed on the RAM-C II flight at discrete axial locations along the payload (4.47, 23.2, 70.1, and 106.0 cm) to monitor the onset and decay of the L, S, X, and Ka band frequencies used [216]. These frequencies corresponded to electron number densities of 1.54 x 10^{16}, 1.39 x 10^{17}, 1.25 x 10^{18}, and 1.52 x 10^{19} m^{-3}, respectively, demonstrated by Figure 3.2. Reflectometer station 1 utilized S, X, and Ka band antennas, while stations 2-4 utilized an additional L-band antenna. The reflectometer antennas were positioned tangentially equidistant, i.e., for station 1 they were 120° apart and for stations 2-4 the antennas were 90° apart. As the presence of surface waves would make interpretation of the data quite complicated, when possible, the reflectometer antennas were brought closer to the plasma by extending their conducting surfaces through the heat shield with metallic-sleeve extensions.

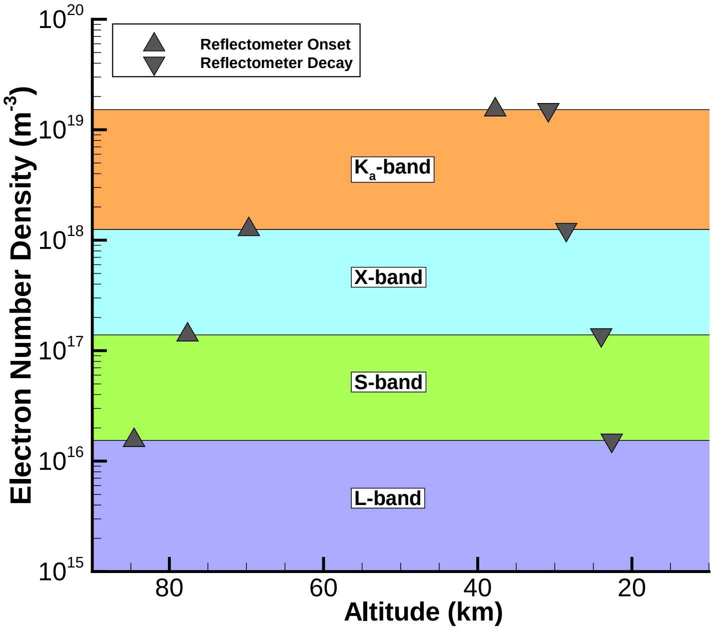

Figure 3.2: Frequency bands and corresponding electron number densities available for the second reflectometer station.

The reflectometers on the RAM payload were designed so that parameters other than the electron density did not play a significant role for most of the data collection period. By use of bidirectional coupler diode outputs, a plasma reflection coefficient was obtained for each transmitted frequency at a 20 Hz sampling rate, except for Ka-band data which was sampled at a 10 Hz sampling rate. For the RAM-C II experiment specifically, the use of a "slope technique" was applied, where a sharp increase of the reflection coefficient indicated the time at which the critical electron number density was reached for each radio wave frequency. This slope technique promoted less dependence on an absolute reflection coefficient value. However, the sharp rise necessitated by the technique requires a low ratio between the collision frequency to the plasma frequency, $\nu_{\mathrm{en}}/\omega_{\mathrm{p}}$. It is implied with Figure 1.6 that this assumption becomes invalid at low altitudes. Ground-based studies had suggested that a reflection coefficient of 20% is enough to signify the onset of a critical electron number density. The altitudes where this condition occurred for each frequency at each reflectometer station were evaluated and tabulated by Grantham [216], and are shown by the upright and inverted triangles in Figure 3.2, where the second reflectometer station is used for demonstration.

It should be noted that the highest frequency, Ka-band did not always reach its cutoff point, as was the case for stations 3 and 4. Therefore, the reflectometer stations can only directly establish six or eight discrete points where a 20% reflection level was either initiated or decayed. The ionization history can be readily interpolated from this source data. Similarly, an approximate plasma distribution along the body can be obtained by interpolating between the data points.

In addition to the limiting nature of such discrete measurements, there exist several restrictions to the use of reflectometer data for validation studies, specifically relevant for the RAM-C II test flight. At 56.4 km, the RAM-C II beryllium nose cap approached its melting point and was consequently pyrotechnically ejected to expose a teflon heat shield (see Figure 3.1). Impurities in the teflon (about 5 ppm total alkali-metal content) caused the flow field to be more challenging to analyze, as Na, K, Rb, and Cs contaminated the clean air. It should be noted that while teflon ablation has been shown to decrease electrons by up to two orders of magnitude [218], the effects of the ablating afterbody are believed to have been negligible [92, 219]. At 38.1 km, the total wind angle of the payload became relatively large (6°) and oscillations in the plasma reflection coefficient became present [216]. At altitudes below about 30.5 km, the electron-neutral collision frequency started to exceed the aforementioned low $\nu_{\mathrm{en}}/\omega_{\mathrm{p}}$ ratio assumption, making it more difficult to interpret the reflectometer data primarily due to a decrease in the sharpness of the reflection coefficient change at critical densities. At around the same altitude, the thickness of the teflon shielding started to recess, making it difficult to interpret the phase difference needed to assess the plasma stand-off distance.

3.1.2 Electrostatic Probe Rake

An alternative technique for obtaining a more non-discrete representation of the plasma distribution is through the use of electrostatic probes. The RAM-C II test flight used one electrostatic probe station located 1.23 m axially along the body, shown in Figure 3.1, which contained eight independent iridium ion collectors positioned 1 to 7 cm radially from the body [220]. The electron number densities were inferred assuming a non-zero flow velocity with free-molecular flow cylindrical probe theory, as described in Ref. [221], where an ion flux is obtained via a measurable ion current. Assuming a neutral plasma, the electron number density could then be determined. The resulting electron number densities at Probes 1 and 8 have been re-transcribed and tabulated from Ref. [220] and are included in Appendix A.

The electrostatic probe data on RAM-C II were bounded by the lowest measurable current and system saturation current, which were 10^{-7} and 10^{-3} A, respectively. This amounted to a measurable electron number density range between approximately 10^{14} and 10^{18} m^{-3}, the lower bound of which was first registered at 85.3 km. To prevent the intense heat loads that could result in surface melting and possible structural damage to the entire payload, the electrostatic probe was retracted at 56.4 km. As this coincided with the beryllium nose cap ejection, the flow field throughout the flight experiment remained clear of teflon-related impurities during the duration of the electrostatic probe measurements.

Nevertheless, there remained several sources of error that must be considered for validation studies. Many ground-based tests were performed on the Langmuir probe methodology at NASA Langley, Stanford, and Cornell, and found a ±20% error for electron number densities ranging between 10^{16} and 10^{17} m^{-3}, and an overall confidence within a factor of two over a broader 10^{15} to 10^{19} m^{-3} electron density range [220]. Additionally, the beryllium oxide leading-edge of the electrostatic probe which insulated the ion and electron collectors was susceptible to leakage currents from thermal degradation at temperatures above 1366 K. Leakage currents resulted in higher-than-actual electron densities recordings, making measurements within this range questionable for use. From the thermocouple probe that was used to determine the altitude at which beryllium oxide degradation occurred, it was found that the more radially outward an electrostatic probe was located, the more susceptible it was to these leakage currents. Finally, although the relative total wind angle remained fairly small (0° to 4°) at the altitudes where the electrostatic probe collected data, the oscillations caused from the electrostatic probe fluctuating between the windward and leeward side during spin stabilization were quite discernible [220]. This is arguably the largest source of uncertainty associated with the data from this diagnostic technique. Each probe data measurement was sampled at 26.4 msec, or about 8% of a total revolution of the payload.

3.2 Chemical Kinetics Models

Due to their popularity and ease of use, Park's reaction rates and equilibrium constants suggested in 1990 [182] are used as the baseline chemical kinetics model for this study. These rates were established by curve-fitting a plethora of experiments that employed various diagnostic techniques including e-beams, photoionization, drift tubes, and afterglow techniques.

For the simulations presented in this chapter, an 11-species air model (N_2, O_2, NO, N, O, N_2^+ O_2^+, NO^+, N^+, O^+, and e^-) is used, unless stated otherwise. In the past, a 7-species air model (N_2, O_2, NO, N, O, NO^+, and e^-) was commonly used in RAM-C calculations to decrease computation cost. Of the electron-producing reactions, this model only includes the N + O associative ionization reaction, as it is generally regarded as the dominant ionization reaction within the flow field conditions experienced by RAM-C. To evaluate the role of this specific reaction, the 7-species model is compared to the 11-species air model. Additionally, the role of three primary associative ionization reactions is assessed through a 9-species model (where N^+ and O^+ are neglected). For the 7-species and 9-species models the charge exchange reactions are removed.

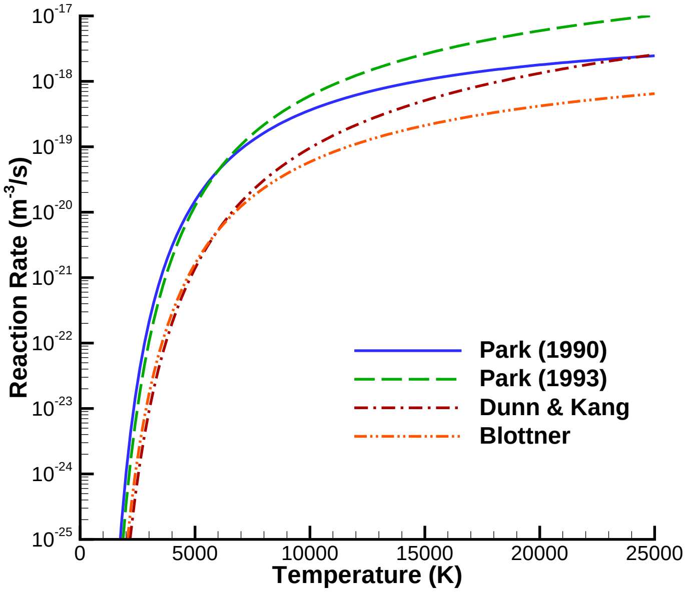

Figure 3.3: Associative ionization reaction rates of the $N + O \leftrightarrow NO^+ + e^-$ reaction.

The experiments that Park used to determine the associative ionization forward reaction rates were performed between 300 K and 3000 K. Park postulated that at higher temperatures, the coefficient n in the modified Arrhenius form expression used to calculate the forward rate coefficients, Eq. 2.35, would be unlikely to remain positive. Therefore, he extrapolated the curve fit from 4000 K assuming n = 0, which resulted in the rates listed in Ref. [182]. In a later study performed in 1993 [186], Park reassessed this claim and used his original positive pre-exponential n values, as they provided results that matched more closely with shock tube data investigating electron densities generated in the 9-12 km/s range. The N + O associative ionization reaction rates from both of Park's models are plotted in Figure

3.3, where it is readily apparent that the differences increase considerably after 3000 K. Further, forward reaction rates recommended by Dunn and Kang [222] and Blottner [223] (who first implemented the reaction rates of Bortner [224]) are investigated. From Figure 3.3, it can be seen that for these two models the dominant N + O associative ionization reactions are similar until around 8000 K where the rate of Blottner increases and approaches those of Park.

The equilibrium constants in Eq. 2.37 are given by Park [225] through curve fits of the form

$$\ln[K_{eq}(T)] = \mathrm{A}_1 \times Z^{-1} + \mathrm{A}_2 + \mathrm{A}_3 \times \ln(Z) + \mathrm{A}_4 \times Z + \mathrm{A}_5 \times Z^2 \tag{3.1}$$

where Z = 10000/T. Recently, Kim adjusted these parameters to be more suitable for high-temperature flows with expansion regions [226]. Figure 3.4 shows Kim's equilibrium constants for the N + O associative ionization reaction in relation to Park's, where the difference at low temperatures is noticeable.

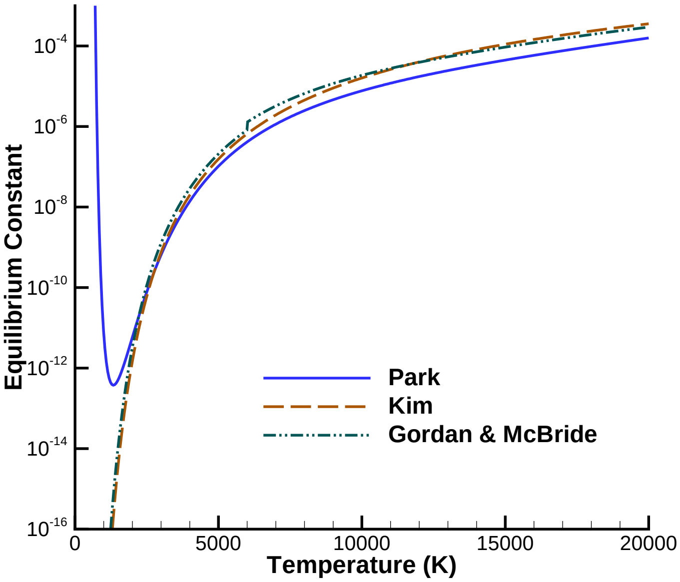

Figure 3.4: Equilibrium constants used for the $\mathrm{N} + \mathrm{O} \leftrightarrow \mathrm{NO}^+ + \mathrm{e}^-$ reaction.

It is also readily apparent from Figures 3.3 and 3.4 that at very low temperatures the forward and backward rates can become significantly small or large, resulting in unphysical reaction rates. To prevent a numerical underflow error resulting from the exponent in Eq. 2.35, the controlling temperature is modified below a set minimum temperature, taken to be $\mathrm{T_{min}}$= 800 K, and is computed as:

$$T_{mod} = 0.5\left[(T_c + T_{min}) + \sqrt{(T_c - Tmin + \epsilon^2)}\right] \tag{3.2}$$

where ϵ is a constant set to 80 K.

Another method for obtaining the equilibrium constants is through a minimization of the Gibbs free energy term. Gibbs free energy describes the maximum amount of reversible work capable of being done at constant temperature and pressure, which is appropriate for describing chemical equilibrium of open systems and is analogous to Helmholtz free energy [159]. The equilibrium composition can be determined by minimizing the Gibbs free energy of the system, or equivalently through the second law of thermodynamics, by the maximization of the entropy. A corresponding equilibrium constant for this approach is given by [152]

$$\mathrm{K_{eq}} = \left(\frac{P_0}{RT_{tr}}\right)^{\sum_s(\beta_{s,r}-\alpha_{s,r})} \exp\left[-\sum_s (\beta_{s,r} - \alpha_{s,r})\left(\frac{h_s^0}{RT_{tr}} - \frac{s_s^0}{R}\right)\right] \tag{3.3}$$

where $\mathrm{P_0}$ is a reference pressure set to 1 bar, and $\mathrm{s_s^0}$ and $\mathrm{h_s^0}$ are the normalized entropy and enthalpy, both provided by polynomial curve fits of thermodynamic data compiled by Gordon and McBride at NASA Lewis Research Center [227, 228]. All three techniques in calculating the equilibrium constants are implemented with Park's forward reaction rates (1990) [182] and compared in this study.

For all the aforementioned reaction rates, there exist inherent limitations that come from using empirical data, especially when applied to regimes outside of the original experiments. To try and address this issue, Chaudhry and Candler recently developed the Modified Marrone-Treanor (MMT) chemical kinetics model using information derived from quasiclassical trajectories computed with high-quality, ab initio Potential Energy Surfaces [229]. The MMT model uses a novel form for the forward reaction rate and vibrational energy change per dissociation, which was found to accurately describe dissociations from over 10 billion simulated molecular interactions. A variable correction factor is also used to account for non-Boltzmann distributions that exist as the gas is dissociated [229, 230]. In the current work, the MMT model describes the dissociation rate of N_2 and O_2 with partners N_2, O_2, NO, N, and O. The rest of the reaction rates are unavailable within this framework and are therefore taken to be that of Park. Amalgamating rates from ab initio and empirical sources in this fashion is rather inconsistent (see discussion in Ref. [231]), but, at present, a more suitable alternative has not been found. Nevertheless, the new rates of forming N and O atoms from dissociation should have an indirect role in affecting the creation of electrons through the associative ionization reactions. Additionally, as Laux et al. observed, the difference in neutral recombination plays a key role in maintaining ionization levels [232]. The MMT chemical kinetics model is compared with that of Park in this chapter.

3.3 Numerical Setup

The RAM-C semi-hemispherical truncated cone geometry consists of a 9 degree cone angle and a length of 1.3 m. At an altitude of 56.4 km, the 30.5 cm diameter beryllium nose-cap of the RAM-C II vehicle was pyrotechnically ejected and a 32.3 cm diameter teflon nose-cap was uncovered. To simulate this trajectory, thirteen points are chosen for the beryllium and teflon nose-cap geometries, listed in Table 3.1. It should be noted that the second trajectory point (73.1 km) marks the approximate onset of where continuum breakdown effects start being considered. However, as the 79.0 km point is still well within the gradient-length local (GLL) Knudsen number limits proposed by Boyd et al. [233], the high-altitude effects will be minimal in terms of plasma formation. Huber et al. postulated that at altitudes lower than 25.0 km, the transition of the boundary layer to turbulence would occur immediately after the stagnation point, fully nullifying the laminar flow assumption used in this study [234]. Consequently, this trajectory point is used as the lower bound.

Table 3.1: Trajectory points simulated with the two RAM-C II nose-cap geometries.

Beryllium Nose-cap	Altitude (km)	79.0	73.1	71.0	68.9	65.5	61.0	56.4	50.9
	Velocity (km/s)	7.65	7.66	7.66	7.66	7.67	7.65	7.64	7.62
Teflon Nose-cap	Altitude (km)	56.4	50.9	43.5	38.9	34.3	29.7	25.0	-
	Velocity (km/s)	7.64	7.62	7.49	7.32	7.01	6.38	5.28	-

Two points, 56.4 km and 50.9 km, are chosen to examine the effects of the shape change from the nose-cap ejection. The model does not account for an introduction of impurities into the flow field which limits the comparative nature of the post-ejection trajectory points. The velocity within the first trajectory range remains fairly constant, so that the differences between the trajectory points can be assumed to be mostly dependent on changes in density and temperature at different altitudes.

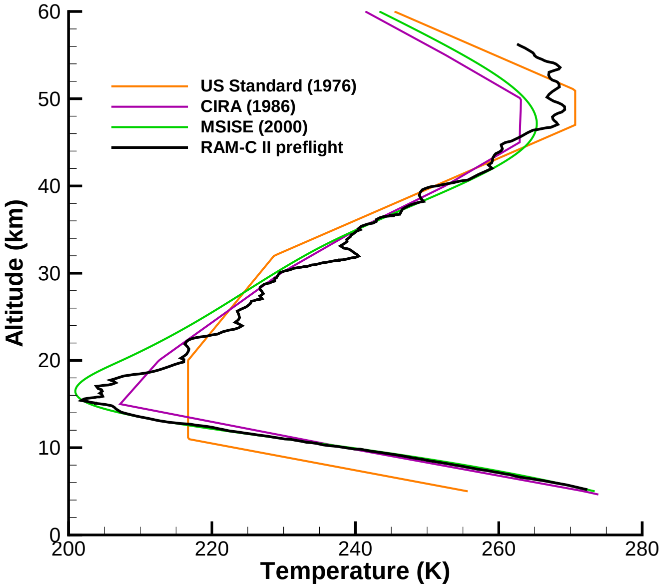

Figure 3.5: Atmospheric models compared with radiosonde meteorological temperature measurements taken on the day of RAM-C II launch above Bermuda.

To determine the free-stream conditions at each altitude, viz., the composition of each air constituent, the density, and the temperature, the Naval Research Laboratory's temperature and density model, MSISE-00 (Mass Spectrometer and Incoherent Scatter Radar Exosphere-2000), is employed [72]. As Figure 3.5 shows, comparison with the pre-launch temperature measurements, available up to 55 km, favors MSISE-00 over other commonly utilized atmospheric models, such as the U.S. Standard Atmosphere [235] and CIRA [236] models. The approximate latitude (33N), longitude (65W), date (August 8, 1968), and time (1516Z) of the RAM-C II flight test are used as inputs in the MSISE-00 atmospheric model.

A two-dimensional, axisymmetric representative mesh is generated for each RAM-C II trajectory point. In order to apply the axisymmetric condition, the total wind angle and body revolutions present within the flight test are neglected. The effects of such an assumption are examined in an ensuing section (3.4.1.1).

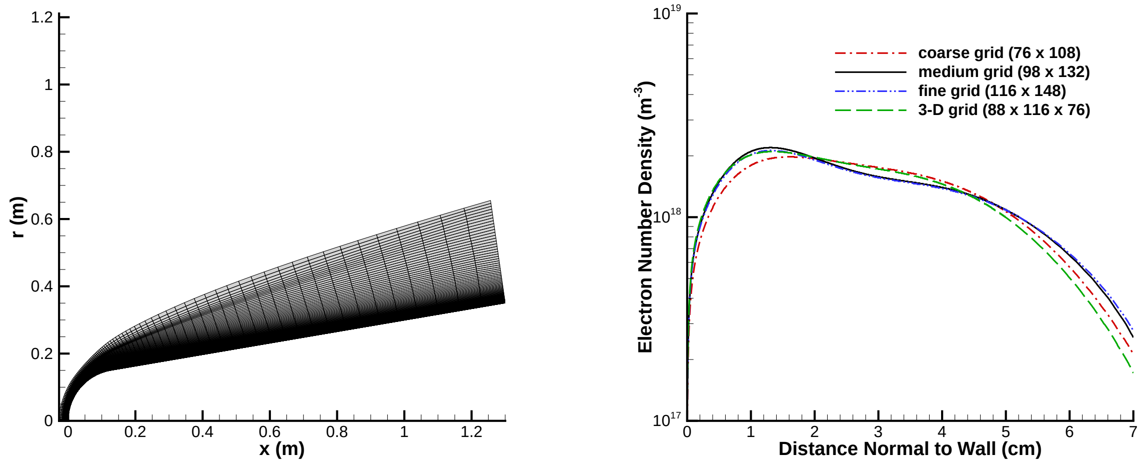

Figure 3.6: Medium-sized mesh used for the 61.0 km trajectory point (left) and convergence of maximum number density at the second reflectometer station (right).

The computational grids for each trajectory point contain approximately 13,000 cells with 98 cells along the surface and 132 in the direction normal to the vehicle, as shown in Figure 3.6. The majority of the wall normal cells are contained near the vehicle surface to capture high gradients expected within the boundary layers. Since there is a wide range of freestream altitude conditions encompassed by the RAM-C II trajectory, it is vital that each grid is constructed such that the shock and any adjacent cell face have the same normal, as recommended in Ref. [237]. This is performed through an iterative process where the elements at the shock location, as defined by the location where the temperature first becomes 1.5 times that of the freestream, are adapted and re-aligned to maintain shock-normalcy.

Additionally, a grid convergence study is performed for all cases with a coarser and finer grid, containing approximately 8,000 and 17,000 cells, respectively. The maximum electron number density throughout the flow at locations of interest, particularly the stagnation line and locations of diagnostic instrumentation, is used to assess grid convergence. Figure 3.6 shows a sample of this process for the second reflectometer station, which is in the expansion region of the flow. A maximum percent difference of 5% between the baseline, medium grids and fine grids indicated adequate mesh-fineness. While this approach is rather similar to the one used in Ref. [238], a more comprehensive description of this specific grid convergence methodology as it is applied to another geometry is detailed in Section 4.3.

An isothermal wall condition fixed at 1200 K is used throughout the cases presented henceforth in this chapter. Previous simulations have assumed a range between 1000 K to 1500 K, as the wall temperature is unknown from flight measurements [152, 212, 214]. Unless stated otherwise, the mixture transport quantities (species diffusion, viscosity, thermal conductivity) of the flow field are calculated using Wilke's semi-empirical mixing rule, with species thermal conductivities and viscosities determined using Eucken's relation and Blottner's curve fits, respectively, and a constant Lewis number of 1.4. Wilke's mixing rule is compared with that of Gupta's in Section 3.4.3.1. The no-slip condition is imposed for the flow velocity. Wall catalycity is treated as promoting surface ion and electron recombination.

3.4 Results

3.4.1 Trajectory Point: 61.0 km

In prior analyses, the 61.0 km trajectory point has often been used for benchmarking and validation studies. This point is used in the current study to provide a more in-depth assessment of the various chemical kinetics models. Figure 3.7 displays the translational-rotational temperature and electron number density contours surrounding the RAM-C vehicle, calculated using the Park (1990) [182] chemistry set model at this trajectory point.

As expected, the highest temperatures (around 22,000 K) are obtained directly behind the bow shock. Likewise, it is also seen that most of the ionization occurs in the stagnation region. The flow temperature rapidly reduces downstream due to the expansion around the spherical nose cap. Although local temperatures are relatively low in the shoulder region, the gas carries a large number of electrons that have been produced near the nose but have not yet recombined. The net recombination rate increases as the temperatures continue to cool downstream.

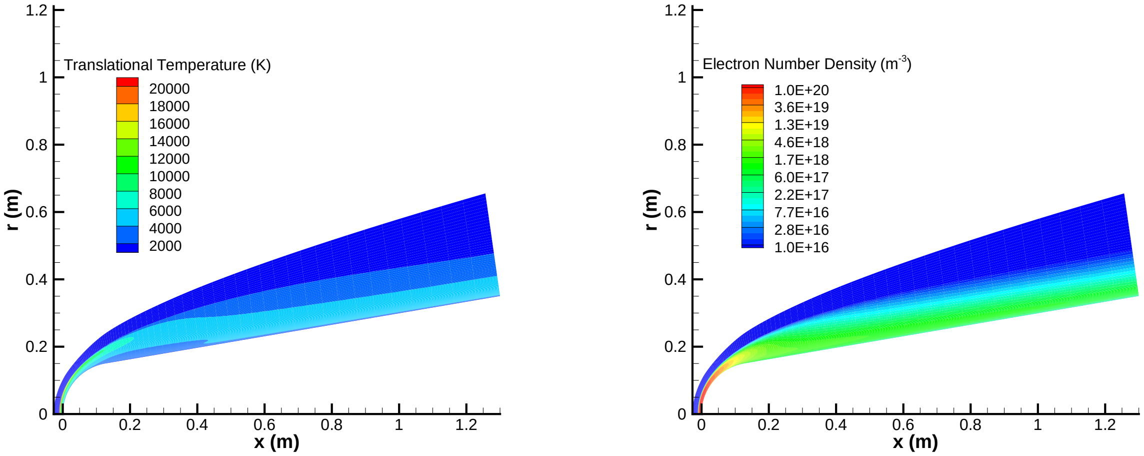

Figure 3.7: Translational-rotational temperature (left) and electron number density (right) contours of RAM-C II at 61.0 km using the 11-species air Park (1990) [182] chemical kinetics model.

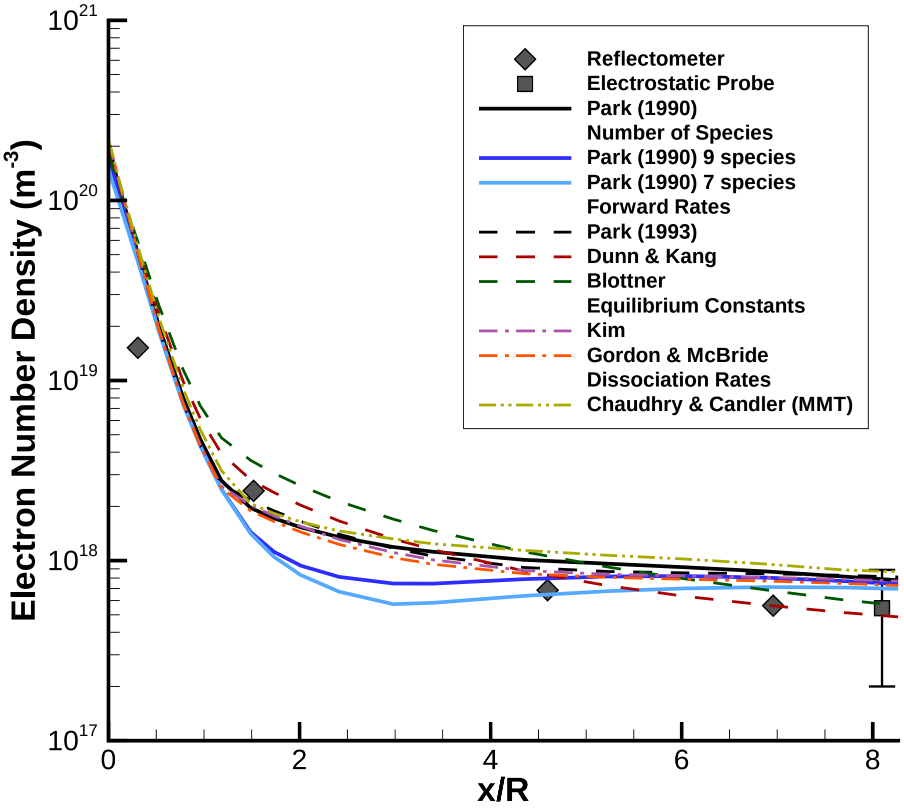

Figure 3.8: Maximum electron number densities normal to the surface of the RAM-C body and comparisons with the four-frequency reflectometer and electrostatic probe measurements.

The maximum electron number densities evaluated along lines emanating radially outward from the wall are plotted against a normalized axial distance for the different chemical kinetics models in Figure 3.8. RAM-C II plasma measurements, as discussed in Section 3.1 are also included in the figure. It must be repeated that a reflectometer station evaluates discrete instances of when a specific transmission frequency is reflected. Therefore, the reflectometer measurements in the plot are interpolated values between two cut-off frequencies. Moreover, the first reflectometer data point on the plot corresponds to the maximum number density obtainable with the highest (Ka-band) frequency of the reflectometer, which had already previously been met at 71.9 km. Consequently, discrepancies may appear with flight data presented in previous works, such as those in Refs. [152, 212–214], epitomizing the uncertain, interpolative nature involved when using the reflectometer flight data at singular trajectory points. The error bars on the electrostatic probe measurement indicate the influence of body motions on readings, as the probe traversed from the leeward to windward side of the vehicle.

In general, there is good agreement between each chemistry model and the flight measurements. Each model agrees within an order of magnitude of the reflectometer measurements and within the bounds set forth by the electrostatic probe. Also, regardless of chemistry model used, there is very little disparity in the stagnation region, indicating that the flow has most likely reached equilibrium conditions at this location.

The difference in the number of species plays a minor role in the amount of ionization present in the bow-shock region. This further verifies the long-standing idea that the N+O associative ionization reaction is the most significant electron producing reaction in this regime [239]. It is not until past the shoulder that the use of a lower number of species starts to degrade the quantity of electrons present. This trend has also been previously observed by many others, including Gimelshein and Wysong [240]. A portion of this difference can be explained by the additional ionizing reactions present in the 11-species model. However, the inclusion of the two additional diatomic ions in the 9-species model introduces a very limited reduction of the disparities, indicating that the charge exchange reactions play a significant role in maintaining the ionization level of the flow around the shoulder region. In Fig. 3.9 the net production rates for each ion-generating reaction on the stagnation line and along the line perpendicular to the second reflectometer station are shown. Indeed, it is apparent that the charge exchange reactions, specifically the $\mathrm{NO}^+ + \mathrm{O}_2$ and $\mathrm{O}_2^+ + \mathrm{N}$ reactions, are very active in the stagnation region. Subsequently, there is a considerable number of diatomic ions converted to N^+ ions that block the available pathways for recombination to occur.

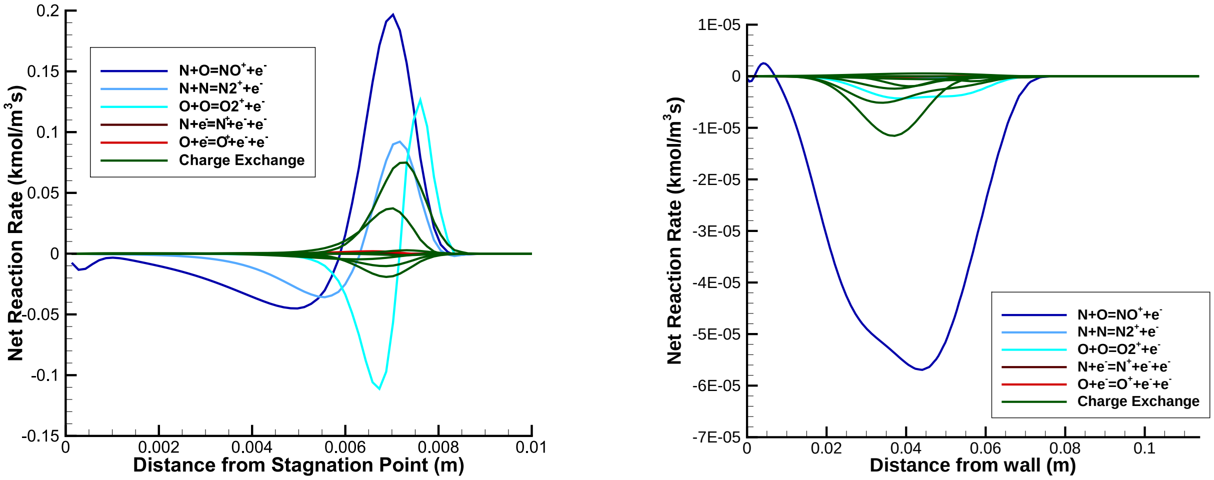

Figure 3.9: Net reaction rates for RAM-C geometry at 61.0 km, using Park (1990) [182] 11-species model, at the stagnation line (left) and reflectometer station 2 (right).

Further downstream, the number of electrons starts to increase for both the 7-species and 9-species models, whereas the number of electrons produced by the 11-species model decreases. In this region, recombination dominates the net rate of electrons, as indicated by Figure 3.9. As recombination is an exothermic process, the increase in the electron-ion recombination of the 11-species model leads to more energy being added into the translational-rotational energy modes. The higher T_{tr} in the 11-species model induces higher vibrational relaxation rates, which in-turn lowers T_{vee} to bring it closer to equilibrium with T_{tr}.

Altering the forward reaction rate models results in the largest variance of the electron number density downstream of the shoulder. The flow in this region has cooled to well below 10,000 K. It is seen in Fig. 3.3 that both Park (1990) [182] and Park (1993) [186] are nearly identical at these temperatures. As a result, there is also marginal difference between both Park models in Fig. 3.8. The use of the forward reaction rates recommended by Dunn & Kang and Blottner at first produce higher electron densities near the shoulder but eventually lead to a decrease further downstream. As the equilibrium constants in Eq. 3.1 are identical for this set of models, the reduced forward rates result in lower reverse reaction rates than that of Park's models. Further downstream, Park's forward rates for the ionizing reactions still dominate recombination, while the rates of Dunn & Kang and Blottner are more dominated by the recombination processes, indicated by the differences in slope. The use of the Gibbs free energy method with Gordon & McBride's rates for calculating the equilibrium constant shows a constant decrease in electron number density when compared to Park's equilibrium constant, once again indicating that the 61.0 km trajectory point is driven largely by electron recombination. The low-temperature adjustment of Kim provides a similar result.

The MMT model of Chaudhry & Candler [229] produces higher electron densities throughout when compared with the results of using Park's (1990) rates. Though the percent difference between the two is at a maximum of 7%, the change demonstrates the indirect role of the dissociation rates of N_2 and O_2 on ionization levels. As the N_2 and O_2 dissociation rates are generally milder within the MMT model [241], there are more reactants available for the two Zeldovich exchange reactions. The Zeldovich reactions, which utilize the same rates in the application of both Park and MMT models for this study, require less activation energy than the N_2 and O_2 dissociation reactions. In turn, more N and O atoms are produced with the MMT model and are available for the NO^+ associative ionization reaction, creating comparatively more free electrons. Even so, only marginal differences exist between the two models which can be attributed to the underlying nature of the selected flow configuration and quantity of interest, i.e., electron number density. Indeed, it has been recently reported in a sensitivity study by Ouyang et al. that of the reactions leading to the dissociation of diatomic molecules, the dissociation of NO ($NO + M \leftrightarrow N + O + M$) is the most influential in the creation of free electrons [242]. The dissociation rates of NO are chosen to be the same for both the MMT and Park models. In other words, the current study does not display a flow behavior that is sensitive to how the MMT and Park models behave differently.

3.4.1.1 Axisymmetric Assumption

The results of the previous section were all calculated under an axisymmetric assumption. In the actual flight test of RAM-C II, the vehicle rotated about the body axis at 3.04 revolutions per second to prevent large perturbations. Still, the vehicle had nonzero wind angles. During the primary data period, the onboard accelerometer recorded a maximum angle of attack of 3 degrees (pitch plane) and maximum sideslip angle of 4 degrees (yaw plane) [216]. The corresponding total wind angle range during this period was between 0 and 4 degrees [220]. Thus, the cumulative nutation from the spin stabilization and total wind angle resulted in peak-to-peak fluctuations in the electron density along the flow field, necessitating scrutinization of the aforementioned axisymmetric assumption. The maximum total wind angle of 4 degrees is translated to an angle of attack (about the x-axis) and used for this assessment.

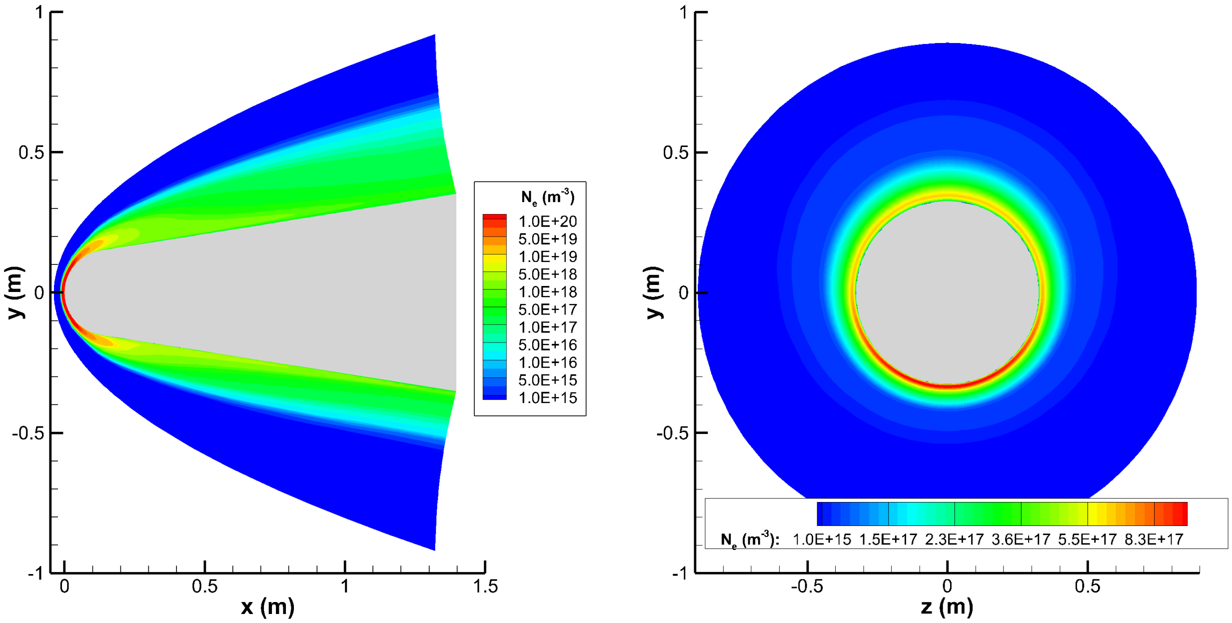

Figure 3.10: Electron number density contours for z = 0 m plane (left) and x = 1.234 m plane (right) slices of a RAM-C II 3-D simulation at 61.0 km with a 4 degree wind angle aligned about the x-axis.

From the 3-D simulation, it is noticed in Figure 3.10 that both the shape of the plasma layer and electron density exhibit asymmetry at the same axial location between the windward (negative y values) and leeward sides of the vehicle. As the windward side is more exposed to the incoming flow than it would be for a zero angle of attack case, the body gives the impression of a blunter shape, causing a stronger bow shock with higher associated temperatures and ionization levels for the gas. Conversely, the leeward side experiences a larger expansion region which cools the flow faster than the symmetric flow case.

The difference in electron density between the windward and leeward sides gradually grows as the flow progresses along the vehicle. Therefore, the furthest downstream measurements, collected by the electrostatic probe, correspond with the largest influence of the vehicle asymmetry. An x-plane slice at the electrostatic probe location is displayed in Figure 3.10. The maximum electron number density of the windward side for this location is 1.02×10^{18} m^{-3}, whereas the leeward side is 6.15×10^{17} m^{-3}, about a 1.7 times reduction. The average value of these maximum electron densities relates well with that of the axisymmetric case, as only a 3.4% difference is found. This implies that the variations of the flight were generally symmetrical. Both of these results are consistent with previous RAM-C modeling efforts that considered the wind angle fluctuations [243–246] and with the electrostatic probe data [220].

While it is evident from this particular study that the physical coning motion of the vehicle is nonnegligible, it is problematic to properly numerically simulate, as it is not clear what the angular configuration should be for each trajectory point. The accelerometer used by RAM-C II did not permit accurate measurements for parts of the trajectory where low dynamic pressures were experienced [216, 220]. Further, while the total wind angle is more representative of the spacecraft configuration, it is the angle of attack that demonstrated better correlation with the data collected by the probe rake. The use of three-dimensional simulations also significantly adds to the computational costs, limiting the amount of simulations that can be performed for comparisons along the trajectory. Thus, a zero angle of attack, axisymmetric flow will be used for the remainder of this work.

3.4.2 Reflectometer Data Comparisons

Plasma profiles perpendicular to the RAM-C II wall are constructed and the maximum electron density is found from these lines for each axial reflectometer station location. A direct comparison between the maximum electron number density generated through trajectory point simulations and the reflectometer data is made to eliminate the assumptions inherent with interpolation. The reflectometer measurements presented in this section are those determined by Grantham [216] with horizontal bars depicting the altitude range in which the reflection coefficient experienced a definite rise. Comparisons are made between models using different number of species and different sets of forward reaction rate coefficients.

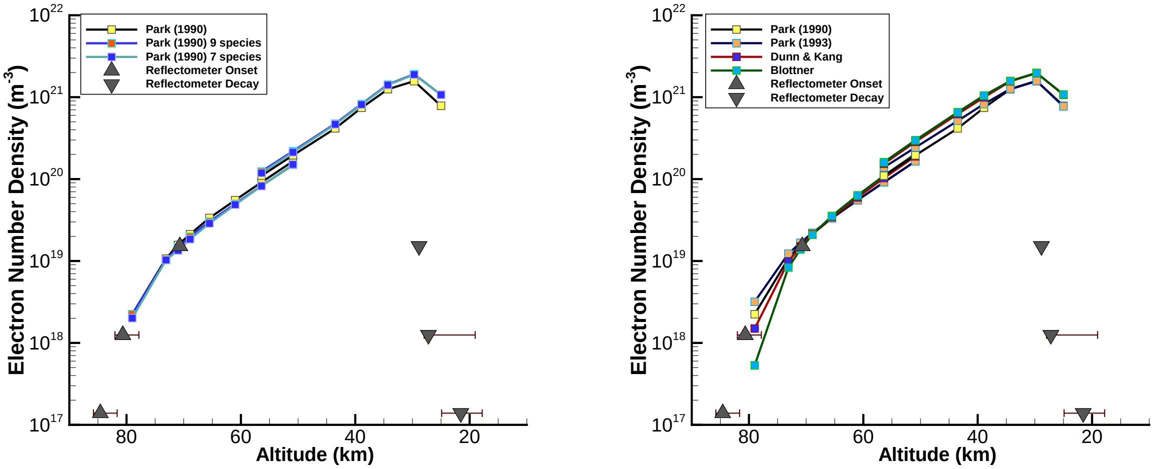

Figure 3.11: Comparison of predictions from several different chemical kinetics models with data from reflectometer station 1 (x = 4.47 cm).

At the first reflectometer station, located just downstream of the bow-shock, there is not much variation between the different chemistry models for the majority of the sampled trajectory points as shown in Figure 3.11. All models also exhibit excellent agreement with the onset of the Ka-band reflection, which occurred at 72 km. Examining the variation of the number of species included, it is clear that the presumption of N+O associative ionization reactions dominating electron generation remains valid. Within the entire trajectory range, the largest percent difference of electron number densities is 28% at 25 km between the 7- and 11-species models. The lower altitudes and lower velocities are associated with weaker bow shock conditions where recombination can start to play a key role within the stagnation region where the first reflectometer is situated. Indeed, at higher altitudes where the role of recombination is more limited, the percent differences in electron number density between each of the three species sets does not exceed 8%.

Conversely, the different forward reaction rate coefficients lead to much wider variations in electron number densities at both the highest and lowest altitudes. At 79.0 km there is a 132% difference between the calculated electron number densities from Blottner's [223] and Park's [186] models. It was shown by Candler that at higher altitudes with similar velocities the shock will be more diffuse and contain larger regions of elevated temperatures [247], resulting in a more nonequilibrium state where the reaction rates will play a larger role. In the stagnation region near the first reflectometer, the translational temperatures at this altitude approach 24,000 K. At these high temperatures the N+O associative ionization forward rate of the Blottner model is almost 15 times smaller than that of Park [186], shown in Figure 3.3. At lower altitudes, the temperatures are much less intense, and electrons start to recombine further upstream in the flow. At 25.0 km altitude, the difference between the calculated electron number densities from Blottner's and Park's [186] models is 31%. As the equilibrium constants are the same for these models, from Equation 2.37, the slower forward rates of Blottner also lead to slower backward rates, which in turn results in a larger electron density. At the lower altitudes, the temperatures even directly behind the bow shock are less than 8,000 K. In this temperature range both of Park's models [182,186] and the models of Blottner and Dunn & Kang [222] have similar behavior which leads to the indiscernible differences in electron number densities in Figure 3.12.

All sets of models severely overpredict the electron number density when compared to the station 1 reflectometer data at blackout decay. Schexnayder and Evans showed that the ablation of Na, which is not included in the present study, will increase the electron number density [92], which further increases the gap between the models and flight data. In studies by Huber et al. and Evans et al. such a discrepancy between the reflectometer data and numerical analysis was examined in detail [234, 248]. It was found that for the decays of the first reflectometer station the effects of transition and high collision frequency mask the influence of the electron number density to the degree where a meaningful interpretation is not possible. The low altitude ν_{en}/ω_p values were around 1 to 6, which indicated a drastic dampening of the reflection coefficient response. The anomalous rapid decay at these altitudes by some of the X-band reflectometer readings was believed to be a result of the transition to turbulence adjacent to the first station location.

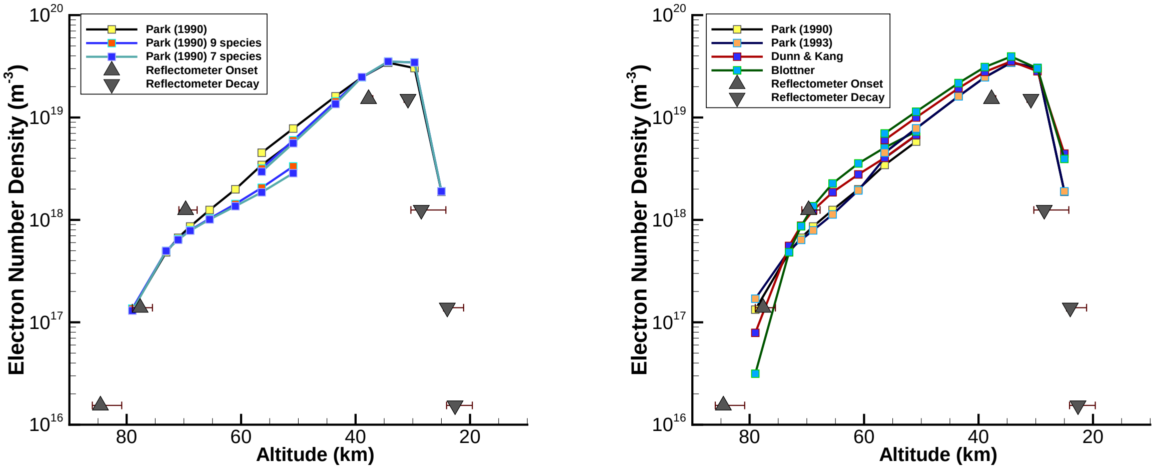

Figure 3.12: Comparison of predictions from several different chemical kinetics models with data from reflectometer station 2 (x = 23.16 cm).

The second reflectometer station provides the largest amount of data as all four frequencies were matched by a cut-off plasma frequency in the flow field. This reflectometer station is located just downstream of the shoulder, where the flow expands, and temperatures decrease considerably. As this region brings upon a coalescence between a significant amount of electrons advected from the bow shock and milder flow conditions well suited for recombination, the largest discrepancies between the chemistry models emerge, as shown in Figure 3.12. Nevertheless, there is still fair agreement (within a factor of 4) throughout between the flight data and various simulations. Excellent agreement occurs between the electron density calculations using Park's [182] model and the onset of S-band blackout at 78 km and between Blottner's model and the onset of X-band blackout at 70 km. The altitudes at which onset (38 km) and decay (31 km) of the Ka-band blackout and decay of the X-band (29 km) blackout occur are consistently overpredicted by the models. However, when the limitations previously discussed in using these low-altitude data are considered, specifically the likely presence of turbulence in the flow, reasonable agreement exists between the chemistry models and the reflectometer data.

At the middle altitudes of the examined trajectory (between 65.5 km and 43.5 km), the difference of predicted electron densities becomes significant when the additional species are neglected. There is a 67% difference between the 7- and 11-species models at 50.9 km. It was previously discussed when examining the 61.0 km trajectory point in detail that the charge exchange reactions are a likely cause of the decreased electron density. Recombination is mainly brought upon by the reverse reactions of NO^+, N_2^+, and O_2^+ colliding with free electrons to generate N and O. For the 7- and 9-species models, all ions are therefore susceptible to recombination. For the 11-species chemistry set, the pathways for which recombination can occur are indirectly limited as a result of the charge exchange reactions.

The use of different forward reaction rates once again leads to the largest differences of the calculated electron number densities at the second reflectometer station. These differences are analogous in nature to those seen at the highest and lowest altitudes at the first reflectometer station, yet even more magnified in the middle altitudes. Once again, the largest percent differences of the electron densities come from the use of Park [186] and Blottner models, which result in differences of 127% and 58% at the 79.0 km and 25.0

km trajectory points, respectively. Unlike the first reflectometer station, the shift in which model produces the largest electron number densities occurs at a higher altitude and with much greater magnitude at the second reflectometer station. This is recognized as a result of the importance of recombination in this region, where again, the slower backward rates of Blottner and Dunn & Kang lead to a larger abundance of electrons.

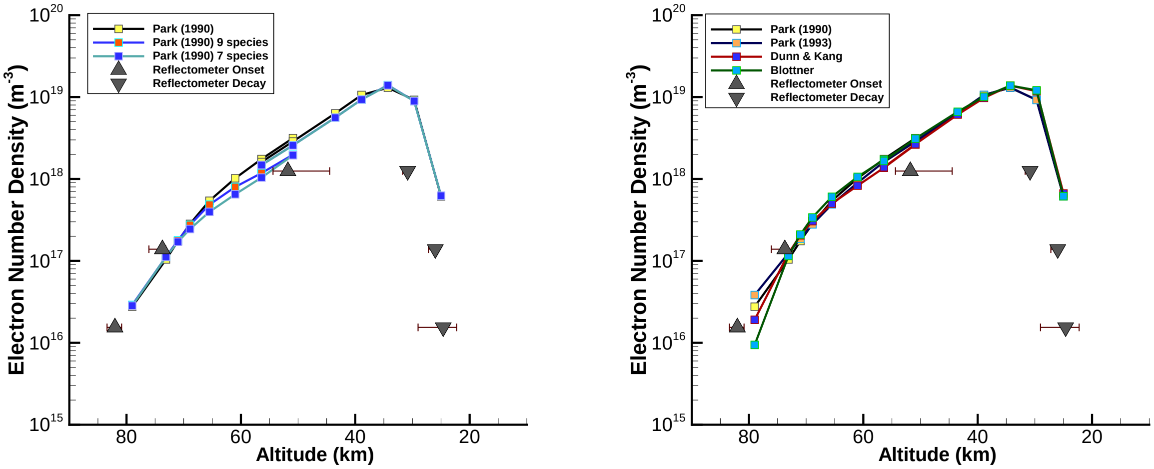

Figure 3.13: Comparison of predictions from several different chemical kinetics models with data from reflectometer station 3 (x = 70.05 cm).

Both the third and fourth reflectometer stations provided three readings where direct comparisons can be made: at S-band and X-band transmission frequencies. In the regions near these reflectometers, the flow has significantly cooled and is strongly dictated by the recombination of ions and electrons. It is shown in Figures 3.13 and 3.14 that the difference of using a reduced number of species once again becomes less prominent further downstream. Likewise, the selection of the different forward reaction rates gradually becomes inconsequential to the calculated electron number densities. Overall, good agreement exists at the higher altitudes between these chemistry models and the flight data from the last two reflectometers, while, once again, an anticipated disagreement is present at the lower altitudes.

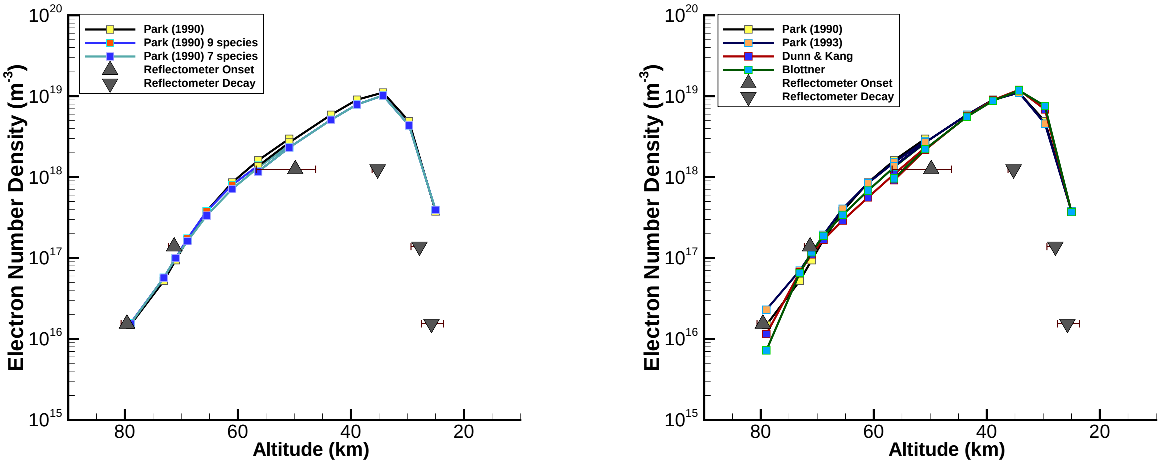

Figure 3.14: Comparison of predictions from several different chemical kinetics models with data from reflectometer station 4 (x = 106.04 cm).

The change from the beryllium nose-cap geometry to the teflon nose-cap geometry at 56.4 km increases electron production in the bow shock region by up to 28%, as indicated by the first two reflectometer stations. This is most likely attributed to two sources: a) the post-ejection geometry is blunter producing a stronger bow shock and b) the first reflectometer station is more upstream in the post-ejection geometry placing it closer to the stagnation region. As the flow expands around the shoulder further downstream, the additional electrons recombine and the difference in plasma densities between the two geometries becomes negligible.

3.4.3 Electrostatic Probe Data Comparisons

Direct comparisons of the electron number densities calculated with the various equilibrium constants are made with the available electrostatic probe rake data (located 1.234 m downstream of the stagnation point). Jones et al. showed that the peak electron densities were recorded by the outermost probe (probe 8) [220]. However, the temperature surrounding probe 8 went past the aforementioned beryllium oxide degradation temperature limit at roughly 65 km, making data from lower altitudes questionable at best for this probe. It was further shown that the temperature likely never reached this limit for only the inner-most probe during the RAM-C II flight. Therefore, both probes 1 and 8 are used here for comparison.

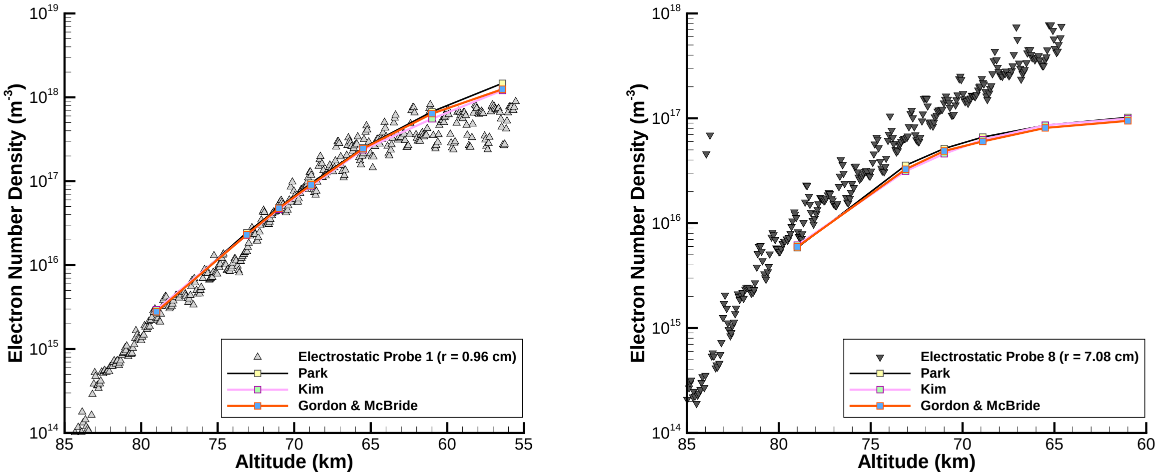

Figure 3.15: Comparison of station 1 (left) and station 8 (right) of the electrostatic probe rake (x = 1.234 m) with electron densities calculated with different equilibrium constants.

Good agreement exists with inferred electron densities from the electrostatic probe 1 and predictions from the different models, regardless of how the equilibrium constant was calculated. As Figure 3.15 shows, the calculated electron densities are consistently enveloped by the probe 1 measurements, further confirming the symmetry of the leeward to windward fluctuations observed and discussed in Section 3.4.1.1. On the other hand, the models all noticeably under-predict the electron densities inferred from the electrostatic probe at location 8 (at a 7.08 cm wall normal distance), especially at lower altitudes. This mismatch is an artifact of the electron density continuing to gradually increase radially outward for the probe station data at all altitudes measured, i.e., based on measurements of the probe rake the maximum number density is not captured. Conversely, the electron density of this work (and others who have compared data at singular trajectory points [249, 250]) has been calculated to be at a maximum within the locations of probes 2-5 and starts to gradually decrease at more radially outward locations.

The differences brought upon by the variation of the equilibrium constant models are also displayed in Figure 3.15 and identify the altitudes where recombination of electrons dictates the plasma flow field. Whereas the electron densities calculated using Kim's and Gordon & McBride's equilibrium constants stay within 7% of each other throughout the trajectory, there is more disparity between these models and that of Park's, especially at lower altitudes. In these lower altitude regimes, the maximum temperatures near the electrostatic probe can be as low as 3,000 K. The differences of the equilibrium constants at low temperatures can play a significant role in electron concentrations, especially those of NO^+ recombination as shown in Figure 3.4 where that of Park is noticeably higher. From Eq. 2.37, these higher equilibrium constants result in slower backward rates which in turn reduce the number of electrons being recombined. At the highest altitudes (down to 65.5 km), the predictions of electron number density only experience at most a 5% difference between the three models. Afterwards the maximum percent differences between Park and the other two models gradually increase up to 33% at the 50.9 km trajectory point. This trend is indicative of a recombination-driven plasma flow field at altitudes near and surpassing 61 km.

As the equilibrium constants calculated via a minimization of Gibbs free energy have shown inconsequential differences to that of Park, are more consistent with the laws of thermodynamics, and are easier to implement for new reactions, as only the forward rate coefficient is needed, this methodology is selected as the default for the remainder of this dissertation.

3.4.3.1 Mixing Rule Model

All of the prior results within this chapter have used Wilke's semi-empirical mixing rule [164]. This relatively simple model is only fully appropriate to accurately capture the transport properties of nonionized and nonpolar flows. Accordingly, the model has been found to start losing accuracy at around 10,000 K [167,168,223,251]. At higher temperatures, Gupta's mixing rule is generally more appropriate because it considers the true nature of the viscosity collision integrals [68]. Still, caution should be applied to using Gupta's mixing rule as the simplifications that it utilizes can become invalid for more strongly ionized flows. The influence of these transport models on electron formation, as applied to Park's (1990) chemical kinetics model, is examined by comparing with the data from the electrostatic probe rake. Further details on the formulation of both transport models are found in Section 2.1.2.

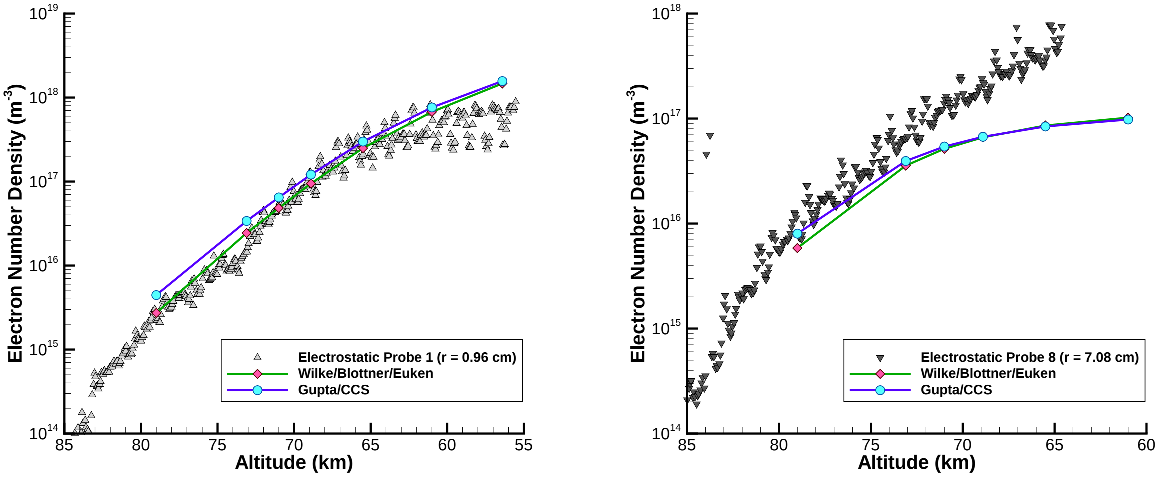

Figure 3.16: Comparison of station 1 (left) and station 8 (right) of the electrostatic probe rake (x = 1.234 m) with electron densities calculated using Wilke's and Gupta's mixing rules.

For higher altitudes, the transport model of Wilke is shown in Figure 3.16 to produce electron densities closer to the probe 1 measurements, as Gupta's mixing rule leads to an over-prediction. Conversely, Gupta's model has better agreement with the electron densities inferred from probe 8 at higher altitudes. The percent difference between the electron densities calculated from the two transport models is as large as 47.9% at 79.0 km, and gradually converges to 5.2% at 56.4 km. This can be directly attributed to the temperatures experienced within the flow field for each trajectory point. While maximum translational-rotational temperatures at 79.0 km exceed 24,000 K, the temperatures at 56.4 km are all found to be less than 18,500 K, or 48.8% closer to the aforementioned 10,000 K proposed suitability limit of utilizing Wilke's transport model. Since Gupta's model is more capable of capturing the behavior of ionized flows, and has been shown to be more computationally efficient [167], it will be employed, when appropriate, moving forward for the work contained in this thesis.

3.5 Chapter Conclusions

Various chemical kinetics models were assessed through detailed CFD analysis of the RAM-C trajectory. Several commonly employed chemistry models were used, and the results were compared with RAM-C II flight measurements, specifically the recordings of the reflectometers and electrostatic probes.

The limitations of using RAM-C II flight data from the reflectometer and electrostatic probe to validate computational models were presented in detailed discussion. Both the inherent shortcomings of the measurement diagnostics, such as the saturation and minimum sensitivity levels of the electrostatic probe, and the many uncertainties of the flow field, such as teflon impurities, can result in improper usage. Additionally, due to the discrete nature of the reflectometer measurements, comparisons used for validation at single trajectory points can only be indirectly done so via interpolated flight data. Thus, it was strongly advised that a detailed trajectory analysis of the RAM-C II flight be performed when direct comparisons with the reflectometer data are desired.

The detailed RAM-C II trajectory analysis showed that, regardless of chemistry model used, the thermochemical nonequilibrium calculations agreed reasonably well with the reflectometer station measurements. In particular, the onset of blackout for the Ka-band and X-band antennas were accurately predicted. Conversely, the decay of blackout was predicted to occur much later than in the flights, often overpredicting the electron number densities by an order of magnitude. This disagreement was seen in earlier findings and is likely attributed to flow field physics that are unaccounted for in the simulations, such as ablation by-products, fluctuating angle of attack and yaw angle, and turbulence.

As expected, the use of an 11-species model proved essential for most of the flight domain and is recommended for use in plasma simulations within similar flight regimes of the RAM-C II trajectory. Alterations to the equilibrium constant models were less consequential than when the forward reaction rate models were altered, especially at high altitudes and velocities. Further along the body, where recombination starts to predominantly dictate the flow field chemistry, the differences resulting from the forward reaction rate models would gradually diminish. Of the forward rate constants investigated, those of Park [182] and Dunn and Kang showed the best agreement to reflectometer data. However, it should be noted that the rates of Dunn and Kang used RAM-C measurements for early validation and, perhaps uncoincidentally, resulted in this agreement with the measurements [222]. The results obtained with the various equilibrium constant models and transport mixing rules are in good agreement with the innermost electrostatic probe but start to considerably underpredict the outermost probe at lower velocities. For all of these comparisons there was no model identified exhibiting substantial favorability. However, the altitude region near the 61.0 km trajectory point was identified as the start of recombination-driven plasma flow fields for the RAM-C II flight path.

For a more in-depth assessment of the flow field and the impact of the chemical kinetics model selection, the 61.0 km trajectory point was utilized. It was found that the largest deviations from the change in models occurred in the shoulder region where the flow expands and cools. The net reaction rates of the ion-generating reactions were presented and showed the importance of including the charge exchange reactions, further reinforcing the case for using an 11-species air model. The benefits of examining a single trajectory point were established in this work and many others, but due care must be given to account for the interpolative nature of the reflectometer measurements [252].

CHAPTER 4

TRAJECTORY AND VEHICULAR SHAPE SELECTION

The production of electrons surrounding a hypersonic vehicle is largely linked to the vehicle geometry and flight trajectory, which in turn dictates the freestream velocity and altitude. As no quick analytical methods currently exist to determine the amount of free electrons in the surrounding flow, there is usually deliberation over whether a unique vehicle design will experience blackout within a particular trajectory. Nevertheless, the effects of these mission parameters are reasonably understood when considered independently.

A higher velocity of the hypersonic vehicle corresponds to a higher kinetic energy available that can be consumed by the endothermic dissociation and ionization chemical reactions that produce free electrons. A lower altitude has a larger overall number density, which corresponds to a larger amount of reactants and particle collisions that also further expedites these reactions. Vehicle geometry also influences the level of ionization. Simple axisymmetric geometries can generally be categorized as blunt or sharp nosed, as shown in Figure 4.1. For a blunt-nosed body, electron generation primarily occurs after the nearly normal shock wave in the stagnation region, with a gradual decay as the flow progresses downstream [82]. Conversely, for sharp-nosed bodies, where an oblique shock remains attached, the plasma layer properties are primarily determined by viscous dissipation [253], where the production of electrons can increase with distance from the apex until an equilibrium condition is met. Realistically due to heat transfer and manufacturing considerations, a slender vehicle configuration, such as those used for hypersonic boost glide trajectories, requires a finite radius leading edge and is therefore described by an intermediate category of slightly blunted. For such a geometry, a normal bow shock exists at the nose where the high-enthalpy gases of the stagnation region feed the forward portion of the boundary layer. At some point downstream the shock will taper off and resemble a weaker oblique shock.

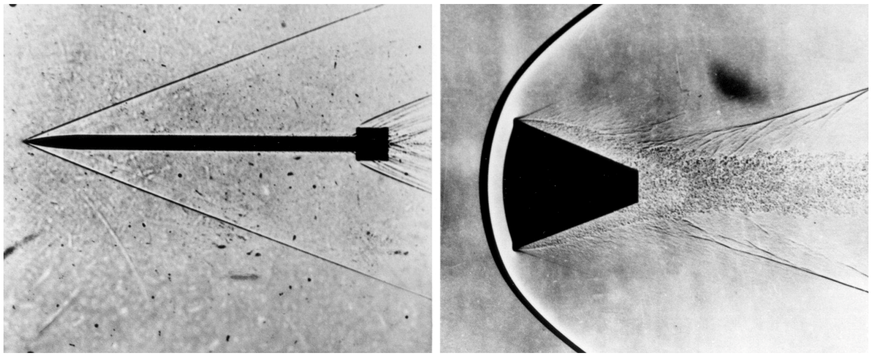

Figure 4.1: Shadowgraph images of two hypersonic vehicle shapes: a sharp nosed body (left) and a blunt re-entry capsule (right). Image from NASA.

There are certainly more complex body shapes, especially for manned reentry vehicles, transport aircraft, and lifting bodies. However, the general trend remains applicable: a slenderer geometry will result in lower ionization levels and a thinner plasma layer. As Steiger et al. observed [254], the maximum electron number density, $\mathrm{N}_{\mathrm{e,_{peak}}}$, at a particular downstream location, x, is proportional to the leading-edge radius, $\mathrm{R_n}$, as follows

$$N_{e,_{peak}}(x) \propto N_{e,0}\rho_\infty^{\frac{1}{2}}\frac{R_n^p}{x^q} \tag{4.1}$$

where $\mathrm{N_{e,0}}$ is the peak electron density in the stagnation region, ρ_∞ is the freestream density, the exponent p is a constant assumed to be 3 and q is a constant observed to be anywhere between 1.5 and 2.5 depending on the vehicle shape and downstream region of interest [254].

Logically it follows that aerodynamic shaping has been proposed as a blackout mitigation strategy [75, 82, 128]. The sharp, tusk-like assemblies proposed by Belov et al., that would contain an antenna ahead of the bow shock [101], radically exemplify the blackout solutions that have been suggested based on aerodynamic shaping. However, as early as this type of solution was proposed, the logistical downfall became quite clear [74,255,256]. Making vehicles as thin as possible to combat blackout resulted in reduced payload capacity and, more importantly, increased localized heat loads for the vehicle TPS to manage. Indeed, as Fay and Riddell showed in 1958 [257], the stagnation point heat transfer, q_{conv}, is inversely proportional to the square root of the leading-edge radius by

$$q_{conv} \propto \sqrt{\frac{\rho_\infty}{R_n}} u_\infty^3 \tag{4.2}$$

where u_∞ is the freestream velocity. From Eq. 4.2, it is also apparent that a high velocity can make the heat flux tremendous to overcome for hypersonic vehicles, and thus, is a key reason why reduced heat loads are a primary design driver for hypersonic missions.

A large portion of hypersonic vehicles have been designed for re-entry and seek significant drag for deceleration purposes. Analysis by Lees and Kubota showed that drag is proportional to the leading-edge radius [258], per

$$D \propto \rho_\infty u_\infty R_n^s \tag{4.3}$$

where the exponent s is 1 for a two-dimensional geometry and 2 for an axisymmetric geometry. Therefore, a large leading-edge radius is doubly beneficial to a re-entry vehicle, which has historically driven designs in very blunt capsule shapes (see Table 1.1). However, when a vehicle is flown to have maximum range properties, as is the case for hypersonic boost glide vehicles, the drag must be minimized, resulting in more slender vehicle shapes. Furthermore, the impact of the surrounding plasma properties on antenna design has larger priority for hypersonic glide systems as a considerable amount of the mission possibly lies within the blackout regime. A continuous communication pathway with hypersonic glide vehicles is typically of elevated importance when compared to re-entry capsules. Thus, a vehicle designer must consider the trade space brought on by all of Eqs. 4.1 to 4.3 when planning a hypersonic glide vehicle. However, as there remains no proven means of managing heat loads for prolonged hypersonic flight on very slender shapes, Eq. 4.2 still takes considerable precedence.

Notwithstanding, it has remained rather unclear whether a hypersonic glide vehicle generates sufficient plasma to warrant concern pertaining to blackout. Hartunian et al. had previously speculated that a slender glide vehicle would not encounter blackout conditions at all [75]. It had also been further suggested by Michael White that glide vehicles suited for defense applications do not encounter the blackout problem during sustained flight [259].

Yet, at the speculated velocities and altitudes of some hypersonic boost glide trajectories [260–262], it has been demonstrated that these slender geometries are capable of forming a plasma cocoon that would in fact induce considerable signal attenuation for certain transmission frequencies of importance. For instance, Dix and Fuhs analytically examined flow over a 10-degree half-angle sharp cone along both an ICBM and equilibrium glide trajectory and determined a peak plasma density of 1 x 10^{18} m^{-3} in the downstream boundary layer [124, 253, 263]. More recent numerical analysis by Savino predicted a GPS blackout condition for a 10 cm radius PHOEBUS space-plane re-entering the atmosphere at orbital velocities [264]. Starkey demonstrated that L-band blackout becomes a concern for slender 20-degree wedges at Mach numbers exceeding 15 [82]. It also was calculated by Surzhikov that for a 1.5 cm radius blunted cone with a 3-degree half-angle flying at 5 km/s and 60 km, a non-trivial downstream plasma density of 1 x 10^{17} m^{-3} can be expected [265].

The concern of blackout for slender glide vehicles was not only observed through numerical methods. Belov et al. investigated, both numerically and experimentally, the electron densities of 0.5 cm and 2 cm radius antenna assemblies and found peaks of 1 x 10^{15} and 1 x 10^{17} m^{-3}, respectively [101]. Steiger et al. compiled flight test data and found X-band signal loss for a 0.6 cm radius, 8-degree half-angle cone at 44 km [254]. The study also presented VHF signal attenuation for geometries as slender as a 0.4 cm radius cone [254]. Earlier flights of Project RAM, where a 2.5 cm radius RAM-A geometry was flown, demonstrated a brief VHF signal attenuation period at 54 km and 5.4 km/s [55]. Lack of a united consensus for plasma density surrounding slender hypersonic glide vehicles has signified that this domain is likely not yet fully understood.

Thus, the objectives of this chapter are clear. While the role on the creation of plasma by the altitude, and to a lesser degree, the vehicle geometry and freestream velocities, were considered in Chapter 3 for the RAM-C II flight, the current chapter assesses the likelihood of plasma induced blackout for slender vehicle shapes along a characteristic trajectory. A trade-space analysis of a generic conic body is made to examine the role of both the leading-edge radius and cone half-angle.

4.1 Vehicle Geometry

Hypersonic glide vehicle geometries are usually complex, three-dimensional shapes that can involve intricate aerodynamics such as shock-shock interactions, crossflow, separation vortices, and compression lift effects [266]. These flows generally require larger grid sizes for numerical simulations at the expense of computational cost. Moreover, each complex shape is inherently designed for a specific mission profile and thus generality can be lost for assessing glide vehicles as a whole.

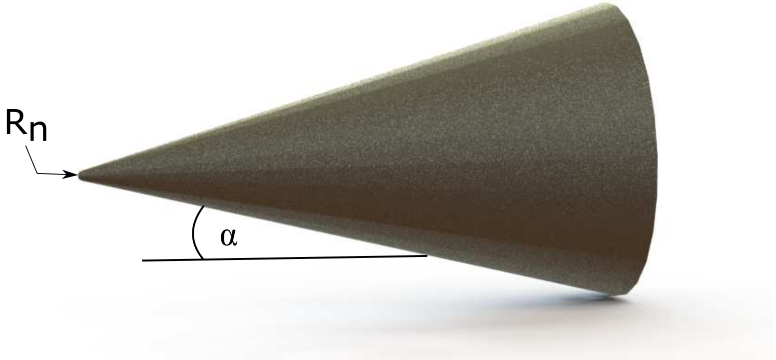

Figure 4.2: Axisymmetric conical representation of a generic hypersonic glide vehicle.

Therefore, the work presented in this chapter uses the generic glide vehicle shape of an axisymmetric blunted conical vehicle, shown in Figure 4.2. The body neglects any joints, control surfaces, TPS recessions, and stabilization appendages. While hypersonic glide vehicles are generally not circular in cross-section, they produce plasma flow fields similar to axisymmetric cones experiencing the same velocity and altitude conditions [75]. As such, the results of the generic conical vehicle produced hereafter are approximations that are nevertheless commensurate with the magnitude of the plasma environment [124] and heat loads [267] obtained by simulations of more detailed glide vehicle geometries.

A 9-dimensional parameter space for the conical glide vehicle shown in Figure 4.2 is generated by varying the cone half-angle ($\alpha = 6^\circ, 12^\circ, 18^\circ$) and leading nose radius ($\mathrm{R_n} =$ 2.0 cm, 4.0 cm, 8.0 cm)[1] . The simulated body is consistently 2.5 m long throughout, with the location of the antenna assumed to be at 2.0 m downstream of the stagnation point. These geometric features have been selected in accordance with dimensions of flown, speculated, or proposed hypersonic glide vehicles within the literature [25, 261, 262, 264, 268–270].

4.2 Glide Trajectory

The atmospheric flight of a gliding hypersonic vehicle over a spherical, non-rotating Earth is simulated in this study using the widely employed, 3 degree of freedom (DOF) particle mechanics model. The kinematic equations describing the radial distance of the vehicle from the center of the Earth ($\mathrm{r = R_E + h}$), the longitude (θ), and the latitude (ϕ), and thus the motion of the point body are [271]:

$$\frac{dr}{dt} = V\sin(\gamma) \tag{4.4}$$

$$\frac{d\theta}{dt} = \frac{V\cos(\gamma)\cos(\psi)}{r\cos(\phi)} \tag{4.5}$$

$$\frac{d\phi}{dt} = \frac{V\cos(\gamma)\sin(\psi)}{r} \tag{4.6}$$

---

[1] As a reminder to the reader, the RAM-C geometries studied in Chapters 3 and 5 have an approximately 15 cm radius nose and a cone half-angle of 9 degrees.

where V is the velocity of the hypersonic vehicle, γ is the flight path angle with respect to the local horizontal plane, and ψ is the azimuth angle. These variables are determined from the force equations that result from the application of Newton's Second Law of Motion to the point body, written as [271, 272]:

$$\frac{dV}{dt} = \frac{F_T}{m} - g\sin(\gamma) \tag{4.7}$$

$$V\frac{d\gamma}{dt} = \frac{F_N cos(\sigma)}{m} - g\cos(\gamma) + \frac{V^2}{r}\cos(\gamma) \tag{4.8}$$

$$V\frac{d\psi}{dt} = \frac{F_N\sin(\sigma)}{m\cos(\gamma)} - \frac{V^2}{r}\cos(\gamma)\cos(\psi)\tan(\phi) \tag{4.9}$$

where $\mathrm{F_T}$ and $\mathrm{F_N}$ are the tangential and normal components of the aerodynamic forces acting upon the glide vehicle, i.e., the lift and drag. Such forces are calculated with appropriate values for the glide vehicle that correspond well with those suggested within the literature [260–262, 268–270, 273]. Ergo, the vehicle in this study is assumed to have a mass, m, of 1000 kg, a ballistic coefficient of 13000 kg/m^2, and a lift-to-drag ratio, L/D, of 2.2. While it should be stated that the simulated axisymmetric vehicle used in the ensuing flow calculations does not generate lift, the presumed L/D used by the trajectory calculations does match well with that expected of conical bodies at small angles of attack [267]. The six ordinary differential equations that govern the flight path, Eqs. 4.4 to 4.9, are solved with the explicit adaptive fourth- and fifth-order accurate Runge-Kutta method proposed by Dormand and Prince [274, 275]. Further details of the numerical methodology employed by this analysis are included by Rataczak et al. in [276].

The equilibrium glide condition is used in this trajectory analysis, which assumes a nearly exact balancing between the weight of the vehicle and the sum of the lift force and apparent centrifugal force. This assumption solves the altitude for which Eq. 4.8 is zero, and therefore generally remains valid at small flight path angles [271]. It is believed that an equilibrium glide trajectory is best suited for reducing the maximum heating rate and mechanical stress on the vehicle fuselage [277]. The trajectory analysis in this work subsequently also neglects additional phases of a hypersonic glide vehicle flight path, e.g., the boost phase, ballistic phase, pull-up, and dive, as the majority of the time spent will be within the glide phase, and thus is a top priority for blackout considerations [260]. Figure 4.3 presents the calculated trajectories for a range of initial glide velocities, which depend on the aforementioned phases of flight prior to the equilibrium glide entry. It is apparent that as the hypersonic glider loses kinetic energy, and consequently velocity due to drag, the equilibrium flight altitude is decreased so that the denser air compensates for the lift lost.

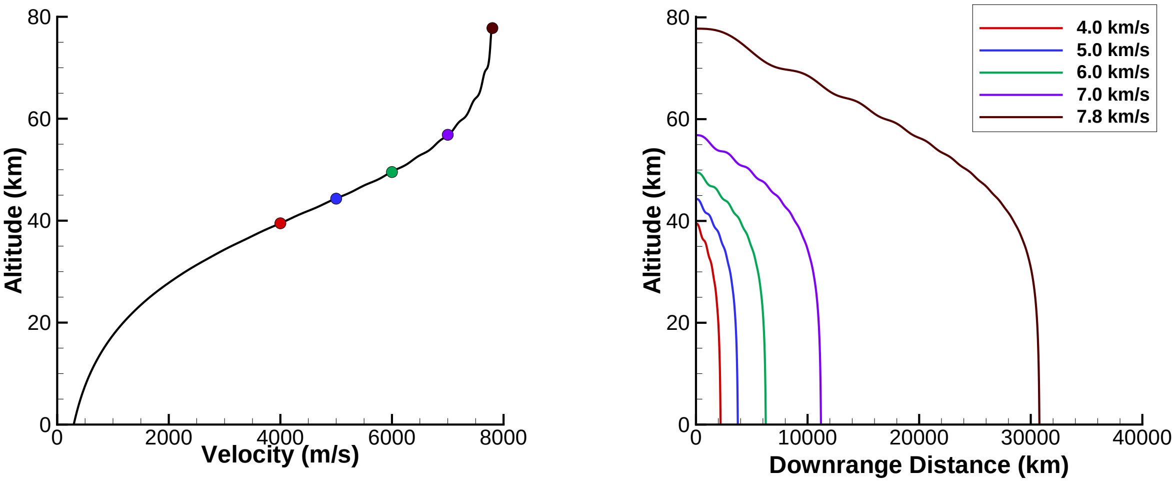

Figure 4.3: Hypersonic glide vehicle altitude as a function of velocity (left) and glide range for various initial velocities (right).

The relation between the downrange distance and initial velocity is a particularly important one. To emphasize this importance, Figure 4.4 displays the downrange distances shown in Figure 4.3 on an azimuthal equidistant projection of Earth. It should be noted that the downrange distance of the 7.8 km/s initial velocity trajectory is not shown as it encompasses the entire globe.

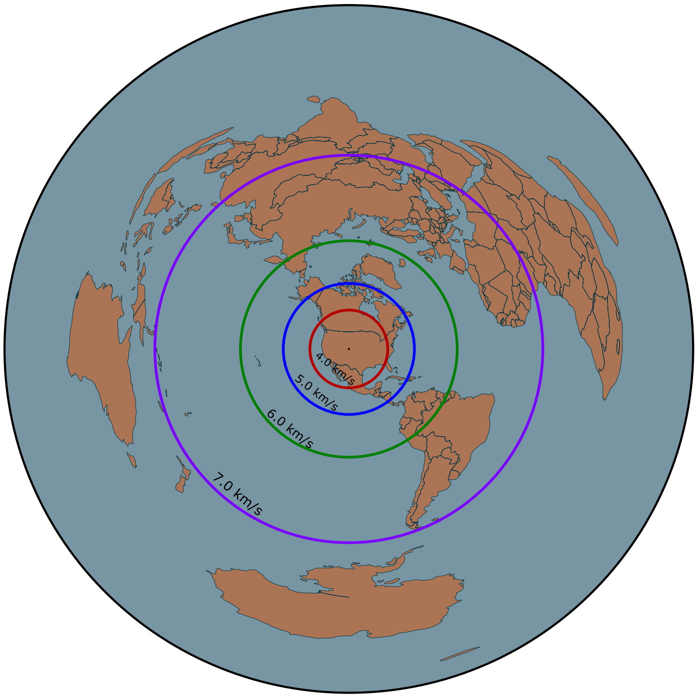

Figure 4.4: Downrange distance with relation to initial trajectory velocities displayed on an azimuthal equidistant projection of Earth centered about Boulder, Colorado.

4.3 Numerical Setup

As discussed, conical geometries with varying half-angles and leading-edge nose radii are assessed along an equilibrium glide flight path. Thus, generality is maintained in a way that still remains useful for the mission designers concerned about blackout. After weighing the probable cut-off frequencies against heat load considerations, a sensible geometry is selected that will be evaluated for possible mitigation strategies in later chapters.

From the assumptions used to numerically solve the Navier-Stokes equations, Eqs. 2.1-2.4, the flow field is modeled as a steady-state, laminar, quasi-neutral flow in continuum. Park's [182] 11-species chemistry set (1990) is used with the minimization of Gibbs free energy to account for chemical nonequilibrium [60, 227], while Gupta's mixing rule [68] is employed for transport properties. It should be reiterated that the simulation utilizes an axisymmetric assumption. Thus while an angle of attack that corresponded with a particular L/D was used to capture the body dynamics for the trajectory calculations, it is not imposed for modeling the flow field. The role of the axisymmetric assumption was examined in Section 3.4.1.1. At the wall, the no-slip condition is imposed for the flow velocity and the wall-catalycity promotes surface ion and electron recombination. The surface temperature is calculated at the wall assuming a radiative equilibrium condition, $q_{\text{rad}} = q_{\text{conv}}$, with an emissivity of 0.9.

The MSISE-00 atmospheric model [72] is once again utilized to obtain the freestream conditions of the five sampled trajectory points, as it is shown in Table 4.1. The nondimensional Mach number, Knudsen number (based on the smallest nose radius), and Reynolds number (based on the entire vehicle length) are also listed for each case. It should be noted that the previous assumptions of laminar flow in continuum start to break down at the extreme altitude ends. While continuum breakdown causes a likely error of around 3% in the heat flux [278] and turbulence has been known to significantly increase heat transfer at the wall of a hypersonic vehicle [279], these assumptions remain sufficient for the general trends and order-of-magnitudes presented in the ensuing sections.

Table 4.1: Freestream conditions of the five trajectory points investigated.

Velocity (km/s)	Altitude (km)	Density kg/m^3	Temperature (K)	Mach number	Knudsen number	Reynolds number
7.8	77.8	2.67×10^{-5}	201.4	27.4	7.41×10^{-2}	2.77×10^{4}
7.0	56.9	4.89×10^{-4}	248.0	22.2	3.97×10^{-3}	3.66×10^{5}
6.0	49.5	1.21×10^{-3}	261.3	18.5	1.41×10^{-3}	7.18×10^{5}
5.0	44.3	2.63×10^{-3}	262.5	15.4	6.80×10^{-4}	1.22×10^{6}
4.0	39.5	4.58×10^{-3}	253.5	12.3	3.47×10^{-4}	2.01×10^{6}

4.3.1 Grid Convergence

Given that nine different conical geometries across five vastly different flight conditions are simulated, each computational grid must be independently adapted to the shock structure and demonstrate grid size convergence. The size of the grids is categorized as either coarse, medium, or fine, with the corresponding number of cells along the body and wall-normal to the body shown in Table 4.2 for each vehicle geometry. Grids are constructed using the CFD mesh generation software Pointwise.

Table 4.2: Grid sizes used for each axisymmetric cone configuration.

		$\alpha = 6°$			$\alpha = 12°$			$\alpha = 18°$		
	R_n (cm) =	2	4	8	2	4	8	2	4	8
Cells along the body	coarse	180	190	200	250	275	300	300	325	350
	medium	200	250	300	320	340	360	350	375	400
	fine	330	340	350	365	375	390	420	430	440
Cells in wall-normal direction	coarse	160	160	160	190	190	190	220	220	220
	medium	200	200	200	240	240	240	280	280	280
	fine	260	260	260	280	280	280	340	340	340

The coarse-sized grid is the first to be adapted for each freestream condition by iteratively fitting the cells to achieve shock-normalcy while enforcing a global wall-normal spacing which yields a y^+ value that is less than 0.5 [241]. These adaptation considerations for the shock shape and wall shear are specifically important for the intended quantities of interest, the heat flux and electron number density [237, 280, 281]. The location of the shock is realized by scanning the flow field with wall normal search lines until the most distant point is obtained where the Mach number is 95% that of the freestream value [238]. A polynomial curve-fit is then performed on these points to define a continuous shock location.

The number of cells within each mesh are held constant along the simulated trajectory but are accordingly redistributed to ensure that the cells are normal to the shock and that the y^+ criterion is met. Consequently, approximately 5% to 20% of the total number of cells are located within the freestream. The medium and fine grids build upon the iterative process of the coarse grid by initializing with the coarse grid shock location. A fine-sized mesh that was iteratively adapted to the shock through this process is shown in Figure 4.5 with contours of the Mach number added for reference.

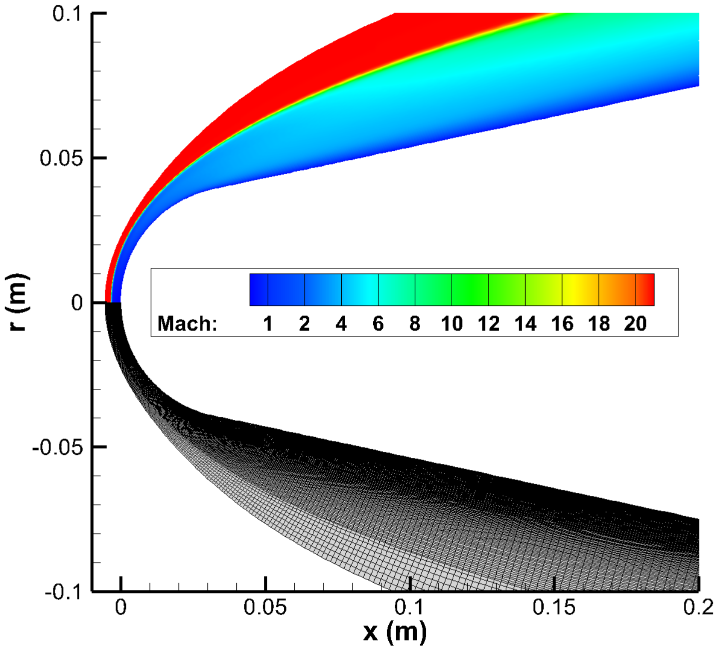

Figure 4.5: Mach number contours (top) and corresponding adapted mesh (bottom) for the 4 cm radius, 12-degree half-angle case at 7.0 km/s.

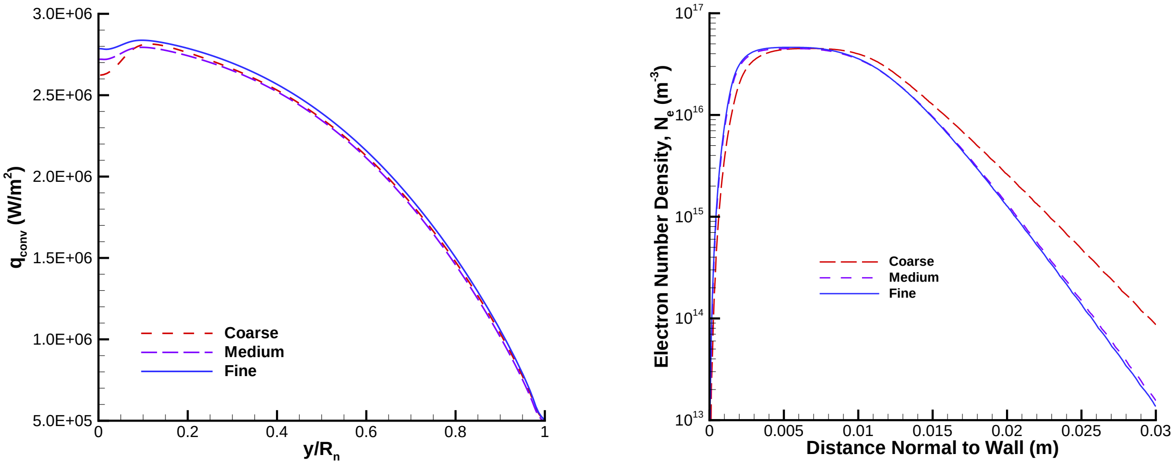

Figure 4.6: Grid convergence of the convective heat flux around the blunted portion of the 4 cm radius, 12-degree half-angle cone (left) and the electron number density at the antenna location (right).

Along with ensuring proper shock- and viscous layer adaptation for each particular flow field arrangement, each grid is also used for a cell-size independence study for the heat flux to the wall at the stagnation point and the maximum electron number density at both the stagnation point and location of the antenna. Grid size independence is demonstrated when a difference of 5% is indicated for both the maximum heat flux and electron densities. This process is depicted in Figure 4.6 for the 4 cm radius, 12-degree half-angle cone mesh at 7.0 km/s.

4.4 Results

Before the trajectories of the three blunted cone geometries are explored in terms of heat transfer and electron density, it is important to illuminate the distinct features of the similar flow fields for the varying geometries. To portray these flow field distinctions occurring between the geometries, the 2 cm nose radius cone with a half-angle of 6 degrees (Figure 4.7) is used for the following qualitative discussion. Flow fields of the other geometries are of course slightly different, but the following discussion remains valid for each.

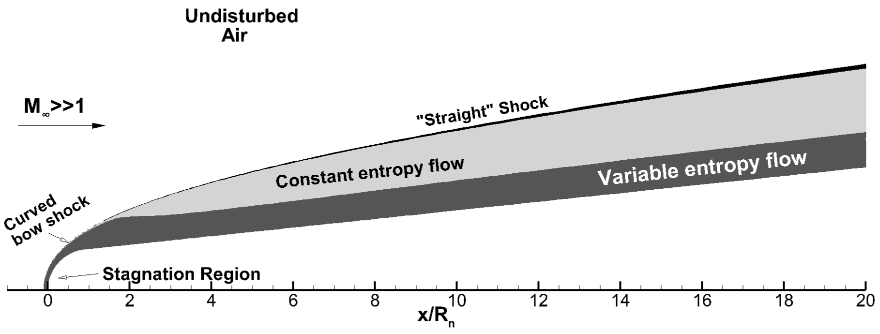

Figure 4.7: Qualitative flow pattern over the 2 cm radius, 6° half-angle blunted cone.

Flow around the slightly blunted cones can be segmented into four zones, which, with the exception of the shock wave, are not sharply bounded [263]. The first zone is the undisturbed air. Air from this zone that passes through the nearly normal section of the curved bow shock will experience the largest increases in temperature, pressure, density, and entropy. The flow within this region has been or almost has been stagnated. As was previously detailed in Chapter 3, this zone includes the largest generation of free electrons within the flow field.

As the flow from this region traverses downstream it is consumed by the viscous boundary layer where large gradients in the wall-normal direction occur for certain flow properties like the entropy, temperature, and electron number density. This consumption length can persist for a significant amount of time in some cases. Indeed, a correlation developed by Blottner and presented by Bertin in Ref. [266] demonstrates that this "swallowing distance" can take several hundreds of nose radius lengths. Further, while the correlated distance was shown to be independent of the Mach number, the cone half-angle had a considerable impact on its location. For instance, and of relevance to the current study, the swallowing distance in terms of nose radii, was shown to decrease by an order of magnitude between the 6° and 18° half-angle cones [266]. Recall that chemical equilibrium is predicated on reaching a maximum entropy state. Thus, a decrease in the swallowing distance due to a decrease in cone angle is also related to an upstream shift of the reaction zone [281].

At this point the flow field also starts to asymptotically approach that of a perfectly sharp cone. The shock wave at this point becomes a nearly straight[2] oblique shock where the shock angle relates to that of a perfectly sharp cone [266]. Air along a streamline that passed through the weak oblique shock and enters the inviscid region retains a constant entropy.

4.4.1 Trajectory Simulations

The effects of the varying flight conditions along the characteristic glide trajectory and the flow field differences brought on by modifying the blunted nose radius are examined by

---

[2] The shock is not perfectly straight, as weak waves crossing the shock layer produce second order perturbations [266].

keeping the cone half-angle constant, first at 6 degrees.

Figure 4.8 displays the maximum electron number densities normal to the wall for the three geometries along the flight path at the previously suggested location of the antenna, or 2.0 m downstream of the stagnation point. It is immediately evident from Figure 4.8 that the flight conditions, listed in Table 4.1, have a considerable impact on the generation of plasma. While the 78 km trajectory point involves the highest velocity of 7.8 km/s, it also includes by far the least dense freestream. Indeed, the freestream air at 57 km is 18 times denser than that at 78 km. Conversely, the second largest density difference is between the freestreams of 50 km and 57 km, where only a 2.5 times increase is observed. This large density change between the highest altitude trajectory points directly corresponds with the largest variations of electron densities, with an almost five orders-of-magnitude difference resulting from the 2 cm nose radius case.

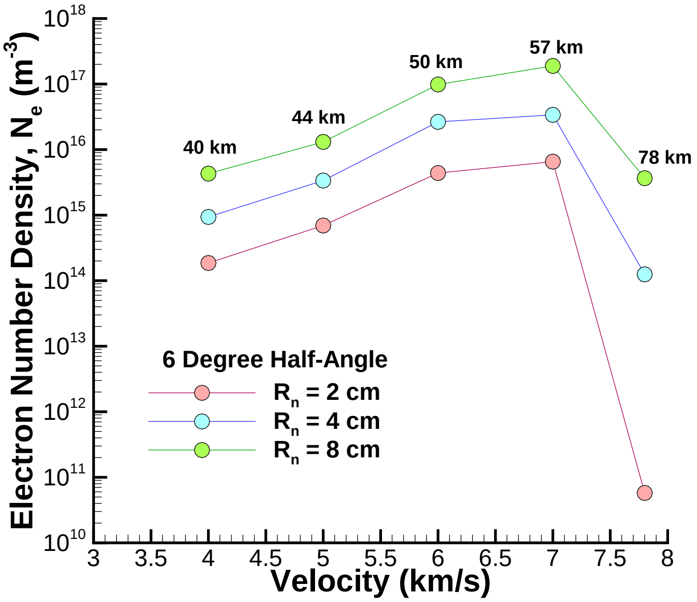

Figure 4.8: The maximum electron number densities at x = 2.0 m for the three 6° half-angle, blunted radii configurations along the representative flight path.

For the lower four trajectory points the differences in density are less significant and therefore changes in the electron density at the antenna location are more influenced by the differences in velocities. Thus, the electron densities peak at the 57 km point where the freestream velocity is 7.0 km/s. Also, while the 7.8 km/s initial velocity trajectory has the least plasma formed during the trajectory entry, it will eventually have blackout occurring at the same or higher frequency band as that of the 7.0 km/s initial velocity trajectory. This trend has a significant impact from a mission design perspective. As Figures 4.3, 4.4, and 4.8 imply, a larger glide distance, which requires a higher initial velocity, results in a higher frequency band cut-off. This marks a trade-off between achievable glide distances and the corresponding plasma properties of the flow surrounding an antenna. In other words, if a vehicle is solely designed for a larger glide distance it will have inferior communication characteristics.

Figure 4.8 also demonstrates the major impact of increasing the nose radius of the blunted cone. A larger nose radius gives rise to a stronger bow shock, which in turn results in elevated temperatures within the shock layer and higher levels of ionization [282]. At the 78 km trajectory point the bow shock is already very diffuse for the relatively strong shocks created by the 8 cm radius cone. When the radius is decreased to 2 cm, the bow shock becomes weaker and even more diffuse. In turn there is a large difference of free electrons generated after the nearly normal portions of the bow shock waves, which, as Figure 4.8 shows, results in a five orders-of-magnitude difference between the electron density at the antenna location for the 2 cm and 8 cm radius geometries. Such a large range of electron densities at high altitudes, particularly at 85 km, was also noted by Savino et al. for geometries with nose radii between 1 cm and 10 cm [264]. For the lower four trajectory points where the flow is more ionized, the differences of electron densities between the three geometries have less variance. Between the 2 cm and 4 cm radius geometries at altitudes between 57 km and 40 km, the percent differences between the electron densities at the antenna location range between 75% and 84%. A similar observation is made among the 4 cm and 8 cm radius geometries, where the electron densities have percent differences between 115% and 128%. These trends resemble those suggested by Steiger et al., expressed by Eq. 4.1. However, for the lower four trajectory points a value between 2.25 and 2.75 for the "p" exponential term fits the present data set better, as opposed to the value of 3 suggested [254].

Thus, to minimize the plasma surrounding the vehicle, and in particular around the antenna, it is optimal to have a decreased nose radius. At the 57 km trajectory point for instance, the 2 cm radius geometry has a cut-off frequency of 0.73 GHz, while the 8 cm radius geometry has a cut-off frequency of 3.9 GHz. This has a substantial impact on the available frequency bands that could be utilized, as Figure 1.8 exhibits.

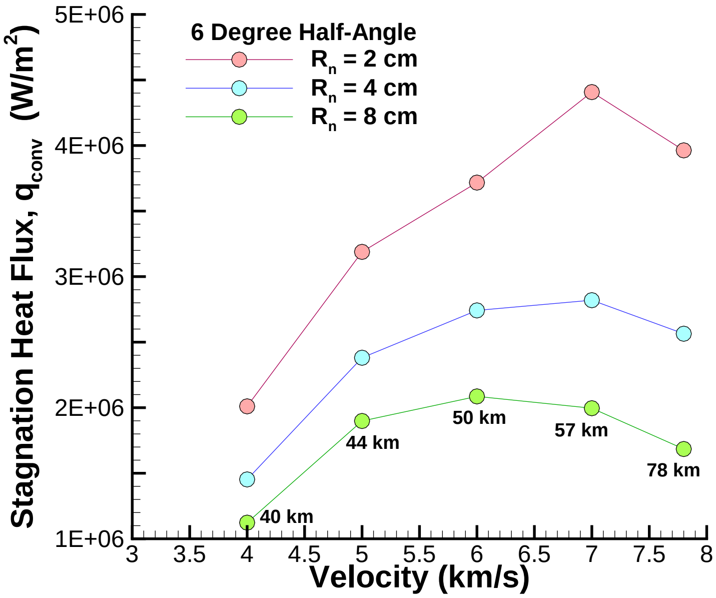

Figure 4.9: The convective heat fluxes at the stagnation point for the three 6° half-angle, blunted radii configurations along the representative flight path.

However, as Figure 4.9 shows, improved communication characteristics in turn come at the cost of an undesirable increase in the heat flux to the vehicle. A body with a smaller nose radius has a reduced inclination of the adjacent bow shock wave relative to the freestream flow. In turn the velocity of the incoming air particles does not change as drastically across the shock and thus, when deceleration does indeed occur near the vehicle surface due to viscosity, the energy is converted into heat and high temperatures in the boundary layer [266]. The high temperature gradients normal to the surface, and in turn the high convective heat transfer rates, are difficult yet crucial to protect against to avoid any catastrophic failures.

Indeed, as Figure 4.9 shows, an increase in nose radius from 2 cm to 4 cm instigates a percent decrease for the convective heat flux at the stagnation point of about 34% for 78 km, 35% for 57 km, 26% for 50 km, 26% for 44 km, and 28% for 40 km. Similarly, an increase in nose radius from 4 cm to 8 cm results in a decrease of the stagnation point heat flux of about 34% for 78 km, 30% for 57 km, 24% for 50 km, 22% for 44 km, and 24% for 40 km. Of note, Fay and Riddell's relation in Eq. 4.2 predicts a roughly 30% increase when the leading-edge radius is doubled.

The influence of the freestream conditions provided by the flight trajectory, specifically the velocity and density of the freestream, are also demonstrated in Figure 4.9. Mirroring the trends shown by the maximum electron density in Figure 4.8, the stagnation point heating increases going from the 78 km to the 57 km point by about 11% for the 2 cm radius body, 10% for the 4 cm radius body, and 18 % for the 8 cm radius body. For the two slender geometries the maximum heat flux occurs at around the 57 km point, while the maximum heat flux occurs at around 50 km for the 8 cm nose radius cone geometry. On average across the three geometries, there is a 0.95 reduction in maximum heat flux from 57 km to 50 km, a 0.88 reduction from 50 km to 44 km, and a 0.61 reduction from 44 km to 40 km. This trend is in good agreement with the empirical correlation of Fay and Riddell, where the respective reductions predicted by Eq. 4.2 are 0.99, 0.81, and 0.71. Hypersonic flows in nonequilibrium are not particularly captured well by the Fay and Riddell formula, which in a recent study by Lee et al. has been found to result in up to a 50% error for fully catalytic surfaces and up to a 70% error for noncatalytic surfaces [283].

The effects of increasing the cone half-angle are comparatively minimal, as Figures 4.10

and 4.11 show. Since the nose radii stay the same for the varying half-angles, the maximum heat flux, which is located at the stagnation point, remains approximately the same for each geometry along the trajectory points investigated. While the maximum electron densities generated within the stagnation region also remain the same, an increase in cone half-angle shifts the swallowing distance, and consequently the regions of chemical nonequilibrium, further upstream [266, 281]. Averaging across the three geometries and across all the trajectory points, it is observed that the plasma frequency increases by 28% with a standard deviation of 11% when the cone half-angle is increased from 6° to 12°, and the plasma frequency increases by 31% with a standard deviation of 19% when the half-angle is increased from 12° to 18°. This bodes well with the general rule of thumb suggested by Dix et al. That is, for every degree of increase in half-angle, the plasma frequency increases by approximately 5% to 10% [263]. The changes in maximum electron density at the antenna location brought on by increasing the half-angle also correspond well with analogous trends observed by Ouyang et al. and Ramjatan et al. for similar geometric configurations [246, 284].

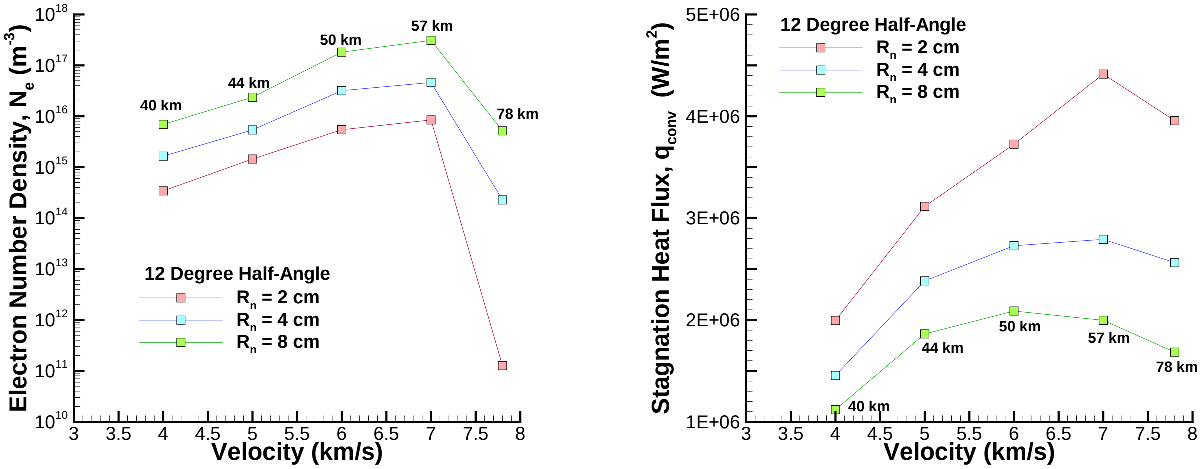

Figure 4.10: The maximum electron number densities at x = 2.0 m (left) and convective heat fluxes at the stagnation point (right) for the three 12° half-angle, blunted radii configurations along the representative trajectory.

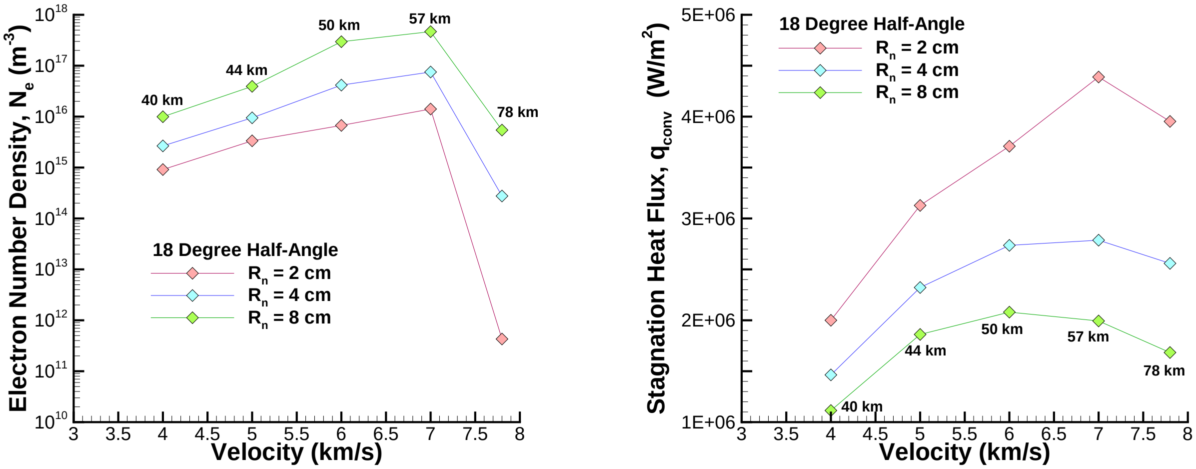

Figure 4.11: The maximum electron number densities at x = 2.0 m (left) and convective heat fluxes at the stagnation point (right) for the three 18° half-angle, blunted radii configurations along the representative trajectory.

4.4.2 Selected Geometry

On account of its middling characteristics in terms of both stagnation heat flux and electron density at the antenna location, the 4 cm nose radius, 12° half-angle blunted cone body is selected for use as a platform in scrutinizing possible blackout amelioration approaches. Specifically, the 7.0 km/s trajectory point is set as the flight condition in these studies, as it corresponds with the highest electron densities and heat fluxes. Figures 4.12 and 4.13 provide an overview of the flow field properties for this test case.

As it is indicated in Figure 4.12, the translational-rotational temperature decays significantly along the body. At the stagnation point the highest temperatures occur, of around 20,000 K, and drop to around 5,000 K at the location of the antenna, 2 meters downstream. Similarly, the electron number densities reach a maximum of approximately 2×10^{20} m^{-3}, only to decrease to 4.5×10^{16} m^{-3} at the antenna location.

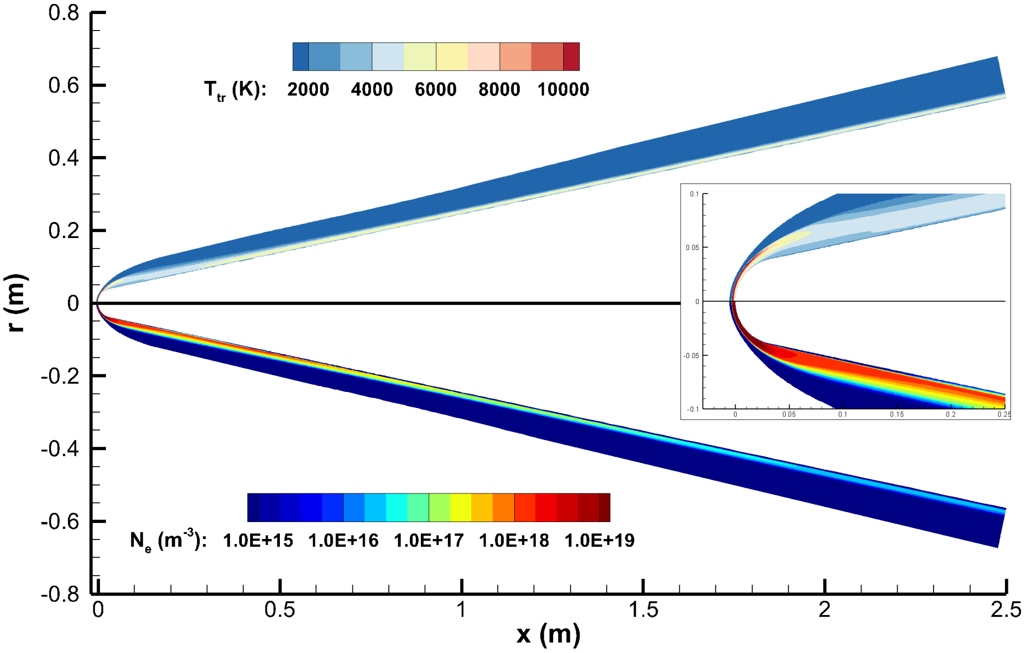

Figure 4.12: Translational-rotational temperature (top) and electron number density (bottom) contours of the 4 cm radius, 12° half-angle blunted cone body at the 57 km, 7.0 km/s trajectory point.

The maximum electron number density by the antenna corresponds to a plasma frequency of 1.93 GHz, as Figure 4.13 shows. This is significant as it surpasses the L-band, and in particular, the GPS frequency bands. Also, surrounding the antenna, within the plasma layer, the ratio of $\nu_{\mathrm{en}}/\omega_{\mathrm{p}}$ is at most 0.18, which is not surprising at a 57 km altitude. Thus, while the collision frequency undeniably has a role in the attenuation and blackout of radio wave transmission (e.g., Eq. 1.24), it can be sensibly assumed for the investigations hereafter that blackout is driven by the plasma frequency and in turn the number density of electrons.

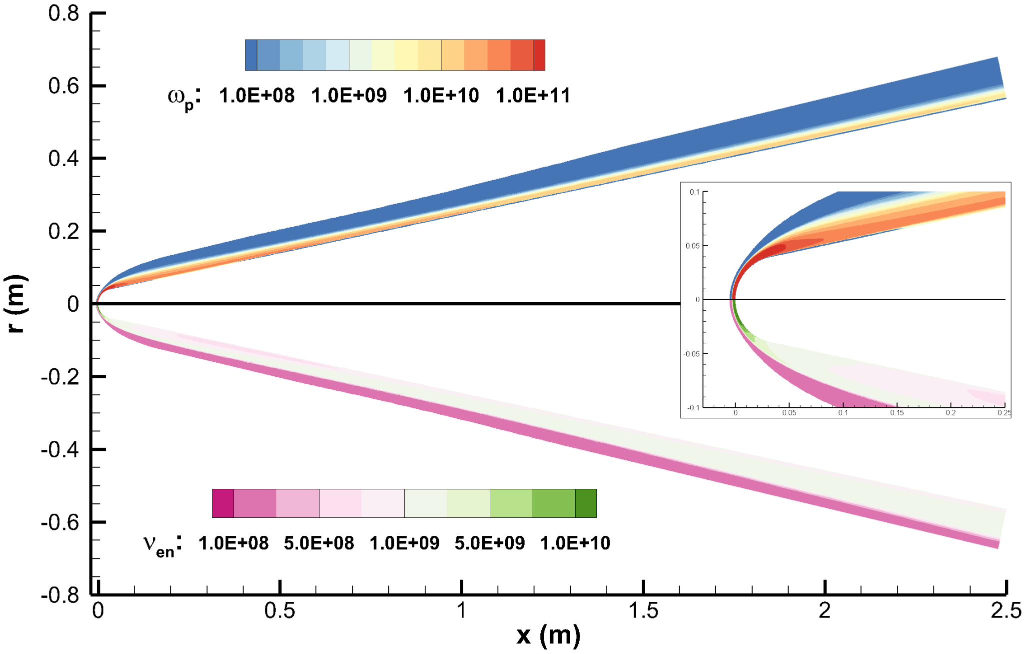

Figure 4.13: Angular plasma frequency (top) and electron-neutral collision frequency (bottom) contours of the 4 cm radius, 12° half-angle blunted cone body at the 57 km, 7.0 km/s trajectory point.

4.5 Chapter Conclusions

The current chapter detailed a major trade-off involved within hypersonic glide vehicle design, namely heat flux at the stagnation point vs. ionization levels surrounding an antenna. The study assessed these quantities of interest for different nose radii and half-angles of a generic glide body approximating more complex geometric designs. The flow conditions that dictated the freestream properties were chosen from an archetypal equilibrium glide flight path. Both the geometric and trajectory trade spaces were in agreement with values described in the literature and thus resemble realistic mission profiles. Thus, the conclusions acquired by this analysis are applicable in a broad sense to potential hypersonic glide designs.

The chapter examined the make up of the distinct flow field features associated with slightly blunted cones. The physical interplay between the high-entropy laden stagnation region after the nearly normal bow shock and the key swallowing effect by the boundary layer of this flow was discussed. From the physical description and the numerical simulations, it is seen that larger cone half-angles generally result in a 5% increase in plasma frequency for each half-angle degree increased. An increased nose radius leads to more ionization throughout the flow and poorer communication characteristics. However, the increased nose radius has a benefit of reducing heat flux, at approximately a 30% increase when the nose radius is doubled, in agreement with Fay and Riddell's empirical correlation. The flight conditions are also found to have a considerable effect on the both the maximum heat flux and electron densities. This results in a further trade-off that was discussed, particularly the downrange distance of the glide vehicle versus the ionization levels surrounding an antenna.

After weighing the probable cut-off frequencies against the nose heating, a geometry was selected that will be used as a platform for evaluating possible mitigation strategies in the forthcoming two chapters. The selected geometry is particularly interesting because it has a plasma frequency at the selected antenna location that just surpasses the associated GPS frequencies. Thus, while a hypersonic glide vehicle is associated with more rigorous mitigation strategy limitations, such as tighter constraints on mass and volume, the mitigation strategy does not need to be as effective at reducing the ionization levels when compared to the requirements of blunt capsules.

CHAPTER 5

EFFICACY OF WATER VAPOR INJECTION ON PLASMA REDUCTION

A reliable means of combating radio wave blackout is to lower the electron density. One of the most studied methods of achieving this goal is to add material into the flow that introduces a pathway with which free electrons are directly depleted, promotes faster rates of recombination, or prevents plasma from being generated at a high rate in the first place. Proposed material additives have been suggested in three phases of matter: solid particles (e.g., tungsten-oxide [129, 285], alumina [73, 128], and kaolin [286]), liquids (e.g., hydrogen peroxide [287], nitrogen [288], and propane [123, 124]), and gases (e.g., fluoride compounds, such as sulfur hexafluoride [75, 124–126, 289, 290] and rhenium hexafluoride [75], and carbon tetrachloride [291]), and have been designed to be added into the hypersonic flow either through injection systems involving nozzles or through impregnated ablative surfaces.

Each proposed material additive involves a tailored procedure from which the ultimate goal of electron reduction is achieved (refer to discussion in Section 1.2), and a sizable portion of these materials have shown excellent potential for use within either analytical or ground test settings. However, it is to the best of the author's knowledge, that of these many studied materials, only two groups of chemical compounds have been tested in flight thus far: i) water, in the flights of Project RAM [57, 292, 293] and Gemini [54, 294], and ii) fluorocarbons, in the flights of Project RAM (Freon E-3 [$F(C_3F_6O)_3CHFCF_3$]) [57] and Trailblazer (Freon 114B2 [$C_2Br_2F_4$]) [56, 218, 295].

While electrophilic chemicals have been shown to be more effective than water at reducing the electron density, water has shown favorable results in reducing thermal loads when compared to electrophilics [54, 295, 296]. As discussed, minimizing thermal loads is usually seen as a primary design driver for hypersonic vehicles, making this chemical additive a more attractive option for the slender glide vehicles. Further, electrophilic chemicals tend to also be very toxic, some even being banned globally due to environmental safety concerns [128]. Subsequently, water injection has considerable potential for use in hypersonic glide vehicles and is the focus of this study.

5.1 Modus Operandi of Electron Reduction via Water Additives

The driving mechanisms for electron reduction due to water addition will vary considerably based on the phase of the water. For the flight test examples previously discussed, injecting water in the liquid phase was a congruent decision. When the water is injected as a liquid, the ensuing jet rapidly atomizes by either vapor pressure breakup or aerodynamic breakup into a spray of fine droplets which are roughly uniformly distributed [288, 297]. During high altitudes and at high velocities, the local ambient pressure of the flowfield is less than the vapor pressure of the liquid water and consequently there is “flashing” vapor atomization. Conversely, at lower altitudes the dynamic pressure of the flow field is large enough where aerodynamic breakup dominates. For instance, it was found with good reason from extensive ground testing that the altitude with which the breakup process changed to aerodynamic breakup occurred at around 75 km for the RAM-C I flight [298]. For altitudes below this point the volume-mean drop diameter (D_{30}) could be found through a modified Volynskiy empirical correlation of the form:

$$\frac{D_{30}}{d_0} = \frac{48}{\left[\mathrm{W_L}^{3/8}\left(\frac{\mathrm{Re}}{\mathrm{M}}\right)^{1/4}\right]} \tag{5.1}$$

where d_0 is the hydraulic diameter of the injection nozzle, Re is the Reynolds number, M is the Mach number, and $\mathrm{W_L}$ is the Weber number of the injected fluid, a measure of the relative influence of inertial forces to surface tension [298]. Thus, using the RAM-C I flight as an example, the mean droplet diameter is calculated to be on the order of 1 micron along the flight path.

Regardless of the mechanism of atomization, the finite rate of heat transfer to the resulting droplets ensures a long enough lifetime where their presence is non-negligible. The water droplets remove electrons from the ionized flowfield through accretion [299]. From a higher frequency of collisions with the faster electrons, the water droplets collect a negative charge. At some point the negatively charged droplets start to repel additional electrons and attract ions, as a steady-state condition can be obtained through subsequent ion collisions where the net current returns back to zero [127]. In other words, the droplets act as spherical Langmuir probes at floating potential, where the rate of ion collisions matches the rate of electron removal. If, however, the flow conditions are particularly volatile for the water droplet, it is possible that rapidly evaporating droplets quickly acquire a collection of electrons and then vaporize as negatively charged molecules. Indeed, it is more probable for a negatively charged molecule to evaporate since the system terminates in a lower energy state [300].

The effectiveness of electron reduction due to water droplets has been extensively studied through direct numerical analyses [127,299,301,302]. One kinetics-based study in particular, carried out by Sodha and Evans [303], investigated the aforementioned relevant physics pertaining to the reduction of free electrons by the addition of water droplets. While this study neglected the ionization and recombination of the plasma, assumed uniform droplet size, and ignored droplet size variation due to evaporation, the results do provide insight into the role of water droplets at varying conditions. Figure 5.1 shows a replication of this work for an initial electron density of 10^{18} m^{-3} at 5000 K, where $\mathrm{N}_{\mathrm{d,H2O}}$ is the number density of water droplets, r is the radius of the droplets, T is the water injection temperature, and α_{ae} is the accommodation coefficient, which for water droplets is about 0.04 at room temperature and 0.8 within high temperature gases. It is immediately evident from Figure 5.1 that a higher number density of water droplets and higher water injection temperatures give rise to a faster decay of free electrons in the plasma, indicative of the two mechanisms discussed prior. Further, from Figure 5.1 it is also apparent that the lifetime of a group of droplets has a tremendous role in plasma reduction.

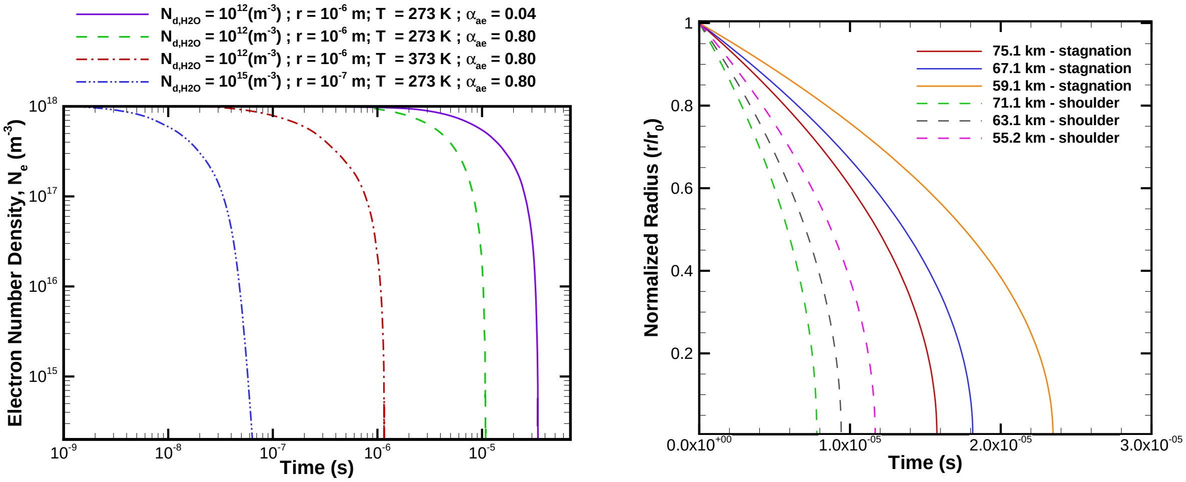

Figure 5.1: Electron decay of plasma by the addition of water droplets predicted by a kinetics model (left) and evaporation times of a single droplet within conditions of the RAM-C I flight (right). Plot on the left is reproduced from work of Sodha and Evans [303].

The lifetime of a droplet is primarily predicated on the heat transfer induced by the surrounding high temperature gases [304]. The change of the particle radius with respect to time can be expressed within a Lagrangian dispersed phase formulation by assuming a continuum with a constant parcel size as:

$$\frac{dr_d}{d_t} = -\frac{\rho_g D_s \mathrm{B_p Sh}}{2\rho_d r_d} \tag{5.2}$$

where ρ_g is the density of the surrounding air, $\mathrm{D_s}$ is the diffusion coefficient, $\mathrm{B_p}$ is the Spalding transfer number, and Sh is the Sherwood number [305]. Equation 5.2 can be further simplified by assuming an isolated droplet in a quasi-steady state, constant particle velocity flow, yielding

$$r_d^2(t) = r_{d,0}^2 - \xi t \tag{5.3}$$

where ξ is the evaporation coefficient [306, 307]. Eq. 5.3 is known as the d-squared law, originally observed by Langmuir in Ref. [308]. Although simple in nature, Eq. 5.3 has shown good agreement with experimental data and higher-fidelity simulations for a variety of different particle and gas compositions at different conditions [305,307,309,310]. The evaporation coefficient is independent of the evaporating particle size and is instead dependent on the involved temperature gradients and species. Using Eq. 5.1 and Eq. 5.3 with conditions obtained from the RAM-C I simulations in this study, along with evaporation coefficients taken from that of Ref. [311], an approximate estimate of the evaporation times are calculated and shown in Figure 5.1. It should be noted that there are certainly limitations to the use of the d-squared law in this analysis, such as the important omission of free molecular flow effects as the particle shrinks [124, 310, 312], and there are certainly higher-fidelity models available to ascertain the evaporation times for more accurate numbers [304,313–315]. Still, the trends present can be justifiably inferred from both plots in Figure 5.1, namely that depending on the specific flowfield and injected liquid water conditions, the role of the droplet on electron reduction can change substantially over a particular flight path. Specifically for the RAM-C I flight, the shoulder injection site produces smaller initial droplets, owing to the associated higher Weber numbers, which in turn results in faster evaporation rates. Similarly, the higher temperatures associated with higher altitudes result in larger evaporation coefficients. Thus, the role of water in droplet form should generally diminish at the shoulder location and at higher altitudes.

During vaporization of the water droplet, which is an endothermic process, the droplet acts as a thermal quenchant and takes energy away from the plasma. As a gas, the water vapor will readily start to dissociate and further cool the surrounding plasma. The released hydrogen and hydroxyl molecules will then react with the constituents of the post-shock air, which in turn will supplant and suppress the amount of associative ionization reactions that can occur by competing with the dominant nitric oxide associative ionization reaction. Additionally, a key difference between direct liquid jet and vapor injection is the larger initial disturbance brought on by the gas injection which can either contribute to reducing plasma as a gas-spike or thin film layer [316, 317], or be detrimental by causing secondary shock waves that induce additional ionization [288].

Due to the aforementioned supplemental electron reduction pathways associated with water droplets, among other key advantages over a purely vapor system such as its storage and ease of use in handling, blackout mitigation studies involving water have overwhelmingly been concerned with the injection of water in the liquid phase. Thus, the sole role of water vapor on a weakly ionized flowfield is not entirely understood. Indeed, water vapor has been postulated by previous works to be between negligible [127, 300] to considerable [124, 318] for its effect on electron reduction. Nevertheless, it has been known for quite some time that water vapor has a non-negligible influence on the plasma properties, as its unknown presence in early electron-ion recombination rate studies for an originally assumed pure gas resulted in unexpectedly increased rates [124, 318]. Using plasmas generated through pulsed microwave discharges, Kuhns and Cooper observed that as little as 3% water vapor of an ionized air mixture materially improved transmission performance [318].

Perhaps the most extensive numerical analysis on the topic of plasma reduction induced by water vapor was performed by Good and Rossi [126]. Through the use of a two stream-tube framework, they conjectured that although the plasma temperature could be reduced by the injection of a coolant gas, the plasma electron density would experience minimal change due to a slow electron-ion recombination rate. Yet, the cooling of the chemically nonequilibrium air flow was entirely modeled through a psuedo-reaction describing the interchange of energy and momentum between the two stream-tubes. The coolant itself was merely assumed to be a high-heat capacity non-reacting gas. Further, the temperature decay along the stream-tubes was based more so on yielding the simplest closed form solution than on pure physical reasoning. These major assumptions, along with the outdated reaction rates used, necessitate further scrutinization of the conclusions made in Ref. [126].

Thus, the work in this chapter investigates the influence of water vapor on weakly ionized hypersonic flows. The sole use of water vapor injection is investigated as a possible blackout mitigation solution. The current work also impacts any liquid water injection system, as the role of water after evaporation will provide needed insight when evaluating the efficacy of any water injection technique.

5.1.1 Modeling Water Vapor Injection

To numerically solve the Navier-Stokes equations, Eqs. 2.1- 2.4, that govern both the hypersonic air flow and the water vapor injection, the flow field is modeled as a steady-state, laminar, quasi-neutral flow in continuum. More specifically, the injection of water vapor is modeled in this work as a modification to the surface boundary condition in LeMANS (refer to Section 2.2 for more details).

In addition to the 11-species air chemistry set of Park [182], nine species are added that enable an adequate modeling of distilled water vapor injection: H, H_2, H_2O, OH, NH, HNO, H_2O_2, HO_2, and H^+. The kinetic rates of the resulting 41 additional chemical reactions involving these species are drawn from those collected by Martin et al. in Ref. [191].

While it has been previously discussed that Gupta's mixing rule should be utilized when appropriate, the complex collision pairs brought on by the inclusion of water and its by-products with air reduce the reliability of the collision cross section data. Furthermore, the appropriateness of a constant Lewis number for this 20-specie mixture is likely untenable. As such, the current work employs the bifurcation model offered by Bartlett et al. [173] and expressed in Eq. 2.22, which assumes unequal diffusion coefficients based on molecular weight. The mixture transport quantities (species diffusion, viscosity, thermal conductivity) of the flow field are further calculated using Wilke's semi-empirical mixing rule, with species thermal conductivities and viscosities determined using Eucken's relation and Blottner's curve fits, respectively.

5.2 Comparisons with the RAM-C I Flight Test

As it was alluded to earlier, liquid water injection has been applied successfully in previous flights for reducing the levels of ionization. Therefore, it is beneficial to compare the effectiveness of a water vapor injection system with that of a liquid injection system through data compiled during one such carefully chosen flight test.

These tests were primarily flown in accordance with two particular flight programs. The Gemini III manned-spacecraft, which flew at 7.3 km/s, utilized liquid water injection to successfully overcome UHF blackout within the wake, while C-band signal reception in the forebody was enhanced [54, 294]. However, due to its large geometry, the Gemini capsule does not segue well into investigations pertaining to the hypersonic glide bodies of interest.

Throughout the 1960s, seven successful flight experiments were conducted through Program RAM (Radio Attenuation Measurements) to study the degradation effects of the hypersonic plasma layer on space vehicle communications and test several amelioration approaches for blackout [27, 55]. Three of these flight tests, RAM-B 2, RAM-C I, and RAM-C III, evaluated the injection of liquid water and Freon E-3. While the RAM-B 2 test had an attractive slender shape with a 10 cm radius nose and flew at 5.5 m/s, the test flight unfortunately did not employ any direct diagnostic instrumentation to quantify the plasma flowfield, although it was shown that water addition was an effective means of overcoming communications blackout [293]. Further, the RAM-C I injection nozzles were injected perpendicular to the flow, unlike the RAM-C III nozzles which were at a 51-degree angle from the surface [296, 298]. As modeling a wall-normal injection significantly simplifies the numerical approach, the RAM-C I experiment is chosen for comparison.

5.2.1 RAM-C I Flight Test

The primary objective of the first RAM-C flight was to test the effectiveness of liquid water injection as a communications blackout suppressant by relating the mass flow rate, orifice size and shape, and location of injection to the consequential signal attenuation and electron density of the flow field [27]. The RAM-C vehicle geometry, shown in Figure 5.2, was a 9-degree hemispherical cone with a nose radius of 15.95 cm and a length of 1.3 m [292]. The hemisphere was protected by a 2.95 cm thick NARMCO 4028 phenolic-graphite charring ablator, while the afterbody was covered with teflon [319].

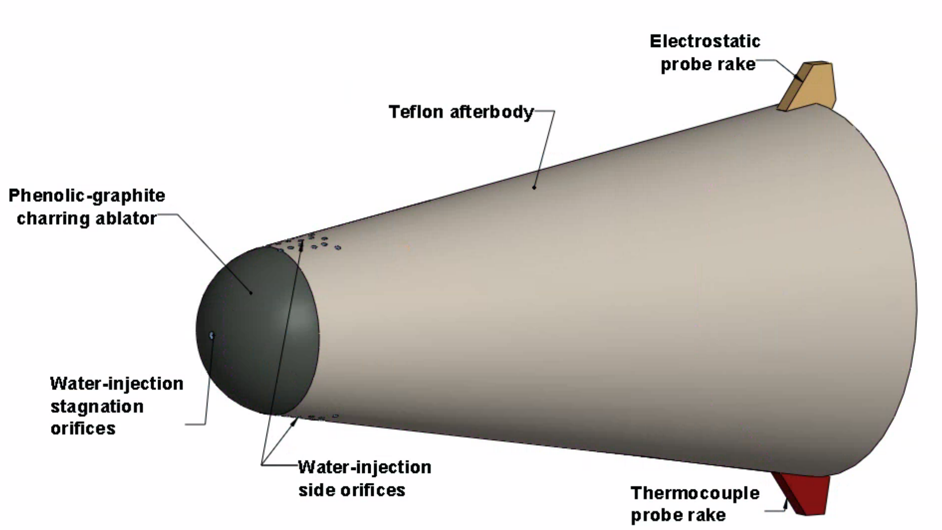

Figure 5.2: RAM-C I payload configuration showing locations of injection orifices and electrostatic probe rake.

As Chapter 3 highlighted, the RAM-C geometry, within the context of the RAM-C II flight, has been commonly modeled with acceptable levels of agreement. While the RAM-C I and RAM-C II payloads were configured similarly and had nearly identical trajectories, the heat shield of the former contaminated the flow field with ablation by-products. Specifically, the NARMCO 4028 ablator likely contained up to 4700 μg/g of alkali (1100 μg/g sodium and 3600 μg/g potassium). Thus the charring ablator fed these easily ionizable alkali metals into the surrounding air, and in the process, increased the electron density. Indeed, when compared to the RAM-C II flight where a beryllium nosecap was employed, the RAM-C I electrostatic probe measured up to a factor of 2 increase in electrons between 85.3 km and 73.2 km [220]. It should be also restated that while teflon ablation has been shown to decrease electrons by up to two orders of magnitude [218], the effects of the ablating afterbody are believed to be negligible above 56.4 km and therefore do not adversely affect the majority of the electrostatic probe data [92, 219].

The primary diagnostic aboard the 121.8 kg payload for quantifying the plasma was the electrostatic probe rake located 1.234 m downstream of the stagnation point, as depicted in Figure 5.2. Indirect inferences of the electron density could also be made using the VHF slot (259.7 MHz) and X-band horn (9.21 GHz) antennas on the vehicle through the use of Eq. 1.10. The rake utilized eight iridium ion collectors stationed incrementally at 1 to 7 cm radially from the body. Each data measurement required about 26.4 msec, or about 8% of a total revolution of the payload. The electrostatic probe collected data from 85.3 km to 53.3 km, as indicated from Figure 5.3, and had a measuring range of around 10^{14} to 10^{18} electrons/m^3. The resulting electron number densities of the innermost probes, Probes 3 to 6 have been re-transcribed and tabulated from Ref. [220] and are included in Appendix A.

While the limitations of making comparisons between the electrostatic probe with models are discussed in more in detail in Section 3.1 and in Ref. [252] for the RAM-C II flight, there are some additional caveats to its use with RAM-C I. As previously discussed, arguably the largest uncertainty associated with the data comes from the 3 revolutions per second coning motion of the vehicle and the resulting oscillatory nature of the angle of attack. As the RAM-C I flight reached a larger maximum wind angle of 5 degrees, the resulting peak-to-peak fluctuations were also larger in the recorded electron number densities. The effect of these vehicle motions slightly muddles the effect of water injection when interpreting measurements. Further, from altitudes of 67.0 km to 61.0 km, there was an anomaly with the subcarrier oscillator connected to the logarithmic amplifier of the electrostatic probe where calibration levels unexpectedly went to zero[1] [220]. The amplifier is said to have returned back to normal whilst water injection cycles were occurring. Thus, the clean air measurements made during this time-frame are unreliable and cannot be used for modeling comparisons. It should also be restated that the beryllium oxide leading-edge of the electrostatic probe which insulated the ion and electron collectors was susceptible to leakage currents from thermal degradation at temperatures above 1366 K, making measurements in this range questionable for use. Fortunately, the cooling effects of the water injection limited the thermal degradation, and the saturation currents were likely reached before it became an issue [220].

Water injection during the flight of RAM-C I emerged from orifices located at either the stagnation region or at two diametrically opposed locations near the shoulder of the vehicle, as depicted in Figure 5.2. The water injection system consisted of a pressurized reservoir containing 1.9 kg of water, eleven solenoid valves, an electronic controller, and a pressurized nitrogen supply bottle. The nitrogen gas, which provided the head pressure for the injection system, was separated from the water reservoir with a neoprene bladder. The gas was continuously fed at a constant rate to ensure increasing flow rates as the vehicle descended the atmosphere, illustrated in Figure 5.3. Of the eleven solenoid valves, seven valves were directly connected to nozzles containing groups of 0.458 mm diameter orifices. Each nozzle insert had a clearance hole for the charring ablator, which was 1.6 mm in diameter for the stagnation orifices and 2.5 mm in diameter for the side orifices. The water injection flow rates were controlled by the number of orifices available for each set of nozzles. Valves 5, 6, and 7 corresponded to nozzles near the stagnation point containing 6, 21, and 39 orifices, respectively. Similarly, the four sets of side nozzles (numbered 1-4) had 6, 18, 45, and 81 orifices, respectively. A valve-on cycle consisted of a series of seven pulses, each separated by 500 milliseconds. The valves were each left on for 230 milliseconds during a pulse and

---

[1] This problem was fixed for the RAM-C II flight by connecting the output of the amplifier to a differential-input subcarrier oscillator, instead of having it connected single-ended to the input of the oscillator.

a cycle was repeated every 4 seconds. As seen in Figure 5.3, the injection period occurred between 83.2 and 33.8 km where the water injection flow rates ranged from 4.54 g/s to 703 g/s [292]. The first cycles produced no apparent injection due to a slow fill rate in the lines.

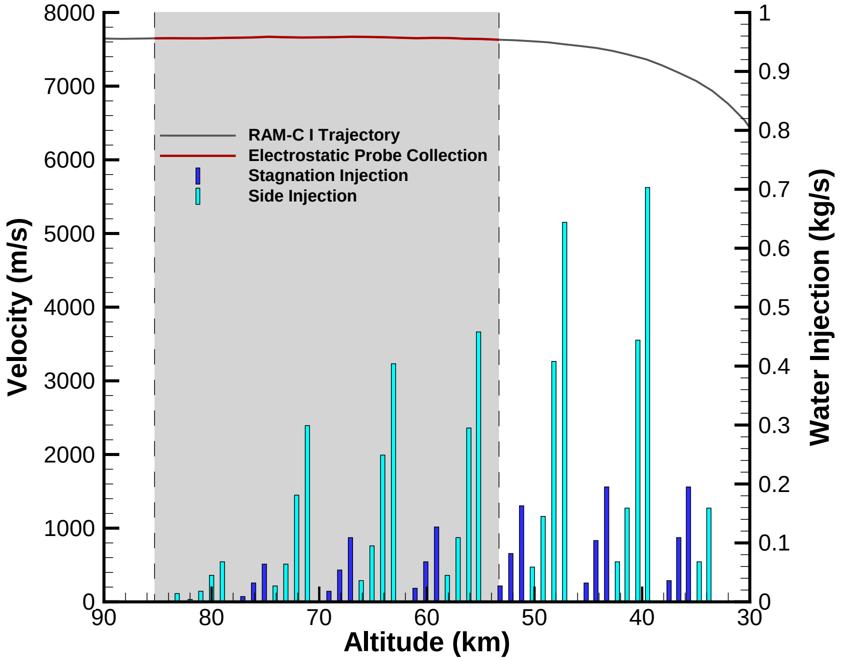

Figure 5.3: RAM-C I trajectory with the corresponding injection cycle flow rate sequence. Data collection period for the electrostatic probe rake is indicated with gray shadowing.

5.2.2 Numerical Setup

The semi-hemispherical conical geometry of the RAM-C I vehicle is simulated in this work with an axisymmetric approximation. The axisymmetric side injection nozzles are therefore physically represented by a lateral frustum surface. This approximation assumes a negligible spanwise dispersion of the injected water vapor. It should also be noted that Eq. 2.41 places a numerical constraint on the mass flux, $\dot{m}''_w$, such that the discriminant needs to remain positive. As an example, for the flight test case at 61.1 km, the maximum mass flux based on this constraint is 79.7 kg/s/m^2, compared to the actual injection flux of 1906 kg/s/m^2. This is compensated in the current model by spreading the mass injection over a larger area while maintaining a consistent mass flow rate with the flight conditions. Thus the current work primarily compares the two types of injection systems based on their efficacy in utilizing the same rate of water weight injected.

Table 5.1: Simulated RAM-C I trajectory points with qualities of the corresponding injection cycle.

Injection Cycle	Orifice(s) Position	Injection Valve	Altitude (km)	Velocity (km/s)	Flow Rate (g/s)
3	Stagnation	5	77.1	7.66	9.0
		6	76.1	7.66	32.0
		7	75.1	7.67	64.0
	Side	1	74.1	7.67	27.0
		2	73.1	7.66	64.0
		3	72.1	7.66	181.0
		4	71.1	7.66	299.0
4	Stagnation	5	69.1	7.66	18.0
		6	68.1	7.66	54.0
		7	67.1	7.67	109.0
	Side	1	66.1	7.67	36.0
		2	65.1	7.67	95.0
		3	64.1	7.66	249.0
		4	63.1	7.66	404.0
5	Stagnation	5	61.1	7.65	23.0
		6	60.1	7.65	68.0
		7	59.1	7.65	127.0
	Side	1	58.1	7.65	45.0
		2	57.1	7.65	109.0
		3	56.1	7.64	295.0
		4	55.2	7.64	458.0

From Figure 5.3, it is seen that there are three full injection cycles that are within the bounds of the electrostatic probe measurement period. Details of the valve pulses and their corresponding trajectory conditions are found in Table 5.1. From Table 5.1 it is evident that while the flight conditions remain mostly unchanged within specific injection cycles, the stagnation mass flow rates first approximately triple between valves 5 and 6 and then double between valves 6 and 7. Similar incremental increases are observed for the side injection flow rates, corresponding to the increased number of injection orifices used. Consequently, modeling each injection cycle provides insight into the influence of position and flow rate on the efficacy of water vapor injection. To obtain the pre-shock, freestream conditions at each altitude, (the composition of each air constituent, the density, and the temperature) the Naval Research Laboratory's temperature and density model, MSISE-00, is utilized [72]. The approximate latitude (33N), longitude (65W), date (October 19, 1967), and time (1733Z) of the RAM-C I flight test are used as inputs in the MSISE-00 atmospheric model.

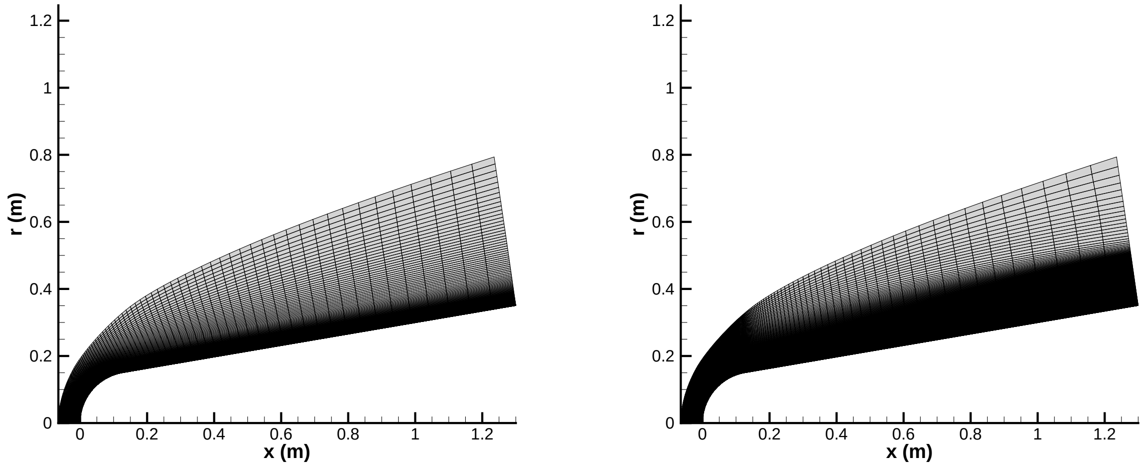

Figure 5.4: Computational grid used for the Cycle 5 stagnation (left) and side (right) injection cases.

The structured computational meshes that are employed in this study consist of a 144 x 228 quadrilateral-element grid. The grids, shown in Figure 5.4, are tailored to the shock and contain a large concentration of elements around, and downstream of, the injection sites. Mesh convergence is verified for the largest injection rates at each cycle examined by doubling the grid elements in both directions and observing a less than 10% change in maximum electron number density at the electrostatic probe location. The largest percent change between the two grid-sizes occurred at the highest altitudes examined.

Unless otherwise specified, the temperature of the injected water is assumed to be that of a 1200 K isothermal wall. The no-slip condition is prescribed at the wall for the flow velocity. The wall is assumed to be non-catalytic for neutral species, while also employing a catalytic condition which enforces electron-ion recombination. The mass fraction of the injected material is fully-distilled water vapor with no impurities.

5.2.3 Results

The previously listed twenty-one trajectory points (in Table 5.1) are simulated in the context of the RAM-C I flight, where, using the same mass flow rates, the electrostatic probe data collected during the liquid injection phase of the flight test is compared to that of the simulated water vapor injection results. Before such comparisons are made, it is important to discuss the physical differences brought on by injecting water vapor at two different orifice locations, namely at the stagnation point and downstream at the shoulder. For purposes of such a discussion, the 59.1 km and 57.1 km trajectory points are investigated as they offer both similar freestream conditions and mass flow rates.

5.2.3.1 Stagnation Injection at 59.1 km

At the 59.1 km trajectory point during the RAM-C I flight, the largest mass flow rate of liquid water that was injected from the stagnation region entered the flow from thirty-nine 0.458 mm diameter orifices. Figure 5.5 shows a comparison between a simulated baseline, no-injection case at this altitude with that of an analogous 127.0 g/s water vapor injection. It is evident from Figure 5.5 that the electron number density immediately sees a reduction, starting from within the stagnation region behind the bow shock. The overall maximum electron number density experiences a 57.9% decrease when water vapor injection is added. After the flow expands around the shoulder of the vehicle and the temperatures decrease, the number of electrons remains relatively constant for both cases. There is also noticeably a smaller electron density near the wall throughout for the injection case when compared to the baseline configuration. These overall trends are similar to that of the translational-rotational temperature, also displayed in Figure 5.5. As will be discussed in more detail shortly within this section, the electron density and temperature reductions directly next to the wall correspond with a continuous film containing a high concentration of water vapor.

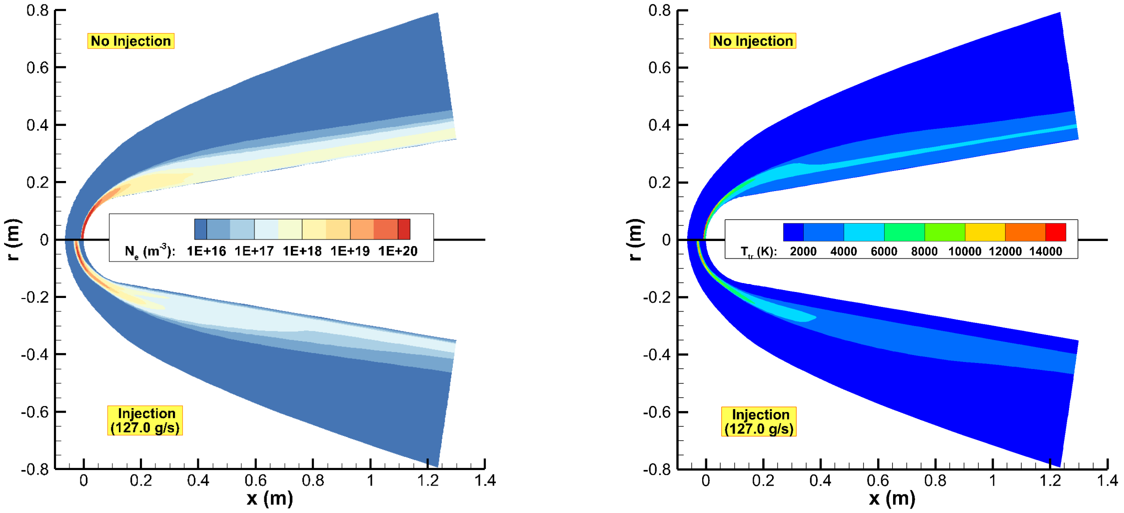

Figure 5.5: Electron number density (left) and translational-rotational temperature contours (right) of RAM-C I at 59.1 km with no injection and a 127.0 g/s water vapor injection at the stagnation point.

From Figure 5.5 it is also apparent that the water vapor injection at the stagnation region alters the bow shock by increasing the stand-off distance and making the vehicle shape appear more slender, similar to the gas-spike strategy [316]. This is further illustrated by the temperatures of the stagnation line, shown in Figure 5.6. The peak translational-rotational temperature experiences a shift outward of 240%. Additionally, with an injection of water vapor, the maximum translational-rotational temperature in the stagnation region decreases by 40.1%, while the maximum vibrational-electron-electronic temperature has a 27.6% decrease. It should be restated that, as larger disturbances to the shock are associated with gas injection when compared with that of liquid injection [288], this large stand-off distance increase was unlikely to occur during the RAM-C I flight test.

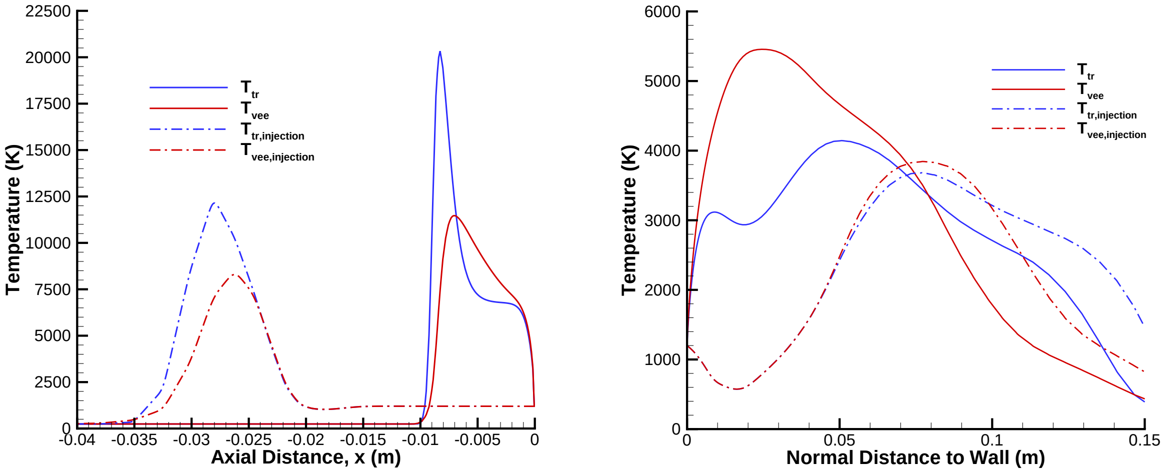

Figure 5.6: Translation and vibrational temperature comparisons between the baseline and injection cases at 57.1 km along the stagnation line (left) and along a line radially normal to the vehicle surface at x = 0.6 m (right).

As previously discussed, one of the primary mechanisms with which water vapor eliminates free electrons is through the means of thermal quenching. Thus, it is no surprise that the rest of the flowfield is consequently considerably cooled by the water vapor injection. Indeed, from Figure 5.6, which also displays the two temperatures radially outward from the wall at a point downstream (x = 0.6 m), the two temperatures from the blowing case are still noticeably lower than that of the baseline case. For instance, there is an 18% decrease experienced in the maximum vibrational temperature. These differences in temperature show that the water is effective as a coolant, either directly from the lower temperature water being injected or indirectly by altering the apparent vehicle geometry. Figure 5.6 additionally shows that as the water vapor-air mixture further cools around the expansion region of the shoulder, the translational and vibrational temperatures start to converge towards thermal equilibrium.

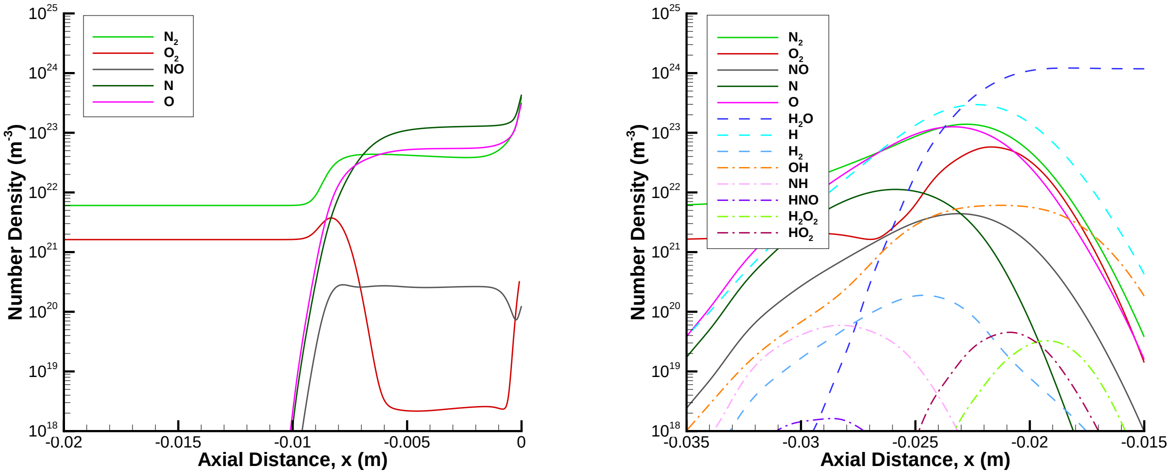

Figure 5.7: Number densities of neutral species along the stagnation line for both the non-injection (left) and water vapor injection (right) cases at 59.1 km.

Another mechanism used by water vapor to reduce free electrons in the flow is through ionization retardation via the diminishment of the possible associative ionization reactions by readily reacting with the atomic nitrogen and oxygen. Figure 5.7 shows the number densities of the neutral chemical species for both cases examined. It is shown that indeed the maximum number density of N decreases along the streamline. However, a subsequent increase in N_2 implies that the decrease in temperature may be at least partially responsible, from lowering the dissociation rates of N_2. Further, the O atoms increase in the water injected flow. As both the NO and O_2 number densities also increase, reactants and products of the dominant second Zeldovich reaction, it is indicated that the increase of O atoms originates from the addition, and subsequent molecular breakup, of water. Specifically, the increase in oxygen levels arises from the very active hydrogen exchange reaction with hydroxyl radicals. However, this increase is limited by the production of HO_2, H_2O_2, and HNO, as Figure 5.7 shows. The increase in atomic oxygen also leads to increased O_2 levels, via the active exchange reaction between oxygen and hydroxyl radicals. Further, the role of water vapor injection on decreased atomic nitrogen levels is exhibited by Figure 5.7 with the production of HNO and NH, though this is minimal in comparison to the decrease caused by the cooler air mixture.

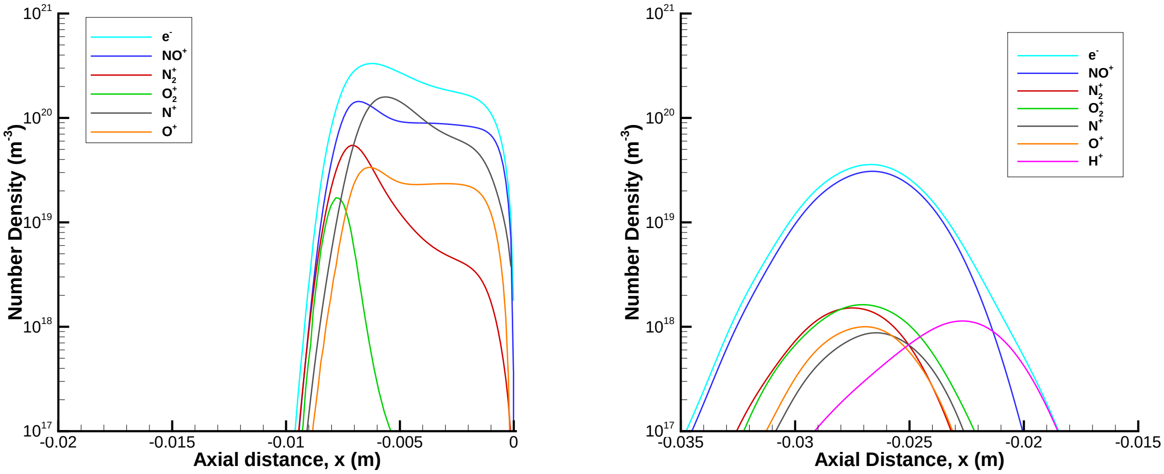

Figure 5.8: Number densities of charged species along the stagnation line for both the non-injection (left) and water vapor injection (right) cases at 59.1 km.

It is also apparent from Figure 5.7 that there is a prevalent amount of hydrogen atoms in the flow. In turn, as Figure 5.8 shows, there is a nontrivial amount of free electrons being created by electron impact with hydrogen, the simplest ionization process. Conversely, the rest of the ionized species decrease, leading to an overall decrease of quasi-neutral plasma along the stagnation line for the water injected flow. Still, as it has been shown that there is no considerable decrease present in the available associative ionization reactants from the introduction of water to the stagnation region, this decrease is a consequence of the resulting milder temperature conditions. Thus, as will be discussed throughout this section, there is a major trade-off present when increasing the mass flow rate of the water vapor at the stagnation point, namely between the decrease in temperature due to the change in the apparent geometry and the increase in atomic oxygen and ionized hydrogen.

5.2.3.2 Side Injection at 57.1 km

At the RAM-C I 57.1 km trajectory point, a comparable mass flow rate (1.16 times less) of liquid water to that of the 59.1 km trajectory point was simultaneously injected at two diametrically opposed locations at the shoulder of the vehicle, each with eighteen 0.458 mm diameter orifices. The primary difference between the two injection locations is that, whereas in the stagnation region the surrounding high temperatures promote ionization, further downstream the flowfield cools and starts to become more recombination driven. Although there is an increase of temperature and subsequent ionization present from the adjacent oblique shock, it can be assumed that a large portion of the ions downstream have been advected from the stagnation region.

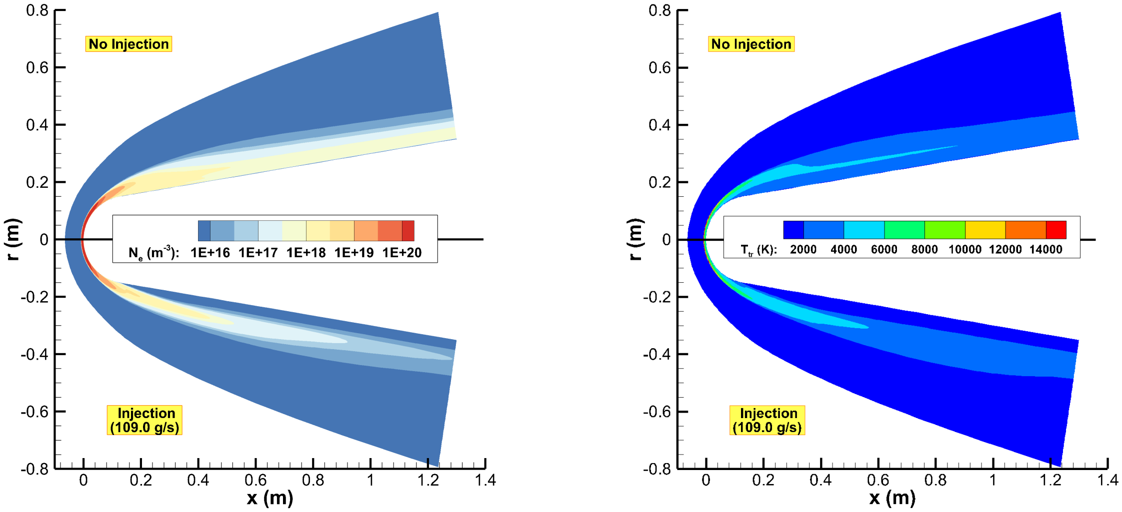

Figure 5.9: Electron number density (left) and translational-rotational temperature (right) contours of RAM-C I at 57.1 km with no injection and a 109.0 g/s water vapor injection at the shoulder.

Figure 5.9 shows comparisons of the electron number density and translational temperature contours between the clean air, baseline case and that of a 109.0 g/s water vapor injection case. Once again, it is directly evident from Figure 5.9 that shortly after the injection region there begins a reduction in the electron density, especially directly adjacent to the wall where a thin film is present containing a high concentration of water. This thin water film continuously shifts the ionized air outwards, away from the body. Analogously, the translational-rotational temperature, also displayed in Figure 5.9, becomes gradually lower over the axial distance with the injection of water vapor, albeit with less differences observed when compared to the stagnation point injection at 59.1 km. This is evidenced further with the wall normal lines plotted in Figure 5.10, where the maxima of the two temperatures are very similar between the baseline and injection cases. In fact, near the water-air interface in the region by the injection site (the left-hand plot in Figure 5.10) there are higher translational temperatures in the injected flow than that of the clean air. As the flow traverses downstream, the injected flow becomes progressively cooler and the differences between the maximum temperatures of the two cases grow. Once again, it is shown that the injected flowfield approaches thermal equilibrium at a faster rate.

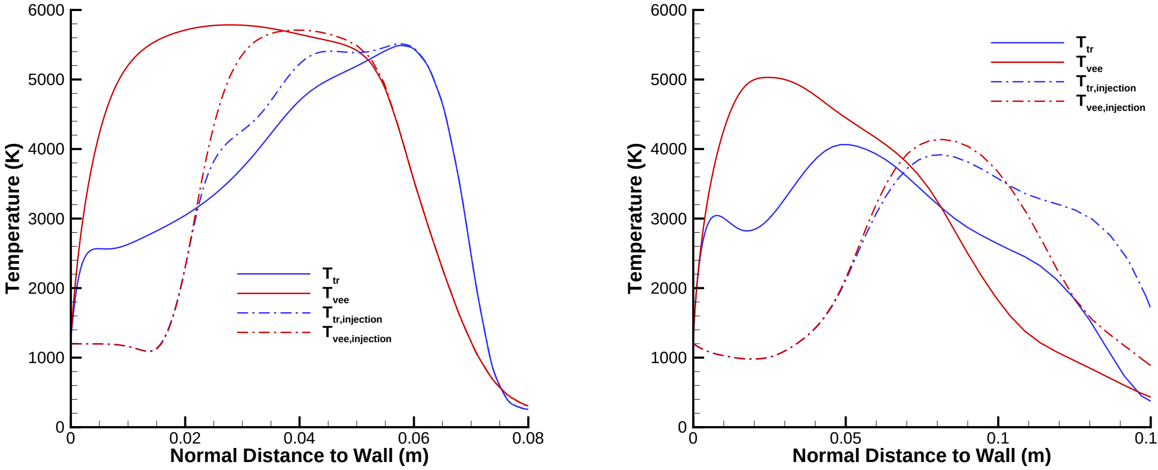

Figure 5.10: Translation and vibrational temperature comparisons between the baseline and injection cases along a line radially normal to the vehicle surface at x = 0.16 m (right) and at x = 0.6 m (right).

The higher translational-rotational temperatures at the interface between the water vapor and air are the primary cause of a 140% increase in the maximum electron density near the injection site, as Figure 5.11 shows. At this axial location, the baseline, no injection case has regions of cooler air which promote faster recombination rates. Miyashita et al. have observed similar increases in electron density directly after the injection of an air film, indicating that these increases are due to the introduction of a flow disturbance and not the composition of the water vapor [317]. Subsequently, the number densities of the ionized NO^+, N^+, O^+, and N_2^+, species are also increased within this region for the injected flowfield. The increase in NO^+ and O_2^+ alongside the water-air mixing interface are not solely due to differences in translational temperature but also from an increased presence of atomic oxygen from the water composition, which Figure 5.12 displays.

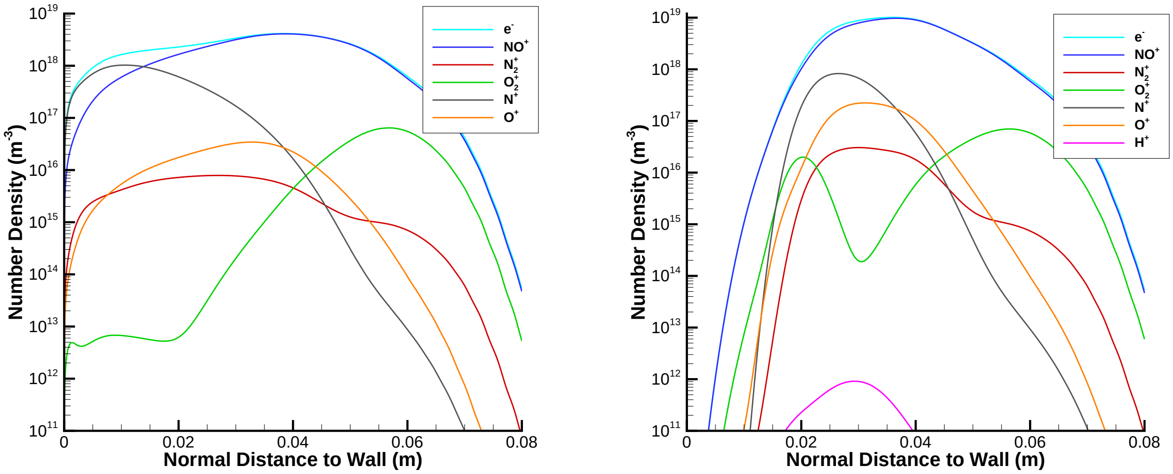

Figure 5.11: Number densities of charged species along a line normal to the vehicle surface at x = 0.16 m for both the non-injection (left) and water vapor injection (right) cases at 57.1 km.

Also observed within this region is an increase in the neutral N_2, O_2, and NO molecules. Similar to the stagnation injection, more O is generated through the hydrogen exchange reaction with OH, and O_2 is in turn generated through the oxygen exchange reaction with OH. Furthermore, one of the main benefits of injecting at the shoulder is seen in Figure 5.12, specifically the decrease in N atoms. This is a result of the N + OH exchange reaction, which has a relative significance at these lower temperature conditions, and is also a contributing factor for the increase in NO. The lowered levels of N number density resulting from injection at the shoulder are crucial in pacifying any electron generation that can occur from increased temperature levels across the oblique shock and within the flowfield. Indeed, as Figure 5.13 shows, there are decreased levels in ions associated with nitrogen as the flow traverses further downstream. However, the lower temperatures shown in Figure 5.10 also primarily contribute to these increased recombination rates. Comparisons between Figures 5.11 and 5.13 also show a gradual shift radially for the shock-layer when water injection is introduced.

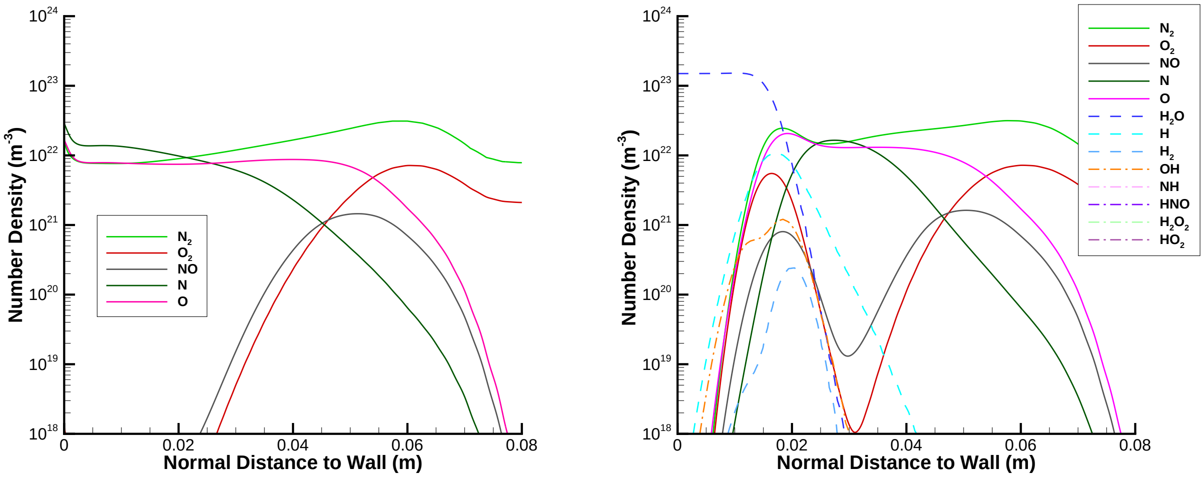

Figure 5.12: Number densities of neutral species along a line normal to the vehicle surface at x = 0.16 m for both the non-injection (left) and water vapor injection (right) cases at 57.1 km.

It is noteworthy to mention that while there is still a considerable number of hydrogen atoms present for the side injected flow, the number of H^+ ions is considerably less than that produced from an injection within the stagnation region. While the maximum vibrational-electron-electronic temperature only decreases by 30% when going from the stagnation injection to the shoulder injection, this results in almost a four-orders of magnitude decrease in the electron impact ionization rate of hydrogen. This is identified as one of the biggest differences between the flows of the two injection sites, resulting from the different temperatures experienced.

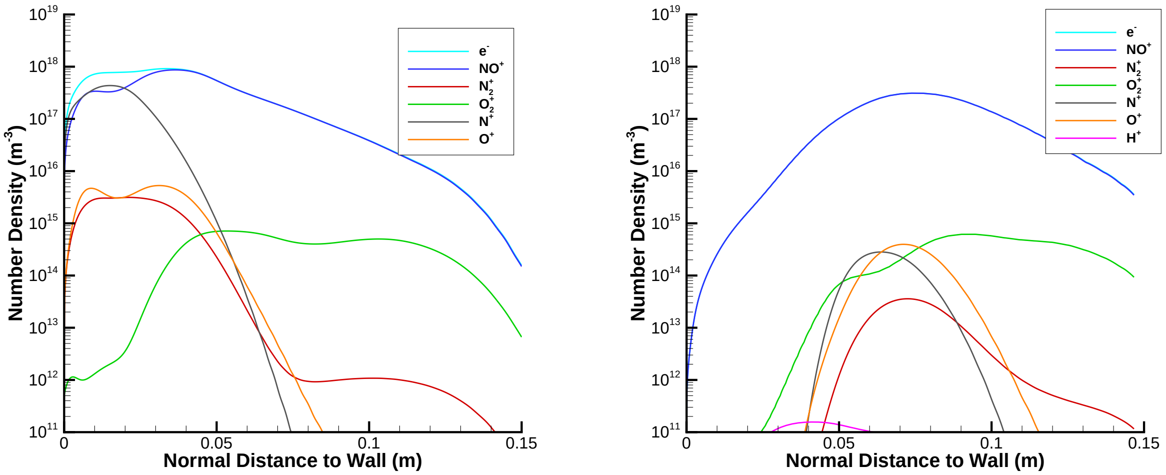

Figure 5.13: Number densities of charged species along a line normal to the vehicle surface at x = 0.6 m for both the non-injection (left) and water vapor injection (right) cases at 57.1 km.

While key differences between the previously discussed injection driven flows have been recognized, it is informative to further distinguish between the effects arising from temperature decreases and ionization retardation by examining water vapor injected at varying temperature conditions and by vibrationally and chemically freezing the injected water.

“Frozen” Water Conditions

To more directly quantify the role of both the chemical reactions and resulting species introduced by water vapor with relation to the role of the physical vapor film, a “chemically frozen” water vapor is injected, where all reactions involving the decomposition of water are removed. Further, as the water molecules can store more vibrational energy due to the additional degrees of freedom, the role of the vibrational energy quenching from the introduced water vapor is investigated through “vibrationally freezing” the injected water.

This is accomplished by increasing the vibrational relaxation time by six orders of magnitude, per the methodology suggested in Ref. [160]. For both of these conditions the rest of the airflow remains unchanged.

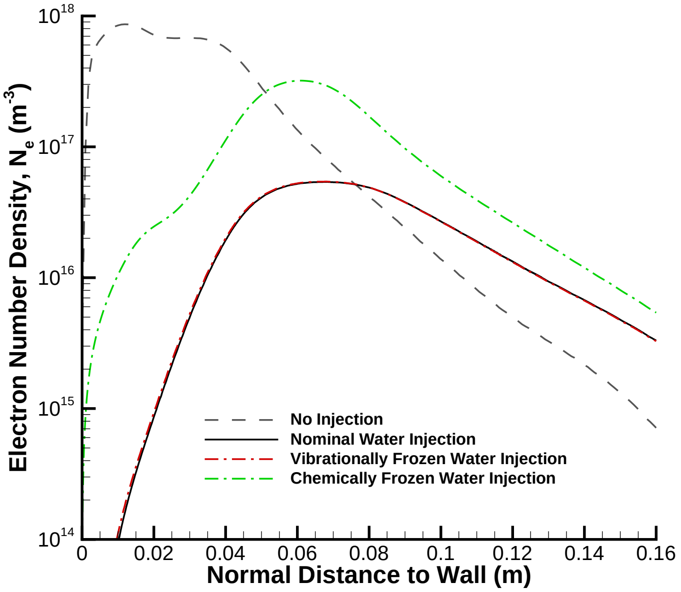

Figure 5.14: Electron number density along a line normal to the wall at the location of the electrostatic probe (x = 1.234 m) for no injection, nominal injection, and frozen injection conditions.

Figure 5.14 displays the electron number densities at the location of the electrostatic probe for these frozen water vapor conditions along with the nominal injection and baseline cases. It is immediately apparent that the role of the vibrationally frozen water is relatively inconsequential to the plasma reduction, with only a 0.18% difference for the maximum electron density between the vibrationally frozen and nominal injection flows. Conversely, there is a 140% difference between the chemically frozen and nominal injection flows, indicating a significant role of the chemical reactions introduced by the specific injection of water. From an analogous perspective, while there is a 0.06 reduction of maximum electron number density ($\mathrm{N_{e,inj}/N_{e,0}}$) induced by the nominal water vapor injection, there is only a 0.37 reduction accounted for by the physical disturbance and thin film layer brought on by the injection. Thus, it is clear that the chemical composition of the injectant has a vital importance on the properties of the water vapor-contaminated flowfield.

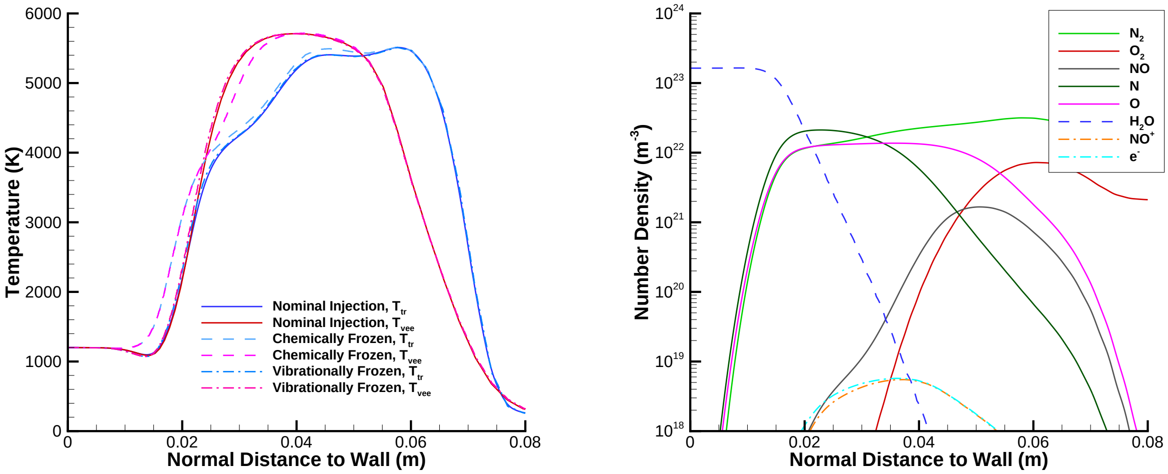

Figure 5.15: Temperature profiles of the nominal, vibrationally frozen, and chemically frozen water injection conditions (left) and number densities of the chemically frozen water injection case (right) along a line normal to the vehicle surface at x = 0.16 m.

Indeed, as Figure 5.15 shows, the temperature profile of the chemically frozen flow is noticeably different than that of both the vibrationally frozen water and nominal water injections. Conversely the differences in temperatures of the latter two conditions are indiscernible. There is a maximum temperature difference of 23% between the chemically frozen and nominal water injection cases at the location where the molecular dissociation of water is the highest. It is thus strongly implied that the endothermic dissociation reactions of water and its by-products decrease the temperature considerably.

Figure 5.15 also displays the number densities along a line that is wall normal to the body near the injection site. Comparing Figure 5.15 with analogous plots shown in Figure 5.12, it is found that the thin film of water vapor at the wall physically displaces the air constituents. Thus, the corresponding number densities of the adjacent air, including that of the free electrons, are negligible in the near wall region. Further, the chemically frozen water vapor favorably does not give rise to an increase of O or O_2. However, the increase of temperature for the chemically frozen water case results in an increase in the levels of N primarily from the first Zeldovich reaction, leading to a slight, 4% increase in the maximum electron density.

Injection Temperature

The temperature of the injected water in this work is assumed to be the same as the 1200 K isothermal wall. For liquid water injection systems, the injection temperature plays a significant role and is controlled appropriately. As Figure 5.1 shows, a higher water droplet temperature can be beneficial to plasma reduction. However, superheated liquids injected in a partial vacuum can nucleate into vapor within the nozzle if the injection temperature is sufficient, degrading the performance of the liquid water injection system [313]. Unfortunately, as there were no thermocouple measurements made on the injected droplet stream or within the injection system for the RAM-C I flight experiment the injected water temperature is unknown. However, data from RAM-C I ground tests performed at the Langley Mach 8 variable-density hypersonic tunnel, the high Mach number test section of the Langley Unitary Plan wind tunnel (UPWT), and a Mach 5.5 cyanogen-oxygen tunnel provide insight into what the water temperature may have been during the flight test [298, 320]. Thermocouple readings of the water temperature in a nozzle plenum chamber were consistently around 289 K during all tests. Measurements of the injected spray were seen to be between 295 K and 400 K. Consequently, it was hypothesized that 297 K would be the most probable water temperature during the C-I flight [298]. Still, these tests were performed at less thermally demanding conditions than what was expected during the flight experiment. Furthermore, the RAM-C I nozzles orifices and clearance holes had non-negligible length-to-diameter ratios (L/d_0) of up to 5mm/0.5mm and 30mm/1.5mm, respectively, which would be adequate for heat transfer to occur from the vehicle walls and heat shield [292, 298, 319]. As such, a set of water vapor injection temperatures ranging from 297 K to 1200 K are used to assess the sensitivity of the original assumption used within these simulations.

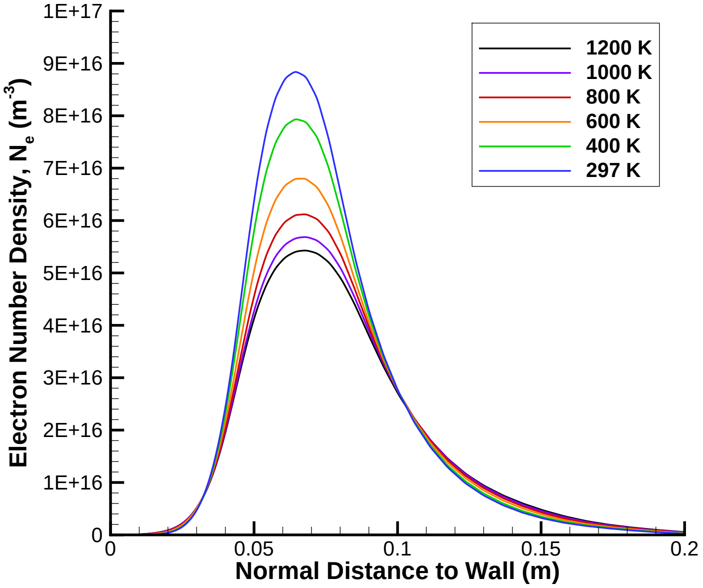

Figure 5.16: Electron number density along a line normal to the wall at the location of the electrostatic probe (x = 1.234 m) for the various temperature injection conditions.

Figure 5.16 shows plots of the electron density profiles at the electrostatic probe location for six different temperatures of injected water vapor. Perhaps somewhat counter-intuitively, it is shown that there is a direct correlation between higher injection temperatures and lower electron number densities. Decreasing the injection temperature from 1200 K to 297 K results in a 62% increase in the maximum electron number density at the probe location, or a corresponding 0.6 GHz increase in the cut-off frequency. Hence it is observed within this study that a higher water vapor temperature at the injection site is beneficial to blackout mitigation. It should be noted, however, that the flows of each injection temperature condition result in a plasma reduction with respect to the baseline, no injection case.

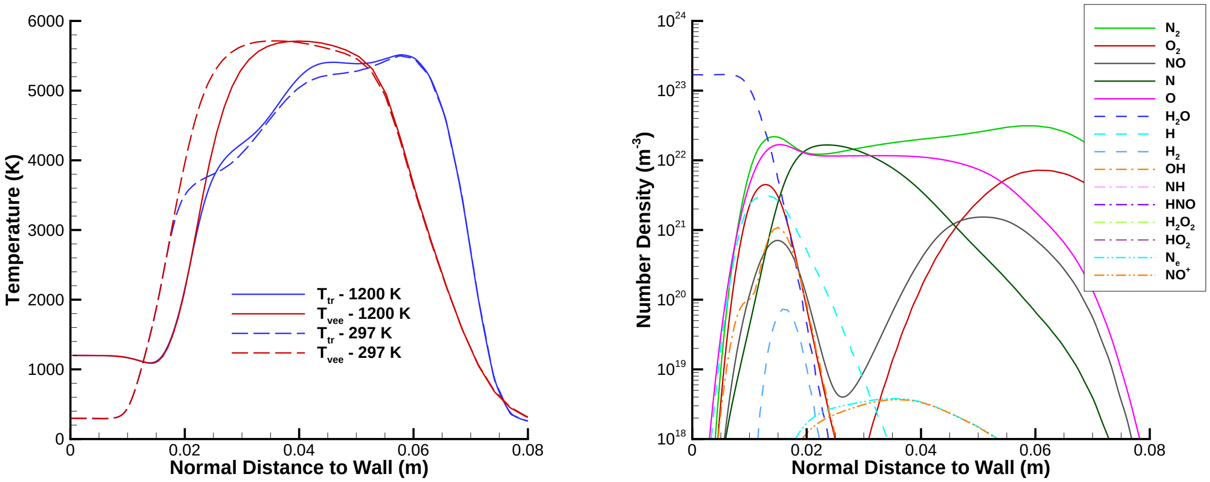

Figure 5.17: Two-temperature profile of the water vapor flow, with initial injection temperature set to 297 K and 1200 K (left) and the number densities of the 297 K water injection case (right) along a line normal to the vehicle surface at x = 0.16 m.

Figure 5.17 shows a comparison of the two temperature profiles at the injection site for the most extreme injection temperature conditions considered, namely 1200 K and 297 K. It is shown within this plot that the less thermally intense of these two scenarios closely resembles that of the previously discussed chemically frozen water injection condition. Therefore, while the 1200 K water injection case starts out at a higher temperature, the endothermic dissociation reactions which are much more active at these temperatures cool the flow at a faster rate than the associated temperature gradient of the 297 K injection condition within the water vapor and air interface. This is once again evidenced by an initial decrease in temperature for the 1200 K case before a subsequent increase, a trend that is not seen with either the 297 K or chemically frozen water vapor conditions.

Figure 5.17 also display the electron number densities at the electrostatic probe location for the 297 K water vapor injection condition. The steeper increase of temperature for the 297 K condition leads to the onset of the by-products of the water reactions closer to the wall. This shifting of the reacting water-air interface is the largest change between the 297

K injection temperature flow and that of the nominal 1200 K injection temperature case (see Figure 5.12). As the reactions between the water injection and air occur closer to the wall, including those that have been found to be beneficial to plasma reduction, there is a decrease in the electron density close to the wall when cooling the air flow. For instance, at the electrostatic probe location with a wall normal distance of 10 mm, there is a 67% decrease in electron density when decreasing the temperature of the injected water from 1200 K to 297 K. However, as the maximum electron density is prominent further away from the wall, where the 297 K injected water temperature has less of an impact, the trend changes where an increase in temperature is more beneficial. In other words, it is found that the higher the injection temperature, the more penetration the chemically reacting water has into the air.

It is important to also note that as the cooler injected water vapor traverses downstream, the isothermal 1200 K wall heats the flow. This is a nonphysical limitation of the isothermal assumption, as a gradually cooler air flow should also result in a gradually cooler wall temperature downstream of the injection site. While results in the near wall region may therefore lose some validity, it is assumed that the extra energy lost by the water from cooling the wall is negligible with respect to that gained from the high temperature air.

5.2.3.3 Injection Cycle 3

Comparisons between the water vapor injection simulations and the RAM-C I electrostatic probe flight data during liquid water injection are made in the following subsections. Specifically, the comparisons are primarily focused in the near wall region, at a radial wall normal range of 0.096 cm to 7.08 cm, where the probes were located [220]. The ensuing electrostatic probe data points that are plotted represent the average values collected within one vehicle rotation (330 milliseconds) before the time of injection, with the maxima and minima represented by uncertainty bars. The lowest recorded electron number density during the valve-on period (230 milliseconds) is marked on these plots to indicate the result of the liquid water injection. It should be noted that while there is good "agreement" present during injection for some of the particular flight conditions and flow rates considered, this should by no means be indicative of a validation effort as the physics of the liquid water droplets are not entirely included in this study and are therefore not well quantified. Thus, it can only be currently speculated whether this is merely a coincidence or an indication of the relative role of the liquid droplets to the evaporated water vapor.

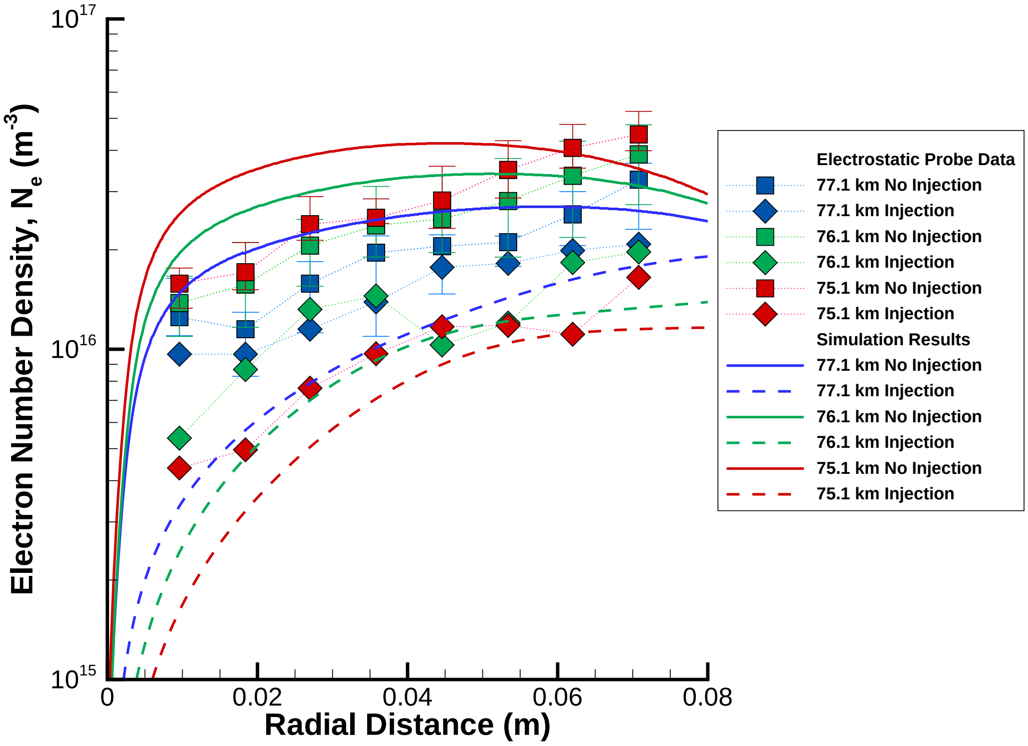

Figure 5.18: Electron number densities along the wall-normal radial distance at the location of the electrostatic probe, taken from flight data during the 3rd RAM-C I liquid water stagnation injection cycle and the water vapor simulations.

The water injections made around the stagnation point during the 3rd cycle (shown in Figure 5.18) occurred from 77.1 km to 75.1 km. At these altitudes the pressure of the freestream is quite low and thus the impact of the water vapor injection on altering the shock shape is considerable. Further, the flow rates at these injection points are some of the lowest studied (9 to 64 g/s) and lead to a low number of oxygen atoms and hydrogen ions which are introduced into the flow, even though the post-shock temperatures are at their highest during these injection conditions. Hence, the water vapor flowfields within this stagnation injection cycle are primarily dictated by the altering of the shock shape, and an increase in mass flow rate directly corresponds with an increase in the amount of plasma reduction.

The clean air simulations are in fair agreement with the flight data recorded by the electrostatic probes. Similar to the RAM-C II comparisons that were detailed in Chapter 3, the simulations overpredict the innermost electrostatic probes (Probes 1-3) and then underpredict the outermost probes (Probes 6-8). This is observed throughout for each of the trajectory points studied hereafter, since, whereas the simulations predict a maximum electron number density located within the 8 probe locations, the flight data measures a constant increase across all probes, implying that the maximum may not have been captured by the probe diagnostics.

The reduction in electron density predicted by water vapor injection is comparable to that measured for liquid water injection during the cycle 3 stagnation injections. Water vapor injection in fact performs better than its liquid water equivalent, attributed to the stronger shock alterations associated with gas injection. The liquid water injection, as measured by the flight data, has no discernible optimum in terms of mass flow rate, as more injection does not necessarily equal more plasma reduction for the stagnation injection. Although this trend is not predicted by the water vapor simulations during this cycle, the lack of a direct correlation between the mass flow rate and electron reduction factor is a common theme for both water vapor and liquid water stagnation injections throughout this study.

During the side injections of Cycle 3, shown in Figure 5.19, there are more readily noticeable trends occurring for both liquid and vapor injections. Specifically, a higher injection rate is directly correlated to a higher reduction in the electron number density. However, the benefits of the mass flow rate also start to gradually diminish at the highest flow rates.

While the introduction of more water vapor at these specific conditions further reduces the amount of atomic nitrogen and shifts the location of the maximum electron density more outwards, it also coincides with an increased introduction of atomic oxygen that offsets the benefits of the additional water vapor.

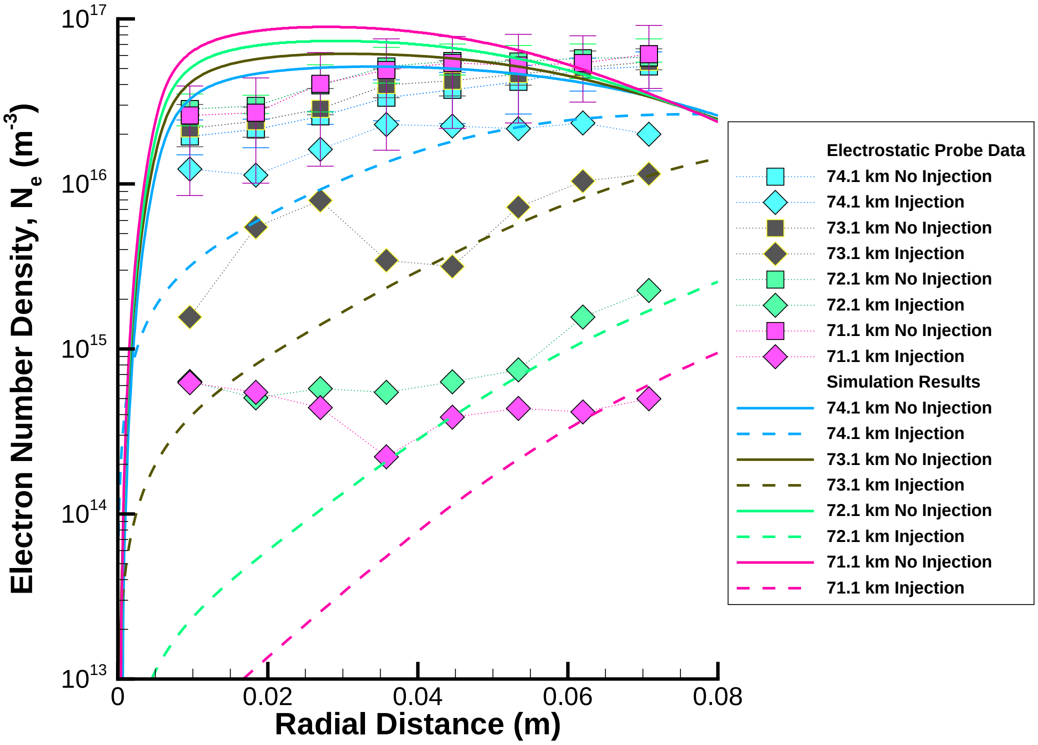

Figure 5.19: Electron number densities along the wall-normal radial distance at the location of the electrostatic probe, taken from flight data during the 3rd RAM-C I liquid water side injection cycle and the water vapor simulations.

5.2.3.4 Injection Cycle 4

During the stagnation Cycle 4 water vapor injections, shown in Figure 5.20, it is predicted that there is no clear benefit related to injection at higher mass flow rates. Although the shock is indeed altered from these injections leading to milder flowfield conditions, the higher associated freestream pressures result in less of an impact when compared to the higher altitude points investigated. Further, as the flow rates needed to accomplish a significant shock shift also introduce a considerable amount of hydrogen ions and atomic oxygen, it is observed that adding more water into the flow quickly becomes detrimental.

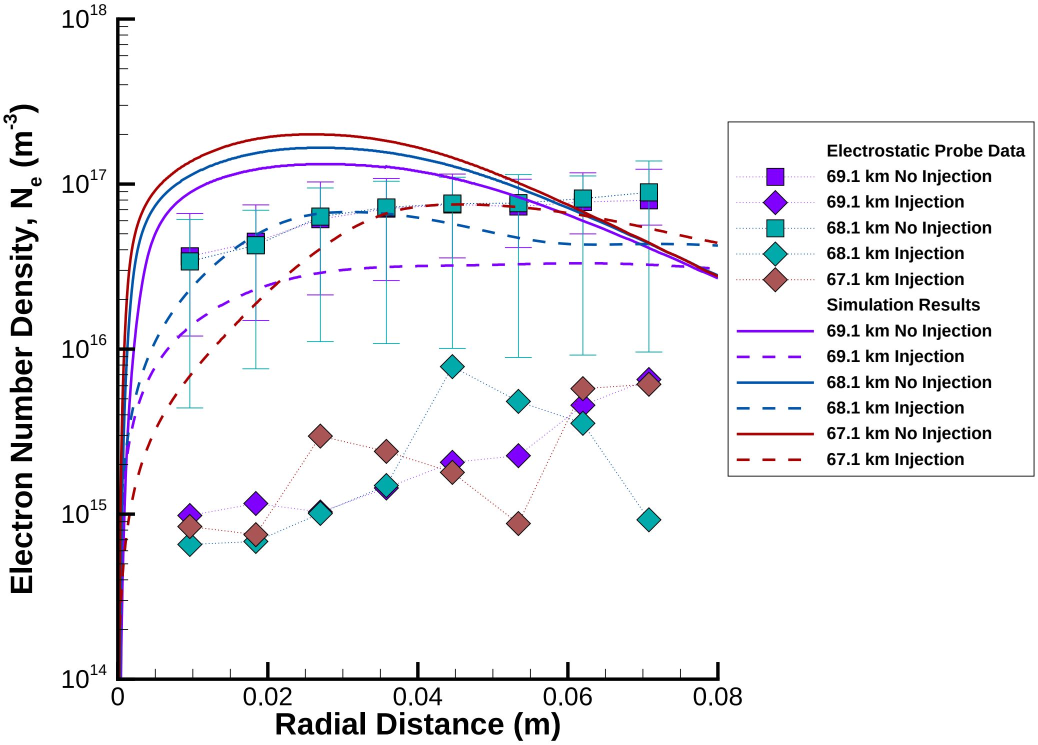

Figure 5.20: Electron number densities along the wall-normal radial distance at the location of the electrostatic probe, taken from flight data during the 4th RAM-C I liquid water stagnation injection cycle and the water vapor simulations.

When compared to the plasma reduction recorded by the flight data pertaining to liquid water injection, the advantages of water vapor are predicted to be approximately an order of magnitude less. Also, regardless of the phase of the water with the conditions observed at the stagnation point, there is no benefit that arises from increasing the flow rates. It was qualitatively assessed in the beginning of this chapter that the role of the water in liquid droplet form should generally increase at the stagnation point location and at lower altitudes, a tendency that also becomes apparent when comparing the data of the three cycles.

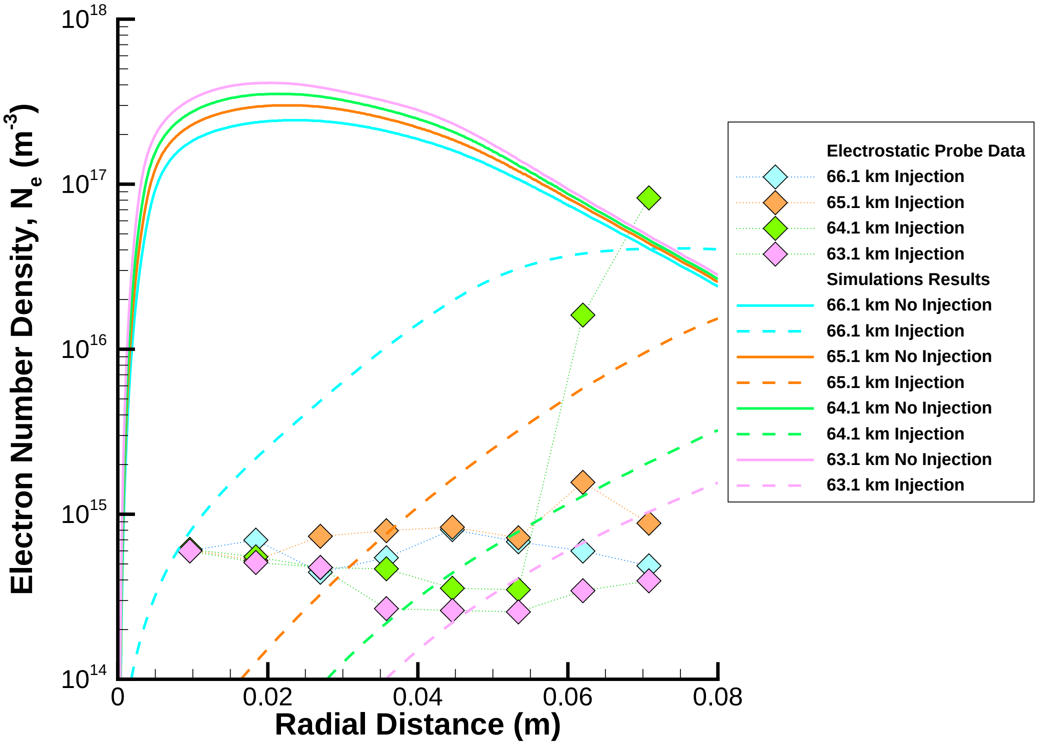

Figure 5.21: Electron number densities along the wall-normal radial distance at the location of the electrostatic probe, taken from flight data during the 4th RAM-C I liquid water side injection cycle and the water vapor simulations.

Note, the anomaly with the subcarrier oscillator connected to the logarithmic amplifier occurred during the clean air conditions between 67.0 km and 61.0 km. The electrostatic data points within these altitudes have consequently been expunged. For the side injections of Cycle 4, presented in Figure 5.21, this includes all of the clean air measurements. Regardless, the side injection of liquid water during the flight demonstrates similar reduction as that of the water vapor simulations. However, while the increase in liquid water flow rate gradually leads to larger depletion of the electron density, the opposite effect occurs for water vapor injection, namely that an increasing flow rate starts to progressively have less advantageous properties.

5.2.3.5 Injection Cycle 5

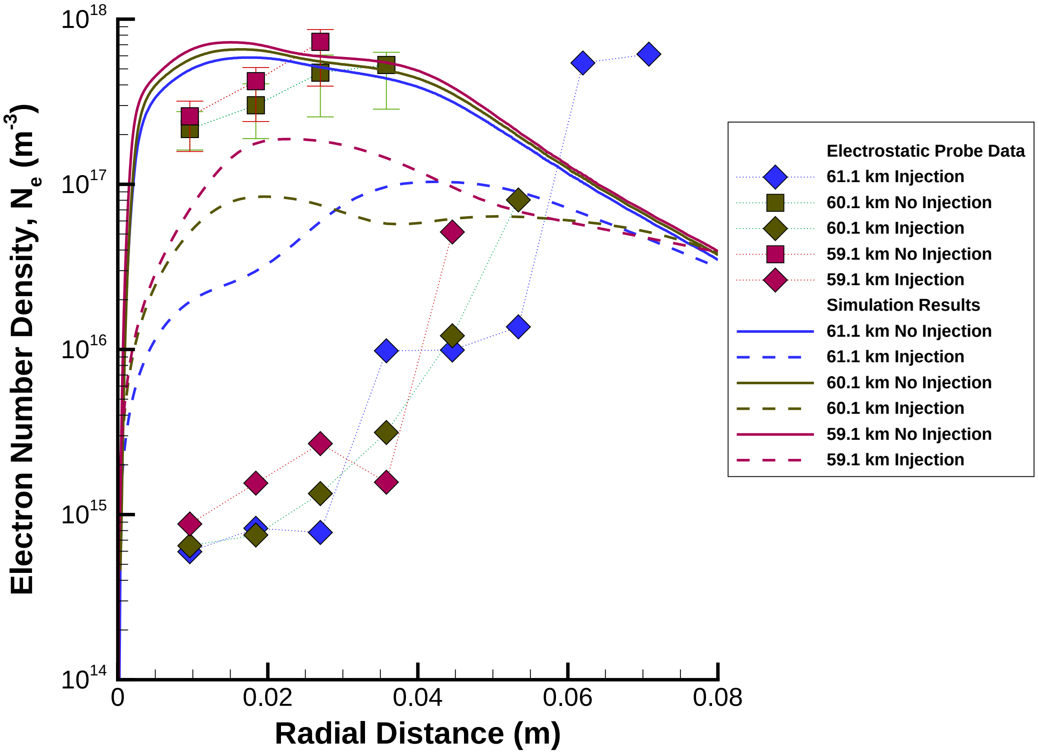

Figure 5.22: Electron number densities along the wall-normal radial distance at the location of the electrostatic probe, taken from flight data during the 5th RAM-C I liquid water stagnation injection cycle and the water vapor simulations.

The water vapor stagnation point injections from the 61.1 km to 59.1 km trajectory points are plotted and shown in Figure 5.22. Once more, a higher mass flow rate of water vapor does not correspond with a higher reduction in plasma. Indeed, the stagnation point injection with the mass flow rate studied has the poorest performance of the three within this altitude regime. While these lower altitude freestream conditions equate to higher pressures, and a decrease in Mach numbers and post shock temperatures, this is offset by the large amounts of water added.

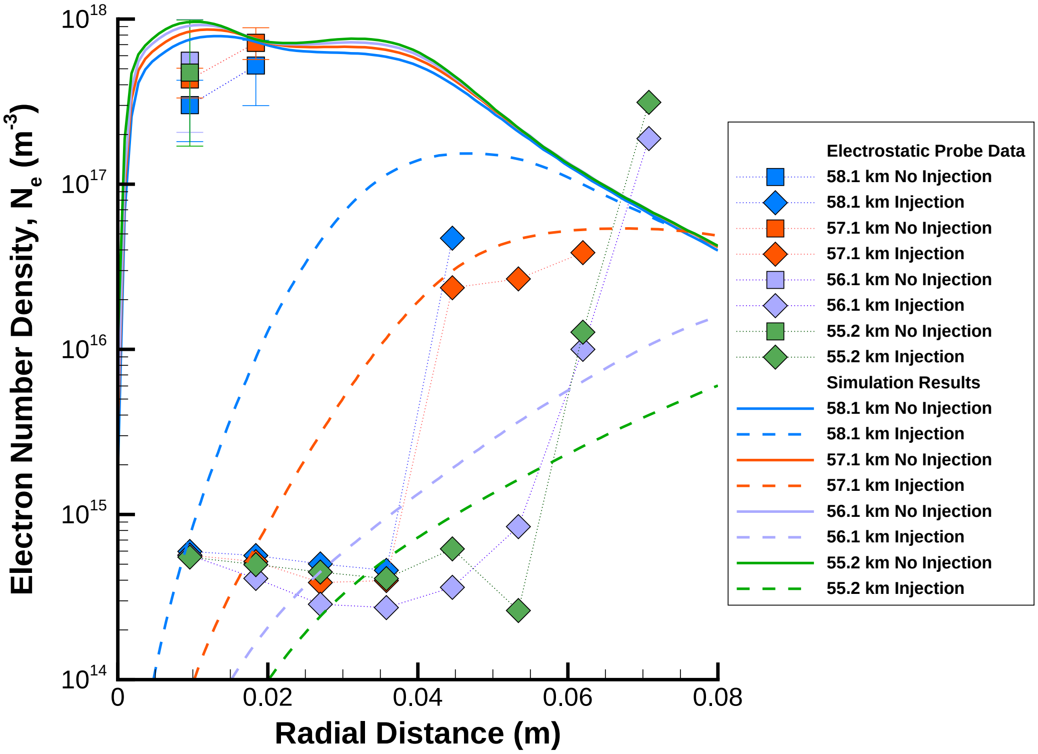

Figure 5.23: Electron number densities along the wall-normal radial distance at the location of the electrostatic probe, taken from flight data during the 5th RAM-C I liquid water side injection cycle and the water vapor simulations.

The RAM-C I probe data are also shown in Figure 5.22, where measurements made during periods of saturated current or beryllium insulation degradation from high temperatures are not included. The amplifier anomaly was also still present during the clean air read-outs at 61.1 km. It is shown from the flight data that a similar ambiguous correlation exists between the mass of water injected and reduction in plasma density. Although the driving mechanism for plasma reduction with water droplets is unique and plausibly results in the two-orders-of-magnitude gap between the liquid and vapor injections, the limitations of liquid water is the same as that of water vapor. More liquid water injection equates to a higher number density of droplets, improving plasma reduction. However, once the droplets vaporize they too will introduce more atomic oxygen and hydrogen ions into the flow.

During the side injections of the 5th cycle, shown in Figure 5.23, an increase in water vapor both pushes the maximum electron density further away from the wall and, through the decrease in temperature and nitrogen atoms, results in an increased depletion of free electrons. The advantage of increasing the mass flow rate languishes as the amount of water introduced into the flow increases. The flight data of the liquid water injection shows similar resulting electron number densities for the wide range of 45 g/s to 458 g/s flow rates.

5.2.3.6 Trajectory Simulations

Direct comparisons with the electrostatic probe data along the flight trajectory further highlight the general trends that were observed in more detail throughout each injection cycle. The recorded electron number densities of the middle probes (3-6) are shown in Figure 5.24 along with the corresponding simulation results of the water vapor injection. As the middle probes demonstrated the best agreement with the clean air simulations, they set the stage for more insightful comparability.

While both the flight conditions and mass flow rates vary within large ranges across the examined trajectory, there are consistencies observed throughout. In particular, for both the water vapor injection calculations and flight data of the liquid water injection, there is an apparent limit to how much water can be applied in the stagnation region before the additional hydrogen ionization and atomic oxygen that is introduced becomes detrimental to the reduction of the plasma. Conversely, within the lower temperature conditions of the shoulder, an increase in injected water mass is correlated with a reduction in plasma. In these conditions, the addition of atomic hydrogen and oxygen do not ionize as quickly as they do in the high temperatures associated with the stagnation region. Further, the N + OH exchange reaction which reduces atomic nitrogen plays a relatively larger role within this regime, increasing the benefits of the additional water.

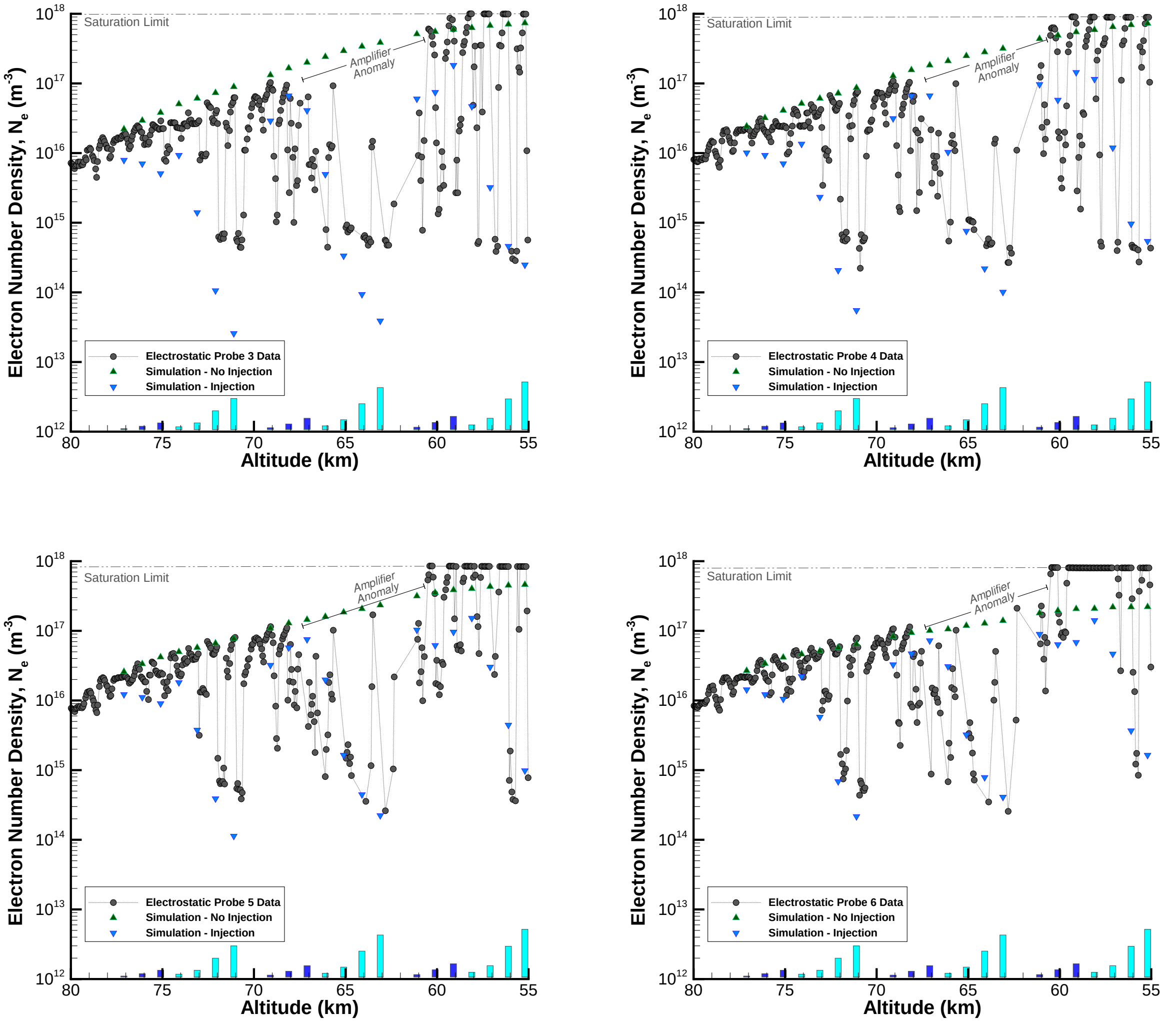

Figure 5.24: Comparison between the station 3 (top left), station 4 (top right), station 5 (bottom left) and station 6 (bottom right) of the electrostatic probe rake and the electron densities calculated with the corresponding water vapor injections. The injection profile, seen in more detail in Figure 5.3, is overlaid on the bottom of each plot for reference.

While the comparisons between the water vapor simulations and the RAM-C I flight data are useful in understanding the particular mechanisms related to the water vapor, they are limited to the near wall region where the probes are situated. However, due to the water film by the wall, the location of the maximum electron density generally shifts outwards for the water vapor simulations. Thus, it is also important to quantify the overall reduction in the maximum plasma frequency for a better assessment of how the water vapor injection technique operates as a blackout mitigation scheme. Figure 5.25 shows the ratio of the cutoff frequency between the water vapor injected flowfield and the baseline, clean air flowfield at the location of the electrostatic probe. It is readily apparent that even for the side injection there too is a diminishing return with the use of higher water mass flow rates. In other words, during side injection the plasma frequency reduction approaches an asymptotic limit with regards to an increasing flow rate that is associated with the flowfield conditions. For example, during the cycle 5 side injections, increasing the water vapor flow rate from 295 g/s to 458 g/s only results in a 5% decrease in the plasma reduction ratio [321].

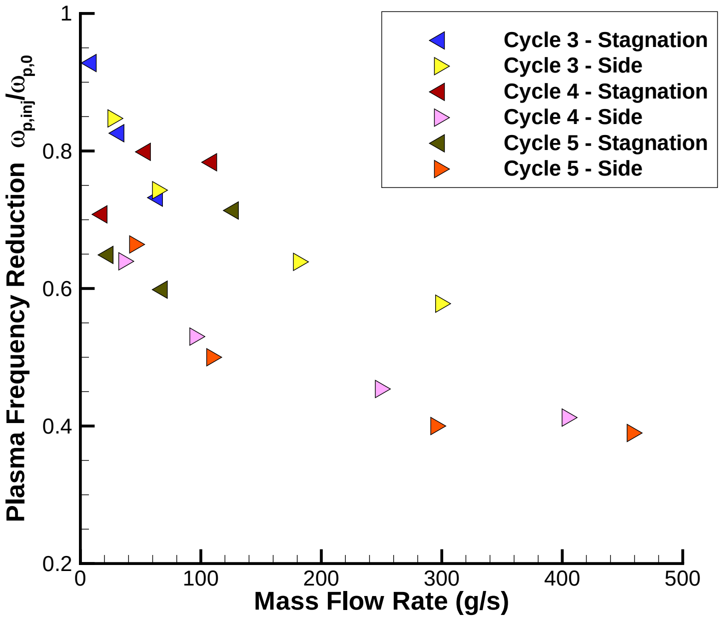

Figure 5.25: Ratio of the maximum plasma frequency of the flowfield with water vapor injection to that of the clean air conditions at the electrostatic probe location (x = 1.2 m) for each simulated flow rate.

5.3 Applicability to Glide Vehicles

For the RAM-C I vehicle, the largest injected mass flow rate of 458 g/s decreased an X-band cut-off frequency by 84%. While an admirable reduction, for the particular vehicle and trajectory configuration this injection rate still prevents GPS frequency reception. However, a similar reduction for a slender conical glide vehicle, such as that examined in Chapter 4, could result in a worthwhile mitigation scheme. The maximum plasma frequency for such a geometry configuration corresponded to 1.93 GHz. Thus, even if only a fraction of the same reduction factor is obtainable, the water vapor injection scheme can be successful for a slender vehicle.

It was also shown during the RAM-C I injection calculations that high temperature flowfield conditions (10,000+ K) do not particularly equate well with good plasma reduction characteristics for high water flow rates. Therefore, the relatively lower flowfield temperatures of the slender vehicle further present an environment with which this mitigation scheme can succeed.

While the flowfield conditions of the slender vehicle are seemingly favorable for such a mitigation scheme, the mass and volume constraints are in turn more limiting. For instance, the volume of the truncated conical after-shoulder region decreases by 43% from the RAM-C geometry to the slender glide geometry using equivalent lengths. While minimizing weight is of utmost importance for any re-entry spacecraft, a glide vehicle must also maintain strict weight constraints as to optimize the downrange distance.

As Figure 5.26 shows, the allowable mass of the entire injection system, including the storage tank, pipes, valves, and nozzles, has a vital role in the total time with which injection can be feasibly performed. For instance, an allowable injection mass of 100 kg with a required water flow rate of 100 g/s is suitable for over 8 minutes of use for this blackout mitigation scheme. However, if the onboard weight constraints permit only 25 kg, the total injection time decreases more than 6 minutes, which may be too long of a blackout period. In Figure

5.26, the total system mass has been assumed to be double the mass of the stored water, in accordance with previous studies of Dix et al. [124]. Other system-to-injectant mass ratios have been proposed, such as Good and Rossi, who assumed a 6 to 1 ratio for a SF_6 gas injection system [126]. However, both of these studies occurred over half a century ago and modern additive manufacturing techniques have significantly improved the functionality of a unit mass. For instance, Caldelas has recently employed direct metal laser sintering on Inconel superalloys to accomplish a 26-gram nozzle system capable of injecting SF_6 at 20 g/s [322]. Nevertheless, as a relative upper-bound for water vapor injection, the current study employs the ratio suggested by Dix et al. and conveyed within Figure 5.26.

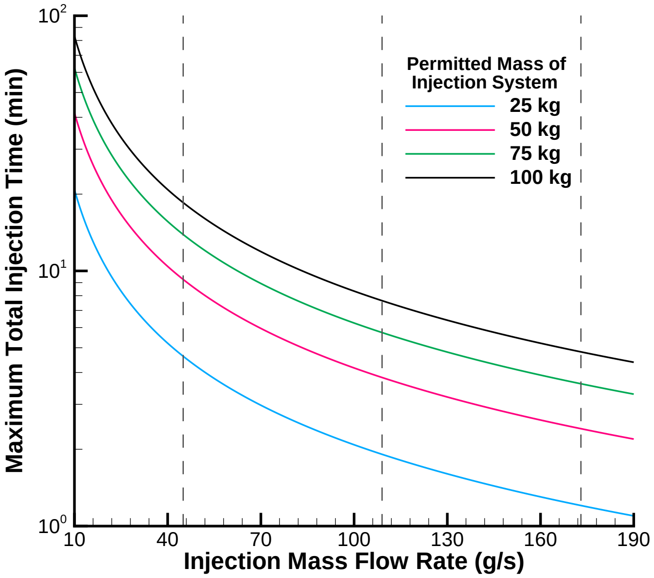

Figure 5.26: The maximum allowable injection time based upon the permitted onboard total system mass. A system-to-water weight ratio of 2.0 is used.

A water vapor injection system also adds additional design considerations which are briefly discussed henceforth. The injection system that is considered throughout this chapter is asymmetric. While several axisymmetric nozzle configurations exist, such as a plug nozzle used in advanced rocket designs, the simplest design for such a system is analogous to that employed for the high mass flow rates of RAM-C I. Specifically, the 81 pairs of orifices utilized from the side injections corresponding with valve 4 could be patterned in a toroidal configuration around the shoulder of the vehicle instead of concentrated at two diametrically opposed locations.

Thus, in such a nozzle layout, the injection energy comes in the form of a pressure difference of the stored water. Therefore, the main power considerations are associated with the valves and the heating of the water vapor. A typical solenoid valve that is appropriate for the estimated maximum pressure differential (2 psia was used in the RAM-C I systems) will draw approximately 12 W of power at 12 V DC [323]. The larger power draw would be to maintain or create the gaseous state of the water. While water vapor can be pressurized during ground procedures, it is more practical and robust if the water is stored in the liquid phase and pressurized through a bladder-feeder gas interface. For such a system, the water would be vaporized in the feed tubes right before injection. With the efficiency of pipe heater cables, η_{ph}, the required power to properly heat the water, $\mathrm{P_w}$, could be expressed as

$$P_w = \frac{C_{p,w}\dot{m}_w\Delta T}{\eta_{ph}} \tag{5.4}$$

where $\mathrm{C_{p,w}}$ is the specific heat of the water, $\dot{\mathrm{m}}_\mathrm{w}$ is the mass flow rate ΔT is the change in temperature between the stored water and the boiling point within the pipe. Note, special considerations are necessitated to the piping material as to alleviate cavitation concerns.

5.3.1 Numerical Setup

The 4 cm radius, 12-degree half-angle conical geometry selected in Chapter 4 is used to assess the feasibility of water vapor injection on slender glide vehicle bodies. The highest generating trajectory point is examined, with a velocity of 7.0 km/s at an altitude of 56.9 km. The MSISE-00 atmospheric model is one again utilized to obtain the freestream conditions.

Since water vapor injection was investigated at similar freestream conditions for the RAM-C I geometry, the corresponding flow rates are used for comparison on the glide vehicle.

Specifically, flow rates of 45 g/s and 109 g/s are employed, along with a third, 173 g/s, flow rate. From the RAM-C I calculations and flight data it is shown that injection from the shoulder of the vehicle body is more effective in reducing electron densities than injection from the stagnation point area. Further, as it was observed that the benefits of the water vapor injection take some downstream axial distance to develop, two locations are used in this study as the injection sites: x = 0.7 m and x = 1.5 m. Note, from Chapter 4, that the hypothetical location of the antenna is at x = 2.0 m.

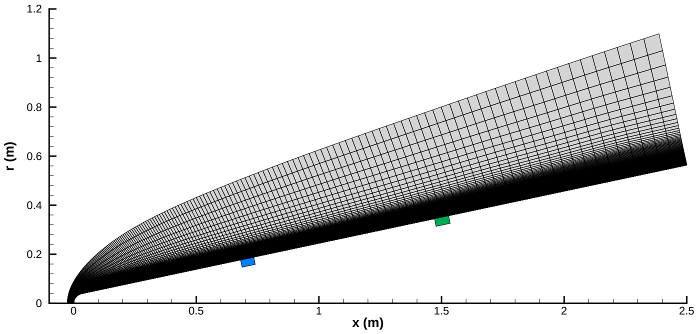

Figure 5.27: Computational grid used for assessing water vapor injection on a slender body.

The structured computational meshes that are employed in this study consist of a 300 x 225 quadrilateral-element grid. Analogous to the methodology used for the RAM-C I vehicle, the grids, shown in Figure 5.27, are tailored to the shock and contain a large concentration of elements around, and downstream of, the injection sites. Mesh convergence is once again verified by using the largest injection rate and doubling the number of grid elements in both axial and radial directions. The maximum electron number density at the selected location of the antenna remained within a 7% difference for both of the sized meshes.

The mass fraction of the injected material is a fully-distilled water vapor with no impurities. A 1500 K isothermal wall is chosen based on an average of the post-shoulder wall temperatures calculated with the radiative equilibrium wall conditions. Subsequently, the temperature of the injected water is also assumed to be 1500 K. The no-slip condition is prescribed at the wall for the flow velocity. The wall is assumed to be non-catalytic for neutral species, while also employing a catalytic condition which enforces electron-ion recombination.

5.3.2 Results

The maximum electron number densities evaluated along lines emanating radially outward from the wall are plotted along the axial distance for the six different injection cases in Figure 5.28. It is immediately apparent from these plots that, just as for the RAM-C I simulations, an increase in water vapor flow rate leads to a decrease in electron densities. However, the diminishing returns are also once again observed. For instance, increasing the lowest injection flow rate at the x = 0.7 m location by 64 g/s results in an additional 39% decrease in electron density at the antenna location. Another 64 g/s increase in the flow rate only amounts to an additional 13% decrease.

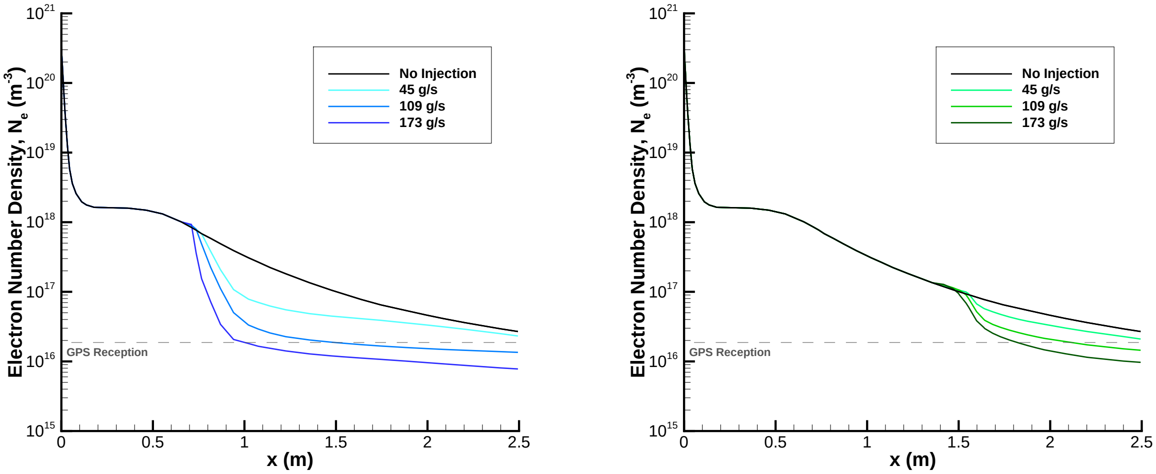

Figure 5.28: Maximum electron number densities normal to the surface of the slender conical body with injection at x = 0.7 m (left) and x = 1.5 m (right).

It is also evident from Figure 5.28 that there is an initial increase in the electron density in the area by the injection site before an abrupt decrease. This is also shown in the electron number density contours of Figure 5.29. After the initial sharp decrease, the maximum electron density changes steadily and approaches that of the baseline, no injection flow. Both of these tendencies are also observed in the recent numerical analysis of a thin air film mitigation method [317].

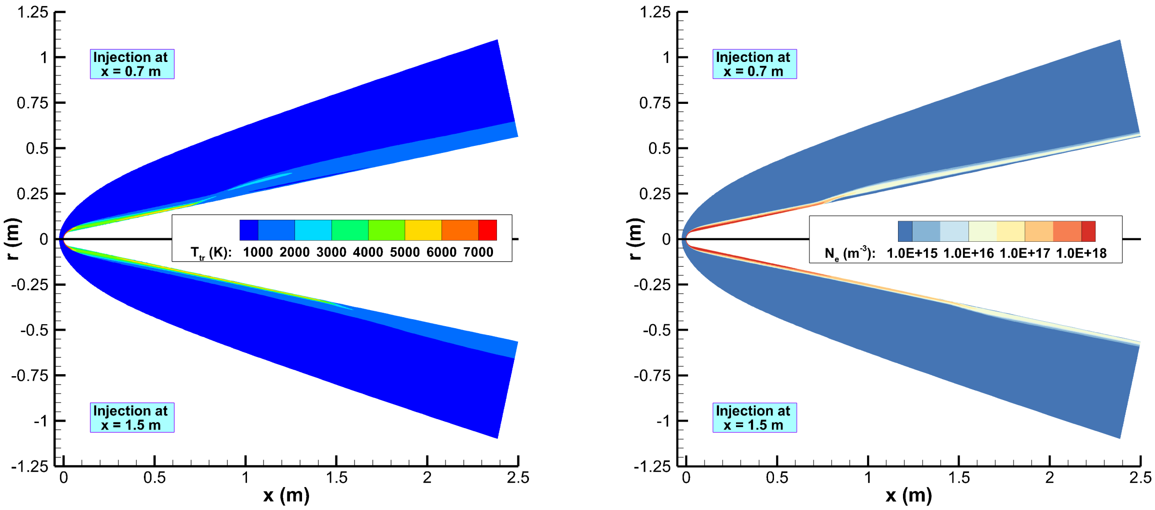

Figure 5.29: Translational-rotational temperature (left) and electron number density (right) contours of the slender conical vehicle with 109 g/s water injection.

It is also shown in Figure 5.28 that the injection of water at the further upstream location results in a larger electron density reduction at the antenna location. It has been repeatedly conveyed in this study that the performance of the water vapor injection technique is very variable and dependent on the freestream conditions. Indeed, as Figure 5.29 displays, there is a 26% decrease in the translational temperature when traversing between the two injection sites. These milder conditions, along with the proximity of the antenna to the further downstream injection site, result in the differences of the two locations when the same mass flow rates and injection areas are used. Comparisons with the RAM-C I simulations further confirm this premise. At a location of 1.1 m away from the side injection site of the RAM-C I vehicle, the 45 g/s water vapor flow rate leads to a 0.2 reduction factor in plasma density, whereas the 109 g/s flow rate results in a 0.06 reduction. Conversely, at 1.1 m away from the 0.7 m injection site of the slender vehicle, the 45 g/s and 109 g/s flow rates only result in 0.6 and 0.2 reduction factors in the plasma density, respectively.

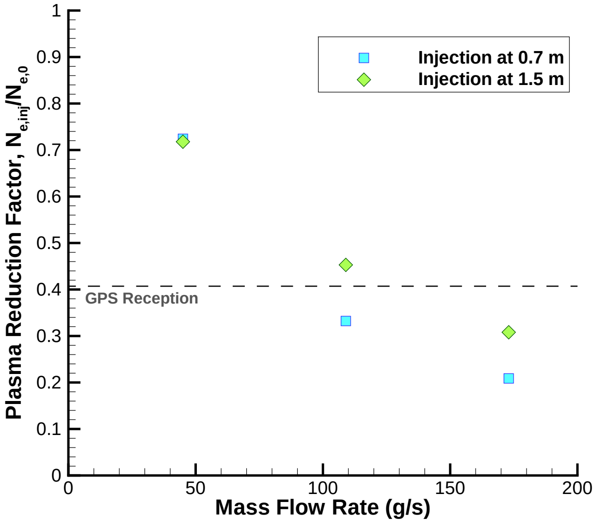

Figure 5.30: Reduction of electron number density due to water vapor injection from the glide body.

It is shown from Figure 5.30 that a desirable reduction in plasma density to achieve GPS reception is viable with the 109 g/s flow rate from the x = 0.7 m injection site and the 173 g/s flow rate for both sites. While the 173 g/s flow rate injections provide greater confidence in operational success, they also significantly decrease the maximum total injection time, shown in Figure 5.26. In fact, the use of the 173 g/s flow rate with a permitted total injection system mass of 100 kg, only allows for 4.8 minutes of usage. Conversely, the 109 g/s flow rate increases the blackout mitigation system usage to a more attractive 7.6 minutes. If the permitted mass decreases, the time disparity increases and becomes even more crucial. Thus, of the investigated locations and flow rates, the 109 g/s water vapor flow rate at the 0.7 m radial distance location is the most practical.

It should also be noted that the water vapor injection instills a significant decrease in the convective heating around the antenna. For instance, with the 109 g/s injection at the further upstream location, the convective heating at the wall of the antenna decreases from 254 kW/m^2 to 32 kW/m^2. Thus, this mitigation technique also presents a more feasible opportunity for the use of a protruding remote antenna assembly [101].

5.4 Chapter Conclusions

The efficacy and role of water vapor injection with respect to the reduction of the free electrons was investigated in the context of a hypersonic flowfield. The flight trajectory and injection conditions in terms of mass flow rates of the RAM-C I flight was used to both provide insight into the water vapor mitigation scheme and provide a platform for comparisons with the flown liquid water injection technique. It was qualitatively shown that the role of the water in liquid droplet form generally increased at the stagnation point location and at lower altitudes. It was also universally observed during this assessment that regardless of the flow rate and location, the electron density depleted at a faster rate when in presence of injected water vapor.

However, it was also discovered that the flowfield conditions with which the water vapor injection occurs play a significant role in the efficacy of the system. During the stagnation point injections, where the flow temperature is at its highest, an increase of the mass flow rate was not linearly correlated to a higher plasma reduction. A higher mass flow rate resulted in an increase to the shock stand-off distance and made the vehicle shape appear more slender, which in turn lowered the production of electrons in the stagnation region. However, an increased amount of water vapor in the flow was found to lead to a detrimental addition of atomic oxygen and hydrogen ions.

During water vapor injection from the forebody within lower temperature conditions, an increase in injected water mass was found to be correlated with a reduction in the electron density. Within these conditions, it was found that the additional atomic hydrogen and oxygen were not as easily ionizable. It was also observed by chemically freezing the water vapor that the reactions and species associated with the breakup of water have a beneficial effect on the free electron depletion. The addition of water vapor reduced the atomic nitrogen, primarily through the N + OH exchange reaction, which acted as an ionization suppressant. Thus, it was found that even for water vapor injection from a location in the forebody, there eventually is still a diminishing return from an increased flow rate.

Thus, it was found that there is a tight interplay occurring between the specific chemistry introduced by the water and the effects of the injection on the flow temperature and electron density. Nevertheless, the water vapor scheme was applied and assessed for a slender vehicle shape, which did not necessarily require a significant reduction in the plasma density due to its weaker ionized conditions. It was found that although the reduction in plasma was indeed less in these conditions, it led to a desirable decrease to enable GPS frequency reception. It was also demonstrated that the location along the axial distance away from the antenna plays a key role, as it takes distance for the water vapor to have optimal reduction results. While it was found that water vapor injection provided a feasible means of blackout mitigation for glide vehicles, there are key limitations to its practical use. The most important of these are weight reduction to prolong the maximum injection time, and the aforementioned interplay. As a mitigation technique the scheme would have to be catered to the exact flight conditions, making it not a particularly straightforward method to implement.

CHAPTER 6

FEASIBILITY OF PLASMA REDUCTION ON GLIDE VEHICLES THROUGH MHD SCHEMES

The primary cause of communications blackout is from the motion of the electrons reacting to the transmitted radio frequency wave. Thus, a reasonable methodology to overcome blackout is to either constrain the electrons so that they are unresponsive to the driving force of the propagating wave or move them away from the antenna region altogether.

By orienting magnetic field lines such that the motion of the electrons is constrained through gyration, the dispersion relation in Eq. 1.20 becomes altered where a wave below the plasma frequency can propagate. The magnetic field limits the transverse motion of the electrons, and for an infinitely strong magnetic field, no interaction would take place between the transverse wave and electrons. Additionally, when a wave confronts a plasma layer in the presence of a magnetic field, two circularly polarized waves are created from the circular motion of the electrons. It has been investigated in both numerical and laboratory settings that when the magnetic field strength is strong enough so that the plasma frequency is less than the corresponding electron cyclotron frequency, a right-handed circularly polarized, Whistler wave can propagate [12, 82, 324–327].

Instead of immobilizing the electrons, a second electromagnetic approach focuses on physically expelling electrons away from the area surrounding an antenna. Employing one of these two approaches is in turn the aim of any electromagnetic manipulation technique. The work within the current chapter focuses on the latter of these two approaches.

6.1 Plasma Manipulation via MHD

The coupling between electromagnetic and aerothermodynamic flow properties has been known for some time to alter the flow field surrounding the vehicle, and in turn open up numerous possibilities for enhanced performance [328]. Over seventy years have passed, and several thousand man-years have been spent understanding the development of these MHD systems [329] and have in turn resulted in applications spanning various fields of power generation, heat load mitigation, propulsion, flow control, drag reduction, ground testing, and communications blackout mitigation [329, 330].

Early MHD studies were limited by the available computing power, hypersonic test facilities, and flight-ready magnets [331]. Specifically, permanent magnets within the constraints of a hypersonic vehicle are limited to around 0.15 T and are hampered by the Curie temperature [128, 133]. A superconducting electromagnet would weigh over 500 kg and be difficult to implement [134]. With current improvements in flight-weight magnet technology however, there is a resurgence in applying MHD techniques to hypersonic vehicles. Specifically, projected advancements in carbon nanotube composites can lead to strong magnets weighing less than 50 kg [135]. Further advancements to high-temperature superconducting magnets can drop the expected mass even further, to around 10 kg [136, 137, 324].

Of particular interest to this study are the MHD-focused techniques related to mitigating communications blackout. It has been shown that using a time varying, or traveling magnetic field (TMF), can reduce the required magnetic field by creating a Hall electric field that depletes the surrounding plasma density [138, 139]. A magnet has been proposed to be removed altogether, in a static or time-varying pulsed electric field which can also result in a depleted electron density [81, 96]. The hybrid use of applied fields has also shown promise. This technique utilizes crossed electric and magnetic fields to collect both electrons and ions and accelerate the charged particles past the antenna, lowering the adjacent electron number density. This $\mathbf{E} \times \mathbf{B}$ drift technique has been demonstrated for use in blackout mitigation through both computer modeling and experiments employing a helicon plasma [78, 81, 140, 141].

In its simplest form, a static magnetic field can also solely be used to reduce the electron density. Kim showed the sole use of a magnetic field still generates a current density in the absence of an electric field, giving rise to a Lorentz force that accelerates particles away from the antenna area [81]. Specifically, it was observed that for the OREX capsule a 0.5 T magnet results in a plasma reduction factor of 0.3, a desirable result for the slender glide vehicle shapes investigated in Chapter 4.

However, it was shown in some of the earliest analytical MHD studies carried out by Bush that the performance of an MHD technique is highly dependent on the magnetic interaction parameter, a ratio of the Lorentz or magnetic body forces to the inertial forces [332]. The magnetic interaction parameter, or Stuart number, can be expressed as [333]:

$$\mathrm{S}_{\mathrm{MIP}} = \frac{\sigma B^2 L_c}{\rho u} \tag{6.1}$$

where σ is the electrical conductivity, B is the magnetic field strength, and $\mathrm{L_c}$ is the characteristic length. It has been shown that a Stuart number of about 0.1 is at a bare minimum necessary to have any influence on the flowfield [328, 332, 334]. The Stuart number is plotted in Figure 6.1 for flight relevant conditions, where the characteristics length is taken to be that of a standard L-band aperture size plus room for the assumed 30-degree maximum deviation of the incident to the boresight angle. It is immediately apparent from Figure 6.1, that a low electrical conductivity can be the downfall of any MHD technique. Indeed, previous studies conducted in very weakly ionized air conditions have shown little influence from an MHD scheme in terms of electron number density reduction [202, 330]. As the Stuart number is proportional to the square of the magnetic field strength, a low conductivity environment can generally be compensated by a larger magnetic field. Of course, this has physical limitations as a substantially heavy magnet will likely not be flight-weighted for quite some time.

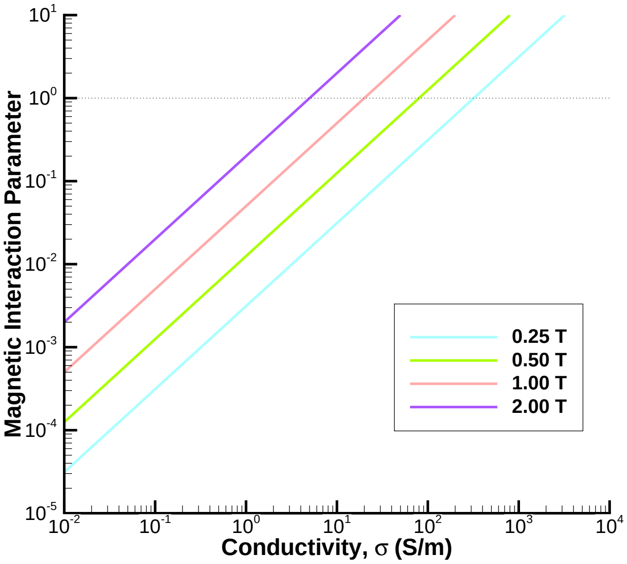

Figure 6.1: Stuart number (or magnetic interaction parameter) for a flow with properties of : $\rho = 5 \times 10^{-4}$ kg/m^3, u = 4000 m/s, L_c = 10 cm, and a varying magnetic field strength.

Thus, the current study examines steady-state MHD techniques related to blackout mitigation by modeling a simple dipole magnet configuration. An assessment is made of the feasibility of success when the MHD scheme is applied to the weakly ionized flows associated with hypersonic glide vehicles.

6.2 Numerical Setup

To properly simulate the effects of the magnetic field on the hypersonic flow field, the Navier-Stokes equations are modified with the inclusion of an MHD source term, as described in Section 2.3 and expressed in Eqs. 2.42. As a review, the magnetic field in Eq. 2.52 is prescribed as an input, while the electrical conductivity tensor and velocity vector are acquired from the flow solver. Once the electrical potential is found, the electric field and current density are subsequently calculated with Eq. 2.51 and Eq. 2.49, respectively. The outputs of the MHD module, namely **B**, **E**, and **j**, are then used to update the MHD source terms in Eqs. 2.42 within each time step of the fluid solver.

In the generalized Ohm's law, Eq. 2.48, the electrical conductivity tensor concisely includes the effects of both the ion slip and Hall effect phenomena. The Hall effect is the curved nonlinear motion of electrons between collisions that is produced by the Lorentz force emerging from a perpendicular magnetic field. It has been shown that the inclusion of the Hall effect does not have any detrimental effect on the efficacy of an MHD flow control technique in flow conditions similar to the ones examined herein [81, 330]. Further, at low electrical conductivity conditions the maximum electron Hall parameter, a product of the electron cyclotron frequency and mean collision free time, has been shown to be on the order of 0.1 [330, 335]. The ion slip is the resulting velocity difference between positively charged and neutral particles due to a nontrivial portion of the current being carried by the ions. As the ion slip parameter is also a function of the Hall parameter, and the species ionization fraction is also likely to be low, the effects of ion slip can be neglected. Thus the electrical conductivity tensor is simplified into a scalar (multiplied by the identity matrix) and the Poisson equation reduces accordingly to yield [330, 336]:

$$\nabla \cdot (\sigma \nabla \phi) = \nabla \cdot [\sigma (\mathbf{u} \times \mathbf{B})] \tag{6.2}$$

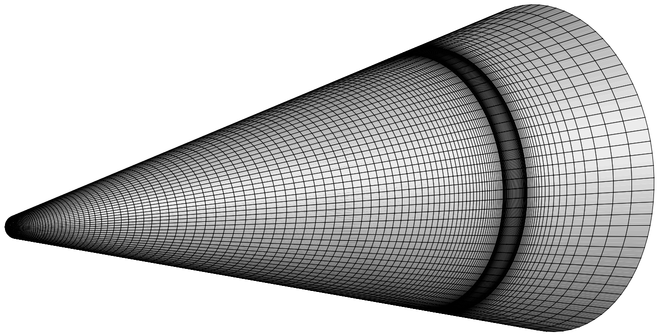

Figure 6.2: Three-dimensional surface mesh of the conic glide vehicle used in the applied magnetic field simulations.

The flight conditions are those which were selected in Chapter 4, specifically a flight velocity of 7.0 km/s at an altitude of 56.9 km. Once again, the MSISE-00 atmospheric model is employed to attain the freestream conditions. A 1500 K isothermal wall which enforces electron-ion recombination is used. To allow for non-axisymmetric magnetic field configurations, a three-dimensional computational mesh is utilized. The grid, composed of 1.3 million quadrilateral cells and displayed in Figure 6.2, includes a large concentration of elements radially about the location of the dipole magnet. Baseline simulations are consistent with the grid-converged axisymmetric results of Chapter 4. As it will be discussed shortly within this chapter, the inclusion of an applied magnetic field does not show any appreciable differences, thus nullifying the need for further mesh convergence studies.

6.2.1 Applied Magnetic Field

The applied magnetic field utilized in this study is an ideal dipole with its magnetic moment oriented with the y-axis. The configuration of the magnetic flux density is described by the equation of a dipole field in Cartesian coordinates as [196, 200, 330, 337, 338]:

$$\boldsymbol{B} = \frac{B_{max}}{(\hat{x}^2 + \hat{y}^2 + \hat{z}^2)^{5/2}} \begin{bmatrix} 3\hat{x}\hat{y} \\ 3\hat{y}^2 - (\hat{x}^2 + \hat{z}^2) \\ 3\hat{y}\hat{z} \end{bmatrix} \tag{6.3}$$

where B_{max} is the peak magnetic field strength, and $\hat{x}$, $\hat{y}$, and $\hat{z}$ are adjusted to center the dipole magnet at x = 2.0 m, y = 0.35 m, and z = 0 m, a location that is directly underneath the antenna. The configuration of the applied magnetic field, shown by the magnitude of the magnetic field normalized by the peak field strength, is displayed in Figure 6.3. The contours of the normalized magnetic field that are less than 0.05 begin at an approximately 20 cm radius around the peak and are removed from the figure.

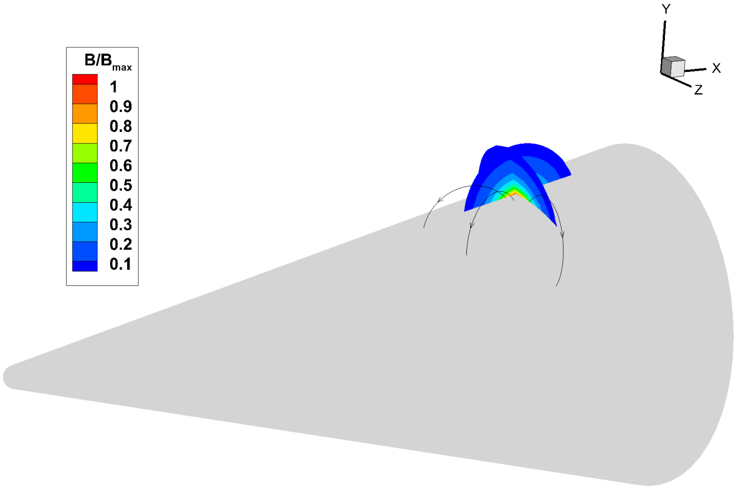

Figure 6.3: Contours of the normalized magnetic field and corresponding vector lines of an ideal dipole oriented about the y-axis and centered at x = 2.0 m, y = 0.35 m, and z = 0 m.

6.2.2 Conductivity Model

It has been made apparent from discussion on the magnetic interaction parameter that the success of an MHD system heavily relies on the capability of a gas to conduct electricity [330]. Specifically, the current density, which dictates the magnitudes of both the Lorentz force and Joule heating source terms, is related to the electrical conductivity by Eq. 2.48.

Physically, the electrical conductivity of a gas relies on the drift of charged particles. At room temperature conditions, air is not considered conducting as it is very weakly ionized. However, after considerable heating and subsequent ionization occurs after the air passes through a shock wave of a hypersonic vehicle, free electrons are released which in turn give rise to a conducting air medium [330]. An increase in electrical conductivity is accomplished by an increasing number of charged particles and a decreasing number of collisions with particles that can obstruct the drifting motions [339]. Thus, the electrical conductivity of the air relies on the thermodynamic conditions, chemical makeup, and electrical transport properties [340].

The sensitivity of predicting the success of an MHD system from an accurate conductivity model has been well-established ever since some of the pioneering studies in this domain [339, 341]. Rosa showed that the electrical conductivity of an ionized gas could be expressed as [342]:

$$\sigma = \frac{n_e e^2}{m_e \nu_m} \tag{6.4}$$

where ν_m is the electron momentum transfer collision frequency. By using expressions for mean electron velocity, $\mathrm{c_e}$, and collision cross section for electrons and ions, $\mathrm{Q_{ei}}$, suggested by Rosa (since $\nu_\mathrm{m} = \mathrm{c_e Q_{ei}}$), and by making certain simplifying conjectures, such as neglecting electron-electron collisions and assuming that ionization occurs primarily from a single ion, Sutton and Sherman presented an expression for the electrical conductivity, that was plotted and is reproduced in Figure 6.4 for 1 torr [208]. Eq. 6.4 can also be solved, without making these limiting assumptions, directly with Boltzmann's equation. However, in conditions where a Maxwellian distribution cannot be assumed, the Boltzmann equation must be solved through computationally rigorous means, which is generally prohibitive in CFD simulations. As such, several semi-analytical models have been widely utilized that are appropriate for the regimes they were designed for.

Two limiting cases for the degree of ionization in air have been used to craft semi-analytical models. When the degree of ionization is low, so that charged particles primarily collide with neutral particles [339], it can be assumed that there is coupling between the charge and mass diffusion terms as to simplify the electron energy distribution term dictated by the Boltzmann equation [157]. The result is an expression for electrical conductivity that is proportional to $\alpha \mathrm{T}^{-1/2}$ [339], as derived by Chapman and Cowling [343]:

$$\sigma = 3.34 \times 10^{-10} \frac{\alpha}{Q\sqrt{T}} \qquad [S/m] \tag{6.5}$$

where Q is the collision cross section of the gas and is assumed to be 5×10^{-19} m^2, set from employing the hard sphere model [149, 200]. It should be noted that the expression in Eq. 6.5 is somewhat misleading as the α term is strongly dependent on the temperature.

On the other hand, if the collisions between charged particles are frequent, due to a degree of ionization approaching unity, the conductivity becomes independent of α and is proportional to $\mathrm{T}^{3/2}$ [339]. Spitzer and Härm used this assumption, along with neglecting electron-electron interactions and movement of the ions [157], to derive an expression for electrical conductivity [344]:

$$\sigma = \frac{1.56 \times 10^{-2} T^{3/2}}{\ln\left(1.23 \times 10^{4} T^{3/2} n_e^{-1/2}\right)} \qquad [S/m] \tag{6.6}$$

which is also a function of electron number density. While the above expressions for electrical conductivity depend on the amount of free electrons in some capacity, it has been shown that the conductivity is highly dependent on the temperature [208]. Consequently, two additional expressions relate electrical conductivity solely as a function of the temperature of the flow. In early MHD studies, Bush introduced an expression for electrical conductivity through similarity solutions [201]:

$$\sigma = \sigma_0 \left(\frac{T}{T_0}\right)^4 \tag{6.7}$$

where σ_0 and T_0 are reference values, taken to be 5100 S/m and 12000 K, in accordance with Refs. [157,340]. Though the exponent of 4 is used in the current work, others have used 2 instead, recently by Kim in his assessment of the $\mathbf{E} \times \mathbf{B}$ blackout mitigation scheme [81]. Raizer also used the known primary temperature dependence of the electrical conductivity in deriving a suitable expression. By assuming that the drift of electrons is primarily caused by interactions with heavy particles, along with a thermal equilibrium state, Raizer derived an expression to yield [345]:

$$\sigma = 8300 \exp\left(\frac{-36000}{T}\right) \qquad [S/m] \tag{6.8}$$

The electrical conductivity of air at 1 torr is plotted for temperatures of interest using the discussed conductivity models in Figure 6.4. The composition of the air is attained by assuming a local thermodynamic equilibrium state with the model introduced by Godin and Trépanier [346], in accordance with the work of Ref. [157]. Also shown in Figure 6.4, is the electrical conductivity observed from shock tube experiments conducted at 1 torr of incident air by Lamb and Lin [347] and Koritz and Keck [348]. In the former experiment, an axisymmetric magnetic field was introduced into post-shock air where the displacement created by the magnetic fields was measured by a nearby pickup coil [347]. The conductivity was then deducted from the known speed of the moving gas and the strength of the magnetic field, using the interaction technique suggested in Ref. [349]. A similar experiment was conducted, but instead employed a symmetrical bridge probe containing twin coils that became unbalanced and charged due to the oscillating magnetic field within the conducting post-shock air [348]. While both of these experiments were plotted against the Mach number, a post-shock temperature is calculated and employed by assuming equilibrium conditions.

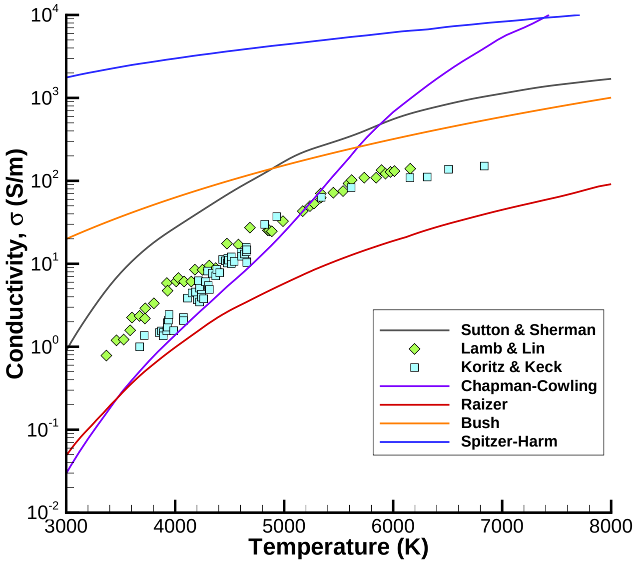

Figure 6.4: Electrical conductivity at 1 torr calculated from the conductivity models of Refs. [201, 208, 343–345] and observed through experiments in Refs. [347, 349].

It is shown in Figure 6.4 that the best agreement with the experimental results comes from the semi-empirical model of Chapman and Cowling, especially with the data attributed to Koritz and Keck at temperatures below 5500 K. The electrical conductivity calculated with

Bush's model, and especially with the Spitzer-Härm model, overpredict the experimental data, while an underprediction is shown with Raizer's model. It has also been shown during surrogate modeling efforts for solving the conductivity through the Boltzmann's equation by Bisek et al., that the Chapman-Cowling semi-empirical model showed the best agreement at both 10^{-3} and 1 atm conditions. It was postulated in these studies that this is likely attributed to its degree of ionization-dependent nature [157]. Accordingly, the Chapman-Cowling semi-empirical model is utilized throughout this current study.

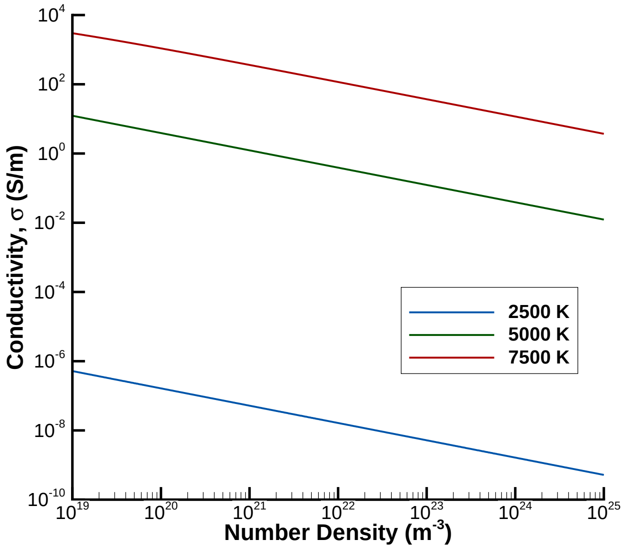

Figure 6.5: Electrical conductivity as a function of total number density for three different temperatures, calculated using the Chapman-Cowling semi-empirical model and the Saha equation.

It should be noted that unlike the entirely temperature dependent models of Bush or Raizer, the Chapman-Cowling conductivity model is indirectly related to the pressure and number density of the air by the degree of ionization term. Therefore, while Figure 6.4 shows that the electrical conductivity calculated by the Chapman-Cowling method ranges in agreement with the other models, with good agreement to that of Raizer displayed at around

3500 K and that of Bush at 5500 K, this compatibility can vary considerably at different air pressures. As was detailed in Section 1.1.2.2 with discussion on the Saha equation, the degree of ionization is strongly related to the total number density and temperature of the air. In turn, as Figure 6.5 shows, the electrical conductivity predicted by the Chapman-Cowling model can range several orders of magnitude depending on the associated total number density. Figure 6.5, which was plotted using the Saha equation to determine the degree of ionization, also shows the model's strong dependence on temperature.

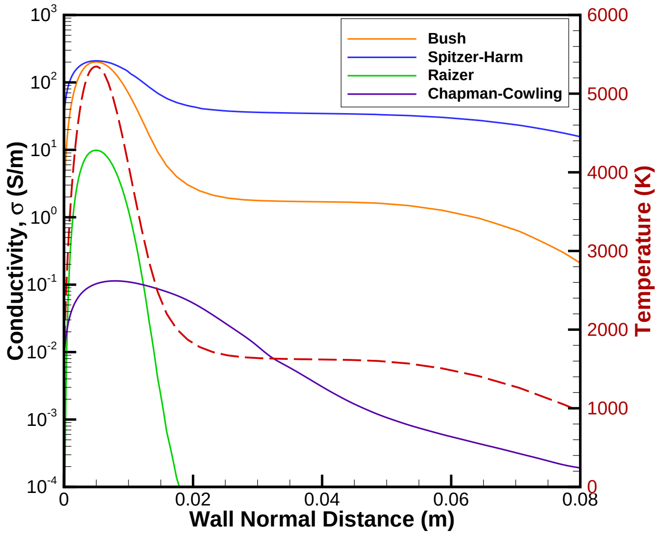

Figure 6.6: Electrical conductivity as calculated from various semi-empirical models along a wall normal line at 2.0 m in the axial direction for the glide body. The translational temperature is represented by a dashed red line.

Calculating the electrical conductivity of the flow around the glide vehicle without an applied magnetic field demonstrates the shifting agreements between the conductivity models further. Figure 6.6 shows the electrical conductivity along a radial line from the surface of the vehicle the suggested location of the antenna, x = 2.0 m. Note, the maximum translational temperature at this location is approximately 5300 K. For these flow conditions, it is shown that once again the Spitzer-Härm model predicts the highest conductivity. However, unlike the conditions examined in Figure 6.4, Bush's model demonstrates good agreement with that of Spitzer-Härm for the maximum electrical conductivity, with only a 3.9% difference between the two at the radial location of the maximum temperature. Conversely, Chapman-Cowling predicts an electrical conductivity three orders of magnitude less than that of Spitzer-Härm and Bush. The low degree of ionization surrounding the antenna is in turn responsible for this predicted low electrical conductivity level.

6.3 Results

A crucial property to consider when simulating the magneto-aerodynamic interaction is the strength of the applied magnetic field. In order to offset the low electrical conductivity predicted by the Chapman-Cowling semi-analytical model, a very strong, $B_{max} = 2.0$ T magnetic field is utilized in this study.

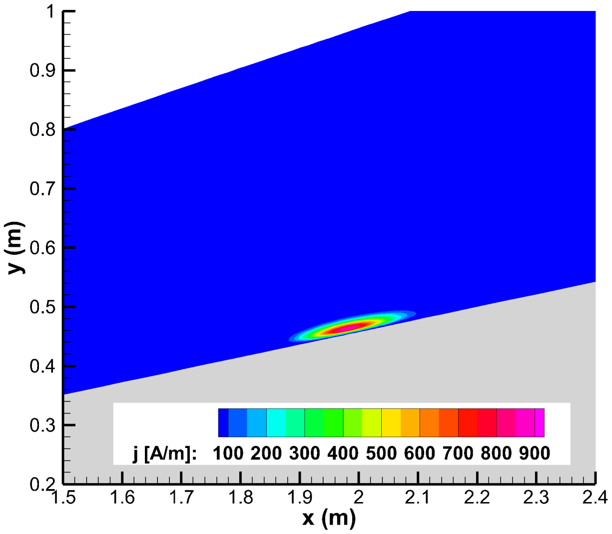

Figure 6.7: Contours of the current density magnitude for a flow with an applied 2.0 T magnetic field.

Figure 6.7 displays the current density contours for the flow region adjacent to the antenna and magnet. A maximum current density of 904 A/m is achieved, primarily owing to the exceptionally large magnet field strength. However, even with such a strong magnetic field, the difference to the flow is indiscernible. Indeed, as Figure 6.8 shows, there is no noticeable difference to the field structure and the corresponding translational temperature. There is a minuscule (less than 0.5%) increase in the temperature in the flow containing the applied magnetic field, attributed to the Joule heating source term, which is dependent on the current density and in turn the low electrical conductivity.

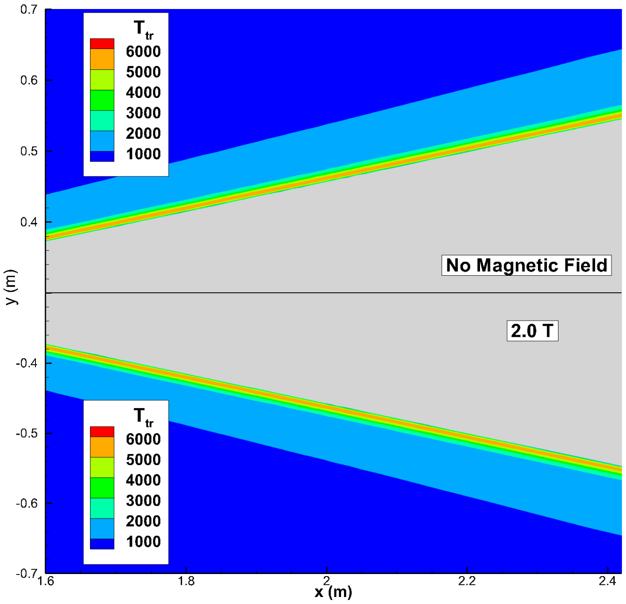

Figure 6.8: Translational temperature contours for the flowfield with no applied magnetic field (top) and with a 2.0 T max applied magnetic field (bottom).

Further, and more relevant to the objective of mitigating blackout, it is shown in Figure 6.9 that as a result of the low electrical conductivity, the change to the electron number density is also insignificant. This is in agreement with earlier discussions on the Stuart Number, which is a maximum of 10^{-2} for these flow conditions. Thus, the use of a static magnetic field is an unattractive option for blackout mitigation on hypersonic vehicles, where the low temperatures and resulting low degrees of ionization lead to low electrical conductivity levels.

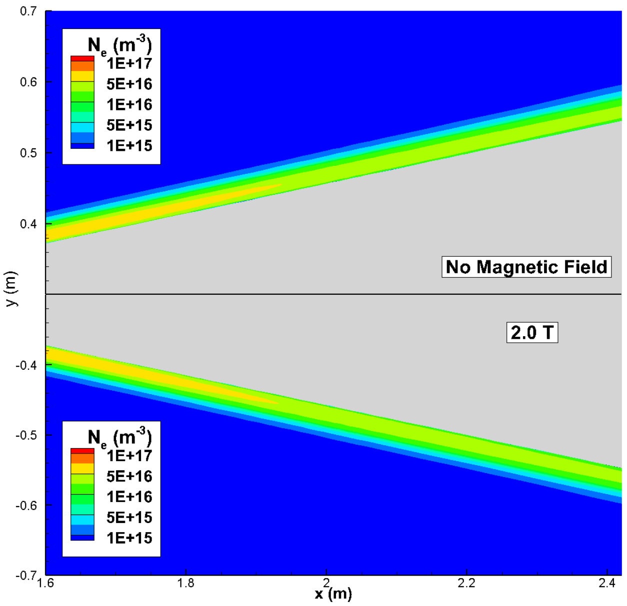

Figure 6.9: Electron density contours for the flowfield with no applied magnetic field (top) and with a 2.0 T max applied magnetic field (bottom).

From the results of this work, and in accordance with previous studies, low conductivity levels are postulated to be the downfall of any practical MHD-based blackout mitigation technique within the flow regimes associated with the afterbody of hypersonic glide vehicles. For instance, in a numerical analysis by Bisek et al. [330], a 0.5 T magnet was not enough to overcome the low conductivity of air, where $\sigma_{\text{max}} \approx 0.05$ S/m. While more advanced techniques such as an $\mathbf{E} \times \mathbf{B}$ layer have shown great promise in relatively stronger ionized flows, they too rely on adequate conductivity levels to generate a suitable Lorentz force that can accelerate the charged particles past the antenna. The work of Lemmer showed the operation of an $\mathbf{E} \times \mathbf{B}$ layer to be successful in an argon plasma produced by a helicon source where the electrical conductivity is estimated to be approximately 6 S/m.[1] However,

---

[1] The electrical conductivity of the argon is approximated using the lowest recorded electron temperature of 1.2 eV and experimental data within Ref. [349].

while an analogous $\mathbf{E} \times \mathbf{B}$ layer configuration was simulated to be successful for use in the post-shock region of an OREX geometry in Earth's atmosphere [81], it failed to sufficiently manipulate the plasma on the Mars Pathfinder due to an electrical conductivity that was 2-4 orders of magnitude less [202]. Paradoxically, methods that have been suggested to increase conductivity, such as flying at lower altitudes at the same velocity and seeding the flow with easily ionizable materials [330], would in turn further degrade the communication properties by increasing the electron number density.

6.4 Chapter Conclusions

This chapter examined the feasibility for the application of a Lorentz force to shift electrons away from the area surrounding the antenna and in turn restore communication links. Specifically, a slender glide vehicle was selected as the testing platform. A static magnetic field was applied to the flow and the effects were accounted for and solved by the addition of the MHD source terms. Although currently impractical in terms of weight considerations, a simple 2.0 T dipole magnet configuration located underneath the antenna was utilized to try and overcome the low magnetic interaction parameter that resulted from a low conductivity of the weakly ionized air.

While the Chapman-Cowling model for electrical conductivity is several orders-of-magnitude lower than other models such as Bush or Spitzer-Härm, it has shown good agreement with experimental data and with surrogate models of Boltzmann solutions. Thus, as experimental data is limited, it is unclear whether a different model is more appropriate. Although the slender vehicle did not require much reduction in terms of plasma density, the low plasma density ended up being the downfall for the applicability of this technique. It was found that the MHD scheme is insufficient towards mitigating blackout for slender glide bodies in conditions which resemble those which were studied. However, for different flight trajectories, blunter shapes, and further upstream locations of the magnet, which allow for a more conductive air medium, the potential usage of MHD schemes remains.

CHAPTER 7

CONCLUSION

The key results and conclusions of this dissertation are summarized, and the germane implications are discussed in this final chapter. The major original contributions to the community from the research herein are listed. Finally, the chapter ends with detailed recommendations of potential avenues for future work.

7.1 Summary of Dissertation

This dissertation presented a detailed analysis on the formation of plasma during hypersonic flight. The work built upon this analysis and examined two prospective blackout mitigation schemes, namely the use of water vapor injection and a static magnetic field to reduce the electron number density.

In Chapter 1 the fundamental aspects of radio wave communications blackout were presented, along with a historical perspective and discussion on the significance in finding a solution. This chapter also briefly discussed many potential avenues that have been examined for finding a successful mitigation technique and landed on two popular categories: material additives and electromagnetic manipulation.

Chapter 2 detailed the numerical methodologies that were utilized within this dissertation. The motivation for specifically employing a CFD approach was described and contextualized with ground experimentation and flight testing. The governing equations, constitutive relations, and implementation practices used to computationally investigate the flows of interest, particularly weakly ionized flows in thermochemical nonequilibrium that may include magnetohydrodynamic effects, were discussed in detail.

In Chapter 3, the accuracy and sensitivity of plasma generation predicted by several different chemical kinetics models was investigated in the context of weakly ionized hypersonic flowfields around the RAM-C vehicle. Thirteen independent trajectory points along the RAM-C II flight, and an assessment of the chemistry models was made by comparing results to available flight measurements. The limitations of making such comparisons with the raw flight data was established in detail, including the inherent shortcomings associated with interpolating the flight data to assess a single trajectory point. Two separate geometries were evaluated within this chapter, as the initial RAM-C geometry was altered during flight after its nose cap was pyrotechnically ejected. The blunter post-ejection geometry produced more electrons in the stagnation region. In general, good agreement was found between each chemistry model and flight data from both the electrostatic probe and reflectometer stations above 56 km. An expected sizable gap exists between the simulations and reflectometer data at lower altitudes. The impact of forward reaction rates, equilibrium constants, and number of species varied considerably based on altitude, velocity, and position along the body, based on the level of thermochemical nonequilibrium in the flow.

Chapter 4 detailed a major trade-off involved within hypersonic glide vehicle design, namely heat flux at the stagnation point against the ionization levels surrounding an antenna. The study in this chapter assessed these quantities of interest for different nose radii and half-angles of a generic glide body approximating more complex geometric designs. The flow conditions that dictated the freestream properties were chosen from an archetypal equilibrium glide flight path. Both the geometric and trajectory trade spaces were in agreement with values described in the literature and thus resemble realistic mission profiles. Thus, the conclusions derived from this analysis are applicable in a broad sense to potential hypersonic glide designs. It was found that an increased nose radius leads to more ionization throughout the flow and poorer communication characteristics. However, the increased nose radius was found to benefit in reducing heat flux. The flight conditions were also found to have a considerable effect on both the maximum heat flux and electron densities. This resulted in another trade-off that was discussed, specifically the downrange distance of the glide vehicle versus the ionization levels surrounding an antenna. After weighing the probable radio cut-off frequencies against the nose heating, a geometry was selected that was used as a platform for evaluating possible mitigation strategies.

In Chapter 5, the efficacy and role of water vapor injection with respect to the reduction of the free electrons was investigated in the context of a hypersonic flowfield. The flight trajectory and injection conditions in terms of mass flow rates of the RAM-C I flight were used to provide insight into the water vapor mitigation scheme and provide a platform for comparisons with the flown liquid water injection technique. It was also universally observed during this assessment that regardless of the flow rate and location, the electron density depleted at a faster rate when in presence of injected water vapor. It was also discovered that the flowfield conditions with which the water vapor injection occurs play a crucial role in the efficacy of the system. The water vapor scheme was applied and assessed for a slender vehicle shape, which did not require a significant reduction in the plasma density to allow for L-band reception due to its weaker ionized conditions. It was found that although the reduction in plasma was indeed less in these conditions, it led to a desirable decrease to enable GPS frequency reception. It was also demonstrated that the location along the axial distance away from the antenna plays a key role, as it takes distance for the water vapor to have optimal plasma reduction effects. Key limitations to the practical use of such a system were discussed.

Chapter 6 investigated the feasibility for the application of a Lorentz force to shift electrons away from the area surrounding the antenna and in turn restore communication links was examined for a slender glide vehicle. A 2.0 T static magnetic field was applied to the flow to try and overcome the low magnetic interaction parameter that resulted from a low conductivity of the weakly ionized air as predicted by the Chapman-Cowling model.

Although the slender vehicle did not require much reduction in terms of plasma density to enable GPS communication linkage, this low plasma density ended up being the downfall for the applicability of this technique. It was accordingly found that the MHD scheme is insufficient towards mitigating blackout for slender glide bodies in conditions which resemble those which were studied.

7.2 Novel Research Contributions

The key objective of the research detailed within this dissertation was to use numerical tools to evaluate the formation of plasma and assess a couple of blackout mitigation techniques, with added emphasis on the context of hypersonic glide vehicles. The distinct research contributions that are attributed to this work are summarized as follows:

- **Validated and compared trajectory simulations with RAM-C flight data:** Although individual trajectory points of the RAM-C II flight have been utilized in the literature as validation platforms for modeling weakly ionized hypersonic flows, there are key limitations pertaining to the interpolation of both flight plasma diagnostic tools. Thus, this study used a significant portion of the entire flight trajectory to compare with the flight data directly, which in turn improved the quality and confidence of the validation effort. Such comparisons between the available RAM-C flight data within this capacity and high-fidelity computational modeling were unique and thus reinvigorate a platform for validating flowfields containing plasma, a currently limited resource within the literature.

- **Evaluated the role of hypersonic thermochemistry modeling within the scope of plasma formation:** The sensitivities associated with the chemical kinetics models when predicting the formation of free electrons were investigated by using various forward reaction rate sets, equilibrium constants, and number of species. The role of the selected transport mixing rule was also assessed in terms of its impact on the electron density in the flow. General recommendations were suggested when modeling weakly ionized flows, specifically for utilizing the full 11-species air chemistry set and Gupta's mixing rule.

- **Quantified the interplay of reducing heat flux against the presence of free electrons:** It has been well studied within the literature how shape and trajectory conditions affect the stagnation heat flux to the vehicle. Similarly, analogous efforts have been performed to exclusively predict the generation of plasma. This work directly weighed the trade-off between these two quantities of interest in a parameterization study of different slender geometric configurations along various trajectory points. By merging these two normally separate analyses, the work demonstrated why aerodynamic design for mitigating communications blackout has historically taken a back seat to the more vital consideration of minimizing heat loads to the vehicle.

- **Explored the effects of introducing water vapor to a hypersonic flowfield:** The inclusion of an additional 9 species and 41 chemical reactions related to water allowed an analysis on the thermochemical impact that water vapor has on a weakly ionized hypersonic flow. The effects of the role water vapor plays on the temperatures and chemical composition were examined and isolated.

- **Investigated the feasibility of a water vapor injection technique in reducing the electron density:** From an investigation along the RAM-C II flight trajectory, it was established that there exists a trade-off between the beneficial and detrimental effects that water vapor injection brings into the flow. The practical considerations of implementing a water vapor additive blackout mitigation scheme were assessed and contextualized for a slender hypersonic glide vehicle.

- **Investigated the feasibility of MHD control techniques as viable blackout mitigation strategies:** In the context of a slender hypersonic glide body, the effects of an ideal dipole magnetic field on the flowfield was simulated. It was found that due to the low electrical conductivity level, as predicted by the Chapman-Cowling model, MHD schemes which focus on utilizing the Lorentz force are likely impractical.

7.3 Recommendations for Future Work

The work presented herein provided insight into how two prospective mitigation techniques perform for slender hypersonic bodies. It still appears that the communications blackout problem has no immediate universal resolution in the near future. However, the continued, seventy-year search for a solution provides many avenues for further research which can build upon the conclusions and insights of the current work. Some of these future research areas are recommended in a detailed listing below.

7.3.1 Higher-Fidelity Chemical Kinetics Models

The work in this thesis attempted due diligence in making sure the chemical kinetics model of Park is at the very least adequate for use in modeling plasma generation. As a validation platform the RAM-C II and, to some extent RAM-C I, were utilized showing generally good agreement with the flight data in regimes where the physics (laminar, low angle-of-attack, absence of ablation products) were accounted for. However, it has been shown in this study and many others which compare results with the electrostatic probe station data, that there exists a mismatch, not just with differences in the electron densities at each probe location, but also with the locations of the maxima. It is possible that this is a result of the measurement system itself, as the probe created a physical disturbance in the flow. However, it is also possible, that the empirical chemical kinetics models that have been ubiquitously used in these studies do not adequately capture the involved chemistry. In particular, the crucially important reaction rates of the associative ionization reactions may not be well described. The description of the associative ionization reactions by one constant is not entirely accurate as the process is at least a two-step reaction in which the collisions of N and O atoms form an excited NO* which has a high probability of decomposing into an NO^+ ion [265]. Recent analysis has further shown that these reactions are predicated on tracking the excited states of the involved atoms themselves [350]. Therefore, this motivates comparisons between higher-fidelity models and the ones studied within this work, using the trajectory of RAM-C as a validation platform.

The work also briefly examined the role of the dissociation rates through the novel MMT chemistry set. However, some of the most influential reactions were kept the same as the baseline Park chemistry set due to a lack of informed rates. Recent QCT-derived rates for both the Zeldovich reactions and the dissociation of nitric oxide have now been updated [351] and should provide additional insight into the role of the reactions which create atomic oxygen and nitrogen.

In an analogous sense, the water vapor simulations can be improved upon by inclusion of additional relaxation terms. It has been shown that nitrogen de-excites in the presence of water, as water molecules exhibit special properties that make them effective vibrational excitation quenchers. Specifically, a vibrationally excited nitrogen molecule transfers its vibrational energy through a very rapid transition process to the vibrational-rotational energy of the water molecule [352]. The inclusion of this relaxation process would likely show further advantages associated with the injection of water vapor for plasma reduction. Further, the study of plasma formation in air demonstrated the importance of capturing all the relevant ionizable species, particularly when going from 9-species to 11-species. Thus, at the expense of computational cost, additional species, such as OH^-, should be assessed for their role in electron density when modeling water vapor.

7.3.2 Electromagnetic Wave Propagation Solver

The work within this thesis operated under the assumption that the cut-off plasma frequency that is related to the maximum electron density is the cardinal parameter in defining whether or not blackout occurs. While this methodology is accurate in assessing order of magnitude observations, there are many other phenomena that may be important to consider, such as the role of signal attenuation, refraction, reflection, spectral broadening, and phase modulation. One way to properly capture many of these phenomena is to transpose the results of the flow solver into more advanced electromagnetic wave propagation models, such as geometrical optics or ray tracing techniques [50, 353], or by solving the Maxwell equations directly through a finite differencing scheme [243] or through a finite volume approach [326].

7.3.3 Inclusion of Turbulence

The effects of turbulence on both the electron number density and the propagation of radio waves have not been considered within this thesis. A turbulent flow induces fluctuations in the electron density that not only decreases the accuracy from assuming a steady state average, but also, depending on the frequency of the turbulent-induced fluctuations with respect to the operational frequency, can cause detrimental modulation effects on the transmitted radio waves [64, 354–356]. These studies have generally taken liberties when assuming values for the noise attributed to turbulence, as both experimental measurements and high-fidelity numerical analyses involving turbulent hypersonic plasma are severely limited. Thus, blackout analyses will benefit from well characterized descriptions of plasma fluctuations in both the spatial and temporal space.

It should also be noted that the water vapor injection could potentially trip the boundary layer and causes an earlier transition to turbulence. A turbulent flow could have detrimental effects on the effectiveness of the water injection scheme as the thin water film layer by the surface of the vehicle would be dispersed. Thus, further exploration of the scenarios considered within this thesis through high-fidelity turbulence modeling can be beneficial to understanding the important phenomena at play.

7.3.4 Improved Material Injection Modeling

This work modeled the injection of water vapor through a surface momentum balance condition. A natural improvement to the work herein would be to incorporate aspects of injecting water in a liquid droplet phase. Such a future effort would bridge the gap created between that of the current work and the many previous studies that have modeled the behavior of water droplets within a weakly-ionized plasma. Modeling a multi-phase hypersonic flow would not be trivial, but incremental additions to the current model could be made. Particle laden hypersonic flows have been simulated in the past, for instance to capture the aerothermodynamics of ablating rocket nozzles [357]. An analogous gas-particle model which describes the injection of water in particle form would need to adequately model the vaporization of water and the electron capture by the droplets, both as alterations to the chemical source term associated with the air-water vapor mixture. A potential additional improvement to the current model would be to include additional energy equations, as the current model assumes vibrational energy equilibrium between the molecules of widely ranging vibrational degrees of freedom.

7.3.5 Modeling Alternative Injection Compositions

Although water vapor has many desirable attributes related to reducing the plasma density that were discussed in this work, the products related to its chemical breakup can also cause detrimental effects. The fine-tuning associated with getting the most out of the water vapor from a design perspective, in terms of its suitable location on the vehicle and the amount required, may lead to the consideration of other injectants. While many chemical additives have been studied, successful reduction of plasma density has generally resulted from several desirable properties, which can be used to narrow the scope of suitable injectants.

Specifically, successful chemical compositions have shown several of the following attributes: i) a high affinity for electrons, ii) long durations in droplet form to promote recombination on their surface, iii) include large compositions of atoms that result in many endothermic dissociation reactions, iv) contain species with high rates of reaction with atomic nitrogen and oxygen, and v) contain species which do not easily ionize at the conditions of injection. Thus, future efforts into the material additive blackout mitigation technique not associated with water should focus on chemicals that display several or all of these characteristics.

7.3.6 Parameterization of MHD techniques

It was shown through the work of this thesis that the MHD technique is seemingly not appropriate for hypersonic glide bodies in the regimes that were simulated. This is a consequence of the low conductivity around the dipole magnet utilized. It would be an important future research endeavor to properly quantify the hypersonic flow conditions that are appropriate for this MHD technique, whether in the form of exploring additional trajectories or vehicular shapes.

An improvement to the magnetic interaction parameter could also be made by placing the magnet in the stagnation region where conductivity is the highest. If the Lorentz force is utilized appropriately, so as to not create undesirable secondary shocks, the shock shape could be altered in a beneficial way, analogous to that of a gas-spike and the water vapor injection performed in this study. Thus, the levels of ionization further downstream could be lower allowing for better communication characteristics.

7.3.7 Electrical Conductivity Model

The orders-of-magnitude variation of electrical conductivities for air predicted by the various semi-analytical models examined in this work epitomizes the wide-spread, urgent need for a conductivity model that is proven to be accurate over a broad range of plasma conditions, namely across varying ionization levels, temperatures, and densities. Such computationally inexpensive, semi-analytical models would require a large assortment of experimental measurements. Although surrogate models of direct Boltzmann solutions exist, they too would benefit from experiments that would provide more accurate cross-section data and insight into the associated normalized electric fields. The use of an electrical conductivity model which demonstrates both generality and accuracy would directly result in higher confidence levels when modeling MHD techniques within the plasma regimes associated with hypersonic flight.

7.3.8 Flight and Ground Test Data

As indicated by the use of 53-year-old flight data for validation, there is a significant need for modern-day flight measurements which characterize the plasma properties of a hypersonic flow field. Such measurements would be invaluable in further justifying the numerous assumptions, models, and boundary conditions that are commonly employed when simulating weakly ionized flows. Indeed, this work, and the work of many others, would be placed on more secure footing from additional experiments conducted either on the ground or in the air.

BIBLIOGRAPHY

[1] Larmor, J., "XCVIII. Why Wireless Electric Rays Can Bend Round the Earth," The London, Edinburgh, and Dublin Philosophical Magazine and Journal of Science, Vol. 48, No. 288, 1924, pp. 1025–1036. doi:10.1080/14786442408634561.

[2] Darrow, K. K., "The Ionosphere," Electrical Engineering, Vol. 59, No. 7, 1940, pp. 272–283. doi:10.1109/EE.1940.6434987.

[3] Mimno, H. R., "The Physics of the Ionosphere," Rev. Mod. Phys., Vol. 9, Jan 1937, pp. 1–43. doi:10.1103/RevModPhys.9.1.

[4] Newell Jr, H. E., "A Review of Upper Atmosphere Research from Rockets," Eos, Transactions American Geophysical Union, Vol. 31, No. 1, 1950, pp. 25–34. doi:10.1029/TR031i001p00025.

[5] Seddon, J. C., "Propagation Measurements in the Ionosphere With the Aid of Rockets," Journal of Geophysical Research, Vol. 58, No. 3, 1953, pp. 323–335. doi:10.1029/JZ058i003p00323.

[6] Anderson Jr, J. D., Hypersonic and High-Temperature Gas Dynamics, AIAA Education Series, 2006.

[7] Heppenheimer, T. A., "Facing the Heat Barrier: A History of Hypersonics," NASA History Series SP-2007-4232, Spetember 2007.

[8] Becker, M., Bourdeau, R., and Burnight, T., "Upper Atmosphere Research Report Number 2. Part 2. Ionization Experiments in the V-2," Report R-3031, Naval Research Lab, Washington D.C., 1946.

[9] Sanger, E., Goercke, P., and Bredt, I., "On Ionization and Luminescence in Flames," NACA TM-1305, April 1951.

[10] Smelt, R., "Problems of Hypersonic Flows," 1318th Meeting, Proceedings of the Academy and Affiliated Sciences, 1949.

[11] Lin, S.-C., "A Rough Estimate of the Attenuation of Telemetering Signals Through the Ionized Gas Envelope Around a Typical Re-Entry Missile," Avco-Everett Research Laboratory Research Report 74, 1956.

[12] Dirsa, E. F., "The Telemetry and Communication Problem of Re-Entrant Space Vehicles," Proceedings of the IRE, Vol. 48, No. 4, 1960, pp. 703–713. doi:10.1109/JRPROC.1960.287451.

[13] Taylor, W. C., "Analysis and Prediction of Radio Signal Interference Effects Due to Ionized Layer Around a Re-Entry Vehicle," Planetary and Space Science, Elsevier, Vol. 7, 1961, pp. 286–300. doi:10.1016/0032-0633(61)90307-5.

[14] Baldwin, K., Bassett, O., Hawthorne, E., and Langberg, E., "Telecommunications During Re-Entry," Planetary and Space Science, Elsevier, Vol. 6, 1961, pp. 207–218. doi:10.1016/0032-0633(61)90021-6.

[15] Ellis Jr, M. C. and Huber, P. W., "Radio Transmission Through the Plasma Sheath Around a Lifting Reentry Vehicle," NASA TN-D-507, 1961.

[16] Glick, H. S., "Interaction of Electromagnetic Waves with Plasmas of Hypersonic Flows," ARS journal, Vol. 32, No. 9, 1962, pp. 1359–1364. doi:10.2514/8.6286.

[17] Siddiqi, A. A., "Challenge to Apollo: The Soviet Union and the Space Race, 1945-1974," NASA SP-2000-4408, 2000.

[18] Huber, P. W., "Deduction of Reentry Plasma Properties about Manned Orbital Spacecraft from Radio Signal Attenuation Data," NASA TN D-4118, August 1967.

[19] Krause, P. M., "The Effect of Glide Re-Entry Shock Induced Ionization on the Communication System of the ASSET Vehicle," Third Symposium on the Plasma Sheath: Plasma Electromagnetics of Hypersonic Flight, Vol. 2, AFCRL-67-0280, May 1967, pp. 95–124.

[20] Lewis Jr, J. and Scallion, W., "Flight Parameters and Vehicle Performance for Project FIRE Flight 1, Launched April 14, 1964," NASA TN D-2996, 1965.

[21] Lehnert, R. and Rosenbaum, B., "Plasma Effects on Apollo Re-entry Communication," NASA TN D-2732, March 1965.

[22] Orloff, R. W., "Apollo by the Numbers: A statistical reference for the manned phase of Project Apollo," National Aeronautics and Space Administration, Vol. 22, June 1996.

[23] Hall, R. and Shayler, D., Soyuz: A Universal Spacecraft, Springer Science & Business Media, 2003.

[24] Viehlbock, F., "Soyuz-The Russian Human Transportation System," Space Programs and Technologies Conference and Exhibit, 1994, p. 4604. doi:10.2514/6.1994-4604.

[25] Poirier, J. L., Rotman, W., Hayes, D. T., and Lennon, J. F., "Effects of the Reentry Plasma Sheath on Microwave Antenna Performance: Trailblazer II Rocket Results of 18 Jun 1967," Air Force Cambridge Research Laboratories AFCRL-69-0354, 1969.

[26] Lennon, J. F. and Poirter, J., "Interpretation of Microwave Antenna Results from a Reentry Flight Test: A Comparison of Methods," Air Force Cambridge Research Laboratories AFCRL-TR-74-0389, 1974.

[27] Akey, N. D., "Overview of RAM Reentry Measurements Program," The Entry Plasma Sheath and Its Effects on Space Vehicle Electromagnetic Systems, Vol. 1, NASA SP-252, October 1970, pp. 19–31.

[28] Seiff, A., Reese, D. E., Sommer, S. C., Kirk, D. B., Whiting, E. E., and Niemann, H. B., "PAET, An Entry Probe Experiment in the Earth's Atmosphere," Icarus, Vol. 18, No. 4, 1973, pp. 525–563. doi:10.1016/0019-1035(73)90058-4.

[29] Rakich, J. and Lanfranco, M., "Numerical Computation of Space Shuttle Heating and Surface Streamlines," AIAA 11th Thermophysics Conference, No. AIAA Paper 1976-0464, 1976. doi:10.2514/6.1976-464.

[30] Schiesser, E., "Use of Radio Equipment for Space Shuttle Navigation," IEEE Transactions on Communications, Vol. 26, No. 11, 1978, pp. 1514–1520. doi:10.1109/TCOM.1978.1094035.

[31] Cartier, D. E., "Shuttle Communications Design Study," NASA CR-141761, 1975.

[32] Levin, D. A., Finke, R. G., Candler, G. V., Boyd, I. D., Howlett, C., Erdman, P., and Zipf, E., "In-situ Measurements of Transitional and Continuum Flow UV Radiation from Small Satellite Platforms," 32nd Aerospace Sciences Meeting and Exhibit, No. 94-0248, 1994. doi:10.2514/6.1994-248.

[33] Inouye, Y., "OREX Flight: Quick Report and Lessons Learned," Aerothermodynamics for Space Vehicles, Proceedings of the 2nd European Symposium held in ESTEC, Noordwijk, The Netherlands, Vol. 367, 1995, p. 271.

[34] Tomita, H., Suzuki, H., Matsumoto, S., Harigae, M., Itsukaichi, A., Maeda, H., and Miyano, T., "Flight Data Analysis of OREX Onboard GPS Receiver," Proceedings of the 7th International Technical Meeting of the Satellite Division of The Institute of Navigation (ION GPS 1994), 1994, pp. 1211–1220.

[35] Ito, T., Takaki, R., and Teraoka, K., "Measurement of Plasma Electron Density Around HYFLEX Vehicle Using Radio Wave Cut-Off," 29th AIAA, Plasmadynamics and Lasers Conference, 1998, p. 2480. doi:10.2514/6.1998-2480.

[36] Morino, Y. and Caristia, S., "Thermal Responses of a Large Nose Cap Model Tested at SCIROCCO," 43rd AIAA Aerospace Sciences Meeting and Exhibit, 2005, p. 174. doi:10.2514/6.2005-174.

[37] Morabito, D., "The Spacecraft Communications Blackout Problem Encountered During Passage or Entry of Planetary Atmospheres," IPN Progress Report 42–150, 2002.

[38] Macret, J. and Leveugle, T., "The ARD (Atmospheric Reentry Demonstrator) Program-An Overview," 9th International Space Planes and Hypersonic Systems and Technologies Conference, 2000, p. 4934. doi:10.2514/6.1999-4934.

[39] Lo, M. W., Williams, B. G., Bollman, W. E., Han, D., Hahn, Y., Bell, J. L., Hirst, E. A., Corwin, R. A., Hong, P. E., Howell, K. C., et al., "Genesis Mission Design," The Journal of the astronautical sciences, Vol. 49, No. 1, 2001, pp. 169–184. doi:10.1007/BF03546342.

[40] Cheatwood, F. M., Merski Jr, N. R., Riley, C. J., and Mitcheltree, R. A., "Aerothermodynamic Environment Definition for the Genesis Sample Return Capsule," 35th AIAA Thermophysics Conference, No. AIAA Paper 2001-2889, 2001. doi:10.2514/6.2001-2889.

[41] Lebreton, J.-P., Witasse, O., Sollazzo, C., Blancquaert, T., Couzin, P., Schipper, A.-M., Jones, J. B., Matson, D. L., Gurvits, L. I., Atkinson, D. H., et al., "An Overview of the Descent and Landing of the Huygens Probe on Titan," Nature, Vol. 438, No. 7069, 2005, pp. 758–764. doi:10.1038/nature04347.

[42] Wright, M., Olejniczak, J., Walpot, L., Raynaud, E., Magin, T., Callaut, L., and Hollis, B., "A Code Calibration Study for Huygens Entry Aeroheating," 44th AIAA Aerospace Sciences Meeting and Exhibit, 2006, p. 382. doi:10.2514/6.2006-382.

[43] Reynier, P. and Evans, D., "Postflight Analysis of Inflatable Reentry and Descent Technology Blackout During Earth Reentry," Journal of Spacecraft and Rockets, Vol. 46, No. 4, 2009, pp. 800–809. doi:10.2514/1.41480.

[44] Zhong, J., Ozawa, T., and Levin, D. A., "Modeling of Stardust Reentry Ablation Flows in the Near-Continuum Flight Regime," AIAA Journal, Vol. 46, No. 10, 2008, pp. 2568–2581. doi:10.2514/1.36196.

[45] Yamada, T., Inatani, Y., and Ishii, N., "Reentry of Hayabusa Sample Return Capsule and Post-Flight Analysis of the Recovered Heatshield," Trans. JSASS Aerospace Tech. Japan, Vol. 10, No. ists28, 2012, pp. Te11–Te14. doi:10.2322/tastj.10.Te11.

[46] Seedhouse, E., SpaceX's Dragon: America's Next Generation Spacecraft, Springer, 2015.

[47] Morabito, D. D., Schratz, B., Bruvold, K., Ilott, P., Edquist, K., and Cianciolo, A. D., "The Mars Science Laboratory EDL Communications Brownout and Blackout at UHF," IPN Progress Report 42–197, 2014.

[48] Barth, A., Mamich, H., and Hoelscher, B., "Post-flight Analysis of the Guidance, Navigation, and Control Performance During Orion Exploration Flight Test 1," American Astronautical Society GN&C Conference, No. JSC-CN-32764, 2015.

[49] Zanetti, R., Holt, G., Gay, R., DSouza, C., Sud, J., Mamich, H., Begley, M., King, E., and Clark, F. D., "Absolute Navigation Performance of the Orion Exploration Flight Test 1," Journal of Guidance, Control, and Dynamics, Vol. 40, No. 5, 2017, pp. 1106–1116. doi:10.2514/1.G002371.

[50] Ramjatan, S., Lani, A., Boccelli, S., Van Hove, B., Karatekin, Ö., Magin, T., and Thoemel, J., "Blackout Analysis of Mars Entry Missions," Journal of Fluid Mechanics, Vol. 904, 2020. doi:10.1017/jfm.2020.714.

[51] Haruki, M., Nakamura, R., Matsumoto, S., Kobayashi, S., Kawashima, I., Aoki, K., and Kikuchi, N., "Post-Flight Evaluation of the Guidance and Control for Reentry Capsule HSRC," 8th European Conference for Aeronautics and Space Sciences (EUCASS), 2019. doi:10.13009/EUCASS2019-428.

[52] Burghardt, M. l., "Boeing CST-100 Commercial Crew Transportation System," August 2011.

[53] NASA, "Boeing Starliner Orbital Flight Test Landing," `https://www.youtube.com/watch?v=lPzNHeX7OYM&ab_channel=NASA`, Dec 2019.

[54] Schroeder, L. and Russo, F., "Flight Investigation and Analysis of Alleviation of Communications Blackout by Water Injection During Gemini 3 Reentry," NASA TN X-1521, March 1968.

[55] Schroeder, L., "RAM Flight-Test Results and Conclusions," Communicating Through Plasmas of Atmospheric Entry and Rocket Exhaust (declassified), NASA SP-52, January 1964, pp. 225–223.

[56] Rochefort, J. S., Sukys, R., and Symmes, R., "Instrumentation and Flight Results of Reentry Plasma Diagnostic and Alleviation Experiments on Trailblazer II Rockets," Air Force Cambridge Research Laboratories AFCRL-72-0695, October 1972.

[57] Schroeder, L. C. and Akey, N. D., "Material Injection Alleviation During the RAM C-III Flight," Journal of Spacecraft and Rockets, Vol. 10, No. 3, 1973, pp. 170–174. doi:10.2514/3.61866.

[58] Urzay, J., "Hypersonics, Chapter 2: The Physical Characteristics of Hypersonic Flows," July 2020.

[59] Hayes, W. D. and Probstein, R. F., Hypersonic Flow Theory (Applied Mathematics and Mechanics), New York and London 1959. Academic Press., 1959.

[60] McBride, B. J. and Gordon, S., "Computer Program for Calculating and Fitting Thermodynamic Functions," NASA RP-1271, 1992.

[61] Vincenti, W. G. and Kruger, C. H., Introduction to Physical Gas Dynamic, New York, Wiley, 1965.

[62] Chen, F. F., Introduction to Plasma Physics, Springer Science & Business Media, 2012.

[63] Saha, M. N., "LIII. Ionization in the Solar Chromosphere," The London, Edinburgh, and Dublin Philosophical Magazine and Journal of Science, Vol. 40, No. 238, 1920, pp. 472–488. doi:10.1080/14786441008636148.

[64] Lin, T. and Sproul, L., "Influence of Reentry Turbulent Plasma Fluctuation on EM Wave Propagation," Computers & Fluids, Vol. 35, No. 7, 2006, pp. 703–711. doi:10.2514/6.2002-2106.

[65] Parent, B., "Electron Heating and Cooling in Hypersonic Flows," Physics of Fluids, Vol. 33, No. 4, 2021, pp. 046105. doi:10.1063/5.0046197.

[66] Boyd, I. D. and Schwartzentruber, T. E., Nonequilibrium Gas Dynamics and Molecular Simulation, Vol. 42, Cambridge University Press, 2017.

[67] Gnoffo, P. A., Gupta, R. N., and Shinn, J. L., "Conservation Equations and Physical Models for Hypersonic Air Flows in Thermal and Chemical Nonequilibrium," NASA TP-2867, February 1989.

[68] Gupta, R. N., Yos, J. M., Thompson, R. A., and Lee, K.-P., "A Review of Reaction Rates and Thermodynamic and Transport Properties For an 11-Species Air Model for Chemical and Thermal Nonequilibrium Calculations to 30000 K," NASA RP-1232, 1990.

[69] Itikawa, Y., "Cross Sections for Electron Collisions with Nitrogen Molecules," Journal of Physical and Chemical Reference Data, Vol. 35, No. 1, 2006, pp. 31–53. doi:10.1063/1.1937426.

[70] Itikawa, Y., "Cross Sections for Electron Collisions with Oxygen Molecules," Journal of Physical and Chemical Reference Data, Vol. 38, No. 1, 2009, pp. 1–20. doi:10.1063/1.3025886.

[71] Itikawa, Y., "Cross Sections for Electron Collisions with Nitric Oxide," Journal of Physical and Chemical Reference Data, Vol. 45, No. 3, 2016, pp. 033106. doi:10.1063/1.4961372.

[72] Picone, J. M., Hedin, A. E., Drob, D. P., and Aikin, A. C., "NRLMSISE-00 Empirical Model of the Atmosphere: Statistical Comparisons and Scientific Issues," Journal of Geophysical Research: Space Physics, Vol. 107, No. A12, 2002. doi:10.1029/2002ja009430.

[73] Gillman, E. D., Cathode Spot Injection of Dielectric Particles with Applications for Communications Blackout Plasma Depletion, Ph.D. thesis, Department of Aerospace Engineering, University of Michigan, 2012.

[74] Rybak, J. P. and Churchill, R., "Progress in Reentry Communications," IEEE Transactions on Aerospace and Electronic Systems, , No. 5, 1971, pp. 879–894. doi:10.1109/TAES.1971.310328.

[75] Hartunian, R., Stewart, G., Fergason, S., Curtiss, T., and Seibold, R., "Causes and Mitigation of Radio Frequency (RF) Blackout During Reentry of Reusable Launch Vehicles," Aerospace Report NO. ATR-2007(5309)-1, Aerospace Corporation, January 2007.

[76] Langmuir, I., "Oscillations in Ionized Gases," Proceedings of the National Academy of Sciences of the United States of America, Vol. 14, No. 8, 1928, pp. 627. doi:10.1073/pnas.14.8.627.

[77] Gartenhaus, S., Elements of Plasma Physics, Holt, Rinehart and Winston, 1964.

[78] Lemmer, K. M., Use of a Helicon Source for Development of a Re-Entry Blackout Amelioration System, Ph.D. thesis, Department of Aerospace Engineering, University of Michigan, 2009.

[79] US Department of Commerce National Telecommunications and Information Administration, "United States Frequency Allocations: The Radio Spectrum," 2022.

[80] National Academies of Sciences, Engineering, and Medicine and others, Handbook of Frequency Allocations and Spectrum Protection for Scientific Uses, National Academies Press, 2015.

[81] Kim, M. K., Electromagnetic Manipulation of Plasma Layer for Re-Entry Blackout Mitigation, Ph.D. thesis, Department of Aerospace Engineering, University of Michigan, 2009.

[82] Starkey, R. P., "Hypersonic Vehicle Telemetry Blackout Analysis," Journal of Spacecraft and Rockets, Vol. 52, No. 2, 2015, pp. 426–438. doi:10.2514/1.a32051.

[83] Wu, Y., Yao, J., and Qu, X., "An Adaptive Reentry Guidance Method Considering the Influence of Blackout Zone," Acta Astronautica, Vol. 142, 2018, pp. 253–264. doi:10.1016/j.actaastro.2017.10.041.

[84] Jones, C. H., "Report from the Workshop on Communications Through Plasma During Hypersonic Flight," AFOSR AFFTC-PA-08-08292, August 2006.

[85] Lux-Baumann, J. and Burkes, D. A., "Hyper-X (X-43A) Flight Test Range Operations Overview," International Foundation for Telemetering, 2005.

[86] Malik, T., "Superfast Military Aircraft Lost in Test Flight," `https://www.space.com/12607-darpa-launches-hypersonic-glider-mach-20-test-flight.html`, August 2011.

[87] Board, G. M. I., Genesis Mishap Investigation Board Report: Volume I, November 2005.

[88] Gehman, H. W., Columbia Accident Investigation Board, Vol. 2, Columbia Accident Investigation Board, August 2003.

[89] Hankey, W. L., Re-Entry Aerodynamics, AIAA Education Series, 1988.

[90] Beck, R. A., "Ablative Thermal Protection System Fundamentals," Thermal and Fluids Analysis Workshop, No. TFAWS 2017, Huntsville, Alabama, August 2017.

[91] Duffa, G., Ablative Thermal Protection Systems Modeling, American Institute of Aeronautics and Astronautics, Inc., 2013.

[92] Schexnayder Jr, C. and Evans, J., "Influence of Ablation Impurities on Blunt Body Re-Entry Ionization," AIAA Journal, Vol. 12, No. 6, 1974, pp. 805–811, https://doi.org/10.2514/3.49354.

[93] Shao, C., Nie, L., and Chen, W., "Analysis of Weakly Ionized Ablation Plasma Flows For a Hypersonic Vehicle," Aerospace Science and Technology, Vol. 51, 2016, pp. 151–161. doi:10.1016/j.ast.2016.02.005.

[94] Van de Kamp, M. M., "Statistical Analysis of Rain Fade Slope," IEEE Transactions on Antennas and Propagation, Vol. 51, No. 8, 2003, pp. 1750–1759. doi:10.1109/TAP.2003.808542.

[95] Series, P., "Attenuation by Atmospheric Gases and Related Effects," Recommendation ITU-R, 2019, pp. 676–12.

[96] Krishnamoorthy, S., Alleviation of Reentry Communications Blackout by Electrostatic Methods, Ph.D. thesis, Stanford University, 2017.

[97] Liu, D., Li, X., Xie, K., and Liu, Z., "The Propagation Characteristics of Electromagnetic Waves Through Plasma In the Near-Field Region of Low-Frequency Loop Antenna," Physics of Plasmas, Vol. 22, No. 10, 2015, pp. 102106. doi:10.1063/1.4932993.

[98] Bachynski, M., "Electromagnetic Wave Penetration of Reentry Plasma Sheaths," Radio Science Journal of Research NBS/USNC-URSI, Vol. 69D, No. 2, 1965.

[99] Taylor, W., Scharfman, W., and Morita, T., "Voltage Breakdown of Microwave Antennas," Advances in Microwaves, Vol. 7, 1971, pp. 59–130. doi:10.1016/B978-0-12-027907-4.50008-5.

[100] Gramling, J. and Chrissotimos, N., "Three Generations of NASA's Tracking and Data Relay Satellite System," SpaceOps 2008 Conference, 2008, p. 3313. doi:10.2514/6.2008-3313.

[101] Belov, I., Borovoy, V. Y., Gorelov, V., Kireev, A., Korolev, A., and Stepanov, E., "Investigation of Remote Antenna Assembly for Radio Communication with Reentry Vehicle," Journal of Spacecraft and Rockets, Vol. 38, No. 2, 2001, pp. 249–256. doi:10.2514/2.3678.

[102] Langberg, E., "Optical Communication During Hypersonic Re-entry," IRE Transactions on Communications Systems, Vol. 7, No. 2, 1959, pp. 68–70. doi:10.1109/TCOM.1959.1097551.

[103] Bykova, N. G., Gochelashvily, K. S., Karfidov, D. M., Makarenko, G. F., Senatorov, A. K., Sergeichev, K. F., Shatalov, O. P., and Zabelinskii, I. E., "Experimental Demonstration of the Feasibility of Laser Communication with Reentry Spacecraft at 1.55 μm," Applied Optics, Vol. 56, No. 10, 2017, pp. 2597–2603. doi:10.1364/AO.56.002597.

[104] Mitchell, J., "NASA Optical Communications Update," NASA-CSIRO Optical/Quantum Workshop, May 2022.

[105] Zang, Q., Bai, X., Yang, Y., Ma, P., Huang, J., Ma, J., Yu, S., Yang, Q., Shi, H., Sun, X., et al., "Phase Characteristic and Information Transmission of Laser Signals Through Plasma in Shock Tube," Physics of Plasmas, Vol. 26, No. 2, 2019, pp. 022107. doi:10.1063/1.5065481.

[106] Li, H., Tang, X., Hang, S., Liu, Y., and Chen, D., "Potential Application of X-Ray Communication Through a Plasma Sheath Encountered During Spacecraft Reentry into Earth's Atmosphere," Journal of Applied Physics, Vol. 121, No. 12, 2017, pp. 123101. doi:10.1063/1.4978758.

[107] Mackey, L. E. and Boyd, I. D., "Assessment of Hypersonic Flow Physics on Aero-Optics," AIAA Journal, Vol. 57, No. 9, 2019, pp. 3885–3897. doi:10.2514/1.J057869.

[108] Gupta, A. and Argrow, B., "Analytical Approach for Aero-Optical and Atmospheric Effects in Supersonic Flow Fields," AIAA Scitech 2020 Forum, 2020, p. 0684. doi:10.2514/6.2020-0684.

[109] Liu, Y., Li, H., Li, Y., Hang, S., and Tang, X., "Transmission Properties and Physical Mechanisms of X-Ray Communication for Blackout Mitigation During Spacecraft Reentry," Physics of Plasmas, Vol. 24, No. 11, 2017, pp. 113507. doi:10.1063/1.4998786.

[110] Zang, Q., Bai, X., Ma, P., Huang, J., Ma, J., Yu, S., Shi, H., Sun, X., Liu, Y., and Lu, Y., "Laboratory Simulation of Laser Propagation Through Plasma Sheaths Containing Ablation Particles of ZrB 2-SiC-C During Hypersonic Flight," Optics Letters, Vol. 42, No. 4, 2017, pp. 687–690. doi:10.1364/OL.42.000687.

[111] Stutzman, W. L. and Thiele, G. A., Antenna Theory and Design, John Wiley & Sons, 2012.

[112] Gao, X. and Jiang, B., "A Matching Approach to Communicate Through the Plasma Sheath Surrounding a Hypersonic Vehicle," Journal of Applied Physics, Vol. 117, No. 23, 2015, pp. 233301. doi:10.1063/1.4921751.

[113] Balanis, C. A., Advanced Engineering Electromagnetics, John Wiley & Sons, 2012.

[114] Sakai, O. and Tachibana, K., "Plasmas as Metamaterials: A Review," Plasma Sources Science and Technology, Vol. 21, No. 1, 2012, pp. 013001. doi:10.1088/0963-0252/21/1/013001.

[115] Webb, B. A. and Ziolkowski, R. W., “Metamaterial-Inspired Multilayered Structures Optimized to Enable Wireless Communications Through a Plasmasonic Region,” Applied Physics Letters, Vol. 118, No. 9, 2021, pp. 094102. doi:10.1063/5.0041196.

[116] Veselago, V. G., “The Electrodynamics of Substances with Simultaneously Negative Values of epsilon and mu,” Physics-Uspekhi, Vol. 10, No. 4, 1968, pp. 509–514. doi:10.1070/PU1968v010n04ABEH003699.

[117] Engheta, N. and Ziolkowski, R. W., Metamaterials: Physics and Engineering Explorations, John Wiley & Sons, 2006.

[118] Messiaen, A. and Vandenplas, P., “Theory and Experiments of the Enhanced Radiation From a Plasma-Coated Antenna,” Electronics Letters, Vol. 1, No. 3, 1967, pp. 26–27. doi:10.1049/el:19670021.

[119] Lin, C. and Chen, K.-M., “Improved Radiation From a Spherical Antenna by Overdose Plasma Coating,” IEEE Transactions on Antennas and Propagation, Vol. 17, No. 5, 1969, pp. 675–678. doi:10.1109/TAP.1969.113950.

[120] Webb, B. A. and Ziolkowski, R. W., “A Metamaterial-Inspired Approach to Mitigating Radio Frequency Blackout When a Plasma Forms Around a Reentry Vehicle,” Photonics, Vol. 7, MDPI, 2020, p. 88. doi:10.3390/photonics7040088.

[121] Nazarenko, S., Newell, A., and Zakharov, V., “Communication Through Plasma Sheaths Via Raman (Three-Wave) Scattering Process,” Physics of Plasmas, Vol. 1, No. 9, 1994, pp. 2827–2834. doi:10.1063/1.870521.

[122] Korotkevich, A., Newell, A., and Zakharov, V., “Communication Through Plasma Sheaths,” Journal of Applied Physics, Vol. 102, No. 8, 2007, pp. 083305. doi:10.1063/1.4921751.

[123] Atallah, S., Sanborn, W. A., and Hoodbhoy, A., “The Effect of Chemical Additives on Microwave Transmission in an Air Plasma,” Third Symposium on the Plasma Sheath: Plasma Electromagnetics of Hypersonic Flight, Vol. 2, AFCRL-67-0280, May 1967, pp. 320–341.

[124] Dix, D. M., Golden, K. E., Taylor, E. C., Kolpin, M. A., and Caron, P. R., “Lifting Reentry Communications, Volume 1: A Comparative Evaluation of Potential Systems,” Aerospace Corporation Technical Report No. TR-669(6220-10)-3, 1966.

[125] Carswell, A. I. and Richard, C., “Plasma Sheath Reduction by Electron Attachment Processes,” Third Symposium on the Plasma Sheath: Plasma Electromagnetics of Hypersonic Flight, Vol. 3, AFCRL-67-0280, May 1967, pp. 281–318.

[126] Good, R. E. and Rossi, J. J., “An Injection System for Alleviation of Radio Blackout During Re-Entry,” Scientific Report AFCRL-66-160 ; MC-63-78-R2, Mithras Cambridge MA, 1966.

[127] Evans, J., “Reduction of Free Electron Concentration in a Reentry Plasma by Injection of Liquids,” Third Symposium on the Plasma Sheath: Plasma Electromagnetics of Hypersonic Flight, Vol. 3, AFCRL-67-0280, May 1967, p. 343.

[128] Gillman, E. D., Foster, J. E., and Blankson, I. M., “Review of Leading Approaches for Mitigating Hypersonic Vehicle Communications Blackout and a Method of Ceramic Particulate Injection via Cathode Spot Arcs for Blackout Mitigation,” NASA TM-2010-216220, February 2010.

[129] Modica, A., Stepakoff, G., and Rosenbaum, H., “A Shock Tube Study of Plasma Alleviation By Oxide Dust,” The Entry Plasma Sheath and Its Effects on Space Vehicle Electromagnetic Systems, Vol. 1, NASA SP-252, October 1970, pp. 531–539.

[130] Hodara, H., “The Use of Magnetic Fields in the Elimination of the Re-entry Radio Blackout,” Proceedings of the IRE, Vol. 49, No. 12, 1961, pp. 1825–1830. doi:10.1109/JRPROC.1961.287709.

[131] Russo, F. P. and Hughes, J. K., “Measurements of the Effects of Static Magnetic Fields on VHF Transmission in Ionized Flow Fields,” NASA TM-X-907, March 1964.

[132] Rawhouser, R., “Overview of the AF Avionics Laboratory Re-entry Electromagnetics Program,” NASA SP-252, January 1970.

[133] Cheng, J., Jin, K., Kou, Y., Hu, R., and Zheng, X., “An Electromagnetic Method for Removing the Communication Blackout with a Space Vehicle Upon Re-Entry into the Atmosphere,” Journal of Applied Physics, Vol. 121, No. 9, 2017, pp. 093301. doi:10.1063/1.4976213.

[134] Leung, E., Hilal, M., Parmer, J., and Peck, S., “Lightweight Magnet for Space Applications,” IEEE Transactions on Magnetics, Vol. 23, No. 2, 1987, pp. 1331–1335. doi:10.1109/TMAG.1987.1065070.

[135] Chapman, J., Schmidt, H., Ruoff, R., Chandrasekhar, V., Dikin, D., and Litchford, R., “Flightweight Magnets for Space Application Using Carbon Nanotubes,” AIAA Paper 2003-0330, 2003, 10.2514/6.2003-330.

[136] Voronov, A., Troitskiy, A., Egorov, I., Samoilenkov, S., and Vavilov, A., “Magnetoplasmadynamic Thruster With an Applied Field Based On the Second Generation High-Temperature Superconductors,” Journal of Physics: Conference Series, Vol. 1686, IOP Publishing, 2020, p. 012023. doi:10.1088/1742-6596/1686/1/012023.

[137] Otabe, E., Nemoto, S., Kiuchi, M., Matsushita, T., Hayashi, T., Fujino, K., and Ni, B., “Bi-2223 Superconducting Magnet Generating Over 1T In Liquid Nitrogen,” Journal of Physics: Conference Series, Vol. 234, IOP Publishing, 2010, p. 032046. doi:10.1088/1742-6596/234/3/032046.

[138] Stenzel, R. and Urrutia, J., "A New Method for Removing the Blackout Problem on Reentry Vehicles," Journal of Applied Physics, Vol. 113, No. 10, 2013, pp. 103303, 10.1063/1.4795148.

[139] Zhou, H., Li, X., Xie, K., Liu, Y., and Yu, Y., "Mitigating Reentry Radio Blackout by Using a Traveling Magnetic Field," AIP Advances, Vol. 7, No. 10, 2017, pp. 105314, 10.1063/1.4999039.

[140] Kim, M., Keidar, M., and Boyd, I. D., "Analysis of an Electromagnetic Mitigation Scheme for Reentry Telemetry Through Plasma," Journal of Spacecraft and Rockets, Vol. 45, No. 6, 2008, pp. 1223–1229. doi:10.2514/1.37395.

[141] Keidar, M., Kim, M., and Boyd, I. D., "Electromagnetic Reduction of Plasma Density During Atmospheric Reentry and Hypersonic Flights," Journal of Spacecraft and Rockets, Vol. 45, No. 3, 2008, pp. 445–453, 10.2514/1.32147.

[142] The Ohio State University ElectroScience Laboratory, "Survey of Technology on Communication Through the Plasma Sheath," Technical Report AFALTR-70-123, AF Avionics Laboratory, July 1970.

[143] Gu, S. and Olivier, H., "Capabilities and Limitations of Existing Hypersonic Facilities," Progress in Aerospace Sciences, Vol. 113, 2020, pp. 100607. doi:10.1016/j.paerosci.2020.100607.

[144] Schneider, S. P., "Hypersonic and Hypervelocity Ground Test Facilities: A Brief Informal Summary," Purdue university, November 2007.

[145] Sayler, K. M., Hypersonic Weapons: Background and Issues for Congress, Congressional Research Service, July 2019.

[146] Bugel, M., Reynier, P., and Smith, A., "Survey of European and Major ISC facilities for Supporting Mars and Sample Return Mission Aerothermodynamics and Tests Required for Thermal Protection System and Dynamic Stability," International Journal of Aerospace Engineering, Vol. 2011, 2011. doi:doi:10.1155/2011/937629.

[147] Bose, D., Brown, J. L., Prabhu, D. K., Gnoffo, P., Johnston, C. O., and Hollis, B., "Uncertainty Assessment of Hypersonic Aerothermodynamics Prediction Capability," Journal of Spacecraft and Rockets, Vol. 50, No. 1, 2013, pp. 12–18. doi:10.2514/1.A32268.

[148] Sziroczak, D. and Smith, H., "A Review of Design Issues Specific to Hypersonic Flight Vehicles," Progress in Aerospace Sciences, Vol. 84, 2016, pp. 1–28. doi:10.1016/j.paerosci.2016.04.001.

[149] Hanquist, K., Modeling of Electron Transpiration Cooling for Leading Edges of Hypersonic Vehicles, Ph.D. thesis, Department of Aerospace Engineering, University of Michigan, 2017.

[150] Candler, G. V., Subbareddy, P. K., and Brock, J. M., "Advances in Computational Fluid Dynamics Methods for Hypersonic Flows," Journal of Spacecraft and Rockets, Vol. 52, No. 1, 2015, pp. 17–28.

[151] Ferziger, J. H., Perić, M., and Street, R. L., Computational Methods for Fluid Dynamics, Vol. 3, Springer, 2002.

[152] Scalabrin, L. C., Numerical Simulation of Weakly Ionized Hypersonic Flow Over Reentry Capsules, Ph.D. thesis, Department of Aerospace Engineering, University of Michigan, 2007.

[153] MacCormack, R. W. and Candler, G. V., "The Solution of the Navier-Stokes Equations Using Gauss-Seidel Line Relaxation," Computers & fluids, Vol. 17, No. 1, 1989, pp. 135–150. doi:10.1016/0045-7930(89)90012-1.

[154] Steger, J. L. and Warming, R., "Flux Vector Splitting of the Inviscid Gasdynamic Equations with Application to Finite-Difference Methods," Journal of computational physics, Vol. 40, No. 2, 1981, pp. 263–293. doi:10.1016/0021-9991(81)90210-2.

[155] Jawahar, P. and Kamath, H., "A High-Resolution Procedure For Euler and Navier–Stokes Computations on Unstructured Grids," Journal of Computational Physics, Vol. 164, No. 1, 2000, pp. 165–203. doi:10.1006/jcph.2000.6596.

[156] Karypis, G. and Kumar, V., "METIS: A Software Package for Partitioning Unstructured Graphs, Partitioning Meshes, and Computing Fill-Reducing Orderings of Sparse Matrices," University of Minnesota TR 97-061, 1997.

[157] Bisek, N. J., Numerical Study of Plasma-Assisted Aerodynamic Control for Hypersonic Vehicles, Ph.D. thesis, Department of Aerospace Engineering, University of Michigan, 2010.

[158] Deschenes, T. R., Extension of a Modular Particle-Continuum Method for Nonequilibrium Hypersonic Flows, Ph.D. thesis, Department of Aerospace Engineering, University of Michigan, 2011.

[159] Chen, S., Modeling of Material-Environment Interactions for Hypersonic Thermal Protection Systems, Ph.D. thesis, Department of Aerospace Engineering, University of Michigan, 2020.

[160] Holloway, M. E., Detailed Analysis of Thermochemistry Modeling for Hypersonic Air Flows, Ph.D. thesis, Department of Aerospace Engineering, University of Michigan, 2021.

[161] Sutton, K. and Gnoffo, P., "Multi-Component Diffusion With Application To Computational Aerothermodynamics," 7th AIAA/ASME Joint Thermophysics and Heat Transfer Conference, 1998, p. 2575. doi:10.2514/6.1998-2575.

[162] Stokes, G. G., “On the Theories of the Internal Friction of Fluids in Motion and of the Equilibrium and Motion of Elastic Solids,” 1854. doi:10.1017/CBO9780511702242.005.

[163] Fourier, J. B. J., Théorie analytique de la chaleur (The Analytical Theory of Heat), 1822.

[164] Wilke, C., “A Viscosity Equation for Gas Mixtures,” The Journal of Chemical Physics, Vol. 18, No. 4, 1950, pp. 517–519. doi:10.1063/1.1747673.

[165] Blottner, F. G., Johnson, M., and Ellis, M., “Chemically Reacting Viscous Flow Program for Multi-Component Gas Mixtures,” 1 1971. doi:10.2172/4658539.

[166] Eucken, A., “Über das Wärmeleitvermögen, die spezifische Wärme und die innere Reibung der Gase,” Phys. Z, Vol. 14, No. 8, 1913, pp. 324–332.

[167] Palmer, G. E. and Wright, M. J., “Comparison of Methods to Compute High-Temperature Gas Viscosity,” Journal of Thermophysics and Heat Transfer, Vol. 17, No. 2, 2003, pp. 232–239. doi:10.2514/2.6756.

[168] Palmer, G. and Wright, M., “A Comparison of Methods to Compute High-Temperature Gas Thermal Conductivity,” 36th AIAA Thermophysics Conference, 2003, p. 3913. doi:10.2514/6.2003-3913.

[169] Alkandry, H., Boyd, I. D., and Martin, A., “Comparison of Transport Properties Models for Flowfield Simulations of Ablative Heat Shields,” Journal of Thermophysics and Heat Transfer, Vol. 28, No. 4, 2014, pp. 569–582. doi:10.2514/1.T4233.

[170] Wright, M. J., Bose, D., Palmer, G. E., and Levin, E., “Recommended Collision Integrals for Transport Property Computations Part 1: Air Species,” AIAA Journal, Vol. 43, No. 12, 2005, pp. 2558–2564. doi:10.2514/1.16713.

[171] Gosse, R. and Candler, G., “Diffusion Flux Modeling: Application to Direct Entry Problems,” 43rd AIAA Aerospace Sciences Meeting and Exhibit, 2005, p. 389. doi:10.2514/6.2005-389.

[172] Bird, R., “Diffusion in Multicomponent Gas Mixtures,” Kagaku Kogaku, Vol. 26, 1962, pp. 718–721.

[173] Bartlett, E. P., Kendall, R. M., and Rindal, R. A., “An Analysis of the Coupled Chemically Reacting Boundary Layer and Charring Ablator Part 4-A: Unified Approximation for Mixture Transport Properties for Multicomponent Boundary-Layer Applications,” NASA CR-1063, 1968.

[174] Neitzel, K., Thermochemical Modeling of Nonequilibrium Oxygen Flows, Ph.D. thesis, Department of Aerospace Engineering, University of Michigan, 2016.

[175] Candler, G., The Computational of Weakly Ionized Flow in Nonequilibrium, Ph.D. thesis, Stanford University, 1988.

[176] Lee, J.-H., "Basic Governing Equations for the Flight Regimes of Aeroassisted Orbital Transfer Vehicles," 19th Thermophysics Conference, 1984, p. 1729. doi:10.2514/5.9781600865718.0003.0053.

[177] Hammerling, P., Teare, J., and Kivel, B., "Theory of Radiation from Luminous Shock Waves in Nitrogen," The Physics of Fluids, Vol. 2, No. 4, 1959, pp. 422–426. doi:10.1063/1.1724413.

[178] Marrone, P. V. and Treanor, C. E., "Chemical Relaxation with Preferential Dissociation from Excited Vibrational Levels," The Physics of Fluids, Vol. 6, No. 9, 1963, pp. 1215–1221. doi:10.1063/1.1706888.

[179] Treanor, C. E. and Marrone, P. V., "Effect of Dissociation on the Rate of Vibrational Relaxation," The Physics of Fluids, Vol. 5, No. 9, 1962, pp. 1022–1026. doi:10.1063/1.1724467.

[180] Park, C., "Assessment of a Two-Temperature Kinetic Model for Dissociating and Weakly Ionizing Nitrogen," Journal of Thermophysics and Heat Transfer, Vol. 2, No. 1, 1988, pp. 8–16. doi:10.2514/3.55.

[181] Park, C., "Assessment of Two-Temperature Kinetic Model for Ionizing Air," Journal of Thermophysics and Heat Transfer, Vol. 3, No. 3, 1989, pp. 233–244. doi:10.2514/3.28771.

[182] Park, C., Nonequilibrium Hypersonic Aerothermodynamics, Wiley, New York, 1990, pp. 255-306.

[183] Chaudhry, R. S., Modeling and Analysis of Chemical Kinetics for Hypersonic Flows in Air, Ph.D. thesis, University of Minnesota, 2018.

[184] Landau, L. and Teller, E., "Zur Theorie der Schalldispersion," Phys. Z. Sowjetunion, Vol. 10, No. 1, 1936, pp. 34–43.

[185] Millikan, R. C. and White, D. R., "Systematics of Vibrational Relaxation," The Journal of Chemical Physics, Vol. 39, No. 12, 1963, pp. 3209–3213. doi:10.2514/2.7036.

[186] Park, C., "Review of Chemical-Kinetic Problems of Future NASA Missions, I: Earth Entries," Journal of Thermophysics and Heat Transfer, Vol. 7, No. 3, 1993, pp. 385–398. doi:10.2514/3.431.

[187] Martinelli, S., Ruffin, S., McDaniel, R., Brown, J., Wright, M., and Hash, D., "Validation Process for Blowing and Transpiration-Cooling in DPLR," 39th AIAA Thermophysics Conference, 2007, p. 4255. doi:10.2514/6.2007-4255.

[188] Thompson, R. and Gnoffo, P., "Implementation of a Blowing Boundary Condition in the LAURA Code," 46th AIAA Aerospace Sciences Meeting and Exhibit, 2008, p. 1243. doi:10.2514/6.2008-1243.

[189] Martin, A. and Boyd, I., "Simulation of Pyrolysis Gas Within a Thermal Protection System," AIAA Paper 2008-3805, 2008. doi:10.2514/6.2008-3805.

[190] Martin, A. and Boyd, I., "Implicit Implementation of Material Response and Moving Meshes for Hypersonic Re-Entry Ablation," 2009. doi:10.2514/6.2009-670.

[191] Martin, A., Cozmuta, I., Wright, M. J., and Boyd, I. D., "Kinetic Rates for Gas-Phase Chemistry of Phenolic-Based Carbon Ablator in Atmospheric Air," Journal of Thermophysics and Heat Transfer, Vol. 29, No. 2, 2015, pp. 222–240. doi:10.2514/1.T4184.

[192] Chen, S. Y., Boyd, I. D., Martin, N. C., and Fletcher, D. G., "Modeling of Emission Spectra in Nonequilibrium Plasmas for Testing Pyrolyzing Ablators," Journal of Thermophysics and Heat Transfer, Vol. 33, No. 4, 2019, pp. 907–916. doi:10.2514/1.T5615.

[193] Alfvén, H., "Existence of Electromagnetic-Hydrodynamic Waves," Nature, Vol. 150, No. 3805, 1942, pp. 405–406. doi:10.1038/150405d0.

[194] Davidson, P. A., An Introduction to Magnetohydrodynamics, American Association of Physics Teachers, 2002.

[195] Moreau, R. J., Magnetohydrodynamics, Vol. 3, Springer Science & Business Media, 1990.

[196] Griffiths, D. J., Introduction to Electrodynamics, Prentice Hall, 1999.

[197] Hughes, W. F. and Young, F. J., The Electromagnetodynamics of Fluids, Wiley, 1966.

[198] Hosking, R. J. and Dewar, R. L., Fundamental Fluid Mechanics and Magnetohydrodynamics, Springer, 2016.

[199] Shercliff, J. A., Textbook of Magnetohydrodynamics, Pergamon Press, Oxford-New York, 1965.

[200] Bisek, N. J., Boyd, I. D., and Poggie, J., "Numerical Study of Magnetoaerodynamic Flow Around a Hemisphere," Journal of Spacecraft and Rockets, Vol. 47, No. 5, 2010, pp. 816–827. doi:10.2514/1.49278.

[201] Bush, W. B., "The Stagnation-Point Boundary Layer in the Presence of an Applied Magnetic Field," Journal of the Aerospace Sciences, Vol. 28, No. 8, 1961, pp. 610–611. doi:10.2514/8.9114.

[202] Kim, M. and Boyd, I. D., "Effectiveness of a Magnetohydrodynamics System for Mars Entry," Journal of Spacecraft and Rockets, Vol. 49, No. 6, 2012, pp. 1141–1149. doi:10.2514/1.A32256.

[203] Shang, J., Menart, J., Kimmel, R., and Hayes, J., "Hypersonic Inlet with Plasma Induced Compression," AIAA Paper 2006-0764, 2006. doi:10.2514/6.2006-764.

[204] Matsuo, T., Tadamatsu, A., and Shimasaki, M., "3-D Magnetohydrodynamic Field Computation of Supersonic Duct Flow of Weakly Ionized Plasma," IEEE transactions on magnetics, Vol. 39, No. 3, 2003, pp. 1444–1447. doi:10.1109/TMAG.2003.810169.

[205] Meyer, R. X., "Magnetohydrodynamic-Hypersonic Flow in the Quasi-Newtonian Approximation," Reviews of Modern Physics, Vol. 32, No. 4, 1960, pp. 1004. doi:10.1103/RevModPhys.32.1004.

[206] Gaitonde, D. V., "A High-Order Implicit Procedure for the 3-D Electric Field in Complex Magnetogasdynamic Simulations," Computers & Fluids, Vol. 33, No. 3, 2004, pp. 345–374. doi:10.1016/j.compfluid.2003.06.001.

[207] Mitchner, M. and Kruger Jr, C. H., Partially Ionized Gases, John Wiley and Sons, Inc., New York, 1973.

[208] Sherman, A. and Sutton, G. W., Engineering Magnetohydrodynamics, McGraw-Hill, 1965.

[209] Bisek, N., Boyd, I., and Poggie, J., "Three Dimensional Simulations of Hypersonic MHD Flow Control," 40th AIAA Plasmadynamics and Lasers Conference, 2009, p. 3731. doi:10.2514/6.2009-3731.

[210] Bisek, N., Boyd, I., and Poggie, J., "Numerical Study of Electromagnetic Aerodynamic Control of Hypersonic Vehicles," 47th AIAA Aerospace Sciences Meeting including The New Horizons Forum and Aerospace Exposition, 2009, p. 1000. doi:10.2514/6.2009-1000.

[211] Park, C., "The Limits of Two-Temperature Kinetic Model in Air," January 2010, AIAA Paper 2010-911. doi:10.2514/6.2010-911.

[212] Candler, G. V. and Maccormack, R. W., "Computation of Weakly Ionized Hypersonic Flows in Thermochemical Nonequilibrium," Journal of Thermophysics and Heat Transfer, Vol. 5, No. 3, 1991, pp. 266–273. doi:10.2514/3.260.

[213] Grasso, F. and Capano, G., "Modeling of Ionizing Hypersonic Flows in Nonequilibrium," Journal of Spacecraft and Rockets, Vol. 32, No. 2, 1995, pp. 217–224. doi:10.2514/3.26599.

[214] Josyula, E. and Bailey, W. F., "Governing Equations for Weakly Ionized Plasma Flowfields of Aerospace Vehicles," Journal of Spacecraft and Rockets, Vol. 40, No. 6, 2003, pp. 845–857. doi:10.2514/2.7036.

[215] Boyd, I. D., "Modeling of Associative Ionization Reactions in Hypersonic Rarefied Flows," Physics of Fluids, Vol. 19, No. 9, 2007, pp. 096–102. doi:10.1063/1.2771662.

[216] Grantham, W., "Flight Results of 25000 Foot per Second Blunt Body Reentry Experiment Using Microwave Reflectometers to Measure Plasma Electron Density and Standoff Distance," NASA TN D-6062, December 1970.

[217] Grantham, W. L., "Reentry Plasma Measurements using a Four Frequency Reflectometer," The Entry Plasma Sheath and Its Effects on Space Vehicle Electromagnetic Systems, Vol. 1, NASA SP-252, October 1970, pp. 65–109.

[218] Hayes, D., Herskovitz, S., Lennon, J., and Poirier, J., "Flight Test Comparison of Two Electron Attachment Techniques," Journal of Spacecraft and Rockets, Vol. 12, No. 9, 1975, pp. 515–516. doi:10.2514/3.57011.

[219] Schexnayder, C. J., Huber, P. W., and Evans, J. S., "Calculation of Electron Concentration for a Blunt Body at Orbital Speeds and Comparison with Experimental Data," NASA TN D-6294, May 1971.

[220] Jones, W. L. and Cross, A. E., "Electrostatic-Probe Measurements of Plasma Parameters for Two Reentry Flight Experiments at 25000 Feet per Second," NASA TN-D-6617, February 1972.

[221] Scharfman, W., "The Use of Langmuir Probes to Determine the Electron Density Surrounding Re-Entry Vehicles," NASA CR-66108, June 1965.

[222] Dunn, M. G. and Kang, S., "Theoretical and Experimental Studies of Reentry Plasmas," NASA CR-2232, April 1973.

[223] Blottner, F. G., "Viscous Shock Layer at the Stagnation Point with Nonequilibrium Air Chemistry," AIAA Journal, Vol. 7, No. 12, 1969, pp. 2281–2288. doi:10.2514/3.5528.

[224] Bortner, M. H., "Suggested Standard Chemical Kinetics for Flow Field Calculations - A Consensus Opinion," AMRAC Proceedings, Vol. 14, Part 1, University of Michigan Institute for Science and Technology, April 1966, pp. 569–581.

[225] Park, C., Jaffe, R. L., and Partridge, H., "Chemical-Kinetic Parameters of Hyperbolic Earth Entry," Journal of Thermophysics and Heat transfer, Vol. 15, No. 1, 2001, pp. 76–90. doi:10.2514/2.6582.

[226] Kim, J. G., "Expansion of the Equilibrium Constants for the Temperature Range of 300K to 20,000K," International Journal of Aeronautical and Space Sciences, Vol. 17, No. 4, 2016, pp. 455–466. doi:10.5139/ijass.2016.17.4.455.

[227] Gordon, S. and McBride, B. J., "Computer Program for Calculation of Complex Chemical Equilibrium Compositions and Applications. Part 1: Analysis," NASA RP-1311, October 1994.

[228] McBride, B. J., Zehe, M. J., and Gordon, S., "NASA Glenn Coefficients for Calculating Thermodynamic Properties of Individual Species," NASA TP-2002-211556, September 2002.

[229] Chaudhry, R. S. and Candler, G. V., "Statistical Analyses of Quasiclassical Trajectory Data for Air Dissociation," AIAA Paper 2019-0789, 2019. doi:10.2514/6.2019-0789.

[230] Chaudhry, R. S., Boyd, I. D., Torres, E., Schwartzentruber, T. E., and Candler, G. V., "Implementation of a Chemical Kinetics Model for Hypersonic Flows in Air for High-Performance CFD," AIAA Paper 2020-2191, 2020. doi:10.2514/6.2020-2191.

[231] Chaudhry, R. S., Bender, J. D., Schwartzentruber, T. E., and Candler, G. V., "Quasi-classical Trajectory Analysis of Nitrogen for High-Temperature Chemical Kinetics," Journal of Thermophysics and Heat Transfer, Vol. 32, No. 4, 2018, pp. 833–845. doi:10.2514/1.T5484.

[232] Laux, C. O., Gessman, R. J., and Kruger, C. H., "Ionization Nonequilibrium Induced by Neutral Chemistry in Air Plasmas," AIAA Journal, Vol. 34, No. 8, 1996, pp. 1745–1747. doi:10.2514/3.13301.

[233] Boyd, I. D., Chen, G., and Candler, G. V., "Predicting Failure of the Continuum Fluid Equations in Transitional Hypersonic Flows," Physics of Fluids, Vol. 7, No. 1, 1995, pp. 210–219. doi:10.1063/1.868720.

[234] Huber, P. W., Evans, J. S., and Schexnayder, C. J., "Comparison of Theoretical and Flight-Measured Ionization in a Blunt Body Re-Entry Flowfield," AIAA Journal, Vol. 9, No. 6, 1971, pp. 1154–1162. doi:10.2514/3.49926.

[235] NOAA, NASA, and USAF, "US Standard Atmosphere, 1976," Tech. rep., 1976.

[236] Fleming, E. L., Chandr, S., Shoeberl, M. R., and Barnett, J. J., "US Standard Atmosphere, 1976," NASA TM-100697, 1988.

[237] Candler, G., Barnhardt, M., Drayna, T., Nompelis, I., Peterson, D., and Subbareddy, P., "Unstructured Grid Approaches for Accurate Aeroheating Simulations," 18th AIAA Computational Fluid Dynamics Conference, 2007, p. 3959. doi:10.2514/6.2007-3959.

[238] Chaudhry, R. S. and Boyd, I. D., "Parametric Comparison of the Park and MMT Chemical Kinetics Models for Hypersonic Blunt Cones," AIAA AVIATION 2022 Forum, 2022, p. 3952. doi:10.2514/6.2022-3952.

[239] Wray, K. L., Teare, J., Kivel, B., and Hammerling, P., "Relaxation Processes and Reaction Rates Behind Shock Fronts in Air and Component Gases," Symposium (International) on Combustion, Vol. 8, Elsevier, 1961, pp. 328–339. doi:10.1016/S0082-0784(06)80520-5.

[240] Gimelshein, S. F. and Wysong, I. J., "Impact of the Ionization Reaction Set in Nonequilibrium Hypersonic Air Flows," AIAA Journal, Vol. 58, No. 3, 2020, pp. 1255–1265. doi:10.2514/1.J058895.

[241] Chaudhry, R. S., Boyd, I. D., and Candler, G. V., "Vehicle-Scale Simulations of Hypersonic Flows using the MMT Chemical Kinetics Model," AIAA Paper 2020-3272, 2020. doi:10.2514/6.2020-3272.

[242] Ouyang, W., Liu, Q., Zhang, Z., Jin, T., and Wu, Z., "Effect of Non-Ionizing Reaction Rate (Assumed to be Controllable) on the Plasma Generation Mechanism and Communication Around RAMC Vehicle During Atmospheric Reentry," Scientific Reports, Vol. 11, No. 1, 2021, pp. 1–10. doi:10.1038/s41598-021-99584-3.

[243] Takahashi, Y., "Advanced Validation of CFD-FDTD Combined Method Using Highly Applicable Solver for Reentry Blackout Prediction," Journal of Physics D: Applied Physics, Vol. 49, No. 1, 2015, pp. 015201. doi:10.1088/0022-3727/49/1/015201.

[244] Deyang, T. and Kun, Q., "Numerical Simulation and Analysis of Hypersonic Vehicle Plasma Sheath," 47th AIAA Plasmadynamics and Lasers Conference, 2016, p. 3229. doi:10.2514/6.2016-3229.

[245] Surzhikov, S., "Three Dimensional Simulation of Shock Layer Ionization for RAM-C II Flight Tests," 52nd Aerospace Sciences Meeting, 2014, p. 1078. doi:10.2514/6.2014-1078.

[246] Ouyang, W., Liu, Y., and Zhang, X., "Impact of Angle of Attack on Plasma Flow and Electromagnetic Wave Propagation Around Hypersonic Vehicles," Microwave and Optical Technology Letters, Vol. 62, No. 6, 2020, pp. 2270–2280. doi:10.1002/mop.32326.

[247] Candler, G. V., "Rate Effects in Hypersonic Flows," Annual Review of Fluid Mechanics, Vol. 51, 2019, pp. 379–402. doi:10.1146/annurev-fluid-010518-040258.

[248] Evans, J., Huber, P., and Schexnayder Jr, C., "Calculation of Electron Concentration for a Blunt Body at Orbital Speeds and Comparison with Experimental Data," NASA TN D-6294, May 1971.

[249] Andrienko, D., Shang, J. J., Surzhikov, S., and Huang, G. P., "Non-equilibrium Flowfield of RAM-C II Probe," 45th AIAA Plasmadynamics and Lasers Conference, 2014, p. 2376. doi:10.2514/6.2014-2376.

[250] Farbar, E., Boyd, I. D., and Martin, A., "Numerical Prediction of Hypersonic Flowfields Including Effects of Electron Translational Nonequilibrium," Journal of Thermophysics and Heat Transfer, Vol. 27, No. 4, 2013, pp. 593–606. doi:10.2514/1.T3963.

[251] Magin, T. E. and Degrez, G., "Transport Algorithms for Partially Ionized and Unmagnetized Plasmas," Journal of Computational Physics, Vol. 198, No. 2, 2004, pp. 424–449. doi:10.1016/j.jcp.2004.01.012.

[252] Sawicki, P., Chaudhry, R. S., and Boyd, I. D., "Influence of Chemical Kinetics Models on Plasma Generation in Hypersonic Flight," AIAA Journal, 2021, pp. 1–10. doi:10.2514/1.J060615.

[253] Fuhs, A., "Flight Instrumentation for Reentry Plasma Sheath," AIAA Paper 1963-0379, 1963. doi:10.2514/6.1963-379.

[254] Steiger, M., Glatt, L., Fernandez, F., Fedele, J., and Golden, K., "Re-entry Communication: Theoretical Analysis and Flight Test Results," AIAA Paper 1970-220, 1970. doi:10.2514/6.1970-220.

[255] Huber, P. W. and Sims, T., "Research Approaches to the Problem of Reentry Communications Blackout," Third Symposium on the Plasma Sheath: Plasma Electromagnetics of Hypersonic Flight, Vol. 2, AFCRL-67-0280, May 1967, pp. 95–124.

[256] Jacavanco, D. J., Electron Reduction in the Reentry Plasma Sheath, No. AFCRL-69-0154, Air Force Cambridge Research Laboratories, Office of Aerospace Research, 1969.

[257] Fay, J. A. and Riddell, F. R., "Theory of Stagnation Point Heat Transfer in Dissociated Air," Journal of the Aerospace Sciences, Vol. 25, No. 2, 1958, pp. 73–85. doi:10.2514/8.7517.

[258] Lees, L. and Kubota, T., "Inviscid Hypersonic Flow Over Blunt-Nosed Slender Bodies," Journal of the Aeronautical Sciences, Vol. 24, No. 3, 1957, pp. 195–202. doi:10.2514/8.3803.

[259] Reim, G., "Plasma blackout is not a worry for USA's hypersonic missiles: Pentagon," `https://www.flightglobal.com/fixed-wing/plasma-blackout-is-not-a-worry-for-usas-hypersonic-missiles-pentagon/138539.article`, May 2020.

[260] Acton, J. M., "Hypersonic Boost-Glide Weapons," Science & Global Security, Vol. 23, No. 3, 2015, pp. 191–219. doi:10.1080/08929882.2015.1087242.

[261] Tracy, C. L. and Wright, D., "Modeling the Performance of Hypersonic Boost-Glide Missiles," Science & Global Security, Vol. 28, No. 3, 2020, pp. 135–170. doi:10.1080/08929882.2020.1864945.

[262] Candler, G. V. and Leyva, I. A., "Computational Fluid Dynamics Analysis of the Infrared Emission From a Generic Hypersonic Glide Vehicle," Science & Global Security, 2022, pp. 1–14. doi:10.1080/08929882.2022.2145777.

[263] Dix, D., "Typical Values of Plasma Parameters Around a Conical Re-Entry Vehicle," Aerospace Corporation TDR-169(3230-22)TN-1, 1962.

[264] Savino, R., Paterna, D., De Stefano Fum, M., and DElia, M., "Plasma-Radiofrequency Interactions Around Atmospheric Re-Entry Vehicles: Modelling and Arc-Jet Simulation," The Open Aerospace Engineering Journal, Vol. 3, No. 1, 2010. doi:10.2174/1874146001003010076.

[265] Surzhikov, S., "Ionization of Air in Flow Around a Blunt Wedge at Relatively Low Hypersonic Speeds," Journal of Physics: Conference Series, Vol. 1009, IOP Publishing, 2018, p. 012022. doi:10.1088/1742-6596/1009/1/012022.

[266] Bertin, J. J., Hypersonic Aerothermodynamics, AIAA, 1994.

[267] Radcliffe, W., "Hypersonic Glide Vehicle Design Considerations," Convair Astronautics AR-G-002, 1960.

[268] Thomas, N. R., Marayikkottu Vijayan, A., and Levin, D. A., "Heat Transfer Study of a Conically Shaped Hypersonic Vehicle in Glide," AIAA SCITECH 2022 Forum, 2022, p. 1499. doi:10.2514/6.2022-1499.

[269] Li, Y., Cui, N., and Rong, S., "Trajectory Optimization for Hypersonic Boost-Glide Missile Considering Aeroheating," Aircraft Engineering and Aerospace Technology, 2009. doi:10.1108/00022660910926854.

[270] Rizvi, S., Linshu, H., Dajun, X., and Shah, S., "Trajectory Optimisation for a Rocket-Assisted Hypersonic Boost-Glide Vehicle," The Aeronautical Journal, Vol. 121, No. 1238, 2017, pp. 469–487. doi:10.1017/aer.2017.11.

[271] Vinh, N. X., Busemann, A., and Culp, R. D., Hypersonic and Planetary Entry Flight Mechanics, Vol. 81, The University of Michigan Press, 1980.

[272] Regan, F. J., Dynamics of Atmospheric Re-entry, AIAA, 1993.

[273] Council, N. R., US Conventional Prompt Global Strike: Issues for 2008 and Beyond, National Academies Press, 2008.

[274] Dormand, J. R. and Prince, P. J., "A Family of Embedded Runge-Kutta Formulae," Journal of Computational and Applied Mathematics, Vol. 6, No. 1, 1980, pp. 19–26. doi:10.1016/0771-050X(80)90013-3.

[275] Shampine, L. F. and Reichelt, M. W., "The MATLAB ODE Suite," SIAM Journal on Scientific Computing, Vol. 18, No. 1, 1997, pp. 1–22.

[276] Rataczak, J. A., McMahon, J. W., and Boyd, I. D., "Reachability Analysis of a Hypersonic Glide Vehicle using Particle Swarm Optimization," AIAA SCITECH 2023 Forum, 2023.

[277] Eggers, A. J., Allen, H. J., and Neice, S. E., "A Comparative Analysis Of The Performance Of Long-Range Hypervelocity Vehicles," NACA TR-1382, 1957.

[278] Lofthouse, A. J., Boyd, I. D., and Wright, M. J., "Effects of Continuum Breakdown on Hypersonic Aerothermodynamics," Physics of Fluids, Vol. 19, No. 2, 2007, pp. 027105. doi:10.1063/1.2710289.

[279] Schneider, S. P., "Hypersonic Laminar–Turbulent Transition on Circular Cones and Scramjet Forebodies," Progress in Aerospace Sciences, Vol. 40, No. 1-2, 2004, pp. 1–50. doi:10.1016/j.paerosci.2003.11.001.

[280] Sun, Q., Zhu, H., Wang, G., and Fan, J., "Effects of Mesh Resolution on Hypersonic Heating Prediction," Theoretical and Applied Mechanics Letters, Vol. 1, No. 2, 2011, pp. 022001. doi:10.1063/2.1102201.

[281] Ramjatan, S., Magin, T. E., Scholz, T., Van der Haegen, V., and Thoemel, J., "Blackout Analysis of Small Reentry Vehicles," 53rd AIAA Aerospace Sciences Meeting, 2015, p. 2081. doi:10.2514/6.2015-2081.

[282] Mather, D., Pasqual, J., Sillence, J., and Lewis, P., "Radio Frequency (RF) Blackout During Hypersonic Reentry," AIAA/CIRA 13th International Space Planes and Hypersonics Systems and Technologies Conference, 2005, p. 3443. doi:10.2514/6.2005-3443.

[283] Lee, S., Yang, Y., and Kim, J. G., "Evaluation of Fay and Riddell Formula Under Hypersonic Flight Conditions," International Journal of Numerical Methods for Heat & Fluid Flow, , No. ahead-of-print, 2022. doi:10.1108/HFF-01-2022-0051.

[284] Ramjatan, S., Magin, T., Scholz, T., Van der Haegen, V., and Thoemel, J., "Blackout Analysis of Small Cone-Shaped Reentry Vehicles," Journal of Thermophysics and Heat Transfer, Vol. 31, No. 2, 2017, pp. 269–282. doi:10.2514/1.T4825.

[285] MADSON, J., "Plasma Quench Investigations: Tungsten-Oxide Quenchants," 17th Aerospace Sciences Meeting, 1979, p. 253. doi:10.2514/6.1979-253.

[286] Luo, Q. and D'Angelo, N., "Observations of Dusty Plasmas with Magnetized Dust Grains," Journal of Physics D: Applied Physics, Vol. 33, No. 21, 2000, pp. 2754. doi:10.1088/0022-3727/33/21/313.

[287] Sims, T. and Jones, R., "Rocket Exhaust Effects on Radio Frequency Propogation From a Scout Vehicle and Signal Recovery During the Injection of Decomposed Hydrogen Peroxide," NASA TM X-529, 1961.

[288] Beckwith, I. E., "Injection, Distribution, and Evaporation of Liquids in the Flow Fields of Hypersonic Vehicles," Communicating Through Plasmas of Atmospheric Entry and Rocket Exhaust (declassified), NASA SP-52, January 1964, pp. 191–203.

[289] Parmentier, E. M., Wray, K. L., and Weiss, R. F., "Aerophysical Plasma Alleviation," The Entry Plasma Sheath and Its Effects on Space Vehicle Electromagnetic Systems, Vol. 1, NASA SP-252, October 1970, pp. 579–616.

[290] Hunter, S., Carter, J., and Christophorou, L., "Low Energy Electron Attachment to SF6 in N2, Ar, and Xe Buffer Gases," The Journal of Chemical Physics, Vol. 90, No. 9, 1989, pp. 4879–4891. doi:10.1063/1.456582.

[291] Kowari, K.-i., Leung, K., and Shizgal, B. D., "The Coupling of Electron Thermalization and Electron Attachment in CCl 4/Ar and CCl 4/Ne mixtures," The Journal of Chemical Physics, Vol. 108, No. 4, 1998, pp. 1587–1600. doi:10.1063/1.475353.

[292] Akey, N. D. and Cross, A. E., "Radio Blackout Alleviation and Plasma Diagnostic Results From a 25,000 Foot Per Second Blunt-Body Reentry," NASA TN-D-5615, February 1970.

[293] Cuddihy, W. F., "Results of the RAM B2 Material-Addition Flight Experiment," Communicating Through Plasmas of Atmospheric Entry and Rocket Exhaust (declassified), NASA SP-52, January 1964, pp. 203–213.

[294] Schroeder, L., Sims, T., and Cuddihy, W., "Experiment T-1: Reentry Communication on Gemini III," Manned Space Flight Experiments Symposium: Gemini Missions III and IV, NASA SP-252, October 1965, pp. 81–105.

[295] Hayes, D., Herskovitz, S., Lennon, J., and Poirier, J., "Electrostatic Probe Measurements of Chemical Injection Effects During a Re-Entry Flight Test," Journal of Spacecraft and Rockets, Vol. 11, No. 6, 1974, pp. 388–394. doi:10.2514/3.62086.

[296] Weaver, W. L., "Multiple-Orifice Liquid Injection into Hypersonic Air Streams and Application to RAM C-III Flight," NASA TM-X-2486, February 1972.

[297] Ingebo, R. D. and Foster, H. H., "Drop-Size Distribution for Cross Current Breakup of Liquid Jets in Airstreams," NACA TN-4087, October 1957.

[298] Gooderum, P. B. and Bushnell, D. M., "Atomization, Drop Size, and Penetration for Cross-Stream Water Injection at High-Altitude Reentry Conditions With Application to the RAM C-1 and C-3 Flights," NASA TN D-6747, July 1972.

[299] Misra, S., Mishra, S., and Sodha, M., "Kinetics of Complex Plasma with Liquid Droplets," Physics of Plasmas, Vol. 20, No. 12, 2013, pp. 123701. doi:10.1063/1.4839195.

[300] Aisenberg, S. and Nien Hu, P., "The Removal of Free Electrons in a Thermal Plasma by Means of Rapidly Evaporating Liquid Additives," The Entry Plasma Sheath and Its Effects on Space Vehicle Electromagnetic Systems, Vol. 1, NASA SP-252, October 1970, pp. 617–622.

[301] Pergament, H., Mikatarian, R., and Kurzius, S., "Prediction of Electron Concentration Reductions in Re-Entry Flow Fields Due to Electrophilic Liquid and Water Injection," 1972.

[302] Papa, R. J., "Chemical Injection into a Reentry Plasma to Improve High Power EM Wave Transmission," AFCRL 72-0556, Air Force Cambridge Research Laboratories, September 1972.

[303] Sodha, M. and Evans, J., "Reduction of Electron Density in a Plasma by Injection of Liquids," Applied Scientific Research, Vol. 29, No. 1, 1974, pp. 380–398. doi:10.1007/BF00384160.

[304] Beckwith, I. E. and Huffman, J. K., "Injection and Distribution of Liquids in the Flow Fields of Blunt Shapes at Hypersonic Speeds (declassified)," NASA TM X-989, August 1964.

[305] Kersey, J., Loth, E., and Lankford, D., "Effect of Evaporating Droplets on Shock Wave Attenuation," 46th AIAA Aerospace Sciences Meeting and Exhibit, 2008, p. 793. doi:10.2514/6.2008-793.

[306] Bose, T. K., "High Temperature Gas Dynamics," High Temperature Gas Dynamics, Springer, 2004, pp. 259–281.

[307] Williams, F. A., Combustion Theory, CRC Press, 2018.

[308] Langmuir, I., "The Evaporation of Small Spheres," Physical review, Vol. 12, No. 5, 1918, pp. 368.

[309] Hill, P. G., "Condensation of Water Vapour During Supersonic Expansion in Nozzles," Journal of Fluid Mechanics, Vol. 25, No. 3, 1966, pp. 593–620.

[310] Horn, K., Bevc, V., and Kolpin, M., "Evaporation of a Droplet in Free Molecular Flow," AIAA Journal, Vol. 5, No. 9, 1967, pp. 1692–1694. doi:10.1017/S0022112066000284.

[311] Chen, X. and Pfender, E., "Heat Transfer to a Single Particle Exposed to a Thermal Plasma," Plasma Chemistry and Plasma Processing, Vol. 2, No. 2, 1982, pp. 185–212.

[312] Chen, X. and Pfender, E., "Effect of the Knudsen Number on Heat Transfer to a Particle Immersed into a Thermal Plasma," Plasma Chemistry and Plasma Processing, Vol. 3, No. 1, 1983, pp. 97–113.

[313] Pergament, H. S. and Kau, C.-j., "A Computer Code to Predict the Effects of Electrophilic Liquid Injection on Re-Entry Plasma Sheath Properties." Tech. rep., Aerochem Research Labs Inc., Princeton NJ, 1974.

[314] Schexnayder, C. J., Evans, J. S., and Bushnell, D. M., "Stream-tube Analysis Used to Calculate Electron Concentration in the Presence of Accelerating and Evaporating Water Droplets," NASA TN D-6007, 1970.

[315] Moukalled, F. and Darwish, M., "Mixing and Evaporation of Liquid Droplets Injected into an Air Stream Flowing at All Speeds," Physics of Fluids, Vol. 20, No. 4, 2008, pp. 040804. doi:10.1063/1.2912127.

[316] Daso, E. O., Pritchett, V. E., Wang, T.-S., Ota, D. K., Blankson, I. M., and Auslender, A. H., "Dynamics of Shock Dispersion and Interactions in Supersonic Freestreams with Counterflowing Jets," AIAA Journal, Vol. 47, No. 6, 2009, pp. 1313–1326. doi:10.2514/1.30084.

[317] Miyashita, T., Takasawa, H., Takahashi, Y., Oshima, N., Steffens, L., Esser, B., and Guelhan, A., "Numerical Study on Mitigation of Reentry Blackout by Effects of Airfilm," AIAA SCITECH 2022 Forum, 2022, p. 2150. doi:10.2514/6.2022-2150.

[318] Kuhns, P. W. and Cooper, D. W., "Effect of Water Addition on Microwave Transmission Through a Simulated Reentry Plasma Layer," Communicating Through Plasmas of Atmospheric Entry and Rocket Exhaust (declassified), NASA SP-52, January 1964, pp. 105–114.

[319] Sutton, K., Butler, D. H., and Zoby, E. V., "An Evaluation Test of a Full Scale Replica of the RAM-CA Flight Heat Shield in a Rocket Engine Exhaust," NASA TN X-1841, July 1969.

[320] Weaver, W. L. and Hinson, W. F., "Water Injection From a Nine Degree Hemisphere-Cone Into a Hypersonic Airstream," NASA TN D-5739, March 1970.

[321] Sawicki, P., Campbell, N. S., and Boyd, I. D., "Effect of Water Vapor Injection on Plasma Reduction in Hypersonic Flow," AIAA SCITECH 2023 Forum, January 2023.

[322] Caldelas II, H. L., Experimental Design of Electrophilic Gas Injection System for Plasma Blackout Mitigation during Hypersonic Reentry, Master's thesis, Massachusetts Institute of Technology, 2021.

[323] Grainger, "Solenoid Valves and Globe Control Valves," Item# 53AY35 Mfr. Model # 8210G095LF.

[324] Mehra, N., Singh, R. K., and Bera, S. C., "Mitigation of Communication Blackout during Re-Entry Using Static Magnetic Field," Progress In Electromagnetics Research B, Vol. 63, 2015, pp. 161–172.

[325] Thoma, C., Rose, D., Miller, C., Clark, R., and Hughes, T., "Electromagnetic Wave Propagation through an Overdense Magnetized Collisional Plasma Layer," Journal of Applied Physics, Vol. 106, No. 4, 2009, pp. 043301. doi:10.1063/1.3195085.

[326] Kundrapu, M., Loverich, J., Beckwith, K., Stoltz, P., Shashurin, A., and Keidar, M., "Modeling Radio Communication Blackout and Blackout Mitigation in Hypersonic Vehicles," Journal of Spacecraft and Rockets, Vol. 52, No. 3, 2015, pp. 853–862. doi:10.2514/1.A33122.

[327] Usui, H., Matsumoto, H., Yamashita, F., Yamane, M., and Takenaka, S., "Computer Experiments on Radio Blackout of a Reentry Vehicle," 6th Spacecraft Charging Technology, 1998, pp. 107–110.

[328] Shang, J., Kimmel, R., Hayes, J., Tyler, C., and Menart, J., "Hypersonic Experimental Facility for Magnetoaerodynamic Interactions," Journal of Spacecraft and Rockets, Vol. 42, No. 5, 2005, pp. 780–789. doi:10.2514/1.8579.

[329] Jones, J. E., An Assessment of Microwave-Generated Plasmas for use in Magnetohydrodynamic Accelerators, Ph.D. thesis, The University of Alabama in Huntsville, 2000.

[330] Bisek, N. J., Gosse, R., and Poggie, J., “Computational Study of Impregnated Ablator for Improved Magnetohydrodynamic Heat Shield,” Journal of Spacecraft and Rockets, Vol. 50, No. 5, 2013, pp. 927–936. doi:10.2514/1.A32357.

[331] Robinson, W. and Gerwin, R., “MHD Flight Control for Hypersonic Vehicles,” 10th AIAA/NAL-NASDA-ISAS International Space Planes and Hypersonic Systems and Technologies Conference, 2001, p. 1884. doi:10.2514/6.2001-1884.

[332] Bush, W. B., “Magnetohydrodynamic-Hypersonic Flow Past a Blunt Body,” Journal of the Aerospace Sciences, Vol. 25, No. 11, 1958, pp. 685–690. doi:10.2514/8.7845.

[333] Sutton, G. W. and Sherman, A., Engineering Magnetohydrodynamics, Courier Dover Publications, 2006.

[334] Korotaeva, T., Fomichev, V., and Yadrenkin, M., “Numerical and Experimental Simulation of Magnetohydrodynamic Interaction in a Hypersonic Flow of a Blunt Body,” Journal of Applied Mechanics and Technical Physics, Vol. 61, No. 2, 2020, pp. 162–170. doi:10.1134/S0021894420020029.

[335] Fujino, T., Sugita, H., Mizuno, M., Funaki, I., and Ishikawa, M., “Influences of Electrical Conductivity of Wall on Magnetohydrodynamic Control of Aeroynamic Heating,” Journal of Spacecraft and Rockets, Vol. 43, No. 1, 2006, pp. 63–70. doi:10.2514/1.A33340.

[336] Kim, M., Keidar, M., and Boyd, I., “Numerical Modeling of Plasma Manipulation Using an ExB Layer in the Hypersonic Boundary Layer,” 40th AIAA Plasmadynamics and Lasers Conference, 2009, p. 3732. doi:10.2514/6.2009-3732.

[337] Bisek, N., Gosse, R., and Poggie, J., “Use of Impregnated Ablator for Improved Magnetohydrodynamic-Heat Shield Concept,” 42nd AIAA Plasmadynamics and Lasers Conference in conjunction with the 18th International Conference on MHD Energy Conversion (ICMHD), 2011, p. 3468. doi:10.2514/6.2011-3468.

[338] Poggie, J. and Gaitonde, D. V., “Magnetic Control of Flow Past a Blunt Body: Numerical Validation and Exploration,” Physics of Fluids, Vol. 14, No. 5, 2002, pp. 1720–1731. doi:10.1063/1.1465424.

[339] Resler Jr, E. and Sears, W., “The Prospects for Magneto-Aerodynamics,” Journal of the Aerospace Sciences, Vol. 25, No. 4, 1958, pp. 235–245.

[340] Asinovsky, E., Kirillin, A., Pakhomov, E., and Shabashov, V., “Experimental Investigation of Transport Properties of Low-Temperature Plasma by Means of Electric Arc,” Proceedings of the IEEE, Vol. 59, No. 4, 1971, pp. 592–601. doi:10.1109/PROC.1971.8220.

[341] Resler Jr, E. and Sears, W., “The Prospects for Magneto-Aerodynamics: Correction and Addition,” Journal of the Aerospace Sciences, Vol. 26, No. 5, 1959, pp. 318–318.

[342] Rosa, R. J., “Magnetohydrodynamic Energy Conversion,” 1987.

[343] Chapman, S. and Cowling, T. G., *The Mathematical Theory of Non-uniform Gases: An Account of the Kinetic Theory of Viscosity, Thermal Conduction and Diffusion in Gases*, Cambridge University Press, 1990.

[344] Spitzer Jr, L. and Härm, R., “Transport Phenomena in a Completely Ionized Gas,” *Physical Review*, Vol. 89, No. 5, 1953, pp. 977.

[345] Raizer, Y. P. and Allen, J. E., *Gas Discharge Physics*, Vol. 1, Springer, 1991.

[346] Godin, D. and Trépanier, J., “A Robust and Efficient Method for the Computation of Equilibrium Composition in Gaseous Mixtures,” *Plasma chemistry and plasma processing*, Vol. 24, No. 3, 2004, pp. 447–473. doi:10.1007/s11090-004-2279-8.

[347] Lamb, L. and Lin, S.-C., “Electrical Conductivity of Thermally Ionized Air Produced in a Shock Tube,” *Journal of Applied Physics*, Vol. 28, No. 7, 1957, pp. 754–759. doi:10.1063/1.1722849.

[348] Koritz, H. and Keck, J., “Technique for Measuring the Electrical Conductivity of Wakes of Projectiles at Hypersonic Speeds,” *Review of Scientific Instruments*, Vol. 35, No. 2, 1964, pp. 201–208. doi:10.1063/1.1718778.

[349] Lin, S.-C., Resler, E., and Kantrowitz, A., “Electrical Conductivity of Highly Ionized Argon Produced by Shock Waves,” *Journal of Applied Physics*, Vol. 26, No. 1, 1955, pp. 95–109. doi:10.1063/1.1721870.

[350] Boyd, I. D. and Josyula, E., “Analysis of Associative Ionization Rates for Hypersonic Flows,” *Journal of Thermophysics and Heat Transfer*, Vol. 35, No. 3, 2021, pp. 484–493. doi:10.2514/1.T6109.

[351] Torres, E., Gross, T., Geistfeld, E., and Schwartzentruber, T., “Verification of Nonequilibrium Thermochemistry Models for Hypersonic CFD by First-Principles Simulation,” 2022.

[352] Candler, G. V., “Advanced CFD Methods for Hypervelocity Wind Tunnels,” AFRL OSR-VA-TR-2012-0875, 2011.

[353] Giangaspero, V. F., Lani, A., Poedts, S., Thoemel, J., and Munafò, A., “Radio Communication Blackout Analysis of ExoMars re-entry Mission Using Raytracing Method,” *AIAA Scitech 2021 Forum*, 2021, p. 0154. doi:10.2514/6.2021-0154.

[354] Liu, Z., Bao, W., Li, X., Shi, L., and Liu, D., “Influences of Turbulent Reentry Plasma Sheath on Wave Scattering and Propagation,” *Plasma Science and Technology*, Vol. 18, No. 6, 2016, pp. 617.

[355] Yang, M., Li, X., Wang, D., Liu, Y., and He, P., “Propagation of Phase Modulation Signals in Time-Varying Plasma,” *Aip Advances*, Vol. 6, No. 5, 2016, pp. 055110. doi:10.1063/1.4950694.

[356] Sotnikov, V., Leboeuf, J.-N., and Mudaliar, S., "Scattering of Electromagnetic Waves in the Presence of Wave Turbulence Excited by a Flow With Velocity Shear," IEEE transactions on plasma science, Vol. 38, No. 9, 2010, pp. 2208–2218.

[357] Cross, P. G. and Boyd, I. D., "Two-Dimensional Modeling of Ablation and Pyrolysis with Application to Rocket Nozzles," Journal of Spacecraft and Rockets, Vol. 54, No. 1, 2017, pp. 212–224. doi:10.2514/1.A33656.

APPENDIX A

PROJECT RAM FLIGHT MEASUREMENTS

Chapters 3 and 5 utilized raw data points taken from the plasma diagnostic instrumentation onboard the RAM-C II and I flights, respectively. Although this data is tabulated in raw form in Refs. [216, 220], due to its poor quality of transcription it is not readily usable. Therefore, the data has been tabulated here for ease of reuse.

A.1 RAM-C II Reflectometer Data

Table A.1: Inferred electron number densities measured by the reflectometers onboard the RAM-C II flight. Reproduced from [216].

Reflectometer Station	x (cm)	Frequency Band	Electron Number Density (m^{-3})	Altitude (km)	
				Onset	Decay
1	4.47	S	1.39E+17	84	22
		X	1.25E+18	80	28
		Ka	1.52E+19	72	29
2	23.16	L	1.54E+16	84	23
		S	1.39E+17	78	24
		X	1.25E+18	70	29
		Ka	1.52E+19	38	31
3	70.05	L	1.54E+16	82	25
		S	1.39E+17	74	26
		X	1.25E+18	52	31
		Ka	1.52E+19	-	-
4	106.04	L	1.54E+16	80	26
		S	1.39E+17	72	28
		X	1.25E+18	50	36
		Ka	1.52E+19	-	-

A.2 RAM-C II Electrostatic Probe Data

Table A.2: Inferred electron number densities measured by the electrostatic probe 1 on the RAM-C II flight. Reproduced from [220].

Altitude (m)	N_e (m^{-3})	Altitude (m)	N_e (m^{-3})	Altitude (m)	N_e (m^{-3})	Altitude (m)	N_e (m^{-3})	Altitude (m)	N_e (m^{-3})
85740.2	6.18E+13	82430.7	5.45E+14	79304.7	2.38E+15	76173.5	4.55E+15	73025.2	1.64E+16
85694.8	6.18E+13	82376.8	5.58E+14	79209.6	2.86E+15	76119.5	5.02E+15	72970.6	1.83E+16
85641.8	6.18E+13	82281.4	5.31E+14	79156.0	2.75E+15	76065.3	5.45E+15	72874.6	2.23E+16
85548.5	6.18E+13	82227.4	5.35E+14	79102.0	3.01E+15	75969.9	6.96E+15	72819.5	2.63E+16
85494.6	6.18E+13	82172.9	5.57E+14	79008.4	2.31E+15	75915.0	8.18E+15	72760.3	2.80E+16
85440.6	6.18E+13	82077.5	5.38E+14	78954.5	2.22E+15	75859.8	8.88E+15	72664.0	2.59E+16
85345.8	6.19E+13	82023.2	6.19E+14	78900.5	2.34E+15	75759.6	8.00E+15	72609.5	2.34E+16
85291.6	6.18E+13	81969.0	6.20E+14	78806.3	2.12E+15	75704.7	8.72E+15	72554.9	2.34E+16
85237.3	6.19E+13	81873.6	6.22E+14	78762.2	2.10E+15	75650.1	8.01E+15	72460.1	1.94E+16
85141.9	6.19E+13	81818.1	6.96E+14	78706.7	2.61E+15	75554.4	6.65E+15	72405.9	1.94E+16
85088.0	6.19E+13	81763.2	7.28E+14	78612.8	3.24E+15	75499.6	6.82E+15	72351.9	2.13E+16
85033.7	6.19E+13	81659.0	6.63E+14	78559.5	3.79E+15	75445.0	6.99E+15	72257.4	2.49E+16
84938.6	6.81E+13	81604.1	7.16E+14	78506.1	3.98E+15	75349.0	7.17E+15	72202.9	2.95E+16
84884.4	6.19E+13	81548.9	7.27E+14	78411.6	4.25E+15	75293.8	8.22E+15	72148.6	3.46E+16
84829.8	6.19E+13	81452.9	6.39E+14	78358.0	4.18E+15	75238.7	1.30E+16	72054.1	4.29E+16
84734.1	6.20E+13	81398.4	6.83E+14	78303.7	3.58E+15	75142.0	8.23E+15	72000.5	4.52E+16
84675.0	7.37E+13	81343.5	7.25E+14	78208.3	3.20E+15	75087.2	8.04E+15	71947.1	4.25E+16
84468.6	6.20E+13	81248.1	8.40E+14	78153.8	3.02E+15	75032.6	7.85E+15	71853.9	3.34E+16
84413.8	8.51E+13	81193.8	8.91E+14	78099.2	3.11E+15	74936.6	9.90E+15	71800.2	3.10E+16
84318.0	1.01E+14	81139.6	9.13E+14	78003.2	3.21E+15	74881.4	9.35E+15	71754.2	3.10E+16
84262.6	7.95E+13	81044.5	1.04E+15	77948.3	3.44E+15	74826.3	1.03E+16	71660.3	3.06E+16
84207.4	9.61E+13	80990.5	9.59E+14	77893.2	3.75E+15	74727.8	1.21E+16	71606.4	3.26E+16
84110.5	1.17E+14	80936.6	1.09E+15	77796.9	4.12E+15	74674.8	1.32E+16	71552.4	3.50E+16
84053.8	7.38E+13	80842.4	8.15E+14	77734.7	4.34E+15	74620.2	1.36E+16	71457.9	3.89E+16
83898.0	1.02E+14	80788.8	8.67E+14	77679.8	4.34E+15	74524.2	1.03E+16	71434.8	4.12E+16
83845.9	1.78E+14	80742.7	8.79E+14	77584.4	4.43E+15	74469.0	1.01E+16	71350.6	4.30E+16
83793.8	1.32E+14	80636.7	8.68E+14	77529.5	4.06E+15	74413.9	8.62E+15	71256.1	4.30E+16
83698.7	9.97E+13	80595.5	8.94E+14	77474.7	4.43E+15	74317.3	8.96E+15	71202.2	4.39E+16
83643.5	1.44E+14	80542.2	1.02E+15	77379.0	4.43E+15	74262.4	8.63E+15	71148.2	4.44E+16
83588.4	1.19E+14	80447.4	1.13E+15	77324.4	4.69E+15	74207.8	8.45E+15	71053.2	4.86E+16
83492.0	1.12E+14	80394.4	1.34E+15	77270.2	4.79E+15	74111.8	9.05E+15	70998.3	5.26E+16
83437.8	1.06E+14	80340.1	1.66E+15	77175.1	4.79E+15	74056.7	9.57E+15	70944.0	5.64E+16
83383.5	7.48E+13	80245.0	1.48E+15	77121.4	4.52E+15	74001.5	1.06E+16	70847.1	5.93E+16
83289.0	8.11E+13	80190.4	1.36E+15	77067.8	4.28E+15	73904.9	1.19E+16	70789.2	5.64E+16
83235.1	1.63E+14	80135.9	1.32E+15	76974.2	4.02E+15	73850.0	1.19E+16	70734.0	5.31E+16
83181.1	2.89E+14	80037.4	1.27E+15	76920.2	3.61E+15	73795.4	1.13E+16	70638.0	4.98E+16
83086.4	3.84E+14	79987.4	1.26E+15	76866.3	3.96E+15	73699.4	9.77E+15	70570.7	4.35E+16
83032.7	5.25E+14	79930.5	1.39E+15	76780.3	4.37E+15	73644.3	8.66E+15	70527.7	4.21E+16
82978.8	4.74E+14	79834.1	1.47E+15	76727.0	5.55E+15	73589.1	8.10E+15	70431.1	4.53E+16
82884.3	3.65E+14	79779.0	1.90E+15	76674.0	6.60E+15	73492.5	1.11E+16	70376.2	5.10E+16
82831.2	3.72E+14	79716.2	1.83E+15	76580.4	3.36E+15	73437.6	1.21E+16	70321.6	5.99E+16
82777.9	3.40E+14	79619.9	1.72E+15	76526.4	6.93E+15	73383.0	1.28E+16	70225.6	8.54E+16
82692.2	3.85E+14	79564.7	1.81E+15	76472.5	6.16E+15	73287.0	1.35E+16	70170.5	5.64E+16
82637.1	4.17E+14	79502.5	2.14E+15	76377.7	5.01E+15	73231.9	1.42E+16	70115.3	9.81E+16
82581.6	5.33E+14	79429.4	1.85E+15	76323.4	4.54E+15	73176.7	1.45E+16	70018.4	7.65E+16
82484.7	5.09E+14	79359.3	2.21E+15	76268.9	4.72E+15	73080.1	1.45E+16	69963.2	6.74E+16

Table A.2 (Continued)

Altitude (m)	N_e (m^{-3})	Altitude (m)	N_e (m^{-3})	Altitude (m)	N_e (m^{-3})	Altitude (m)	N_e (m^{-3})	Altitude (m)	N_e (m^{-3})
69908.0	6.11E+16	66772.2	1.10E+17	63637.7	2.73E+17	60516.8	4.65E+17	57357.9	2.38E+17
69811.4	5.64E+16	66718.6	1.17E+17	63583.1	3.25E+17	60422.0	5.05E+17	57303.3	2.83E+17
69752.3	5.65E+16	66664.6	1.36E+17	63487.1	4.96E+17	60368.1	5.30E+17	57249.1	3.35E+17
69697.1	6.17E+16	66570.5	2.04E+17	63431.9	5.67E+17	60314.4	5.30E+17	57154.3	6.74E+17
69606.9	7.19E+16	66516.8	2.67E+17	63376.8	6.16E+17	60220.0	5.03E+17	57100.6	7.73E+17
69546.5	7.96E+16	66462.6	3.30E+17	63279.8	3.70E+17	60165.7	5.74E+17	57047.3	8.12E+17
69492.3	8.05E+16	66384.5	3.01E+17	63224.7	3.10E+17	60111.7	6.00E+17	56954.0	7.90E+17
69397.2	8.33E+16	66315.3	2.86E+17	63169.5	3.34E+17	60016.6	6.98E+17	56900.1	7.44E+17
69342.6	8.26E+16	66261.4	2.60E+17	63072.9	3.21E+17	59962.1	7.18E+17	56846.4	7.18E+17
69288.4	8.05E+16	66166.6	2.29E+17	63018.0	3.33E+17	59906.6	6.23E+17	56760.2	7.02E+17
69193.3	8.85E+16	66112.0	2.47E+17	62902.5	3.67E+17	59802.4	3.64E+17	56706.5	7.15E+17
69139.6	9.86E+16	66057.2	2.65E+17	62867.4	3.67E+17	59747.8	2.87E+17	56652.6	7.39E+17
69086.0	1.10E+17	65961.2	2.78E+17	62812.3	3.66E+17	59693.3	2.50E+17	56558.1	6.64E+17
68992.4	1.28E+17	65906.6	2.78E+17	62757.1	3.07E+17	59597.9	2.37E+17	56504.4	5.52E+17
68939.1	1.29E+17	65852.0	3.39E+17	62660.5	2.54E+17	59543.0	2.85E+17	56450.8	4.43E+17
68885.7	1.18E+17	65752.4	1.93E+17	62605.6	2.54E+17	59488.1	2.96E+17	56356.6	2.73E+17
68792.8	8.98E+16	65696.9	1.76E+17	62551.1	2.66E+17	59392.4	4.92E+17	56302.4	2.66E+17
68746.7	7.95E+16	65641.7	1.57E+17	62454.4	3.64E+17	59338.2	6.65E+17	56247.8	2.77E+17
68694.6	7.36E+16	65545.1	1.99E+17	62399.9	4.85E+17	59283.6	6.85E+17	56152.1	4.21E+17
68598.6	6.84E+16	65490.6	2.13E+17	62344.7	6.96E+17	59188.8	6.63E+17	56097.8	5.23E+17
68545.3	7.62E+16	65435.7	3.16E+17	62248.1	7.56E+17	59135.2	6.11E+17	56043.3	6.55E+17
68491.9	9.76E+16	65340.0	3.84E+17	62193.2	7.55E+17	59081.5	5.84E+17		
68397.7	1.51E+17	65284.5	4.59E+17	62138.7	6.54E+17	58987.9	5.58E+17		
68343.5	1.81E+17	65229.3	4.09E+17	62043.0	3.60E+17	58935.8	6.59E+17		
68289.2	1.98E+17	65132.7	2.94E+17	61988.1	3.26E+17	58880.4	6.58E+17		
68193.8	1.62E+17	65078.2	2.06E+17	61933.5	3.01E+17	58794.4	6.06E+17		
68139.0	1.11E+17	65023.3	2.16E+17	61837.5	3.01E+17	58741.1	4.65E+17		
68085.3	1.35E+17	64927.6	1.95E+17	61778.4	3.00E+17	58688.0	3.55E+17		
67990.2	1.17E+17	64872.1	1.45E+17	61723.2	3.58E+17	58594.5	2.67E+17		
67936.0	1.16E+17	64816.9	1.95E+17	61626.9	3.80E+17	58540.5	2.55E+17		
67881.4	1.26E+17	64720.3	2.60E+17	61572.0	3.57E+17	58486.2	2.55E+17		
67778.1	1.38E+17	64665.8	2.92E+17	61517.2	3.39E+17	58391.5	3.32E+17		
67723.5	1.46E+17	64580.4	3.18E+17	61421.5	3.56E+17	58336.9	4.81E+17		
67669.0	1.56E+17	64515.2	3.19E+17	61367.5	3.55E+17	58282.3	6.49E+17		
67573.6	1.42E+17	64460.3	2.91E+17	61313.6	4.25E+17	58186.9	8.11E+17		
67518.7	1.34E+17	64405.8	2.78E+17	61219.4	6.42E+17	58132.1	7.90E+17		
67463.8	1.30E+17	64310.1	3.30E+17	61165.4	7.39E+17	58077.5	7.38E+17		
67368.4	1.45E+17	64254.6	3.17E+17	61112.1	8.20E+17	57981.2	6.45E+17		
67314.5	1.75E+17	64199.4	3.78E+17	61018.2	6.93E+17	57926.9	6.29E+17		
67260.5	2.56E+17	64102.8	5.04E+17	60964.3	5.38E+17	57811.1	6.44E+17		
67166.6	2.96E+17	64047.9	4.31E+17	60910.6	3.52E+17	57768.7	6.83E+17		
67112.4	2.96E+17	63993.4	3.41E+17	60816.7	2.57E+17	57713.6	6.62E+17		
67058.4	2.82E+17	63897.7	2.62E+17	60771.3	2.44E+17	57658.7	6.41E+17		
66964.0	1.96E+17	63842.8	2.12E+17	60718.0	2.68E+17	57556.6	3.47E+17		
66910.6	1.54E+17	63788.2	2.01E+17	60624.7	2.93E+17	57507.8	3.11E+17		
66857.6	1.31E+17	63692.5	2.36E+17	60570.8	3.60E+17	57453.3	2.62E+17		

Table A.3: Inferred electron number densities measured by the electrostatic probe 8 on the RAM-C II flight. Reproduced from [220].

Altitude (m)	$\mathrm{N_e}$ ($\mathrm{m^{-3}}$)	Altitude (m)	$\mathrm{N_e}$ ($\mathrm{m^{-3}}$)	Altitude (m)	$\mathrm{N_e}$ ($\mathrm{m^{-3}}$)	Altitude (m)	$\mathrm{N_e}$ ($\mathrm{m^{-3}}$)	Altitude (m)	$\mathrm{N_e}$ ($\mathrm{m^{-3}}$)
85701.5	5.01E+13	82588.6	9.06E+14	79462.0	7.29E+15	76330.2	1.75E+16	73183.4	6.43E+16
85648.5	9.00E+13	82533.1	1.05E+15	79366.3	7.99E+15	76275.6	1.59E+16	73128.2	6.43E+16
85595.2	1.30E+14	82437.4	1.14E+15	79311.7	9.27E+15	76221.3	1.56E+16	73032.2	6.54E+16
85501.3	1.10E+14	82383.5	1.37E+15	79257.1	1.05E+16	76126.2	1.73E+16	72977.4	6.78E+16
85447.3	8.00E+13	82329.2	1.55E+15	79164.5	1.28E+16	76072.0	1.96E+16	72922.8	8.30E+16
85393.1	1.45E+14	82234.1	2.12E+15	79124.0	1.22E+16	76017.7	2.38E+16	72826.5	1.11E+17
85298.3	5.50E+13	82179.6	2.00E+15	79055.4	1.13E+16	75922.0	2.18E+16	72771.0	1.19E+17
85244.0	6.00E+13	82125.0	1.87E+15	78955.1	8.27E+15	75866.9	3.47E+16	72712.2	1.01E+17
85189.5	6.00E+13	82029.9	2.03E+15	78907.2	7.44E+15	75811.7	3.50E+16	72631.4	8.28E+16
85094.7	6.99E+13	81975.7	2.18E+15	78853.3	7.24E+15	75711.7	3.08E+16	72568.0	6.95E+16
85040.4	1.20E+14	81921.4	1.92E+15	78759.4	7.14E+15	75656.9	2.75E+16	72507.4	6.22E+16
84986.2	2.09E+14	81825.4	2.35E+15	78729.2	7.92E+15	75602.3	2.62E+16	72412.6	5.97E+16
84891.1	2.69E+14	81770.2	2.42E+15	78659.7	1.01E+16	75506.6	2.73E+16	72358.6	6.03E+16
84836.5	2.99E+14	81707.4	2.45E+15	78566.2	1.59E+16	75451.1	2.82E+16	72304.7	6.59E+16
84782.0	3.19E+14	81610.8	2.42E+15	78512.5	2.31E+16	75397.2	3.00E+16	72209.9	9.43E+16
84682.0	2.21E+14	81556.0	2.35E+15	78459.2	2.29E+16	75300.8	3.10E+16	72155.6	1.10E+17
84626.8	2.49E+14	81501.1	2.15E+15	78364.7	1.80E+16	75245.4	3.20E+16	72101.4	1.54E+17
84571.6	2.24E+14	81405.1	2.18E+15	78310.4	1.51E+16	75190.2	3.07E+16	72007.2	1.56E+17
84475.3	1.91E+14	81350.5	2.33E+15	78255.9	1.27E+16	75094.2	2.84E+16	71953.8	1.54E+17
84420.8	2.29E+14	81296.0	2.70E+15	78160.5	1.06E+16	75039.3	2.80E+16	71901.1	1.31E+17
84365.9	2.39E+14	81200.6	3.81E+15	78105.9	9.78E+15	74984.8	3.14E+16	71806.9	9.20E+16
84270.8	2.60E+14	81146.3	5.12E+15	78051.1	1.11E+16	74888.5	3.80E+16	71760.9	8.61E+16
84214.4	3.03E+14	81085.9	5.99E+15	77955.0	1.23E+16	74832.4	4.57E+16	71707.3	9.20E+16
84159.2	3.44E+14	80997.3	6.11E+15	77900.2	1.36E+16	74777.8	5.69E+16	71613.1	8.41E+16
84060.8	2.71E+14	80943.3	5.40E+15	77845.0	1.53E+16	74681.8	6.58E+16	71559.7	9.19E+16
84003.8	3.54E+14	80889.4	4.38E+15	77741.4	1.75E+16	74626.9	6.30E+16	71505.2	1.03E+17
83947.1	4.58E+16	80794.3	3.29E+15	77686.8	1.73E+16	74572.4	5.23E+16	71411.0	1.07E+17
83852.3	8.11E+13	80741.8	3.01E+15	77632.3	1.70E+16	74476.1	3.89E+16	71357.3	1.17E+17
83800.5	6.37E+13	80695.8	2.92E+15	77536.6	1.63E+16	74420.6	3.35E+16	71303.4	1.20E+17
83748.4	6.92E+16	80602.2	3.44E+15	77481.7	1.66E+16	74365.4	3.14E+16	71208.9	1.20E+17
83650.2	5.40E+14	80548.9	3.86E+15	77426.8	1.73E+16	74269.4	3.09E+16	71155.0	1.22E+17
83595.1	5.80E+14	80495.6	5.09E+15	77331.4	1.86E+16	74214.5	3.45E+16	71100.7	1.22E+17
83540.2	5.40E+14	80401.1	7.37E+15	77276.9	1.95E+16	74158.8	4.16E+16	71005.3	1.40E+17
83444.5	4.17E+14	80346.8	8.21E+15	77222.6	1.91E+16	74063.7	6.15E+16	70950.4	1.52E+17
83390.5	4.46E+14	80292.6	7.75E+15	77128.1	1.73E+16	74008.2	7.01E+16	70895.3	1.63E+17
83336.3	4.26E+14	80196.8	6.99E+15	77074.5	1.66E+16	73953.0	1.05E+17	70799.3	1.52E+17
83241.8	4.61E+14	80142.9	5.81E+15	77020.8	1.53E+16	73857.0	7.69E+16	70740.7	1.42E+17
83187.8	5.59E+14	80088.3	5.72E+15	76927.0	1.48E+16	73802.1	6.55E+16	70685.9	1.27E+17
83133.9	7.27E+14	79992.3	5.33E+15	76873.0	1.47E+16	73747.6	5.72E+16	70589.9	1.07E+17
83037.9	1.26E+15	79937.5	5.34E+15	76819.4	1.55E+16	73651.3	5.03E+16	70534.4	1.07E+17
82985.5	1.71E+15	79882.3	5.74E+15	76733.7	2.23E+16	73595.8	4.77E+16	70479.2	1.09E+17
82931.5	2.06E+15	79786.0	6.37E+15	76680.7	2.81E+16	73528.4	4.89E+16	70382.9	1.34E+17
82837.6	1.54E+15	79723.2	6.74E+15	76627.3	4.02E+16	73444.6	5.50E+16	70328.3	1.50E+17
82784.6	1.12E+15	79668.0	6.75E+15	76533.2	3.61E+16	73389.7	5.71E+16	70273.5	1.67E+17
82731.3	9.66E+14	79571.7	7.08E+15	76479.2	2.99E+16	73335.2	6.01E+16	70177.5	2.38E+17
82644.1	8.43E+14	79516.8	6.87E+15	76424.9	2.39E+16	73238.9	6.31E+16	70122.0	2.52E+17

Table A.3 (Continued)

Altitude (m)	N_e (m^{-3})	Altitude (m)	N_e (m^{-3})	Altitude (m)	N_e (m^{-3})	Altitude (m)	N_e (m^{-3})	Altitude (m)	N_e (m^{-3})
70066.8	2.34E+17	66864.3	3.00E+17	63740.4	7.69E+17	60577.5	7.58E+17	57460.0	7.60E+17
69970.2	1.72E+17	66810.9	2.36E+17	63642.5	7.69E+17	60523.5	7.58E+17	57405.4	7.60E+17
69914.7	1.53E+17	66725.3	2.66E+17	63589.8	7.69E+17	60469.3	7.58E+17	57310.0	7.60E+17
69859.6	1.44E+17	66671.3	2.77E+17	63535.0	7.68E+17	60375.1	7.58E+17	57261.9	7.60E+17
69759.0	1.47E+17	66617.4	2.91E+17	63438.9	7.68E+17	60321.1	7.58E+17	57201.5	7.60E+17
69703.8	1.39E+17	66523.5	3.39E+17	63383.5	7.68E+17	60267.2	7.58E+17	57107.3	7.60E+17
69648.9	1.52E+17	66469.9	4.20E+17	63328.3	7.67E+17	60172.7	7.58E+17	57054.0	7.61E+17
69553.2	1.56E+17	66416.2	4.52E+17	63231.7	7.67E+17	60118.5	7.58E+17	57000.7	7.61E+17
69499.0	1.66E+17	66322.0	4.52E+17	63176.2	7.67E+17	60064.2	7.58E+17	56906.8	7.61E+17
69444.7	1.64E+17	66268.1	4.06E+17	63121.0	7.66E+17	59968.5	7.58E+17	56853.1	7.61E+17
69349.6	1.63E+17	66214.1	3.78E+17	63025.0	7.66E+17	59913.3	7.58E+17	56806.5	7.61E+17
69310.3	1.61E+17	66118.7	3.82E+17	62970.2	7.65E+17	59857.5	7.58E+17	56713.2	7.61E+17
69240.5	1.69E+17	66064.2	3.60E+17	62915.6	7.65E+17	59754.5	7.58E+17	56653.2	7.61E+17
69146.3	1.86E+17	66009.0	3.73E+17	62819.3	7.65E+17	59700.0	7.58E+17	56605.3	7.62E+17
69092.7	1.99E+17	65913.3	3.81E+17	62763.8	7.64E+17	59645.4	7.58E+17	56511.8	7.62E+17
69039.0	2.03E+17	65858.8	3.96E+17	62708.6	7.63E+17	59549.7	7.58E+17	56457.5	7.62E+17
68945.5	2.39E+17	65800.2	3.59E+17	62612.6	7.63E+17	59495.1	7.58E+17	56403.9	7.62E+17
68892.4	2.19E+17	65703.9	3.29E+17	62557.8	7.63E+17	59440.3	7.58E+17	56309.1	7.62E+17
68839.1	2.12E+17	65648.7	3.17E+17	62503.2	7.62E+17	59344.9	7.58E+17	56254.5	7.62E+17
68753.4	1.80E+17	65593.6	3.17E+17	62406.9	7.62E+17	59290.3	7.58E+17	56203.0	7.62E+17
68699.5	1.63E+17	65495.4	3.61E+17	62351.4	7.62E+17	59236.7	7.58E+17	56104.5	7.63E+17
68645.8	1.51E+17	65442.7	3.85E+17	62296.2	7.61E+17	59141.9	7.58E+17		
68552.0	1.74E+17	65387.8	4.49E+17	62200.2	7.61E+17	59088.2	7.58E+17		
68498.3	1.93E+17	65291.5	7.78E+17	62145.4	7.61E+17	59035.5	7.58E+17		
68445.0	2.04E+17	65236.3	7.77E+17	62090.8	7.61E+17	58941.0	7.58E+17		
68365.4	2.66E+17	65187.3	7.77E+17	61994.8	7.60E+17	58887.1	7.58E+17		
68295.9	3.53E+17	65084.9	6.89E+17	61940.2	7.60E+17	58833.4	7.58E+17		
68239.8	4.35E+17	65030.3	5.70E+17	61885.4	7.60E+17	58747.8	7.58E+17		
68146.3	3.61E+17	64975.4	4.64E+17	61785.4	7.60E+17	58694.4	7.58E+17		
68092.3	3.06E+17	64879.1	4.24E+17	61730.2	7.60E+17	58641.1	7.58E+17		
68037.8	2.79E+17	64824.0	4.36E+17	61675.1	7.59E+17	58547.2	7.58E+17		
67942.7	2.55E+17	64768.8	5.04E+17	61579.1	7.59E+17	58493.0	7.58E+17		
67888.1	2.58E+17	64672.5	5.85E+17	61524.2	7.59E+17	58438.7	7.58E+17		
67833.5	2.51E+17	64617.9	7.53E+17	61469.3	7.59E+17	58343.6	7.58E+17		
67730.2	2.68E+17	64563.0	7.73E+17	61374.2	7.59E+17	58289.3	7.58E+17		
67675.7	2.68E+17	64467.3	7.73E+17	61320.3	7.59E+17	58234.8	7.59E+17		
67621.1	2.82E+17	64412.5	7.73E+17	61266.3	7.59E+17	58139.1	7.59E+17		
67525.7	2.63E+17	64373.2	7.72E+17	61172.1	7.58E+17	58084.2	7.59E+17		
67470.8	2.54E+17	64261.6	7.72E+17	61118.5	7.58E+17	58029.4	7.59E+17		
67416.3	2.61E+17	64206.4	7.71E+17	61065.2	7.58E+17	57933.6	7.59E+17		
67321.2	2.85E+17	64149.7	7.71E+17	60971.0	7.58E+17	57879.1	7.59E+17		
67267.2	3.16E+17	64055.6	7.71E+17	60917.3	7.58E+17	57816.6	7.59E+17		
67213.6	4.05E+17	64000.1	7.70E+17	60863.7	7.58E+17	57720.6	7.59E+17		
67065.1	7.42E+17	63945.5	7.70E+17	60777.7	7.58E+17	57665.7	7.59E+17		
67011.2	5.64E+17	63849.8	7.70E+17	60724.7	7.58E+17	57610.6	7.59E+17		
66917.3	3.36E+17	63794.9	7.70E+17	60671.4	7.58E+17	57514.9	7.60E+17		

A.3 RAM-C I Electrostatic Probe Data

Table A.4: Inferred electron number densities measured by the electrostatic probe 3 on the RAM-C I flight. Reproduced from [220].

Altitude (m)	N_e (m^{-3})	Altitude (m)	N_e (m^{-3})	Altitude (m)	N_e (m^{-3})	Altitude (m)	N_e (m^{-3})	Altitude (m)	N_e (m^{-3})
83181.4	7.08E+14	80327.9	5.18E+15	77382.9	1.62E+16	74413.3	2.71E+16	71475.3	2.35E+16
83130.5	7.29E+14	80276.7	5.81E+15	77293.3	1.61E+16	74361.8	2.74E+16	71424.4	1.28E+16
83041.2	7.19E+14	80187.1	7.43E+15	77242.7	1.66E+16	74310.2	2.71E+16	71335.1	2.10E+16
82990.9	7.75E+14	80135.6	7.27E+15	77192.1	1.78E+16	74220.0	2.33E+16	71284.5	3.88E+16
82940.7	7.98E+14	80084.1	8.40E+15	77103.4	1.84E+16	74167.9	2.33E+16	71234.2	4.88E+16
82852.6	8.87E+14	79993.8	7.19E+15	77053.1	1.93E+16	74110.0	2.30E+16	71144.3	5.35E+16
82802.6	9.86E+14	79940.8	6.87E+15	77002.8	1.86E+16	74024.6	2.27E+16	71092.8	6.25E+16
82752.6	9.98E+14	79890.5	6.87E+15	76915.4	1.58E+16	73972.2	1.62E+16	71041.3	6.25E+16
82672.4	1.03E+15	79799.4	5.98E+15	76866.9	1.36E+16	73919.5	2.25E+16	70951.0	5.81E+14
82621.8	9.34E+14	79739.3	6.56E+15	76818.4	1.15E+16	73828.0	2.61E+16	70899.5	5.37E+14
82571.2	9.57E+14	79686.6	6.80E+15	76740.7	1.26E+16	73775.9	2.65E+16	70848.3	7.03E+14
82482.2	9.68E+14	79595.2	7.45E+15	76690.7	1.55E+16	73725.0	2.63E+16	70754.7	4.46E+14
82431.3	9.72E+14	79543.4	6.56E+15	76641.4	1.76E+16	73634.8	2.44E+16	70704.5	4.41E+14
82380.4	1.11E+15	79491.8	7.45E+15	76552.7	2.05E+16	73583.3	3.79E+16	70653.9	5.67E+14
82291.1	1.01E+15	79401.6	6.73E+15	76502.4	2.16E+16	73530.0	2.90E+16	70565.2	1.29E+15
82240.5	1.08E+15	79350.1	6.81E+15	76451.8	2.33E+16	73441.6	2.99E+16	70513.7	1.10E+16
82189.9	1.09E+15	79298.6	7.45E+15	76363.4	2.47E+16	73389.4	2.66E+16	70463.1	1.10E+16
82100.9	1.08E+15	79209.0	8.58E+15	76312.8	2.38E+16	73337.3	2.63E+16	70371.9	1.59E+16
82049.7	1.15E+15	79157.8	7.99E+15	76262.2	2.31E+16	73246.5	2.63E+16	70319.8	2.31E+16
81998.8	1.20E+15	79106.9	1.10E+16	76176.2	2.02E+16	73195.0	2.68E+16	70268.0	2.20E+16
81909.2	1.24E+15	79017.6	1.13E+16	76122.3	1.98E+16	73143.5	2.64E+16	70177.2	3.39E+16
81857.4	1.44E+15	78966.1	1.18E+16	76071.1	1.64E+16	73053.2	2.77E+16	70125.6	4.48E+16
81805.3	1.32E+15	78914.9	1.13E+16	75980.5	1.32E+16	73001.1	2.92E+16	70074.1	5.09E+16
81707.1	1.48E+15	78825.5	9.15E+15	75926.9	1.64E+16	72949.3	7.94E+15	69983.6	6.14E+16
81655.6	1.53E+15	78775.6	8.60E+15	75872.6	1.35E+16	72858.2	9.60E+15	69931.8	6.49E+16
81604.1	1.58E+15	78733.2	7.79E+15	75775.1	1.34E+16	72806.7	9.04E+15	69879.7	6.35E+16
81512.7	1.70E+15	78645.4	5.92E+15	75723.0	1.44E+16	72751.5	9.24E+15	69788.5	6.13E+16
81462.7	1.75E+15	78594.8	4.48E+15	75670.9	1.82E+16	72661.3	9.06E+15	69732.8	4.98E+16
81411.2	1.73E+15	78543.9	7.55E+15	75580.0	2.14E+16	72609.5	9.72E+15	69680.9	5.60E+16
81320.9	1.63E+15	78455.2	1.17E+16	75528.5	2.57E+16	72557.6	5.27E+16	69590.1	4.18E+16
81269.7	1.87E+15	78404.6	1.31E+16	75477.0	2.51E+16	72467.7	4.80E+16	69537.7	3.00E+16
81224.6	1.54E+15	78354.0	1.51E+16	75386.8	2.40E+16	72416.5	4.62E+16	69485.6	2.13E+16
81129.2	2.00E+15	78265.3	1.67E+16	75334.7	2.33E+16	72365.6	4.49E+16	69394.7	5.88E+16
81078.6	2.39E+15	78214.1	1.58E+16	75282.9	2.28E+16	72276.9	3.13E+16	69343.5	6.50E+16
81028.0	3.10E+15	78162.6	1.46E+16	75191.7	2.19E+16	72226.0	2.73E+16	69292.0	6.95E+16
80939.9	3.84E+15	78072.4	1.30E+16	75139.6	2.22E+16	72175.4	2.91E+16	69202.4	8.28E+16
80889.0	4.30E+15	78020.9	1.17E+16	75087.5	2.90E+16	72087.0	3.76E+16	69151.5	9.68E+16
80838.4	4.35E+15	77969.4	1.17E+16	74996.6	2.24E+16	72036.1	4.10E+16	69100.3	1.03E+17
80744.0	3.80E+15	77878.8	8.46E+15	74944.5	2.25E+16	71985.2	2.65E+16	69011.6	8.35E+16
80704.9	3.22E+15	77827.3	8.99E+15	74892.4	8.11E+15	71927.0	6.26E+14	68961.3	7.95E+16
80657.7	2.95E+15	77775.8	1.12E+16	74801.6	7.62E+15	71845.9	5.75E+14	68911.0	9.00E+15
80569.9	3.12E+15	77678.3	1.41E+16	74750.1	1.00E+16	71795.3	6.16E+14	68820.2	4.29E+15
80519.0	3.38E+15	77627.1	1.53E+16	74698.6	1.24E+16	71714.6	6.88E+14	68780.6	1.03E+15
80468.1	3.58E+15	77575.9	1.58E+16	74608.3	1.13E+16	71664.6	5.95E+14	68730.0	1.29E+15
80379.1	4.13E+15	77486.0	1.55E+16	74556.2	2.72E+16	71613.7	6.94E+14	68641.6	2.64E+16
66917.3	3.36E+17	77434.4	1.66E+16	74504.7	2.75E+16	71526.2	2.69E+16	68591.3	2.97E+16

Table A.4 (Continued)

Altitude (m)	$\mathrm{N_e}$ ($\mathrm{m^{-3}}$)	Altitude (m)	$\mathrm{N_e}$ ($\mathrm{m^{-3}}$)	Altitude (m)	$\mathrm{N_e}$ ($\mathrm{m^{-3}}$)
68541.0	4.10E+16	63518.2	1.48E+16	58307.3	8.73E+17
68452.6	5.45E+16	62832.7	5.63E+14	58218.3	1.00E+18
68401.4	6.35E+16	62780.9	5.40E+14	58166.8	1.00E+18
68350.5	7.28E+16	62728.8	4.76E+14	58115.3	1.00E+18
68260.9	8.42E+16	62638.8	4.76E+14	58024.8	4.86E+16
68210.0	9.47E+16	62350.5	1.86E+15	57973.0	1.73E+17
68159.1	1.11E+16	61022.2	9.23E+15	57921.1	3.44E+17
68069.2	2.70E+15	60972.8	3.77E+16	57822.7	2.31E+16
68015.8	6.08E+16	60886.5	4.02E+15	57771.2	5.02E+14
67962.5	2.68E+16	60835.9	8.78E+15	57720.0	5.39E+14
67869.8	8.68E+15	60793.0	7.79E+14	57630.4	3.53E+17
67818.3	1.01E+15	60704.3	1.51E+16	57579.2	3.53E+17
67759.2	1.15E+16	60462.0	6.06E+17	57528.0	3.89E+16
67669.3	3.42E+15	60411.4	5.89E+17	57438.6	9.95E+17
67618.1	4.02E+15	60322.4	5.55E+17	57387.1	9.95E+17
67566.8	2.50E+16	60271.2	4.73E+17	57335.9	9.95E+17
67478.8	5.21E+16	60219.9	3.65E+17	57247.2	9.94E+17
67038.9	6.41E+16	60130.0	2.56E+17	57198.2	9.94E+17
66987.4	6.83E+15	60078.8	4.49E+16	57149.4	9.94E+17
66897.8	6.83E+15	60030.7	1.40E+16	56827.2	5.80E+14
66850.3	4.37E+15	59937.7	1.34E+15	56777.2	3.87E+14
66807.3	8.14E+15	59885.3	1.56E+15	56689.1	4.59E+14
66720.1	6.47E+15	59832.8	3.09E+15	56637.6	8.75E+16
66672.6	2.97E+15	59733.5	1.05E+16	56586.4	3.54E+17
66625.6	1.06E+16	59682.3	6.34E+15	56496.8	3.44E+17
66064.8	7.97E+14	59631.1	3.44E+15	56446.8	5.32E+17
65974.3	4.45E+14	59541.5	2.28E+17	56396.5	9.93E+17
65920.6	8.63E+15	59489.6	2.80E+17	56308.1	9.93E+17
65869.4	1.32E+16	59438.1	3.93E+17	56256.3	9.93E+17
65775.2	1.18E+16	59348.5	6.73E+17	56204.5	9.92E+17
65727.1	1.26E+16	59297.0	8.65E+17	56114.0	9.92E+17
65678.6	9.26E+16	59245.8	1.02E+18	55923.2	3.90E+14
64977.3	8.55E+14	59156.8	8.19E+17	55871.4	3.04E+14
64923.6	9.30E+14	59106.2	6.04E+17	55724.8	2.86E+14
64873.3	7.35E+14	59055.9	4.04E+17	55643.4	3.90E+14
64783.4	7.98E+14	58973.9	2.69E+15	55623.0	3.14E+17
64735.3	7.98E+14	58917.2	7.91E+15	55533.3	1.68E+17
64687.1	8.44E+14	58866.6	2.69E+15	55481.2	1.45E+17
64002.5	6.20E+14	58786.2	2.07E+16	55429.4	3.24E+17
63950.1	6.55E+14	58736.2	2.52E+16	55338.3	5.32E+17
63900.4	6.03E+14	58685.9	3.08E+16	55286.8	9.90E+17
63807.7	5.57E+14	58598.1	2.77E+17	55235.6	9.90E+17
63756.5	4.75E+14	58547.5	3.55E+17	55145.0	9.90E+17
63704.4	5.86E+14	58497.2	4.01E+17	55092.9	1.08E+16
63614.8	5.28E+14	58408.8	5.35E+17	55041.1	5.64E+14
63567.0	1.22E+16	58358.2	6.40E+17	54950.3	4.78E+14

Table A.5: Inferred electron number densities measured by the electrostatic probe 4 on the RAM-C I flight. Reproduced from [220].

Altitude (m)	N_e (m^{-3})	Altitude (m)	N_e (m^{-3})	Altitude (m)	N_e (m^{-3})	Altitude (m)	N_e (m^{-3})	Altitude (m)	N_e (m^{-3})
83124.1	7.34E+14	80270.3	7.25E+15	77286.9	2.10E+16	74355.4	3.83E+16	71418.0	1.60E+16
83050.1	7.81E+14	80180.7	8.57E+15	77236.3	2.18E+16	74303.8	3.47E+16	71328.7	2.49E+16
82984.5	8.34E+14	80129.2	8.41E+15	77185.7	2.20E+16	74213.6	2.47E+16	71278.1	4.97E+16
82934.3	8.50E+14	80077.7	8.13E+15	77097.3	2.26E+16	74161.5	2.41E+16	71227.2	5.71E+16
82846.5	9.51E+14	79987.4	8.06E+15	77046.7	2.27E+16	74109.4	2.45E+16	71137.9	7.02E+16
82796.2	1.02E+15	79933.8	8.21E+15	77002.5	2.22E+16	74018.2	2.48E+16	71086.4	7.39E+16
82744.4	1.06E+15	79883.8	7.84E+15	76909.3	2.08E+16	73965.5	2.41E+16	71034.9	7.57E+16
82667.6	1.12E+15	79792.7	7.48E+15	76860.8	1.76E+16	73913.1	2.50E+16	70944.6	4.28E+14
82615.4	1.08E+15	79732.6	7.63E+15	76812.3	1.39E+16	73821.6	3.75E+16	70893.1	2.22E+14
82564.8	1.10E+15	79680.2	8.29E+15	76734.6	1.77E+16	73770.1	3.78E+16	70841.9	6.74E+14
82475.8	1.09E+15	79588.8	8.00E+15	76684.3	1.90E+16	73718.6	2.82E+16	70748.3	5.45E+14
82424.9	1.05E+15	79537.0	8.00E+15	76634.3	2.06E+16	73628.4	2.29E+16	70696.8	5.62E+14
82374.0	1.03E+15	79484.2	8.51E+15	76546.3	2.18E+16	73576.9	4.98E+16	70647.8	6.07E+14
82291.1	1.01E+15	79395.2	8.30E+15	76496.0	2.43E+16	73525.4	4.17E+16	70558.8	9.03E+15
82234.1	1.17E+15	79343.7	8.23E+15	76445.7	2.84E+16	73434.9	4.52E+16	70507.3	2.05E+16
82183.5	1.25E+15	79292.2	9.38E+15	76357.3	3.11E+16	73383.0	3.75E+16	70455.7	2.16E+16
82094.5	1.18E+15	79202.6	1.09E+16	76306.4	2.84E+16	73326.7	3.33E+16	70365.5	2.16E+16
82043.6	1.28E+15	79151.4	1.25E+16	76255.8	2.44E+16	73240.1	3.41E+16	70313.4	2.82E+16
81992.4	1.45E+15	79100.5	1.35E+16	76166.8	2.18E+16	73188.6	3.56E+16	70261.3	2.99E+16
81902.5	1.38E+15	79010.9	1.49E+16	76115.9	2.10E+16	73137.1	3.89E+16	70170.8	4.67E+16
81850.7	1.44E+15	78959.7	1.43E+16	76064.7	1.98E+16	73046.8	4.23E+16	70119.2	5.70E+16
81798.9	1.67E+15	78908.5	1.43E+16	75973.8	1.82E+16	72994.7	2.33E+16	70067.7	6.07E+16
81698.6	1.79E+15	78819.5	1.06E+16	75919.9	1.98E+16	72942.6	3.44E+15	69977.2	7.43E+16
81649.2	1.93E+15	78769.5	9.58E+15	75865.9	1.66E+16	72851.8	1.13E+16	69925.1	7.42E+16
81597.7	1.97E+15	78727.1	8.88E+15	75768.4	1.45E+16	72800.9	1.16E+16	69873.3	7.22E+16
81507.8	2.09E+15	78639.3	6.92E+15	75716.6	2.17E+16	72745.1	9.26E+15	69778.2	7.02E+16
81456.3	1.70E+15	78588.4	6.25E+15	75666.3	2.38E+16	72654.9	1.07E+16	69726.4	7.21E+16
81404.8	1.81E+15	78537.8	7.89E+15	75573.6	2.43E+16	72603.1	7.85E+15	69674.2	6.24E+16
81314.5	1.72E+15	78448.8	1.49E+16	75522.1	2.85E+16	72551.2	6.72E+16	69583.4	5.02E+16
81263.3	1.62E+15	78398.5	1.88E+16	75470.6	2.65E+16	72461.3	6.02E+16	69531.3	3.78E+16
81212.1	2.18E+15	78347.9	2.10E+16	75380.4	2.44E+16	72410.1	5.59E+16	69479.2	2.60E+16
81122.8	2.16E+15	78258.9	2.11E+16	75328.3	2.41E+16	72359.2	5.37E+16	69388.3	6.86E+16
81072.2	3.14E+15	78207.7	2.17E+16	75276.2	2.43E+16	72270.5	4.35E+16	69338.0	7.39E+16
81021.9	3.08E+15	78156.2	2.03E+16	75185.0	2.40E+16	72219.9	4.08E+16	69285.6	8.17E+16
80933.5	4.62E+15	78066.0	1.68E+16	75133.2	2.40E+16	72169.3	4.25E+16	69196.0	9.81E+16
80882.6	5.16E+15	78014.5	1.49E+16	75080.5	2.46E+16	72080.6	4.82E+16	69145.1	1.02E+17
80830.2	5.46E+15	77962.7	1.40E+16	74989.9	2.41E+16	72029.7	5.18E+16	69093.9	1.08E+17
80744.0	4.56E+15	77872.4	1.05E+16	74938.1	2.30E+16	71978.8	2.18E+15	69005.2	7.91E+16
80700.4	4.05E+15	77820.9	1.09E+16	74886.0	9.69E+15	71890.1	6.72E+14	68954.9	9.24E+16
80651.6	3.39E+15	77761.8	1.40E+16	74795.2	1.04E+16	71839.5	5.61E+14	68904.9	1.28E+16
80563.5	4.10E+15	77671.9	1.93E+16	74743.7	1.35E+16	71788.9	6.15E+14	68817.1	4.84E+15
80512.6	4.62E+15	77620.7	2.06E+16	74692.2	1.92E+16	71708.5	5.46E+14	68774.2	1.66E+15
80461.7	4.56E+15	77569.5	2.16E+16	74601.6	2.44E+16	71658.5	7.33E+14	68723.6	1.44E+15
80372.7	4.62E+15	77479.6	2.09E+16	74549.8	3.65E+16	71608.2	5.82E+14	68635.2	3.52E+16
80321.5	6.36E+15	77428.0	2.17E+16	74497.7	4.27E+16	71519.8	3.43E+16	68584.9	4.37E+16
66917.3	3.36E+17	77376.5	2.14E+16	74406.9	4.07E+16	71468.9	2.42E+16	68528.5	5.06E+16

Table A.5 (Continued)

Altitude (m)	N_e (m^{-3})	Altitude (m)	N_e (m^{-3})	Altitude (m)	N_e (m^{-3})
68446.2	6.42E+16	62774.2	2.68E+14	58300.9	8.97E+17
68395.0	7.64E+16	62722.4	4.33E+14	58211.9	8.96E+17
68344.1	8.51E+16	62632.7	3.64E+14	58160.4	8.96E+17
68254.5	9.82E+16	62344.1	1.10E+16	58108.6	8.96E+17
68203.6	1.04E+17	61065.2	1.23E+17	58018.4	6.01E+16
68152.7	1.08E+16	61016.1	1.81E+17	57966.3	2.16E+17
68062.4	6.65E+16	60966.7	2.34E+16	57914.7	2.92E+17
68009.1	5.52E+16	60880.1	9.81E+15	57816.3	9.41E+15
67955.8	6.57E+16	60829.5	4.94E+16	57764.8	5.28E+14
67863.1	2.14E+16	60786.9	1.58E+16	57713.6	4.59E+14
67811.9	1.49E+15	60697.9	2.78E+16	57624.0	3.59E+17
67752.5	1.94E+16	60506.2	4.89E+17	57572.8	3.82E+17
67662.9	2.72E+15	60455.6	6.16E+17	57521.6	4.42E+17
67611.7	1.54E+16	60405.0	6.30E+17	57432.2	8.93E+17
67560.4	3.11E+16	60316.0	6.29E+17	57380.7	8.92E+17
67032.8	2.16E+16	60264.8	6.00E+17	57329.5	8.92E+17
66982.5	3.70E+15	60213.5	4.48E+17	57241.1	8.92E+17
66894.5	9.11E+15	60123.6	2.85E+17	57192.1	8.92E+17
66843.9	7.27E+15	60072.4	2.02E+16	57143.3	8.92E+17
66800.9	6.16E+15	60021.2	1.64E+16	56863.2	3.98E+14
66714.0	8.97E+15	59931.0	4.30E+15	56820.8	5.25E+14
66666.5	2.40E+15	59878.6	3.14E+15	56631.2	1.11E+17
66618.9	1.93E+16	59826.1	7.87E+15	56580.0	3.59E+17
66534.8	5.11E+15	59727.1	1.99E+16	56490.7	4.09E+17
66058.7	5.45E+14	59675.9	1.31E+16	56440.7	6.17E+17
65967.9	1.02E+15	59624.7	4.76E+16	56390.4	8.91E+17
65915.4	1.40E+16	59534.8	2.84E+17	56301.7	8.90E+17
65861.2	1.80E+16	59483.2	3.62E+17	56249.9	8.90E+17
65769.1	1.34E+16	59431.7	4.83E+17	56198.1	8.90E+17
65721.0	1.08E+16	59341.8	9.03E+17	56107.6	8.90E+17
65672.8	9.92E+16	59290.6	9.02E+17	56057.0	4.76E+14
64970.9	1.10E+15	59239.4	9.02E+17	56006.4	4.41E+14
64918.7	1.10E+15	59150.4	9.01E+17	55917.4	4.41E+14
64866.6	1.05E+15	59100.1	7.29E+17	55865.0	4.30E+14
64777.6	1.05E+15	59049.8	2.86E+15	55718.4	4.07E+14
64729.2	1.02E+15	58961.4	8.66E+15	55667.5	2.73E+14
64681.0	7.95E+14	58910.8	1.75E+16	55616.6	3.37E+17
63998.9	4.67E+14	58860.2	1.57E+15	55526.9	1.70E+17
63946.1	5.13E+14	58779.8	1.31E+16	55474.8	2.83E+17
63893.7	5.87E+14	58729.8	3.80E+16	55422.1	4.10E+17
63802.0	4.90E+14	58679.8	3.58E+16	55331.9	7.21E+17
63749.8	4.90E+14	58591.7	3.38E+17	55280.4	8.91E+17
63698.0	5.13E+14	58541.4	4.11E+17	55216.7	8.91E+17
63560.6	1.38E+16	58490.8	4.80E+17	55138.6	8.91E+17
63512.1	1.59E+16	58402.4	5.93E+17	55086.5	1.04E+17
62826.3	2.68E+14	58351.8	7.82E+17	55034.4	4.32E+14

Table A.6: Inferred electron number densities measured by the electrostatic probe 5 on the RAM-C I flight. Reproduced from [220].

Altitude (m)	N_e (m^{-3})	Altitude (m)	N_e (m^{-3})	Altitude (m)	N_e (m^{-3})	Altitude (m)	N_e (m^{-3})	Altitude (m)	N_e (m^{-3})
85052.9	4.26E+14	82177.1	1.06E+15	79196.2	1.09E+16	76300.3	2.96E+16	73324.5	3.86E+16
84962.7	4.16E+14	82088.1	1.10E+15	79145.0	1.22E+16	76249.4	2.80E+16	73233.7	3.91E+16
84910.6	4.32E+14	82037.2	1.19E+15	79094.1	1.32E+16	76160.4	2.18E+16	73182.2	3.94E+16
84858.1	4.42E+14	81986.0	1.15E+15	79004.5	1.35E+16	76109.5	2.11E+16	73130.7	4.26E+16
84767.6	4.79E+14	81899.2	1.10E+15	78953.3	1.36E+16	76058.3	2.00E+16	73040.1	4.67E+16
84712.8	4.79E+14	81844.3	1.36E+15	78902.1	1.27E+16	75967.1	1.85E+16	72988.3	3.16E+15
84661.9	4.74E+14	81792.5	1.37E+15	78813.1	1.08E+16	75913.2	1.85E+16	72936.2	1.32E+16
84571.9	4.85E+14	81694.0	1.60E+15	78763.1	9.81E+15	75859.2	1.35E+16	72845.4	1.32E+16
84519.8	4.43E+14	81642.8	1.47E+15	78720.7	8.52E+15	75762.0	1.03E+16	72793.9	1.49E+16
84468.0	4.80E+14	81591.3	1.84E+15	78632.9	7.24E+15	75709.9	2.32E+16	72738.7	1.40E+16
84377.2	4.56E+14	81501.4	1.61E+15	78582.0	6.68E+15	75658.1	2.31E+16	72648.8	1.26E+16
84325.7	4.56E+14	81449.9	1.84E+15	78531.4	8.61E+15	75567.2	3.58E+16	72596.7	1.22E+16
84274.2	5.17E+14	81398.4	1.69E+15	78442.7	1.59E+16	75516.9	3.48E+16	72544.8	7.04E+16
84184.8	5.27E+14	81306.9	1.76E+15	78392.1	1.92E+16	75464.2	3.38E+16	72454.9	6.38E+16
84134.2	5.06E+14	81256.9	1.73E+15	78341.5	2.05E+16	75373.7	2.68E+16	72404.0	6.10E+16
84084.0	5.06E+14	81205.7	1.54E+15	78252.5	2.13E+16	75321.9	2.62E+16	72353.1	5.66E+16
83994.7	4.80E+14	81116.4	2.07E+15	78201.3	2.08E+16	75269.8	2.41E+16	72264.1	4.68E+16
83942.5	4.85E+14	81065.8	2.44E+15	78149.8	1.93E+16	75178.6	2.32E+16	72213.5	4.57E+16
83890.4	5.17E+14	81015.5	3.33E+15	78059.6	1.67E+16	75126.8	2.41E+16	72162.9	4.68E+16
83799.6	5.33E+14	80927.1	3.61E+15	78008.1	1.59E+16	75074.7	2.49E+16	72074.2	5.30E+16
83747.5	5.49E+14	80876.5	4.43E+15	77956.3	1.36E+16	74983.5	2.39E+16	72023.3	5.85E+16
83691.7	5.65E+14	80825.9	4.63E+15	77866.0	1.14E+16	74931.4	1.82E+16	71972.4	1.48E+15
83601.8	5.96E+14	80737.9	3.06E+15	77814.5	1.18E+16	74879.3	1.17E+16	71883.7	6.97E+14
83551.5	6.33E+14	80695.5	3.70E+15	77755.4	1.47E+16	74788.8	1.50E+16	71833.1	6.38E+14
83501.5	6.38E+14	80645.2	3.66E+15	77665.5	1.94E+16	74737.3	1.86E+16	71782.5	6.68E+14
83412.8	6.39E+14	80557.1	3.41E+15	77614.3	2.06E+16	74685.8	1.38E+16	71702.1	6.86E+14
83361.3	6.25E+14	80506.5	4.04E+15	77563.1	2.06E+16	74595.2	2.19E+16	71652.1	1.07E+15
83309.8	6.48E+14	80455.6	4.09E+15	77473.1	2.08E+16	74543.1	4.09E+16	71601.8	6.32E+14
83219.8	6.20E+14	80366.3	5.52E+15	77421.6	2.13E+16	74491.3	4.62E+16	71513.4	4.04E+16
83168.6	6.38E+14	80315.1	5.94E+15	77370.1	2.13E+16	74400.5	4.74E+16	71462.5	2.65E+16
83117.7	6.60E+14	80263.9	6.77E+15	77280.8	2.13E+16	74348.9	4.23E+16	71411.6	2.17E+16
83028.7	6.58E+14	80174.3	7.74E+15	77229.9	2.17E+16	74297.4	4.03E+16	71322.3	3.39E+16
82978.1	7.09E+14	80122.8	8.16E+15	77179.3	2.16E+16	74206.9	3.13E+16	71271.7	5.39E+16
82927.9	7.64E+14	80071.3	7.33E+15	77090.9	2.22E+16	74155.1	2.59E+16	71220.8	6.24E+16
82840.1	8.82E+14	79981.0	7.75E+15	77040.6	2.23E+16	74103.0	2.32E+16	71131.5	7.52E+16
82790.1	8.52E+14	79929.2	7.40E+15	76990.3	2.21E+16	74011.5	2.24E+16	71080.0	7.82E+16
82740.1	8.91E+14	79877.4	7.34E+15	76903.5	2.10E+16	73959.4	2.40E+16	71028.5	8.06E+16
82659.9	8.79E+14	79786.3	6.92E+15	76854.7	2.00E+16	73906.4	3.23E+16	70938.2	5.44E+14
82609.3	9.11E+14	79725.9	7.67E+15	76806.2	1.77E+16	73814.9	3.86E+16	70886.7	6.43E+14
82558.4	9.39E+14	79673.5	7.90E+15	76728.2	1.85E+16	73763.4	4.00E+16	70835.5	5.26E+14
82469.7	8.67E+14	79570.2	8.25E+15	76678.2	1.96E+16	73711.9	3.41E+16	70739.2	5.23E+14
82418.8	8.58E+14	79530.5	7.90E+15	76627.9	2.00E+16	73622.0	3.63E+16	70691.7	3.86E+14
82367.6	9.55E+14	79478.7	8.18E+15	76540.2	2.28E+16	73570.5	5.58E+16	70641.4	4.74E+14
82278.6	9.70E+14	79388.5	7.84E+15	76489.9	2.64E+16	73519.0	4.74E+16	70552.4	1.74E+16
82228.0	9.08E+14	79337.3	8.18E+15	76439.3	2.96E+16	73428.5	4.62E+16	70500.8	2.34E+16
66917.3	3.36E+17	79285.8	9.00E+15	76350.9	3.37E+16	73376.3	4.23E+16	70449.3	2.57E+16

Table A.6 (Continued)

Altitude (m)	$\mathrm{N_e}$ ($\mathrm{m^{-3}}$)	Altitude (m)	$\mathrm{N_e}$ ($\mathrm{m^{-3}}$)	Altitude (m)	$\mathrm{N_e}$ ($\mathrm{m^{-3}}$)
70358.8	3.10E+16	66976.1	1.82E+16	59872.2	1.21E+16
70313.1	3.87E+16	66887.8	6.23E+15	59812.1	1.58E+16
70254.9	3.99E+16	66837.5	8.85E+15	59720.7	3.53E+16
70151.9	5.46E+16	66794.8	1.15E+16	59669.5	3.28E+16
70112.5	6.28E+16	66708.2	4.97E+15	59618.3	3.03E+17
70061.0	6.45E+16	66660.7	1.79E+15	59528.4	3.89E+17
69970.8	7.64E+16	66613.1	4.31E+16	59476.8	4.94E+17
69918.7	7.32E+16	66528.7	6.63E+15	59425.3	5.88E+17
69866.6	7.95E+16	66103.8	8.07E+14	59335.4	8.49E+17
69771.8	7.63E+16	66052.0	1.98E+15	59284.2	8.48E+17
69719.6	7.31E+16	65961.2	3.21E+15	59233.0	8.48E+17
69667.8	6.43E+16	65908.7	1.81E+16	59144.0	8.48E+17
69577.0	5.50E+16	65850.2	2.34E+16	59093.7	8.48E+17
69524.6	4.37E+16	65763.3	1.23E+16	59043.4	1.49E+17
69472.5	3.57E+16	65714.9	1.04E+16	58955.3	8.38E+17
69381.9	7.33E+16	65666.7	1.02E+17	58904.4	6.03E+16
69330.4	7.77E+16	64964.2	1.48E+15	58854.1	5.36E+16
69279.2	8.85E+16	64912.3	1.80E+15	58773.7	6.18E+16
69189.6	9.57E+16	64860.2	2.32E+15	58723.4	6.33E+16
69138.7	1.06E+17	64771.5	1.24E+15	58673.4	5.14E+16
69087.8	1.15E+17	64723.1	1.54E+15	58585.3	5.06E+17
68999.1	8.62E+16	64674.9	8.35E+14	58535.0	5.72E+17
68948.8	6.74E+16	63887.0	3.56E+14	58484.7	8.46E+17
68898.5	2.26E+16	63602.6	1.16E+15	58396.0	8.45E+17
68810.7	8.29E+15	63556.0	1.58E+16	58345.4	8.45E+17
68767.8	2.84E+15	63506.0	1.70E+17	58294.8	8.45E+17
68717.2	2.06E+15	62819.9	2.61E+14	58205.5	8.45E+17
68629.1	4.65E+16	62389.5	1.04E+15	58154.0	8.45E+17
68578.8	5.48E+16	62337.4	2.18E+16	58102.2	8.44E+17
68528.5	6.09E+16	61059.1	7.55E+16	58012.3	5.85E+17
68439.8	7.61E+16	61009.7	1.28E+17	57960.2	8.44E+17
68388.6	8.45E+16	60960.6	1.79E+16	57908.0	6.34E+17
68337.7	8.98E+16	60873.7	2.59E+16	57809.9	1.60E+17
68248.1	1.02E+17	60823.1	5.72E+16	57758.4	1.15E+17
68197.5	1.10E+17	60780.5	9.91E+15	57707.2	4.71E+16
68146.3	1.01E+16	60691.5	4.27E+16	57617.6	5.84E+17
68055.7	1.88E+16	60499.8	5.37E+17	57566.4	8.43E+17
68002.4	6.37E+16	60449.2	6.40E+17	57515.2	8.43E+17
67949.1	2.79E+16	60398.6	8.54E+17	57425.8	8.43E+17
67856.7	1.83E+16	60309.6	8.53E+17	57374.3	8.42E+17
67797.9	8.61E+15	60258.4	8.53E+17	57323.1	8.42E+17
67746.4	1.35E+16	60207.1	5.90E+17	57235.0	8.42E+17
67656.5	7.83E+15	60117.2	3.42E+17	57186.0	8.42E+17
67605.2	2.82E+16	60066.0	1.75E+16	57137.2	8.42E+17
67554.0	4.55E+16	60015.1	3.77E+16	56857.1	2.36E+16
67026.4	4.23E+15	59924.6	1.68E+16	56814.7	4.29E+16

Table A.7: Inferred electron number densities measured by the electrostatic probe 6 on the RAM-C I flight. Reproduced from [220].

Altitude (m)	N_e (m^{-3})	Altitude (m)	N_e (m^{-3})	Altitude (m)	N_e (m^{-3})	Altitude (m)	N_e (m^{-3})	Altitude (m)	N_e (m^{-3})
83162.2	6.87E+14	80308.7	6.58E+15	77363.7	2.17E+16	74394.1	5.22E+16	71456.1	3.08E+16
83111.3	7.15E+14	80257.5	7.68E+15	77274.4	2.19E+16	74342.5	4.74E+16	71405.2	2.34E+16
83022.3	7.75E+14	80167.9	8.53E+15	77223.5	2.14E+16	74291.0	4.44E+16	71316.2	3.78E+16
82972.0	8.35E+14	80116.4	8.85E+15	77172.9	2.14E+16	74200.5	3.46E+16	71265.3	5.35E+16
82921.8	1.01E+15	80064.9	8.37E+15	77084.5	2.19E+16	74148.4	3.10E+16	71214.7	6.05E+16
82834.0	1.15E+15	79974.3	8.38E+15	77034.2	2.17E+16	74096.6	2.65E+16	71125.1	7.47E+16
82783.7	1.32E+15	79922.8	8.14E+15	76983.9	2.18E+16	74005.1	2.16E+16	71073.6	7.87E+16
82733.7	1.28E+15	79871.0	7.99E+15	76897.4	2.11E+16	73952.4	2.58E+16	71021.8	5.81E+16
82653.5	1.25E+15	79779.6	7.92E+15	76848.6	1.99E+16	73899.7	3.71E+16	70931.8	4.36E+14
82602.9	1.30E+15	79719.5	8.39E+15	76800.2	1.82E+16	73808.5	4.00E+16	70880.3	7.01E+14
82552.0	1.22E+15	79667.1	8.71E+15	76722.1	1.90E+16	73757.0	4.05E+16	70829.1	6.38E+14
82463.3	1.26E+15	79575.7	9.05E+15	76671.8	2.03E+16	73705.5	2.93E+16	70735.9	5.24E+14
82412.4	1.29E+15	79524.1	9.13E+15	76621.8	2.11E+16	73615.6	5.27E+16	70685.6	5.08E+14
82361.2	1.29E+15	79472.3	9.38E+15	76533.8	2.68E+16	73564.1	5.63E+16	70635.0	5.56E+14
82272.2	1.20E+15	79382.1	9.05E+15	76483.5	3.17E+16	73512.6	4.55E+16	70546.0	2.63E+16
82221.6	1.22E+15	79330.9	9.66E+15	76432.9	3.55E+16	73422.1	4.85E+16	70494.4	3.24E+16
82170.7	1.46E+15	79279.4	1.01E+16	76344.5	3.78E+16	73369.9	4.35E+16	70442.9	3.02E+16
82081.7	1.70E+15	79189.8	1.25E+16	76293.9	3.55E+16	73317.8	3.96E+16	70352.4	3.72E+16
82030.8	1.81E+15	79138.6	1.43E+16	76243.0	3.28E+16	73227.3	4.10E+16	70300.3	4.02E+16
81979.6	1.95E+15	79087.7	1.56E+16	76154.0	2.49E+16	73175.8	4.29E+16	70248.5	4.56E+16
81889.7	2.10E+15	78998.1	1.58E+16	76103.1	2.36E+16	73124.3	4.63E+16	70157.6	5.80E+16
81837.9	2.19E+15	78946.9	1.62E+16	76052.2	2.07E+16	73033.7	5.06E+16	70106.1	5.95E+16
81785.8	2.10E+15	78895.7	1.41E+16	75960.4	1.93E+16	72981.6	7.23E+15	70054.0	6.59E+16
81687.6	2.54E+15	78807.0	1.12E+16	75905.3	1.88E+16	72929.8	9.82E+15	69964.1	7.88E+16
81636.4	2.52E+15	78757.0	1.03E+16	75852.5	1.20E+16	72839.0	1.35E+16	69912.3	6.74E+16
81584.9	2.54E+15	78714.6	8.58E+15	75755.6	1.30E+16	72787.5	1.37E+16	69860.2	6.66E+16
81495.0	2.66E+15	78626.5	7.74E+15	75703.5	2.33E+16	72732.3	1.22E+16	69764.1	7.29E+16
81443.5	2.41E+15	78575.9	7.23E+15	75651.4	3.82E+16	72641.8	1.04E+16	69713.2	6.57E+16
81391.7	2.54E+15	78525.0	1.03E+16	75560.8	4.28E+16	72589.9	1.17E+16	69661.4	6.41E+16
81301.7	2.31E+15	78436.3	1.85E+16	75509.3	3.98E+16	72538.4	6.90E+16	69570.3	5.43E+16
81250.5	2.52E+15	78385.7	1.98E+16	75457.8	3.79E+16	72448.5	6.37E+16	69518.2	4.54E+16
81199.3	2.27E+15	78335.1	2.12E+16	75367.3	3.43E+16	72397.6	5.89E+16	69466.1	4.12E+16
81110.0	3.41E+15	78246.1	2.11E+16	75315.2	3.25E+16	72346.7	5.49E+16	69375.5	6.75E+16
81059.7	3.62E+15	78194.6	2.14E+16	75263.3	3.03E+16	72257.7	4.64E+16	69324.0	7.60E+16
81009.1	4.51E+15	78143.4	2.08E+16	75172.2	2.87E+16	72207.1	4.61E+16	69272.8	8.39E+16
80920.7	5.58E+15	78053.2	1.91E+16	75120.1	2.97E+16	72156.5	4.76E+16	69183.2	9.42E+16
80870.1	6.11E+15	78001.7	1.73E+16	75068.0	3.16E+16	72067.8	5.34E+16	69132.3	1.05E+17
80819.5	6.18E+15	77949.9	1.57E+16	74977.1	3.00E+16	72016.9	5.92E+16	69081.4	1.07E+17
80739.1	4.90E+15	77859.6	1.23E+16	74925.0	1.18E+16	71966.0	1.68E+15	68992.7	8.09E+16
80689.1	4.97E+15	77808.1	1.34E+16	74872.9	1.44E+16	71877.3	1.23E+15	68942.4	4.83E+16
80639.1	4.52E+15	77749.0	1.78E+16	74782.4	2.03E+16	71826.7	7.47E+14	68892.4	2.31E+16
80550.7	4.34E+15	77659.1	2.03E+16	74730.9	1.83E+16	71784.1	9.12E+14	68804.3	4.86E+15
80500.1	5.18E+15	77607.9	2.10E+16	74679.4	1.35E+16	71696.0	1.04E+15	68761.7	4.67E+15
80449.2	5.37E+15	77556.7	2.11E+16	74588.8	2.04E+16	71645.7	1.91E+15	68711.1	2.26E+15
80359.9	5.99E+15	77466.7	2.15E+16	74536.7	4.59E+16	71595.7	9.83E+15	68622.7	5.47E+16
66917.3	3.36E+17	77415.2	2.20E+16	74484.6	5.09E+16	71507.3	4.10E+16	68572.4	6.20E+16

Table A.7 (Continued)

Altitude (m)	N$_e$ (m^{-3})	Altitude (m)	N$_e$ (m^{-3})	Altitude (m)	N$_e$ (m^{-3})
68522.1	6.70E+16	61053.0	6.50E+16	58005.3	8.02E+17
68433.4	8.05E+16	61003.6	2.27E+17	57953.5	8.02E+17
68382.2	8.26E+16	60954.5	1.69E+17	57899.8	8.02E+17
68331.3	9.34E+16	60867.3	3.92E+16	57803.5	8.02E+17
68241.7	1.04E+17	60817.0	8.06E+16	57752.0	8.02E+17
68191.1	1.14E+17	60774.1	1.37E+16	57700.8	8.02E+17
68140.2	8.90E+15	60685.1	6.74E+16	57611.2	8.02E+17
68049.0	8.05E+15	60493.4	6.57E+17	57560.0	8.02E+17
67995.7	4.26E+16	60443.1	8.12E+17	57508.7	8.02E+17
67942.4	4.68E+16	60392.5	8.11E+17	57419.4	8.02E+17
67850.3	1.45E+16	60303.2	8.11E+17	57367.9	8.02E+17
67791.2	4.82E+15	60251.9	8.10E+17	57316.7	8.02E+17
67740.0	8.54E+15	60200.4	8.10E+17	57228.9	8.02E+17
67650.1	9.16E+15	60110.8	8.09E+17	57179.9	8.02E+17
67598.8	3.45E+16	60059.6	1.76E+17	57131.1	8.02E+17
67547.6	5.08E+16	60008.7	1.33E+17	56850.7	8.02E+17
67020.0	8.77E+14	59917.9	8.64E+16	56808.0	5.57E+17
66970.0	1.51E+16	59865.5	9.38E+16	56758.3	3.25E+17
66881.7	1.25E+16	59805.4	8.04E+16	56669.9	2.67E+16
66831.4	1.25E+16	59714.3	9.71E+16	56618.4	8.02E+17
66788.4	1.42E+16	59663.1	9.37E+16	56567.2	8.02E+17
66702.1	1.06E+16	59611.9	4.83E+17	56478.2	8.02E+17
66654.6	9.39E+15	59522.0	8.05E+17	56428.2	8.02E+17
66607.0	6.10E+16	59470.4	8.05E+17	56377.9	8.02E+17
66522.3	6.60E+15	59418.9	8.05E+17	56288.9	8.02E+17
66097.4	6.81E+14	59329.0	8.05E+17	56236.8	8.02E+17
66045.6	2.44E+15	59277.8	8.04E+17	56185.0	8.02E+17
65954.8	1.52E+15	59226.9	8.04E+17	56095.1	8.02E+17
65902.3	1.53E+16	59137.9	8.04E+17	56044.2	2.89E+17
65849.9	2.86E+16	59087.3	8.04E+17	55993.6	2.54E+16
65756.9	1.44E+16	59037.0	8.03E+17	55904.0	1.34E+16
65708.8	1.13E+16	58948.9	8.03E+17	55847.9	1.22E+15
65660.6	1.02E+17	58898.3	8.03E+17	55796.1	1.74E+15
64957.8	3.35E+15	58847.7	8.03E+17	55705.9	8.44E+14
64905.6	4.81E+15	58767.3	8.03E+17	55654.7	3.70E+17
64853.8	2.89E+15	58717.3	8.03E+17	55603.7	8.02E+17
64765.4	1.76E+15	58667.0	8.03E+17	55513.8	5.32E+17
64717.3	8.87E+14	58579.2	8.03E+17	55461.7	8.02E+17
64668.8	7.20E+14	58528.6	8.03E+17	55409.9	8.02E+17
63880.6	3.49E+14	58478.3	8.02E+17	55319.1	8.02E+17
63596.5	1.01E+16	58389.9	8.02E+17	55267.6	8.02E+17
63548.4	1.82E+16	58339.0	8.02E+17	55216.0	8.02E+17
63500.2	5.07E+16	58288.4	8.02E+17	55125.5	8.02E+17
62813.2	2.56E+14	58198.8	8.02E+17	55073.4	4.57E+17
62383.1	5.23E+15	58147.3	8.02E+17	55021.6	3.02E+16
62331.0	2.11E+17	58095.2	8.02E+17	54931.4	1.64E+16

Figure A.1: Photo-realistic rendering generated with the DALL-E 2 AI system using the prompt: "A solution to communications plasma blackout for hypersonic vehicles." Interpretation of this result currently remains unresolved.